

Modelisation of the diffusive transport of algal blooms in a coastal environment using a stochastic method

Antoine Joly

▶ **To cite this version:**

Antoine Joly. Modelisation of the diffusive transport of algal blooms in a coastal environment using a stochastic method. Other [q-bio.OT]. Université Paris-Est, 2011. English. NNT : 2011PEST1088 . pastel-00668176

HAL Id: pastel-00668176
https://pastel.hal.science/pastel-00668176

Submitted on 9 Feb 2012

HAL is a multi-disciplinary open access archive for the deposit and dissemination of scientific research documents, whether they are published or not. The documents may come from teaching and research institutions in France or abroad, or from public or private research centers.

L'archive ouverte pluridisciplinaire **HAL**, est destinée au dépôt et à la diffusion de documents scientifiques de niveau recherche, publiés ou non, émanant des établissements d'enseignement et de recherche français ou étrangers, des laboratoires publics ou privés.

Université Paris-Est

Sciences, Ingénierie et Environnement

Thèse

Présentée pour l'obtention du grade de DOCTEUR DE L'UNIVERSITE PARIS-EST

par

Antoine Joly

Modélisation du transport des algues en milieu côtier par une approche stochastique

---

Spécialité

Mécanique des Fluides

Soutenue le 14 décembre 2011 devant un jury composé de :

Rapporteur	**Jean-Marie MOUCHEL**	(Université Paris 6)
Rapporteur	**François SCHMITT**	(Université Lille 1)
Examinateur	**Michel BENOIT**	(EDF R& D / ENPC)
Directeur de thèse	**Damien VIOLEAU**	(EDF R& D)
Examinateur	**Dominique ASTRUC**	(IMFT)
Examinateur	**Jean-Pierre MINIER**	(EDF R& D)
Président du jury	**Pierre SAGAUT**	(Université Paris 6)
Invité	**Rob UITTENBOGAARD**	(Deltares)

Thèse effectué au sein du **Laboratoire d'Hydraulique Saint-Venant**

c/o EDF R& D
6, quai Watier
BP 49
78401 Chatou cedex
France

Résumé

Ce mémoire de thèse a pour but de présenter un modèle de prédiction du transport des algues en mer le long des côtes. La méthode choisie a été d'utiliser un code industriel eulérien pour prédire l'écoulement moyen sur une grande surface, et d'ensuite ajouter un modèle lagrangien pour prédire le mouvement des particules individuelles. Ce modèle lagrangien comporte trois étapes. Premièrement, les caractéristiques moyennes du fluide trouvées avec le modèle eulérien sont utilisées pour alimenter un modèle stochastique pour trouver les vitesses turbulentes du fluide à l'emplacement des particules modélisant les algues. Ensuite ces vitesses turbulentes sont utilisées à travers les composantes de la force de traînée, de l'inertie, de la force de Basset et de la poussée d'Archimède pour trouver les vitesses des corps. La dernière étape consiste à utiliser ces vitesses des corps pour calculer leurs trajectoires. Une méthode avec un intégrateur exact a été développée pour résoudre ces équations. Ce modèle a ensuite été validé grâce à deux expériences. Dans la première expérience, des sphères de tailles différentes ont été lâchées dans deux fluides avec des densités différentes, où une turbulence stationnaire quasi-homogène a été générée en utilisant une paire de grilles oscillantes. Dans la deuxième expérience des particules sphériques ont été lâchées dans un écoulement non-homogène. Cette écoulement a été obtenu en obstruant partiellement un canal, afin qu'une zone de recirculation soit générée. Le modèle de transport des particules a ensuite été testé sur des simulations d'un écoulement réel le long des côtes normandes, dans lequel des particules numériques représentant des algues ont été lâchées.

Mots clés :

Transport stochastique de particules, Couplage eulérien-lagrangien, Intégrateur exact, Turbulence de grilles, Canal partiellement obstrué, Transport côtier des algues

Modelling of the transport of algae in a coastal environment using a stochastic method

Abstract

The aim of this PhD thesis was to develop a model to predict the motion of algae in sea waters along a coastline. The method chosen was to use a large Eulerian industrial code to model the mean flow, and add Lagrangian model to predict the motion of individual particles. This Lagrangian model is a three-step model. In the first modelling step, the mean flow characteristics at the location of the particles (solid bodies modelling the algae) are extracted from the Eulerian model and imputed into a stochastic model to find the turbulent fluid velocities. These fluid velocities are used in the second step to solve for the solid body velocities, by solving for the drag, momentum, buoyant and Basset history forces. The final modelling step is to use these solid body velocities to calculate the trajectories of particles. An exact integrator method was then developed to solve for these equations. The model was then validated using two experiments. Firstly sphere of different size were released in fluids of different densities, where a stationary quasi-homogeneous turbulence. This turbulence was generated by oscillating a pair of grids. In the second experiment spherical particles were released in a non-homogeneous turbulent flow. This flow was achieved by partially obstructing a channel, so that a recirculation zone was generated. The particle transport model was then tested numerically using the simulations of a real flow along the coasts of Normandy where numerical particles representing algae were released.

Keywords:

Stochastic particle transport, Eulerian-Lagrangian coupling, Exact integrator method, Grid generated turbulence, Partially obstructed channel flow, Coastal algae transport

Remerciements

out d'abord je tiens à remercier Monsieur Damien Violeau, mon directeur de thèse, qui est parvenu à être très disponible pendant toute la durée de ma thèse et qui a su répondre à toute mes questions. Je tiens aussi à remercier Monsieur Michel Benoit, le directeur du Laboratoire d'Hydraulique Saint-Venant et mon co-encadrant de thèse, qui a su me faciliter la thèse pendant ces trois ans.

J'aimerai aussi remercier Messieurs Jean-Marie Mouchel et François Schmitt pour avoir accepté d'être rapporteurs de mon travail. Je voudrai aussi remercier Monsieur Pierre Sagaut qui qui a assuré la présidence du jury de thèse.

Je voudrai aussi remercier tout particulièrement Monsieur Jean-Pierre Minier pour toute l'aide qu'il m'a apporté pendant ma thèse ainsi que le temps qu'il a pris pour m'expliquer les modèles stochastiques. Je le remercie aussi d'avoir accepté de faire partie de mon jury de thèse.

Je tiens aussi à remercier Messieurs Dominique Astruc, Frédéric Moulin et Sébastien Cazin, ainsi que le reste de l'équipe de l'IMFT, pour toute l'aide qu'ils m'ont fournie dans la conception et la réalisation des expériences. Je remercie aussi Monsieur Dominique Astruc d'avoir accepté de faire partit de mon jury de thèse.

Je remercie Monsieur Rob Uittenbogaard pour toutes les questions avisées qu'il a pu poser pendant tout le suivi de ma thèse ainsi que pour son déplacement depuis les Pays-Bas pour pouvoir faire partie de mon jury de thèse.

Je continuerai mes remerciements en mentionnant tous les membres d'EDF et du Laboratoire d'Hydraulique Saint-Venant que j'ai pu côtoyer et qui ont su créer une très bonne ambiance de travail, tout en restant professionnels et dynamiques.

Merci ensuite à Jean-Romain, et au reste de l'équipe du Pomphy pour toute l'aide qu'ils m'ont apportée pendant mes expériences. Merci à Réza, qui a été un très bon chef de projet (même si ce fut court). Merci à Chi-Tuan qui m'a fait profiter de plein de places de rugby. Merci à Jean-Michel qui est arrivé à rester très disponible pour toutes les questions sur Telemac que j'ai pu avoir.

Merci aussi à Elodie d'avoir ouvert la voie et merci à Etienne d'avoir accompli sa thèse en parallèle de la mienne. Merci à mon voisin de bureau Cédric pour toutes les conversations rugby que l'on a eu ensemble. Merci aussi à Andrès d'être passé dans notre bureau chaque fois qu'il en avait marre de travailler. Merci à Christophe et Martin pour tous les joggings sur l'île des Impressionnistes

Merci aussi à toutes les autres personnes que j'ai pu côtoyer de près ou de loin à Chatou que ce soit le personnel permanent ou le personnel temporaire.

Merci à mes parents, mes grands-parents, Pascale, Fredo et Armel d'avoir assisté à ma soutenance, et surtout d'avoir essayé de comprendre ma présentation.

Merci enfin à ma chérie Amélie, grâce à elle j'ai pu m'aérer l'esprit et penser à autre chose que mon mémoire pendant la fin de ma thèse. Merci aussi pour tout le soutien et la tendresse qu'elle a pu m'apporter.

Contents

1 Introduction **2**

2 Context **6**

2.1 The algae problematic 7

2.2 Modelling approach 8

2.3 Categorising the problem 8

2.4 Existing algae transport models 9

2.5 Existing particle transport models 10

3 Environmental Flow Modelling **12**

3.1 General principles of fluid mechanics 13

3.2 General principles of turbulence modelling - first-order models 14

3.3 General principles of turbulence modelling - second-order models 19

4 Dynamic Properties of Solid Particle Motion **24**

4.1 Forces acting on the motion of a solid particle in fluid 25

4.2 Simplification to an isotropic body 30

4.3 Testing the impact of different force components 30

4.4 Testing the physical characteristics of solid bodies 33

5 Fluid Velocities Model **38**

5.1 A brief overview of stochastic modelling in fluid mechanics 39

5.2 The Simplified Langevin Model of turbulence 40

5.3 Testing the Simplified Langevin Model 45

6 Numerical Resolution **50**

6.1 Two-phase modelling 51

6.2 Preliminary numerical considerations 52

6.3 The exact integrator method 53

6.4 Asymptotic behaviour of the model 56

7 Particles Falling in Quasi-Homogeneous Turbulence **60**

7.1 Experimental setup . . . 61
7.2 The turbulent regime . . . 61
7.3 Particle tracking . . . 65
7.4 Model Validation . . . 68

8 Particles Released in a Partially Obstructed Channel 78
8.1 Experimental setup . . . 79
8.2 The flow regime . . . 79
8.3 Particle tracking . . . 83

9 Real Life Applications 94
9.1 Information on the type of algae considered . . . 95
9.2 Applying the model to represent algae particles . . . 96
9.3 Application around a real bathymetry . . . 98
9.4 Description of the problematic around Paluel . . . 99
9.5 Transport patterns . . . 102
9.6 Particles exiting the domain . . . 112

10 Conclusion 120
10.1 Conclusion on the validity of the model . . . 121
10.2 Strong points of the model . . . 122
10.3 Limitations and perspectives . . . 123
10.4 Advices to use the model . . . 124

A Calculations relative to the exact integrator model 126
A.1 The three steps solid particle transport model . . . 127
A.2 Analytical solution for the fluid velocities . . . 127
A.3 Analytical solution for the solid particle velocities . . . 128
A.4 Analytical solution for the position of the body . . . 131
A.5 Solving the stochastic integrals . . . 133

B Asymptotic behaviour of the exact integrator model 142
B.1 For $dt \gg T_i^{(s)}$ . . . 144
B.2 For $dt \ll T_i^{(s)}$ . . . 146
B.3 For $dt \gg \tau_{part}$ . . . 149
B.4 For $dt \ll \tau_{part}$ . . . 152

C Video particle tracking image processing 158
C.1 Methodology for the image processing . . . 159
C.2 Flow charts of the algorithms used in the image processing . . . 170

D Stopping particles at boundaries in a triangular mesh **174**

D.1 Finding in which element a particle can be found 175

D.2 Interpolate the nodal values inside an element 176

D.3 Finding inside which element a particle is after its displacement 178

D.4 Finding which boundary was crossed by a particle 179

Bibliography **185**

List of Figures

2 Context **6**

2.1 Surface covered in Ulva in Brittany during the year 2009 7

3 Environmental Flow Modelling **12**

3.1 An example of a recording of a turbulent fluid velocity in time 15

4 Dynamic Properties of Solid Particle Motion **24**

4.1 The evolution of V_Z and τ_{part} for spherical particles falling in a stationary fluid 33

4.2 Typical shape of Taylor eddies 34

4.3 The transport of solid particles with different physical characteristics in Taylor eddies 35

5 Fluid Velocities Model **38**

5.1 Second moments found for fluid particles released in stationary homogeneous isotropic turbulence 46

5.2 Second moments of fluid particle velocities in stationary quasi-isotropic grid turbulence 47

5.3 The autocorrelation of the fluid velocities in stationary quasi-isotropic grid turbulence 48

7 Particles Falling in Quasi-Homogeneous Turbulence **60**

7.1 Scheme of the double-grid setup 61

7.2 An instantaneous PIV recording 62

7.3 The kinetic energy and its dissipation rate in oscillating grid turbulence 63

7.4 Vertical profiles for the characteristic values of turbulence in oscillating grid turbulence. 65

7.5 Dimensionless settling velocities for different particle fluid density ratios. 67

7.6 Volume of measurements for the two perpendicular cameras recording falling bodies. 67

7.7 Example of particles recorded for the two cameras. 68

7.8 Probability density functions for particle velocities present inside the volume of measurement 70

7.9 Probability density functions for numerical particle velocities present inside the volume of measurement transported with different initial particle velocities 72

7.10 Particle statistics used to illustrate the filtering of turbulent eddies by solid particles . 73
7.11 The correlation profiles of velocities for particles released in quasi-homogeneous turbulence 74

8 Particles Released in a Partially Obstructed Channel 78

8.1 Experimental setup 79
8.2 The streamlines for the flow defined by the experimental set up shown in figure 8.1 . 80
8.3 Profiles of the horizontal velocity plotted at different locations along the canal 81
8.4 Profiles of the turbulent kinetic energy plotted at different locations along the canal . . 82
8.5 Profiles of the turbulent kinetic energy dissipation rate plotted at different locations along the canal 82
8.6 Experimental setup to record the particle trajectories 83
8.7 Typical particle trajectories 84
8.8 A disturbed image recorded by the camera due to the air entrainment 84
8.9 An annotated example of the results of the partially obstructed channel experiment . 85
8.10 Partially obstructed channel: proportion of released particles entering a quadrant of the window of measurement 87
8.11 Partially obstructed channel: mean particles residence time inside a quadrant of the window of measurement 88
8.12 Partially obstructed channel: proportion of released particles entering a quadrant of the window of measurement 89
8.13 Partially obstructed channel: mean particles residence time inside a quadrant of the window of measurement 90

9 Real Life Applications 94

9.1 Example of algae 95
9.2 The drag coefficient for an Iridaea flaccida 96
9.3 Comparison between a free falling alga and an equivalent sphere 97
9.4 Trajectories of different bodies released in Taylor eddies 98
9.5 The bathymetry around the Paluel power station 99
9.6 Vector plots showing the importance of radiation stresses 103
9.7 Particles transported in the flow around Paluel using model VII 105
9.8 Particles transported in the flow around Paluel using model VIII 106
9.9 Particles transported in the flow around Paluel using model IV 107
9.10 Particles transported in the flow around Paluel using model III 108
9.11 Particles transported in the flow around Paluel using model II 109
9.12 Particles transported in the flow around Paluel using model V 110
9.13 Particles transported in the flow around Paluel using model VI 111
9.14 Description of the pumps used by the Paluel power station 112

9.15 Bar plots of the number of particles entering each pumps, for different solid body dynamics models . . . 113
9.16 Bar plots of the number of particles entering each pumps, for different solid body shape or size . . . 114
9.17 Fluid velocity vectors around the pumps of the Paluel power station . . . 115
9.18 Mean location at which the particles exit the domain for different particle transport model . . . 116
9.19 Cumulative number of particles entering each pumps for models considering different particles . . . 116

C Video particle tracking image processing **158**

C.1 The tools used to calibrate the cameras of the oscillating grids experiment . . . 159
C.2 Probability density functions of the errors on the positions of the fishing weights . . . 160
C.3 Steps necessary to obtain the position of the bodies from an image recorded by a camera 162
C.4 Steps required to find the position of two superposed bodies . . . 163
C.5 Steps necessary to remove impurities the size of a particle . . . 164
C.6 A disturbed image due to the air entrainment . . . 165
C.7 The starting point to associate recorded particles . . . 166
C.8 Studying the different possible particle counterparts . . . 166
C.9 A position of a particle at time t, and the recognised bodies in each camera at time $t = 1$ 167
C.10 Distance travelled from the intial position at time t . . . 168
C.11 Position of the particles present in the field of vision of both cameras . . . 169
C.12 Flow chart of the algorythm used to calibrate the volume of measurement . . . 170
C.13 Flow chart of the algorythm used to find the position of particles in an image recorded by a camera . . . 171
C.14 Flow chart of the algorithm used to find the three dimensional trajectories of bodies for the oscillating grids experiment . . . 172

D Stopping particles at boundaries in a triangular mesh **174**

D.1 A particle inside a element of a first order triangular mesh . . . 175
D.2 A transformation of coordinates of an element using barycentric coordinates . . . 176
D.3 A triangular element, with three boundaries, surrounded by six neighbouring elements 178
D.4 A particle path crossing a triangular element boundary . . . 179

Nomenclature

Roman Symbols

$\acute{b}_i$	Coefficient relating $T_i^{(s)}$ to T_i	(-)
b_{ij}	Anisotropy tensor	(–)
$B_i^{(s)}$	Coefficient corresponding to the standard deviation of the stochastic part of the solid particle velocity	($m{\cdot}s^{-3/2}$)
C_0	Constant used in the Simplified Langevin Model, typically set to 2.1	(-)
C_B	Basset history force constant	($kg{\cdot}s^{1/2}$)
$C_{i,Bas}$	The Basset history force components independent of the current time	($kg{\cdot}m{\cdot}s^2$)
$C_{D,a}$	Drag coefficient for an alga	(–)
$\check{C}_i$	A constant used in the exact integrator model	(-)
$C_i^{(s)}$	Coefficient regrouping all the mean flow components seen by a solid particle	($m{\cdot}s^{-2}$)
D	Characteristic length of a solid body	(m)
D_a	Diameter of a disk representing an alga	(m)
D_{ist}	Distance between the oscillating grids	(m)
D_s	Diameter of a solid sphere	(m)
f	Frequency of the grid oscillation	(s^{-1})
F_a	Coefficient of the solid particle velocity linked to the evolution of the fluid velocities	(-)
F_b	Coefficient of the solid particle velocity linked to the velocity differences between the fluid and the solid body	(s^{-1})
$F_{i,c}$	Coefficients of the solid particle velocity linked to constant values at time t	($m{\cdot}s^{-2}$)
$\mathbf{g}$	Vectorial acceleration due to gravity	($m{\cdot}s^{-2}$)
H	Mesh size of the oscillating grids	(m)
h	Depth of the fluid	(m)
k	Turbulent kinetic energy	($m^2{\cdot}s^{-2}$)
$\check{K}_i$	A constant used in the exact integrator model	(-)
M	Added mass constant for an isotropic body	(kg)
m	Mass of a solid body	(kg)

M_a	Added mass constant for an alga	(kg)
M_{ij}	Added mass tensor of a body	(kg)
M_s	Added mass constant for a sphere	(kg)
N	Number of subintervals in the numerical window of the Basset history force	(–)
N_r	Number of particles present in the flow	(pcs)
P	Fluid pressure	($\mathrm{kg{\cdot}m^{-1}{\cdot}s^{-2}}$)
$\check{Q}_i$	A constant used in the exact integrator model	(-)
Re	Reynolds number of the flow	(–)
Re_a	Particle Reynolds number of an alga	(–)
Re_p	Particle Reynolds number	(–)
Re_s	Particle Reynolds number of a sphere	(–)
Re_{set}	Particle Reynolds number once the terminal settling velocity has been reached	(-)
S	Cross-sectional area of a solid body	($\mathrm{m^2}$)
S_a	Surface area of a disk representing an alga	($\mathrm{m^2}$)
S_{ij}	Mean rate-of-strain tensor	($\mathrm{s^{-1}}$)
s_{ij}	Fluctuating rate of strain tensor	($\mathrm{s^{-1}}$)
$\mathcal{S}$	Scalar mean rate of strain	($\mathrm{s^{-1}}$)
S_s	Cross-sectional area of a sphere	($\mathrm{m^2}$)
St_{set}	Stokes number used to characterise the influence of the turbulence	(-)
T	Integral of the autocorrelation of fluid velocities in stationary homogeneous isotropic turbulence	(s)
t_a	Thickness of a disk representing an alga	(m)
$T_i^{(s)}$	The integral time scale of the fluid velocities seen by a solid body	(s)
T_t	Turbulent characteristic time (linked to large eddies)	(s)
t_{win}	Time of the numerical window used to solve for the Basset history force	(s)
$\mathbf{U}$	Vectorial fluid velocity	($\mathrm{m{\cdot}s^{-1}}$)
U_i	Fluid velocity along the $\mathrm{i^{th}}$ direction	($\mathrm{m{\cdot}s^{-1}}$)
$\overline{U_i}$	Turbulence-averaged fluid density	($\mathrm{m{\cdot}s^{-1}}$)
U_i'	Turbulent fluctuations of the fluid density around the mean	($\mathrm{m{\cdot}s^{-1}}$)
$\overline{U_i'U_j'}$	Reynolds stresses	($\mathrm{m^2{\cdot}s^{-2}}$)
$U_{rms,i}$	Turbulent intensity	($\mathrm{m{\cdot}s^{-1}}$)
$U_i^{(s)}$	Fluid velocities seen by a solid body	($\mathrm{m{\cdot}s^{-1}}$)
u_l	Characteristic velocity of the large turbulent eddies	($\mathrm{m{\cdot}s^{-1}}$)

u_s	Characteristic velocity of the small turbulent eddies	$(m{\cdot}s^{-1})$
$\mathbf{V}$	Vectorial particle velocity	$(m{\cdot}s^{-1})$
V_i	Particle velocity along the i^{th} direction	$(m{\cdot}s^{-1})$
V_{ol}	Total volume occupied by the particles and the fluid	(m^3)
V_{set}	Settling velocity for solid particles falling in stationary fluid	$(m{\cdot}s)$
W_i	Wiener process	(-)
X_i	Position of a particle	(m)

Greek Symbols

α_i	Constants used in the exact integrator model	(-)
α_x, α_y	Constants used used to correct the parallax of a camera	$(pixels^{-1})$
β	A constant used in the exact integrator model	(-)
β_x, β_y	Constants used used to correct the parallax of a camera	$(mm{\cdot}pixels^{-1})$
Δ	Stroke of the grid oscillation	(m)
Δt	The time of one subinterval used to solve the Basset history force	(s)
ε	Dissipation rate of the turbulent kinetic energy	$(m^2{\cdot}s^{-3})$
η	Free-surface elevation	(m)
Γ_i	The stochastic integral of the solid particle velocity	$(m{\cdot}s^{-1})$
γ_i	The stochastic integral of the fluid velocity	$(m{\cdot}s^{-1})$
λ_l	Characteristic size of the large turbulent eddies	(m)
λ_s	Characteristic size of the small turbulent eddies	(m)
ν	Kinematic viscosity	$(m^2{\cdot}s^{-1})$
ν_T	Turbulent viscosity	$(m^2{\cdot}s^{-1})$
Ω	Volume of a solid body	(m^3)
Ω_a	Volume of a disk representing an alga	(m^3)
Ω_f	Volume fraction of particles	(–)
Ω_s	Volume of a sphere	(m^3)
Φ_i	The stochastic integral of the solid particle position	(m)
ψ_i	The derivative in the integral of the Basset history force	$(m{\cdot}s^{-2})$
ψ_n	The derivative ψ_i at time τ_n	$(m{\cdot}s^{-2})$
ρ_f	Fluid density	$(kg{\cdot}m^{-3})$
ρ_s	Solid body density	$(kg{\cdot}m^{-3})$
$\rho_{s/f}$	Ratio of the density between the solid particle and the surrounding fluid	(-)
τ_l	Characteristic time of the large turbulent eddies	(s)

τ_n The time t minus n time steps Δt ..... (s)

τ_{part} The particle relaxation time ..... (s)

τ_s Characteristic time of the small turbulent eddies ..... (s)

Chapter 1

Introduction

Le mouvement de corps dans un écoulement est un problème classique de mécanique des fluides. Son analyse est nécessaire, par exemple, pour le transport de sédiments le long du littoral, de bulles d'air dans un tuyau ou des aérosols relâchés par un combustible. Ces particules peuvent poser des problèmes de fonctionnement pour beaucoup d'industriels, et des questions environmentales capitales.

Ce mémoire se concentre sur le transport d'algues le long des côtes. Les modèles existants pour ce type de problèmes reposent sur une approche biologique, où l'évolution d'une population d'algues est modélisée à long terme par l'apport de nutriments. Cependant, pour la gestion d'une structure en bord de mer, il est important de connaître les réponses à court terme de ces algues à l'évolution d'un écoulement naturel déterminé par la marée.

Pour prendre en compte les spécificités d'un écoulement côtier il faut pouvoir modéliser les courants de marée, l'effet des vagues ainsi qu'une bathymétrie complexe. Ainsi il est proposé ici de coupler deux modèles ; un modèle eulérien de relativement grande échelle pour l'écoulement moyen et un modèle stochastique lagrangien de petite échelle pour le transport des algues.

Ce mémoire est divisé en sept chapitres. Premièrement le contexte motivant le besoin de la thèse est expliqué (chapitre 2). Ensuite les bases de la mécanique des fluides nécessaires pour comprendre le modèle développé sont rappelées dans le chapitre 3. Vient ensuite une description des forces qui régissent le mouvement d'un corps dans un écoulement (chapitre 4). Pour modéliser ces forces il est nécessaire de connaître la vitesse du fluide à la position d'un corps. Le modèle utilisé est donc décrit dans le chapitre 5. Puis la résolution numérique est ensuite expliquée dans le chapitre 6. Les validations de ce modèle numérique sont ensuite réalisées à partir de deux expériences (chapitres 7 et 8). La première concerne le cas de particules relâchées dans une turbulence stationnaire, quasi-isotrope, générée par des grilles oscillantes, et la deuxième envisage des particules dans un canal partiellement obstrué. Fort de ces validations, le modèle est ensuite testé pour l'écoulement réel autour d'une centrale électrique en Normandie, dont les résultats préliminaires sont donnés dans le chapitre 9.

The presence of bodies in a flow and the transport patterns of these bodies is a classic problem in fluid mechanics. It's analysis is required, whether it is for the transport of sediments along a coastline, the apparition of air bubbles in pipe flow or aerosols released by fossil fuels. It is important to develop tools predicting the motion of those particles, as they can hinder the operation of many industrial structures and affect severely the environment.

The focus of this thesis is on the transport of algae particles along a coastline, as it is a problem that has only been studied from a biological point of view. Typical algae transport model focus on the long term evolution of a population (or bloom) of algae by modelling the inflow of nutriments. However there is an industrial need to predict the short term response of such a population to flow variations due to tidal effects.

The aim of this thesis is therefore to present a model that will predict the transport of algae particles along the coastline. The environmental flow along a coastline has several specificities, including tidal currents, wave-breaking and a complex bathymetry, that need to be accounted for. These affect the flow on a large scale, however the motion of algae particles is also subject to smaller scale effects, such as the inertial properties of the algae, or the turbulence of the flow. In order to combine the large scale effects and the small scale effects efficiently, the transport of algae particles along the coastline is modelled through the coupling of two models. A relatively large scale Eulerian model is used to solve for the mean flow and a small scale Lagrangian stochastic particle model is used to predict the turbulent fluctuations of the flow and the transport of individual algae particles.

This thesis is divided into seven chapters. Firstly the context that led to a need for this research will be explained (chapter 2). Then the theoretical background of fluid mechanics necessary to understand to development of the model will be explained in chapter 3. Thirdly the forces acting on the motion of a particle transported by a flowing fluid will be described (chapter 4). A necessary requirement to predict the transport the motion of solid particles is to know the fluid velocity at the location of the particle, and therefore the model predicting the turbulent velocity at the location of a fluid particle will be explained in chapter 5. The combination of a fluid velocity and particle velocity model creates a complex model to solve numerically, and therefore the development and properties of such a model will be presented in chapter 6. This model will then be validated using two experiments (chapters 7 and 8). The first is for the case of particles released in quasi-isotropic grid generated stationary turbulence, and the second is for particles released in a partially obstructed channel. The model will then be applied and briefly analysed for the real flow around a nuclear power plant in Normandy (chapter 9).

Chapter 2

Context

Où le contexte de la problématique du transport d'algues en bord de mer est expliqué. Les côtes de Bretagne et Normandie sont sujettes à une augmentation du volume d'algues échouées. Ces algues, principalement de type Ulves, ne sont pas toxiques pour l'homme individuellement, mais les quantités échouées créent des problèmes lors du processus de décomposition. Ce phénomène, connu sous le nom de marées vertes, pose ainsi des problèmes de gestion de ces côtes, en terme de propreté et sureté. Pour les industriels, les problèmes viennent du fait que ces algues bloquent partiellement l'accès à l'eau.

Pour répondre à ce problème une approche de modélisation mixte Eulérienne et Lagrangienne est proposée. Dans cette approche un modèle Eulérien est utilisé pour simuler le courant moyen en traitant les mécanismes modélisés par les grandes échelles. Ensuite un modèle Lagrangien est utilisé pour suivre les trajectoires des algues dépendant de mécanismes modélisés par des petites échelles.

Enfin, pour justifier l'approche de modélisation retenue, des nombres adimensionnels classiques sont utilisés. La fraction volumique des particules permet de prédire qu'un couplage fluide–eau sera suffisant pour les applications envisagées ici, et le nombre de Stokes des particules permet de justifier que les corps solides ne peuvent pas être considérés comme de simples particules de fluide. Ensuite une description des modèles de transport d'algues est donnée. Cependant il existe peu de modèles permettant de modéliser le transport d'algues en bord de mer, et ceux-ci se concentrent principalement sur l'évolution d'une population d'algues. Or pour la problématique de la thèse, il faudrait pouvoir prédire la réponse d'un groupe d'algues aux variations de l'écoulement.

Ainsi, pour servir de référence, d'autres modèles de transport de particules dans un écoulement sont décrits, par exemple le transport d'aérosols dans l'atmosphère ou de bulles dans les canalisations.

2.1 The algae problematic

The coast of Normandy and Brittany in France have seen mass deposition of algal blooms, see for example figure 2.1.

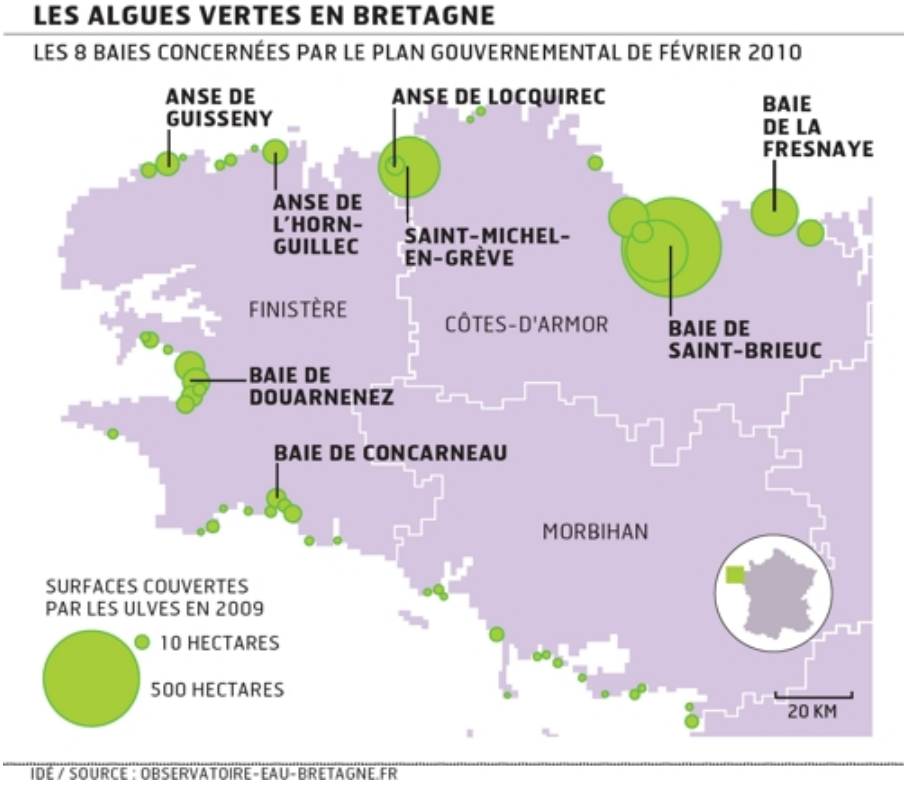


Figure 2.1: Surface covered in Ulva in Brittany during the year 2009 [1]. The green circles represent surfaces covered with alga.

The reason why the regions of Brittany and Normandy are affected so severely are of two origins. Firstly there are geographical reasons. In large beaches, with a small slope, the effect of the waves (usually in combination with a small tidal current) might trap the algae close to the beach, where with a small water depth the algae will be in relatively warm water and have easy access to sunlight. Secondly there is the access to nutriments. The type of sediments and the proximity of these (i.e. in shallow water) can also increase the nutriments present in the water. Secondly during the summer the rivers have a smaller discharge, and therefore they reach the sea with a higher concentration of nutriments. Finally, with the human occupation along the coastline, rain water enters the ocean faster, and through human activity (such as agriculture) a higher dose of nutriments enters the water cycle. Further details on the reasons behind the increase of Ulva populations can be found in Inf'ODE (1999).

Nonetheless these algae are not toxic in their natural form, but the amount that is deposited causes many problems. When deposited on the beach these algae will decompose, and because of the amount present, the fumes emitted from this decomposition prove to be hazardous. Furthermore the presence of these algal blooms in the water will partially block the access to sea water. This proves to be particularly cumbersome for harbours or industrial structures that requires readily available sea water in their manufacturing process.

The only modifications to the growth process of the algal blooms that can be undertaken are to the human factors. However a modification of the human activities will be very long, expensive and complex, and might only shift the problem to another type of algae. For this purpose, the objective

[1] source: http://ecologie.blog.lemonde.fr/2011/07/05/pourquoi-les-algues-vertes-sont-elles-toujours-la/

of this thesis is to develop a model to predict the transport of algal particles in a coastal environment surrounding an industrial complex so that civil engineering solutions can be found to deviate these blooms from the point of interest until curative solutions can be developed to reduce the presence of algal blooms along the coast in the long run.

2.2 Modelling approach

The model developed in this thesis will aim to predict the short term response of macro algae to a change in the flow along the coast, such as during on tide. This is done to provide a tool that can be used to protect industrial structures that require sea water in their manufacturing process from clogging due to algal bloom. Due to the fairly short term response of this problematic some parameters such as the growth and decay of an algal bloom can be ignored, however this requires a good modelling of the flow.

To model accurately the coastal flow around an industrial structure during a time scale of several hours (a tide cycle) several large scale characteristics of the flow need to be taken into account. For example the effects of the bathymetry, of the tides and the wave induced current will need to be considered. However the motion of an individual alga in the flow depends also on smaller scale effects, such as the physical characteristics of the body and the turbulence generated by the flow.

To be able to include all the physical processes occurring over different spatial and temporal scales a mixed Eulerian and Lagrangian approach has been adopted. An Eulerian model will be used to solve for the mean fluid velocities over a large area in order to deal with all the large scale processes. These velocities will then be inputed in a Lagrangian model following the path of individual algae particles. This Lagrangian model will deal with all the smaller scale processes. A mixed Eulerian and Lagrangian approach allows also future developments to be added easily on the model to include further parameters that affect individual alga particles, such as a change of density or even the death of individual algae.

2.3 Categorising the problem

For the problem at hand we saw that looking purely at the scales of physical processes involved, the problematic needs to consider a wide range of motions. Large scales are necessary to predict accurately the environmental flow of the algae problem and small scales to consider the inertial effects of individual algae particles. Poelma *et al.* (2007) gives an overview of parameters that can be used to categorise a particle laden flows. Considering this approach the non-dimensional number Ω_f, which represents the volume fraction of particles as introduced by Elghobashi (2006), will be considered:

$$\Omega_f = \frac{N_r \Omega}{V_{ol}} \tag{2.1}$$

N_r is the number of particles present in the flow, Ω is the volume occupied by a single particle and V_{ol} is the total volume occupied by the particles and the fluid. Elghobashi (2006) showed that for volume fraction of particles smaller than 10^{-6} a one way fluid–particle coupling can be done. A one way fluid–particle coupling means that the information from the fluid is given to the particle motion, but there is no transfer of information from the particles to the fluid flow. A quick calculation shows that a volume fraction of 10^{-6} can correspond to the case of algae that can potentially cover a surface 100×1 m^2 and a millimetre thick transported in a volume of fluid $500 \times 100 \times 2$ m^3, which is typical for the transport of algae.

Another useful non-dimensional quantity is the particle stokes number St introduced by Eaton and

Fessler (1994):

$$\mathrm{St} = \frac{\tau_p}{\tau_s} \tag{2.2a}$$

$$\tau_p = \frac{(2\rho_s + \rho_f)\, D^2}{36\nu\rho_f} \tag{2.2b}$$

$$\tau_s = \left(\frac{\nu}{\varepsilon}\right)^{\frac{1}{2}} \tag{2.2c}$$

Where ρ_s is the particle density (the "s" stands here for "solid"), ρ_f is the fluid density, D is a characteristic length of the body, ν is the kinematic viscosity and ε is the dissipation rate of the turbulent kinetic energy. This Stokes number can be considered as the relationship between two characteristic times. τ_p which is the relaxation time for a particle experiencing only Stokes drag, and τ_s which is the characteristic time for the small turbulent eddies. Eaton and Fessler (1994) show that particle with a Stokes number between 0.01 and 25 can be considered to be partially affected by the motion of the fluid. For alga particles such as those described in section 9.1 transported in a typical environmental with a dissipation rate of the order 10^{-5} $\mathrm{m^2{\cdot}s^{-3}}$ this gives Stokes number ranging from 1-30. We will analyse these characteristic time scales and dimensionless numbers, amongst others, in chapter 7.

Therefore the parameter Ω_f shows that the model developed in this thesis can assume that the particles will not affect the flow, which simplifies the use of a Lagrangian model on top of an Eulerian model. The parameter St shows that the particles will not affect the flow and therefore that small scale effects cannot be ignored. These effects can be easily calculated within a Lagrangian model.

2.4 Existing algae transport models

In literature the only models that deal with the transport of algae particles have approached the problem from a biological point of view. These models focus more the growth and decay of a population of algae within an bay or a lagoon. This therefore requires a model that will cover several kilometres and several weeks of simulations.

If one ignores the articles that focus on the nutrients that affects the population of algae in a body of water there are some articles that try to relate the evolution of a population of algae in relation to hydraulic properties. Biber (2007) has done a study of algae in the Biscayne Bay, in Florida, USA. In this study the author records the amount of Sargassum and Red algae entering and leaving the bay, and finds that these algae enter the bay during flood and leave the bay during ebb. The author also finds that during different periods of the year these volumes are not the same.

In Bosence (1976) a study is done on the presence of algae in Mannin Bay, in Ireland. In this study the author tries to link the presence of coralline algae at different location in the bay to the direction and strength of the currents, the distribution and orientation of wave ripples as well as the bathymetry and bed type.

In Flindt *et al.* (2007) the study goes slightly further as here the authors try to link an average algae velocity to an average current velocity. This is done for four kind of algae: Ulva, Chaetomorpha, Ceramium and Cladophora species. The authors than go to calculate the mean settling rates for these algae.

As can be found from these three articles, there hasn't been an in depth study of the hydrodynamic and physical properties that will govern the motion of algae particles. Nonetheless some numerical models exist. These models often use water quality models to transport nutrients that will affect the growth and decay of a population of algae. These models can be found for example in Solidoro *et al.* (1997) which focus on the evolution of the population of Ulva rigida in the Venice lagoon (Italy) during the years 1990-1991 or in R.Trancoso *et al.* (2005) which focus on the evolution of a non-descript

macro algae (defined through its growth parameters) in the Rio de Aveiro bay (Portugal) during 6 consecutive years.

The two most interesting algae transport models present in literature are those that use the coastal current to transport particles in order to affect the growth of algae. Donaghay and Osborn (1997) for example consider micro algae, such as Aureococcus anophagefferens, in terms of concentrations of this specific pollutant, and because of their size it is assumed that these algae follow exactly the fluid velocities, upon which is added growth and decay model. Salomonsen *et al.* (1999) use also a growth and decay model, but for a macro alga (Ulva lactuca). On top this model is an erosion and sedimentation model to define when algae will be carried by following the current calculated by a hydrodynamic model. This model is then applied to Møllekrogen bay in Denmark, which is typically 10 - 100 km^2, and has a simulation done over several days (up to a month).

Nonetheless these existing models prove to be ineffective for the problematic at hand, and inspiration should be found in particle transport models for other kind of particles.

2.5 Existing particle transport models

Models describing the motion of particles in a fluid have been studied for many years. For example Einstein in 1905 presented a model describing Brownian motion, where summary and translation of this article can be found in Gardiner (2004) and a short description of Brownian motion can be found in section 5.1. For the problem at hand, the trajectories of a group of algae needs to be modelled so that the effectiveness of civil engineering works to protect industrial structures or harbours from the accumulation of algae can be tested. The models presented in this section are, for the most part, mixed Eulerian and Lagrangian models. The amount of information treated, as well as the scales of the simulations, will also be given.

Models such as the ones presented in Monti and Leuzzi (2010), Issa *et al.* (2009), Heemink (1990) or Stijnen *et al.* (2006) predict the motion of particles in environmental flows by adding to the mean flow an estimation of the diffusion due to turbulence. These models focus on a smaller scale of motion, typically 10 m - 1 km and 1 - 24 h, but still large enough to model the specificities of environmental flows such as tides, waves, turbulent diffusion and the effect of bathymetry. However the turbulence is predicted simply, through the use of a diffusion constant (which represents the turbulence), and none of the physical characteristics of the bodies are taken into account.

To find models that consider the physical properties of bodies one needs to look at models used to predict the transport of aerosols or bubbles. Example of aerosol models, which are models that consider solid particles interacting with a gas can be found in Csanady (1963), Minier and Peirano (2001) or Sawford and Guest (1991). Yeo *et al.* (2010) is a good example of a bubble model, which is a model with distinct gas particles transported in a fluid. These models are developed for small particles with a large density difference with the surrounding fluid. The algae particles are large in comparison to these models, and have a very small difference in density with the surrounding fluid. Furthermore these models typically require more information on the flow than is generally available in environmental flow modelling (see chapter 3) and therefore tend to be applicable for a smaller scale of fluid models (because of computing power).

It is also possible to consider larger particles in the flow with Direct Numerical Simulations, in Uhlmann (2008) for example, but these models can only be used for a very small scale of simulation.

Chapter 3

Environmental Flow Modelling

Où les bases de la mécanique des fluides sont rappelées. Dans la première partie de ce chapitre, la différentiation entre les modèles de type Eulérien et Lagrangien est expliquée. Ensuite les équations de Navier-Stokes sont introduites, ainsi que l'équation de continuité. Enfin il est ensuite expliqué comment obtenir les équations de Saint-Venant, qui sont souvent utilisées pour modéliser les écoulements côtiers. La seconde partie introduit la modélisation de la turbulence. Cela commence par l'introduction du nombre de Reynolds, ainsi que la décomposition de la vitesse du fluide qui permet d'obtenir les contraintes de Reynolds. Il est ensuite expliqué comment modéliser ces contraintes à travers deux types de modèles. Les modèles de type viscosité turbulente, avec la mise en avant du modèle k-ε, et les modèles suivant l'évolution dans le temps de ces contraintes. Finalement, les hypothèses de Kolmogorov sont introduites ainsi que les grandeurs caractéristiques qui en découlent.

3.1 General principles of fluid mechanics

Before going more in depth into the model describing the transport of algae particles in coastal water there are a few general principles of fluid mechanics which need to be understood. Firstly there are two different general methods used to describe a flow of fluid. One focuses on individual fluid particles (or individual bundles of fluid particles) and follows them in time. This type of methods are called Lagrangian methods. The second method focus on the behaviour of the fluid within an area. These methods are called Eulerian.

Lagrangian methods can become very time consuming and complex when a large volume of fluid is observed and therefore when modelling the flows Eulerian method are usually preferred. When it comes to environmental flows there are two different flow models which are commonly used. These environmental flows, which are the water flows of interest for the problem considered in this thesis, are considered to be Newtonian, which means that their viscosity (represented with the symbol μ, or if divided by the fluid density ν) which is a measure of their resistance to deformations caused by shear or tensile stresses, is constant. They are also considered incompressible, which means that they have a constant density (represented with the symbol ρ_f).

The first model described, which is the basis for all fluid models which are considered Newtonians, is the Navier-Stokes equation of motion. This equation is found by applying newton's second law of motion (conservation of momentum) to an area of the fluid. In its incompressible form it is given by the following equation (Viollet *et al.*, 2002):

$$\frac{\partial \mathbf{U}}{\partial t} + \mathbf{U} \cdot \nabla \mathbf{U} = -\frac{1}{\rho_f} \nabla P + \mathbf{g} + \nu \nabla^2 \mathbf{U} \tag{3.1}$$

In this equation the symbol $\mathbf{U}$ represents the fluid velocity, P is the fluid pressure, ∇ is the gradient operator, $\mathbf{g}$ is the vectorial representation of the acceleration due to gravity and ∇^2 is the Laplacian operator. Equation 3.1 is written in its vectorial form, where the symbols in bold show vectors. However there are two other form of notations which can be used, and will be introduced here as they will be used later on in the thesis. The Cartesian (x,y,z) projection of the vectorial form of the Navier-Stokes equation is given by:

$$\frac{\partial U_x}{\partial t} + U_x \frac{\partial U_x}{\partial x} + U_y \frac{\partial U_x}{\partial y} + U_z \frac{\partial U_x}{\partial z} = -\frac{1}{\rho_f} \frac{\partial P}{\partial x} + \nu \left(\frac{\partial^2 U_x}{\partial x^2} + \frac{\partial^2 U_x}{\partial y^2} + \frac{\partial^2 U_x}{\partial z^2} \right) \tag{3.2a}$$

$$\frac{\partial U_y}{\partial t} + U_x \frac{\partial U_y}{\partial x} + U_y \frac{\partial U_y}{\partial y} + U_z \frac{\partial U_y}{\partial z} = -\frac{1}{\rho_f} \frac{\partial P}{\partial y} + \nu \left(\frac{\partial^2 U_y}{\partial x^2} + \frac{\partial^2 U_y}{\partial y^2} + \frac{\partial^2 U_y}{\partial z^2} \right) \tag{3.2b}$$

$$\frac{\partial U_z}{\partial t} + U_x \frac{\partial U_z}{\partial x} + U_y \frac{\partial U_z}{\partial y} + U_z \frac{\partial U_z}{\partial z} = -\frac{1}{\rho_f} \frac{\partial P}{\partial z} - g + \nu \left(\frac{\partial^2 U_z}{\partial x^2} + \frac{\partial^2 U_z}{\partial y^2} + \frac{\partial^2 U_z}{\partial z^2} \right) \tag{3.2c}$$

Note that in this case the vertical axis is assumed to be orientated in the upward direction. Finally equation 3.1 can be written following the Einstein notations

$$\frac{\partial U_i}{\partial t} + U_j \frac{\partial U_i}{\partial x_j} = -\frac{1}{\rho_f} \frac{\partial P}{\partial x_i} + g_i + \nu \frac{\partial^2 U_i}{\partial x_j^2} \tag{3.3}$$

Where the subscript i represents the direction of the flow considered, all the subsequent subscripts that are used j or later on k represent a summation over the components of direction.

Furthermore the Navier-Stokes equations need to include the continuity equation, which in incompressible flows is given by (Viollet *et al.*, 2002):

$$\frac{\partial U_x}{\partial x} + \frac{\partial U_y}{\partial y} + \frac{\partial U_z}{\partial z} = 0 \tag{3.4}$$

The continuity equation ensures that in within the volume of measurement, in the absence of a source or a sink of fluid, no fluid will be lost or created.

The second flow model commonly used in environmental problems are the non-linear Shallow Water equations. These are often used in free-surface flows and they can be obtained by integrating the Navier-Stokes equations over the depth of the flow under the hypothesis that horizontal length scale is much greater than the vertical length scale, and that the vertical velocity components are negligible. In its conservative form the Shallow Water equations are given by (Viollet *et al.*, 2002):

$$\frac{\partial U_i}{\partial t} + U_j \frac{\partial U_i}{\partial x_j} = -g \frac{\partial \eta}{\partial x_i} + \frac{\nu}{h} \frac{\partial}{\partial x_j} \left[h \left(\frac{\partial U_i}{\partial x_j} + \frac{\partial U_j}{\partial x_i} \right) \right] \tag{3.5}$$

With η representing the free-surface elevation from the mean elevation and h the depth of the fluid and all the velocity values given here are depth-averaged. For the non-linear Shallow Water equations the continuity equation is given by (Viollet *et al.*, 2002):

$$\frac{\partial h}{\partial t} + \frac{\partial h U_x}{\partial x} + \frac{\partial h U_y}{\partial y} = 0 \tag{3.6}$$

Again the velocity values are depth-averaged.

These models are applied over a domain of interest, and therefore it is necessary to know the behaviour of the flow along the boundaries. This is known as the boundary conditions. For the boundary conditions on the Navier-Stokes equations see Viollet *et al.* (2002), and for the boundary conditions on the non-linear Shallow Water equations see Hervouet (2007). A more sophisticated set of shallow water equations will be presented later on in chapter 9.

3.2 General principles of turbulence modelling - first-order models

During the observation of most real flows it is possible to observe eddies of different size, shape and direction. These eddies create a fluctuation around the mean flow velocities in a process called turbulence. The intensity of the turbulence is usually characterised through a dimensionless number called the Reynolds number (Viollet *et al.*, 2002):

$$\mathrm{Re} = \frac{U d}{\nu} \tag{3.7}$$

The Reynolds number is the ratio between a characteristic fluid velocity U, a characteristic flow length d and the kinematic viscocity ν. The flow is generally considered to be laminar (which means that there are virtually no turbulent fluctuations) for low values of the Reynolds number (typically under 2300). Above this value small perturbations will be amplified to reach a finite value. From this definition of turbulence, Reynolds introduced a decomposition of the fluid velocity given by the following equation (Viollet *et al.*, 2002):

$$U_i = \overline{U_i} + U_i' \tag{3.8}$$

Where $\overline{U_i}$ represents the mean fluid velocity (in the turbulent sense, it should not be confused with the depth-averaged velocities found through the Shallow Water equations) and U_i' represents the fluctuations around this mean value. This decomposition can be applied to other fluid quantities, such as the pressure. Figure 3.1 shows a schematic description of this concept.

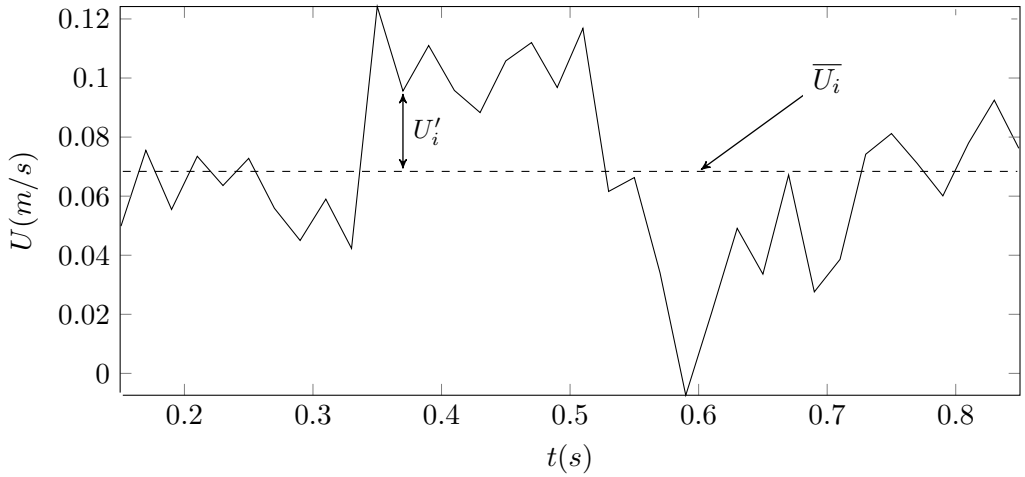


Figure 3.1: An example of a recording of a turbulent fluid velocity in time taken from velocity measurements of the experiment in section 8.2.

The Reynolds decomposition introduced in equation 3.8 can be used to rewrite the Navier-Stokes and the continuity equations (equations 3.3 and 3.4). Averaging these new equations we get the Reynolds equations (Pope, 2000):

$$\frac{\partial \overline{U_i}}{\partial x_i} = 0 \tag{3.9a}$$

$$\frac{\partial \overline{U_i}}{\partial t} + \overline{U_j}\frac{\partial \overline{U_i}}{\partial x_j} = -\frac{1}{\rho_f}\frac{\partial \overline{P}}{\partial x_i} + g_i + \nu\frac{\partial^2 \overline{U_i}}{\partial x_j^2} - \frac{\partial}{\partial x_j}\left(\overline{U_i' U_j'}\right) \tag{3.9b}$$

The terms $\overline{U_i' U_j'}$ are known as the Reynolds stresses, and they represent the momentum transfer by the turbulent fluctuations. Due to these stresses the Reynolds equations are unclosed, and from this closure problem comes all the modelling of the turbulence. This tensor is symmetrical ($\overline{U_i' U_j'} = \overline{U_j' U_i'}$) and the diagonal components ($\overline{U_i' U_i'}$) are normal stresses whereas the off diagonal components are shear stresses. The simplest method to model the Reynolds stresses is to consider that they act as viscous stresses, since turbulent eddies are responsible for mixing and energy dissipation. Therefore an artificial viscosity called the turbulent (or eddy) viscosity ν_T will be introduced. Using Boussinesq's assumption that the Reynolds stresses are proportional to the mean rates of strain (Pope, 2000) gives:

$$-\overline{U_i' U_j'} = 2\nu_T S_{ij} - \frac{2}{3}k\delta_{ij} \tag{3.10}$$

Where S_{ij} is the mean rate of strain tensor is:

$$S_{ij} = S_{ji} = \frac{1}{2}\left(\frac{\partial \overline{U_i}}{\partial x_j} + \frac{\partial \overline{U_j}}{\partial x_i}\right) \tag{3.11}$$

We may observe from equation 3.9a that $S_{ii} = \partial \overline{U_i}/\partial x_i = 0$.

The symbol k is the turbulent kinetic energy (TKE), which is the kinetic energy of the fluctuating part of the flow per unit mass. It is defined by:

$$k = \frac{1}{2}\overline{U_i' U_i'} \tag{3.12}$$

Using this, the Reynolds averaged Navier-Stokes equation (3.9b) can be rewritten as:

$$\frac{\partial \overline{U_i}}{\partial t} + \overline{U_j}\frac{\partial \overline{U_i}}{\partial x_j} = -\frac{1}{\rho_f}\frac{\partial}{\partial x_i}\left(\overline{P} + \frac{2}{3}\rho_f k\right) + g_i + \frac{\partial}{\partial x_j}\left[\left(\nu + \nu_T\right)\frac{\partial \overline{U_i}}{\partial x_j}\right] \tag{3.13}$$

The term $2\rho_f k/3$ is often considered negligible compared to $\overline{P}$.

The simplest way to consider the turbulent viscosity is to assume a constant value throughout the domain, and in many real applications this can be sufficient to obtain an estimation of the mean fluid velocities, however if one is interested in the diffusive abilities of the flow, a more detailed model of the for this viscosity is required. A commonly used model is the k-ε model developed by Jones and Launder (1972). To obtain a model for the turbulent kinetic energy this model starts by subtracting the Reynolds equations from the Navier-Stokes equations. This gives the evolution of the fluctuating velocities:

$$\frac{\partial U_i'}{\partial t} + U_j\frac{\partial U_i'}{\partial x_j} = -U_j'\frac{\partial \overline{U_i}}{\partial x_j} + \frac{\partial}{\partial x_j}\left(\overline{U_i' U_j'}\right) + \nu\frac{\partial^2 U_i'}{\partial x_j^2} - \frac{1}{\rho_f}\frac{\partial P'}{\partial x_i} \tag{3.14}$$

Therefore, from equations 3.14 and 3.12 it is possible to obtain the evolution of the turbulent kinetic energy:

$$\frac{\partial k}{\partial t} + \overline{U_j}\frac{\partial k}{\partial x_j} = -\overline{U_i' U_j'}\frac{\partial \overline{U_i}}{\partial x_j} - \frac{\partial}{\partial x_k}\left(\frac{1}{2}\overline{U_i' U_j' U_j'} + \frac{\overline{U_i' P'}}{\rho_f} - 2\nu\overline{U_j' s_{ij}}\right) - 2\nu\overline{s_{ij} s_{ij}} \tag{3.15}$$

Where s_{ij} is the fluctuating rate of strain tensor given by:

$$s_{ij} = \frac{1}{2}\left(\frac{\partial U_i'}{\partial x_j} + \frac{\partial U_j'}{\partial x_i}\right) \tag{3.16}$$

Equation 3.15 can be rewritten to make visible certain characteristics.

$$\frac{\partial k}{\partial t} + \overline{U_j}\frac{\partial k}{\partial x_j} = \mathcal{P} - \frac{\partial T_j'}{\partial x_j} - \varepsilon \tag{3.17}$$

The symbol $\mathcal{P}$ corresponds to the production of turbulent energy and it is given by:

$$\begin{aligned} \mathcal{P} &= -\overline{U_i' U_j'}\frac{\partial \overline{U_i}}{\partial x_j} \\ &= -\overline{U_i' U_j'} S_{ij} \end{aligned} \tag{3.18}$$

The notation S_{ij} can be used in place of the velocity gradient because of the symmetrical nature of the Reynolds stresses and of S_{ij}. The symbol T_i' corresponds to the flux of turbulent energy and it is given by:

$$T_i' = \frac{1}{2}\overline{U_i' U_j' U_j'} + \frac{\overline{U_i' P'}}{\rho_f} - 2\nu\overline{U_j' s_{ij}} \tag{3.19}$$

And ε is the dissipation of turbulent energy defined by:

$$\varepsilon = 2\nu\overline{s_{ij} s_{ij}} \tag{3.20}$$

The terms to be closed in of equation 3.17 are the flux of the turbulent kinetic energy T_i' and the dissipation rate of the turbulent kinetic energy ε. Using Boussinesq's assumption on Reynolds stresses (equation 3.10) the production $\mathcal{P}$ is given as:

$$\begin{aligned}\mathcal{P} =& -\left(\frac{2}{3}k\delta_{ij} - 2\nu_T S_{ij}\right) S_{ij} \\ =& 2\nu_T \mathcal{S}^2\end{aligned} \tag{3.21}$$

In this calculation, we used the property $S_{ij}\delta_{ij} = S_{ii} = 0$ and the scalar mean rate of strain $\mathcal{S}$ is defined as:

$$\mathcal{S} = \sqrt{2S_{ij}S_{ij}} \tag{3.22}$$

And therefore the production term is known. In the k-ε model the flux of turbulent kinetic energy is modelled as a diffusion gradient:

$$T_i' = -\frac{\nu_T}{\sigma_k}\frac{\partial k}{\partial x_i} \tag{3.23}$$

Note that the turbulent damping coefficient σ_k is a scalar (where the subscript k is a standard notation, and not a vectorial component) generally taken equal to 1. The turbulent viscosity is specified by the following dimensional equation:

$$\nu_T = C_\mu \frac{k^2}{\varepsilon} \tag{3.24}$$

With C_μ being a constant, experimentally found to be 0.09. The evolution of turbulent kinetic energy (equation 3.17) can therefore be simplified to:

$$\frac{\partial k}{\partial t} + \overline{U_j}\frac{\partial k}{\partial x_j} = \mathcal{P} + \frac{\partial}{\partial x_j}\left(\frac{\nu_T}{\sigma_k}\frac{\partial k}{\partial x_j}\right) - \varepsilon \tag{3.25}$$

The k-ε model chooses to model the dissipation rate instead of using the definition 3.20. ε can be considered as the turbulent energy flow rate in the energy cascade (see later in this section), determined

by the large scales of turbulence and assumed to be independent of the viscosity (which is true at high Reynolds numbers). It can therefore be modelled by the heuristic equation:

$$\frac{\partial \varepsilon}{\partial t} + \overline{U_j}\frac{\partial \varepsilon}{\partial x_j} = C_{\varepsilon 1}\frac{\mathcal{P}\varepsilon}{k} + \frac{\partial}{\partial x_j}\left(\frac{\nu_T}{\sigma_\varepsilon}\frac{\partial \varepsilon}{\partial x_j}\right) - C_{\varepsilon 2}\frac{\varepsilon^2}{k} \tag{3.26}$$

The constant of the k-ε model are set as $C_{\varepsilon 1} = 1.44$, $C_{\varepsilon 2} = 1.92$, $\sigma_k = 1.0$ and $\sigma_\varepsilon = 1.3$ (Launder and Sharma, 1974).

Naturally the turbulence models can also be applied to the Shallow Water equations. Integrating equation 3.13 over the vertical gives:

$$\frac{\partial \overline{U_i}}{\partial t} + \overline{U_j}\frac{\partial \overline{U_i}}{\partial x_j} = -g\frac{\partial \eta}{\partial x_i} + \frac{\nu}{h}\frac{\partial}{\partial x_j}\left[h\left(\frac{\partial \overline{U_i}}{\partial x_j} + \frac{\partial \overline{U_j}}{\partial x_i}\right)\right] - \frac{1}{h}\frac{\partial}{\partial x_j}\left(h\overline{U_i'U_j'}\right) \tag{3.27}$$

The turbulent fluctuations of free-surface and of the water depth are assumed to be negligible due to the action of gravity. The shallow water equations can also be written using the turbulent viscosity hypothesis:

$$\frac{\partial \overline{U_i}}{\partial t} + \overline{U_j}\frac{\partial \overline{U_i}}{\partial x_j} = -g\frac{\partial \eta}{\partial x_i} + \frac{1}{h}\frac{\partial}{\partial x_j}\left[h\left(\nu + \nu_T\right)\left(\frac{\partial \overline{U_i}}{\partial x_j} + \frac{\partial \overline{U_j}}{\partial x_i}\right)\right] \tag{3.28}$$

Where all the fluid velocity values are still depth-averaged. The k-ε equations can also be written in a depth-averaged version. These equations are similar to equations 3.25 and 3.26, but with added terms resulting from the depth-averaging (Rodi, 2000):

$$\frac{\partial k}{\partial t} + \overline{U_j}\frac{\partial k}{\partial x_j} = \mathcal{P} + \frac{\partial}{\partial x_i}\left(\frac{\nu_T}{\sigma_k}\frac{\partial k}{\partial x_i}\right) - \varepsilon + P_k \tag{3.29a}$$

$$\frac{\partial \varepsilon}{\partial t} + \overline{U_j}\frac{\partial \varepsilon}{\partial x_j} = C_{\varepsilon 1}\frac{\mathcal{P}\varepsilon}{k} + \frac{\partial}{\partial x_i}\left(\frac{\nu_T}{\sigma_\varepsilon}\frac{\partial \varepsilon}{\partial x_i}\right) - C_{\varepsilon 2}\frac{\varepsilon^2}{k} + P_\varepsilon \tag{3.29b}$$

The two additional terms P_k and P_ε are given by:

$$P_k = \frac{u_*^2\,|\mathbf{U}|}{h} \tag{3.30a}$$

$$P_\varepsilon = C_\varepsilon C_{\varepsilon 2}\frac{\sqrt{C_\mu u_*^5\,|\mathbf{U}|^3}}{h^2} \tag{3.30b}$$

The constants in equations 3.29 and 3.30 are set to: $C_{\varepsilon 1} = 1.44$, $C_{\varepsilon 2} = 1.92$, $C_\varepsilon = 3.6$, $C_\mu = 0.09$, $\sigma_k = 1.0$ and $\sigma_\varepsilon = 1.3$ in Launder and Sharma (1974) and Rodi (2000). Equations 3.29 are then used in equations 3.28 through the usual relation:

$$\nu_T = C_\mu\frac{k^2}{\varepsilon} \tag{3.31}$$

3.3 General principles of turbulence modelling - second-order models

A more complete class of turbulence models exist, focusing on the transport of the Reynolds stresses, which can be obtained from equation 3.14:

$$\frac{\partial}{\partial t}\left(\overline{U_i'U_j'}\right) + \overline{U_j}\frac{\partial}{\partial x_j}\left(\overline{U_i'U_j'}\right) = \mathcal{P}_{ij} + \mathcal{R}_{ij} - \frac{\partial}{\partial x_k}T_{kij} - \varepsilon_{ij} \tag{3.32}$$

Where $\mathcal{P}_{ij}$ is the production tensor and it is defined as:

$$\mathcal{P}_{ij} \equiv -\overline{U_j'U_k'}\frac{\partial \overline{U_i}}{\partial x_k} - \overline{U_i'U_k'}\frac{\partial \overline{U_j}}{\partial x_k} \tag{3.33}$$

$\mathcal{R}_{ij}$ is the pressure rate of strain tensor and it is defined as:

$$\mathcal{R}_{ij} \equiv \overline{\frac{P'}{\rho_f}\left(\frac{\partial U_i'}{\partial x_k} + \frac{\partial U_j'}{\partial x_k}\right)} \tag{3.34}$$

And ε_{ij} is the dissipation tensor, defined by:

$$\varepsilon_{ij} \equiv 2\nu\overline{\frac{\partial U_i'}{\partial x_k}\frac{\partial U_j'}{\partial x_k}} \tag{3.35}$$

T_{kij} are the Reynolds stress flux which are defined by:

$$T_{kij} = T_{kij}^{(u)} + T_{kij}^{(P)} + T_{kij}^{(\nu)} \tag{3.36a}$$

$$T_{kij}^{(u)} \equiv \overline{U_i'U_j'U_k'} \tag{3.36b}$$

$$T_{kij}^{(P)} \equiv \frac{1}{\rho_f}\overline{U_i'P'}\delta_{jk} + \frac{1}{\rho_f}\overline{U_j'P'}\delta_{ik} \tag{3.36c}$$

$$T_{kij}^{(\nu)} \equiv -\nu\frac{\partial \overline{U_i'U_j'}}{\partial x_k} \tag{3.36d}$$

Now that the evolution of the Reynolds stresses are known models are required to provide closure to the Reynolds stress flux, the dissipation and the pressure rate of strain tensor. Pope (2000) gives a thorough overview of such models. We will now consider the simplest one.

For high Reynolds numbers because of local isotropy (see the Kolmogorov hypotheses described later on) the dissipation can be rewritten as:

$$\varepsilon_{ij} = \frac{2}{3}\varepsilon\delta_{ij} \tag{3.37}$$

Rotta's model is often used to close the pressure rate of strain tensor (equation 3.34). To describe this model it is necessary to be aware that the fluctuating pressure field can be decomposed into three contributions, taken from the observation of the Poisson equation for fluctuating pressure (Pope, 2000):

$$P' = P^{(r)} + P^{(s)} + P^{(h)} \tag{3.38}$$

The first contribution $P^{(r)}$ is known as the rapid pressure as it responds immediately to a change of the mean velocity gradients. It is defined through the following relation:

$$\frac{1}{\rho_f}\nabla^2 P^{(r)} = -2\frac{\partial \overline{U_i}}{\partial x_j}\frac{\partial U_j}{\partial x_i} \tag{3.39}$$

The second contribution is known as the slow pressure, because it takes longer than $P^{(r)}$ to respond to mean velocity gradients, and it is defined by:

$$\frac{1}{\rho_f}\nabla^2 P^{(s)} = -\frac{\partial^2}{\partial x_i \partial x_j}\left(U_i'U_j' - \overline{U_i'U_j'}\right) \tag{3.40}$$

The final contribution is the harmonic pressure, which is used to impose the boundary conditions. It is given by the following equation:

$$\frac{1}{\rho_f}\nabla^2 P^{(h)} = 0 \tag{3.41}$$

These definitions can be used to decompose the pressure rate of strain tensor (equation 3.34):

$$\mathcal{R}_{ij} = \mathcal{R}_{ij}^{(r)} + \mathcal{R}_{ij}^{(s)} + \mathcal{R}_{ij}^{(h)} \tag{3.42a}$$

$$\mathcal{R}_{ij}^{(r)} = \overline{\frac{P^{(r)}}{\rho_f}\left(\frac{\partial U_i'}{\partial x_k} + \frac{\partial U_j'}{\partial x_k}\right)} \tag{3.42b}$$

$$\mathcal{R}_{ij}^{(s)} = \overline{\frac{P^{(s)}}{\rho_f}\left(\frac{\partial U_i'}{\partial x_k} + \frac{\partial U_j'}{\partial x_k}\right)} \tag{3.42c}$$

$$\mathcal{R}_{ij}^{(h)} = \overline{\frac{P^{(h)}}{\rho_f}\left(\frac{\partial U_i'}{\partial x_k} + \frac{\partial U_j'}{\partial x_k}\right)} \tag{3.42d}$$

Rotta's model was developed in a scenario where only the slow pressure rate of strain tensor contributes to the Reynolds stresses. In decaying homogeneous anisotropic turbulence there are no production or transport of those stresses so that the exact Reynolds stress equation (3.32) becomes:

$$\frac{d}{dt}\left(\overline{U_i'U_j'}\right) = \mathcal{R}_{ij}^{(s)} - \varepsilon_{ij} \tag{3.43}$$

The anisotropy of the flow can be quantified using the following anisotropy tensor:

$$b_{ij} = \frac{\overline{U_i'U_j'}}{2k} - \frac{1}{3}\delta_{ij} \tag{3.44}$$

In this case the evolution of the anisotropy tensor can be found using equations 3.43, 3.15 (with negligible production or fluxes) and the isotropic turbulent dissipation rate (3.37):

$$\frac{db_{ij}}{dt} = \frac{\varepsilon}{k}\left(b_{ij} + \frac{\mathcal{R}_{ij}^{(s)}}{2\varepsilon}\right) \tag{3.45}$$

Rotta then supposed that the turbulence will return to an isotropic state as it decays linearly, which gives the following model equation for the evolution of the anisotropy tensor:

$$\frac{db_{ij}}{dt} = -\left(C_R - 1\right)\frac{\varepsilon}{k}b_{ij} \tag{3.46}$$

Which is only true if:

$$\begin{aligned}\mathcal{R}_{ij}^{(s)} &= -2C_R\varepsilon b_{ij} \\ &= -C_R\frac{\varepsilon}{k}\left(\overline{U_i'U_j'} - \frac{2}{3}k\delta_{ij}\right)\end{aligned} \tag{3.47}$$

Where C_R is the Rotta constant, which is typically set to 1.5 or 1.8. Equation 3.43 then becomes:

$$\frac{d}{dt}\left(\overline{U_i'U_j'}\right) = -C_R\frac{\varepsilon}{k}\overline{U_i'U_j'} + \left(\frac{2}{3}C_R - \frac{2}{3}\right)\varepsilon\delta_{ij} \tag{3.48}$$

Furthermore observations of the turbulence have lead to the general idea that advection of the large turbulent eddies cause smaller eddies to be created around it. This introduces a notion called the energy cascade, where the energy of a large turbulent eddy is lost in creating smaller eddies, which in turn create smaller eddies, and so forth until the viscosity of the fluid stops the motion of the smallest eddies. It was this observation which caused Kolmogorov to introduce characteristic values to describe the small turbulent eddies. Using the dissipation rate of the turbulent kinetic energy ε , introduced earlier in equation 3.20, which has units $\mathrm{m}^2/\mathrm{s}^3$, then dimensional analysis give the characteristic estimations of the small turbulent eddies through the following equations:

$$\lambda_s \sim \left(\frac{\nu^3}{\varepsilon}\right)^{\frac{1}{4}} \tag{3.49a}$$

$$u_s \sim (\nu\varepsilon)^{\frac{1}{4}} \tag{3.49b}$$

$$\tau_s \sim \left(\frac{\nu}{\varepsilon}\right)^{\frac{1}{2}} \tag{3.49c}$$

Where λ_s is the characteristic size, u_s the characteristic velocity and τ_s the characteristic time of the small turbulent eddies.

These estimations are based on the Kolmogorov hypotheses (Pope, 2000). These state that for a sufficiently large turbulent regime (large Reynolds number) the turbulence can be assumed to be locally isotropic if the observed domain is small (much smaller than the length scale of the large turbulent eddies). Furthermore it can be hypothesised that distribution of the fluid velocities correlations are determined by the viscosity ν and the dissipation rate ε. Secondly, for the correlation of two quantities taken sufficiently apart in time or space (a difference large compared to the small scale of turbulence) then it is only dependent on the dissipation rate.

Similar observations can be done for the large turbulent eddies. These eddies are limited by the production of turbulent kinetic energy, symbolised as k , defined earlier in equation 3.12, for which

units were m^2/s^2, and the rate at which it is dissipated. Therefore through dimensional analysis the following equations are defined:

$$\lambda_l \sim C_\mu^{\frac{3}{4}} \frac{k^{\frac{3}{2}}}{\varepsilon} \tag{3.50a}$$

$$u_l \sim k^{\frac{1}{2}} \tag{3.50b}$$

$$\tau_l \sim \frac{k}{\varepsilon} \tag{3.50c}$$

Where λ_l is the characteristic size, u_l the characteristic velocity and τ_l the characteristic time of the large turbulent eddies. The constant C_μ was added to provide a characteristic length closer to the real size.

Chapter 4

Dynamic Properties of Solid Particle Motion

Où les composantes des forces du transport de corps solides dans un fluide sont exposées. Dans l'ordre de présentation, ces composantes sont la poussée d'Archimède, la traînée, l'inertie, la force de Basset et la portance. La résolution de la force de Basset est décrite en détails, car sa résolution est complexe. Il y est aussi expliqué pourquoi la force de portance peut être ignorée. Ensuite il est expliqué que pour des raisons pratiques, le corps des algues va être identifié à une sphère. Ainsi, pour une sphère transportée dans un écoulement, différents modèles de transport, qui prennent en compte différentes forces (traînée, Basset, etc.) sont comparés. Enfin un test est effectué pour des sphères de différentes caractéristiques physiques dans des tourbillons de Taylor, afin de comprendre l'impact de ces caractéristiques sur le transport des corps.

4.1 Forces acting on the motion of a solid particle in fluid

A solid body (or particle) placed into a moving fluid will experience forcing from this fluid. The forces acting on the body can be categorised into different force components. In chapter 2 the volume fraction of the particles Ω_f was introduced (equation 2.1). It was also established that the particles of interest, the algae, had a low concentration in the flow (a volume fraction smaller than 10^{-6}). Therefore for the calculations later on it is assumed that the particles will not affect the general flow surrounding it. In addition even though the bodies are large enough that their physical characteristics need to be taken into account, they are small enough that the flow variations are negligible along a length scale of the same order as the size of the particle. In turbulent flows this means that the turbulent structure do not rotate the bodies, and therefore they will keep the same orientation in time and are assumed irrotational.

4.1.1 The buoyancy force

The first force component to be considered is the buoyancy force. This force is a result of the difference in density between the solid body and the fluid. For a body of density ρ_s, volume Ω and mass $m = \Omega\rho_s$, and in the absence of other forces (such as friction) the impact of this force as given by Graebel (2001) on the motion of a solid particle can be modelled through the following equation, valid for each space component i:

$$m\frac{dV_i}{dt} = (m - \rho_f\Omega)\, g_i \tag{4.1}$$

Where the symbol V_i represents the components velocity of the solid body $\mathbf{V}$. This force is particularly important for three dimensional particle transport, when considering horizontal two-dimensional particle transport the buoyancy effects will be ignored.

4.1.2 The drag force

The second force component to be considered is the drag force. This force represents the resistance of a particle to the flow through friction or pressure differences along the body. Considering only the added effect of this force on the motion of a solid body, as given by Falkovich (2011), gives the following equation:

$$\begin{aligned} m\frac{dV_i}{dt} =& \frac{1}{2}\rho_f S C_D\left(\mathrm{Re}_p\right)|\mathbf{U}-\mathbf{V}|\left(U_i - V_i\right) \\ &+ (m - \rho_f\Omega)\, g_i \end{aligned} \tag{4.2}$$

The velocity of a solid body is therefore dependent on the relative fluid velocity $\mathbf{U} - \mathbf{V}$, the cross-sectional area S, the fluid density ρ_f and the drag coefficient C_D. This drag coefficient is dependent on the shape and orientation of the solid body as well as the relative velocity of the fluid. It is usually given as a function of the non-dimensional number Re_p, which is the non dimensional particle Reynolds number, and it is given by the following definition:

$$\mathrm{Re}_p = \frac{|\mathbf{U}-\mathbf{V}|\, D}{\nu} \tag{4.3}$$

This number is a relation between the relative fluid velocity, a characteristic length of the solid body D and the kinematic molecular viscosity of the fluid ν.

4.1.3 The momentum of the body

Another force component that is added is to take into account the momentum of the body. To calculate these forces it is assumed that fluctuations of the fluid along the length scale of a body are negligible (which is coherent with the description of the bodies of interest, see chapter 2) and that the fluid is at rest infinitely away from the body (Landau and Lifchitz, 1987). The motion of a solid body is therefore given with the following equation:

$$\begin{aligned} m\frac{dV_i}{dt} =& \rho_f \Omega \frac{dU_i}{dt} - M_{ij}\frac{d}{dt}\left(V_i - U_i\right) \\ &+ \frac{1}{2}\rho_f S C_D\left(\mathrm{Re}\right)\left|\mathbf{U}-\mathbf{V}\right|\left(U_i - V_i\right) \\ &+ \left(m - \rho_f \Omega\right) g_i \end{aligned} \tag{4.4}$$

Where the first term represents the force necessary to overcome the inertia of the body, but the second term represents the force required to overcome the inertia of the fluid surrounding the body through a tensor of components M_{ij} which is known as the added mass tensor.

4.1.4 The Basset history force

We will now consider the Basset history force. This force is often neglected due to its complexity. It implies that the velocity of a solid particle is dependent on the previous motion of this particle through the history of viscous forces. A formulation of this force can be found in Corrsin and Lumley (1956). The Basset history force is added using the formulation for small spherical particle to the general equation of motion:

$$\begin{aligned} m\frac{dV_i}{dt} =& \rho_f \Omega \frac{dU_i}{dt} - M_{ij}\frac{d}{dt}\left(V_i - U_i\right) \\ &+ \frac{1}{2}\rho_f S C_D\left(\mathrm{Re}\right)\left|\mathbf{U}-\mathbf{V}\right|\left(U_i - V_i\right) \\ &+ 6D^2\rho_f\sqrt{\pi\nu}\int_{-\infty}^{t}\frac{1}{\sqrt{t-s}}\frac{d}{dt}\left(U_i - V_i\right)ds \\ &+ \left(m - \rho_f \Omega\right) g_i \end{aligned} \tag{4.5}$$

The formulation of the Basset history force (the second last term in equation 4.5) is given for small spherical particles as it assumes that the disturbance flow behind the particle is at a low Reynolds number. Physically this can be untrue for the problem at hand, and extensions of this formulation to bigger particles can be found in Maxey and Riley (1994), but these require a finer degree of information of the flow than is usually available in large environmental flows. This is why it is assumed that the current formulation of the Basset history force will give a reasonable estimate to the problem of algae motion.

To account for the Basset history force F_{Basset}, van Hinsberg *et al.* (2011) proposed to assume to solve for the Basset history within a numerical window defined by time t_{win}, and then to assume that it is exponentially decreasing. Therefore the Basset history force his divided into its real form F_{win} when $s \leq t_{win}$ and the tail of the Basset history force F_{tail} when $s > t_{win}$:

$$\begin{aligned} F_{i,Basset}(t) =& C_B \int_{t-t_{win}}^{t} \frac{1}{\sqrt{t-s}} \frac{d}{dt} \left(U_i - V_i\right) ds \\ &+ C_B \sum_{p=1}^{q} \int_{-\infty}^{t-t_{win}} a_p \sqrt{\frac{e}{\widetilde{t_p} t_{win}}} \exp\left(-\frac{t-s}{\widetilde{t_p} t_{win}}\right) \frac{d}{dt} \left(U_i - V_i\right) ds \\ =& F_{i,win}(t) + F_{i,tail}(t) \end{aligned} \tag{4.6}$$

C_B is the Basset history force constant it is defined as:

$$C_B = 6D^2 \rho_f \sqrt{\pi \nu} \tag{4.7}$$

It is assumed that in the tail of the Basset history force the Basset kernel $1/(t-s)^{0.5}$ can be reduced to a sum of exponents where a_p and $\widetilde{t_p}$ are constants that have been set by van Hinsberg *et al.* (2011) to reduce the error. These values are given in table 4.1 for the summation of 10 exponents (i.e. $q = 10$) and it should also be specified that e is the number ($2.718...$).

Table 4.1: The constants used to calculate the tail of the Basset history force as described in van Hinsberg *et al.* (2011).

p	$\widetilde{t_p}$	a_p
1	0.1	0.23477481312586
2	0.3	0.28549576238194
3	1	0.28479416718255
4	3	0.26149775537574
5	10	0.32056200511938
6	40	0.35354490689146
7	190	0.39635904496921
8	1 000	0.42253908596514
9	6 500	0.48317384225265
10	50 000	0.63661146557001

To obtain a reasonable numerical result an approximation is done to the derivative in the integral of the Basset history force, it defined as:

$$\psi_i(s) = \frac{d}{dt} \left(U_i(s) - V_i(s)\right) \tag{4.8}$$

In the following, for conviniency, the space labels i will be dropped. The derivative ψ is divided into N subintervals, and is assumed that this derivative is linear in each subinterval (van Hinsberg *et al.*, 2011). This leads to the following definitions:

$$\tau_n = t - n\Delta t \tag{4.9a}$$
$$\psi_n = \psi(\tau_n) \tag{4.9b}$$
$$n = 1, 2, 3, ..., N \tag{4.9c}$$
$$\Delta t = \frac{t_{win}}{N} \tag{4.9d}$$

From these definitions it is possible to rewrite the first term of the Basset history force:

$$F_{win}(t) \approx C_B \sum_{n=1}^{N} \int_{t-t_{win}}^{t} \frac{1}{\sqrt{t-s}} \left[\psi_n + \frac{\psi_{n-1} - \psi_n}{\Delta t} (s - \tau_n) \right] ds \tag{4.10}$$

Since the values ψ_n in this integral are constant it has the following solution:

$$\begin{aligned} F_{win}(t) \approx & C_B \sum_{n=1}^{N} \left\{ 2\psi_n \sqrt{\Delta t} \left[\sqrt{n} + \frac{2}{3}(n-1)\sqrt{(n-1)} - \frac{2}{3} n\sqrt{n} \right] \right. \\ & \left. - \frac{2}{3} \psi_{n-1} \sqrt{\Delta t} \left[\sqrt{(n-1)}(2n+1) - 2n\sqrt{n} \right] \right\} \end{aligned} \tag{4.11}$$

The derivative ψ_0 is particularly important as it is a function of $V_i(t)$, and therefore equation 4.11 can be rewritten as:

$$\begin{aligned} F_{win}(t) \approx & \frac{4}{3} C_B \psi_0 \sqrt{\Delta t} + \frac{2}{3} C_B \psi_N \sqrt{\Delta t} \left(3\sqrt{N} + 2(N-1)^{\frac{3}{2}} - 2N^{\frac{3}{2}} \right) \\ & + \frac{4}{3} C_B \sqrt{\Delta t} \sum_{n=1}^{N-1} \psi_n \left[(n-1)^{\frac{3}{2}} - 2n^{\frac{3}{2}} + (n+1)^{\frac{3}{2}} \right] \end{aligned} \tag{4.12}$$

The tail of the Basset history force (see equation 4.6) is represented by a sum of the force components:

$$\begin{aligned} F_{tail}(t) = & C_B \sum_{p=1}^{q} \int_{-\infty}^{t-t_{win}} a_p \sqrt{\frac{e}{\widetilde{t_p} t_{win}}} \exp\left(-\frac{t-s}{\widetilde{t_p} t_{win}} \right) \psi_i(s) ds \\ = & C_B \sum_{p=1}^{q} a_p F_p(t) \end{aligned} \tag{4.13}$$

F_p can be divided into two parts, one which as to be computed directly and another which can computed recursively:

$$\begin{aligned} F_p(t) = & \int_{t-t_{win}-\Delta t}^{t-t_{win}} \sqrt{\frac{e}{\widetilde{t_p} t_{win}}} \exp\left(-\frac{t-s}{\widetilde{t_p} t_{win}} \right) \psi_i(s) ds + \int_{-\infty}^{t-t_{win}-\Delta t} \sqrt{\frac{e}{\widetilde{t_p} t_{win}}} \exp\left(-\frac{t-s}{\widetilde{t_p} t_{win}} \right) \psi_i(s) ds \\ = & F_{p,di}(t) + F_{p,re}(t) \end{aligned} \tag{4.14}$$

The direct part of the tail of the Basset history force can be solved using the same approximation as equation 4.10 to give the following equation:

$$\begin{aligned} F_{p,di}(t) = & 2\sqrt{e \widetilde{t_p} t_{win}} \exp\left(-\frac{1}{2\widetilde{t_p}} \right) \left\{ \psi_N \left[1 - \varphi\left(-\frac{\Delta t}{2\widetilde{t_p} t_{win}} \right) \right] \right. \\ & \left. + \psi_{N+1} \exp\left(-\frac{\Delta t}{2\widetilde{t_p} t_{win}} \right) \left[\varphi\left(\frac{\Delta t}{2\widetilde{t_p} t_{win}} \right) - 1 \right] \right\} \end{aligned} \tag{4.15a}$$

$$\varphi(z) = \frac{e^z - 1}{z} \tag{4.15b}$$

The recursive part of the tail $F_{p,re}$ can rearranged so that:

$$\begin{aligned} F_{p,re}(t) = & \int_{-\infty}^{t-t_{win}-\Delta t} \sqrt{\frac{e}{\widetilde{t_p} t_{win}}} \exp\left(-\frac{t-s}{\widetilde{t_p} t_{win}}\right) \psi_i(s) ds \\ = & \exp\left(-\frac{\Delta t}{2\widetilde{t_p} t_{win}}\right) \int_{-\infty}^{t-t_{win}-\Delta t} \sqrt{\frac{e}{\widetilde{t_p} t_{win}}} \exp\left(-\frac{t-\Delta t-s}{\widetilde{t_p} t_{win}}\right) \psi_i(s) ds \\ = & \exp\left(-\frac{\Delta t}{2\widetilde{t_p} t_{win}}\right) F_p\left(t-\Delta t\right) \end{aligned} \tag{4.16}$$

Finally using the equations 4.6, 4.12, 4.13, 4.15 and 4.16 the Basset history force can then be modelled as:

$$F_{i,Basset} = \frac{4}{3} C_B \sqrt{\Delta t} \frac{d}{dt}\left(U_i(t) - V_i(t)\right) + C_{i,Bas} \tag{4.17a}$$

$$\begin{aligned} C_{i,Bas} = & \frac{2}{3} C_B \psi_{i,N} \sqrt{\Delta t}\left(3\sqrt{N} + 2\left(N-1\right)^{\frac{3}{2}} - 2N^{\frac{3}{2}}\right) \\ & + \frac{4}{3} C_B \sqrt{\Delta t} \sum_{n=1}^{N-1} \psi_{i,n}\left[\left(n-1\right)^{\frac{3}{2}} - 2n^{\frac{3}{2}} + \left(n+1\right)^{\frac{3}{2}}\right] \\ & + \sum_{p=1}^{q} a_p F_{i,p}(t) + a_p \exp\left(-\frac{\Delta t}{2\widetilde{t_p} t_{win}}\right) F_{i,p}(t-\Delta t) \end{aligned} \tag{4.17b}$$

$$\begin{aligned} F_{i,p}(t) = & 2C_B \sqrt{e \widetilde{t_p} t_{win}} \exp\left(-\frac{1}{2\widetilde{t_p}}\right) \left\{ \psi_{i,N}\left[1 - \phi\left(-\frac{\Delta t}{2\widetilde{t_p} t_{win}}\right)\right] \right. \\ & \left. + \psi_{i,N+1} \exp\left(-\frac{\Delta t}{2\widetilde{t_p} t_{win}}\right)\left[\phi\left(\frac{\Delta t}{2\widetilde{t_p} t_{win}}\right) - 1\right] \right\} \end{aligned} \tag{4.17c}$$

Where $C_{i,Bas}$ regroups all the components of the Basset history force which are independent of the current time t. We recall that the coefficient C_B is given by equation 4.7, the constant a_p and $\widetilde{t_p}$ are given in table 4.1. The notation $\psi_{i,n}$ refers to equations 4.8 and 4.9. When this resolution of the Basset history force is used numerically to solve for the particle transport, it is recommended that the time step Δt be equal to the numerical time step, i.e. $\Delta t = dt$.

The accuracy of this method to solve for the Basset history force has been analysed in van Hinsberg *et al.* (2011), and it proves to be very accurate, even with a small $t_w in$ or a large dt (as long as this dt can account for flow variations).

4.1.5 The lift force

The final force component that can affect the motion of a solid body in fluid is the lift force, which is a force that occurs as the flow passes along the surface of a body. It is normal to the surface this flow. An estimation of the componants of this force $F_{i,L}$ given in Auton *et al.* (1988), is given below:

$$F_{i,L} = C_L \rho_f \Omega \left(\mathbf{U} - \mathbf{V}\right) \nabla \times \mathbf{U} \tag{4.18}$$

$\nabla \times \mathbf{U}$ is the vorticity of the flow, and for environmental flows, since they are assumed irrotational, and since the particle is also assumed to be irrotational, the lift force will be neglected in this thesis.

4.2 Simplification to an isotropic body

To simplify the problem of the transport of solid bodies, these bodies will now be simplified to an isotropic body sphere. This is done under the assumption that an alga transported by the flow can fold upon itself. Furthermore an algal bloom will have virtually all possible orientations, and averaging all the possible orientations will be equivalent to considering an isotropic body. Under this assumption the added mass tensor for an isotropic body is equal to a constant M multiplied by the identity matrix:

$$M_{ij} = M\delta_{ij} \tag{4.19}$$

The algae can also be further simplified to a sphere (the simplest isotropic body). However this remains a starting point, and the extension of the model from a sphere to an alga is described in chapter 9, but unless mentioned otherwise the solid bodies considered are spheres. Firstly the characteristic length of the body D will be chosen to be the diameter of the sphere D_s. This leads to the following definitions for the physical properties of the body:

$$\mathrm{Re}_s = \frac{|\mathbf{U} - \mathbf{V}|\, D_s}{\nu} \tag{4.20a}$$

$$S_s = \frac{\pi D_s^2}{4} \tag{4.20b}$$

$$\Omega_s = \frac{\pi D_s^3}{6} \tag{4.20c}$$

In place of Re_p, S and Ω. The drag coefficient will then be given by the following equation (Almedeij, 2008).

$$C_{D,sphere} = \left[\frac{1}{(\varphi_1 + \varphi_2)^{-1} + (\varphi_3)^{-1}} + \varphi_4\right]^{1/10} \tag{4.21a}$$

$$\varphi_1 = (24\mathrm{Re}_s^{-1})^{10} + (21\mathrm{Re}_s^{-0,67})^{10} + (4\mathrm{Re}_s^{-0,33})^{10} + (0,4)^{10} \tag{4.21b}$$

$$\varphi_2 = \frac{1}{(0,148\mathrm{Re}_s^{0,11})^{-10} + (0,5)^{-10}} \tag{4.21c}$$

$$\varphi_3 = (1,57 \times 10^8 \mathrm{Re}_s^{-1,625})^{10} \tag{4.21d}$$

$$\varphi_4 = \frac{1}{(6 \times 10^{-17}\mathrm{Re}_s^{2,63})^{-10} + (0,2)^{-10}} \tag{4.21e}$$

With the added mass constant M_s for a sphere given as (Viollet *et al.*, 2002):

$$M_s = \frac{1}{2}\rho_f \Omega_s \tag{4.22}$$

4.3 Testing the impact of different force components

There are three force models which will be analysed. Using the isotropic body simplification (but not necessarily a sphere) the three force scenarios are defined from equations 4.2, 4.4 and 4.5 using the resolution of the Basset history force given in equations 4.17 as:

$$m\frac{dV_i}{dt} = \frac{1}{2}\rho_f S C_D\left(\mathrm{Re}_p\right)|\mathbf{U}-\mathbf{V}|\left(U_i-V_i\right) + \left(m-\rho_f\Omega\right)g_i \tag{4.23a}$$

$$m\frac{dV_i}{dt} = \rho_f\Omega\frac{dU_i}{dt} - M\frac{d}{dt}\left(V_i-U_i\right) + \frac{1}{2}\rho_f S C_D\left(\mathrm{Re}\right)|\mathbf{U}-\mathbf{V}|\left(U_i-V_i\right) + \left(m-\rho_f\Omega\right)g_i \tag{4.23b}$$

$$m\frac{dV_i}{dt} = \rho_f\Omega\frac{dU_i}{dt} - M\frac{d}{dt}\left(V_i-U_i\right) + \frac{1}{2}\rho_f S C_D\left(\mathrm{Re}\right)|\mathbf{U}-\mathbf{V}|\left(U_i-V_i\right) + \frac{4}{3}C_B\sqrt{\Delta t}\frac{d}{dt}\left(U_i(t)-V_i(t)\right) + C_{i,Bas} + \left(m-\rho_f\Omega\right)g_i \tag{4.23c}$$

For ease of understanding these are summarised table 4.2.

Table 4.2: The different force scenarios which will be solved.

	Buoyancy	Drag	Momentum	Basset history	source
Model I	yes	yes	no	no	eqn 4.23a
Model II	yes	yes	yes	no	eqn 4.23b
Model III	yes	yes	yes	yes	eqn 4.23c

Furthermore equations 4.23 can be rearranged to give the evolution of the solid particle velocity in terms of three components:

$$dV_i = F_a dU_i + F_b\left(U_i-V_i\right)dt + F_{i,c}dt \tag{4.24}$$

This equation can be used numerically, with dt being the numerical time step (remember $\Delta t = dt$). In this equation the first coefficient is linked to the evolution of the fluid, and according to the different force component is given by the following equation:

$$F_a = \begin{cases} 0 & \text{drag only} \\ \dfrac{\rho_f\Omega + M}{m+M} & \text{drag and momentum} \\ \dfrac{\rho_f\Omega + M + \frac{4}{3}C_B\sqrt{dt}}{m+M+\frac{4}{3}C_B\sqrt{dt}} & \text{drag, momentum and Basset} \end{cases} \tag{4.25}$$

The second coefficient is linked to the velocity differences between the fluid and the solid body:

$$F_b = \begin{cases} \dfrac{\rho_f S C_D|\mathbf{U}-\mathbf{V}|}{2m} & \text{drag only} \\ \dfrac{\rho_f S C_D|\mathbf{U}-\mathbf{V}|}{2\left(m+M\right)} & \text{drag and momentum} \\ \dfrac{\rho_f S C_D|\mathbf{U}-\mathbf{V}|}{2\left(m+M+\frac{4}{3}C_B\sqrt{dt}\right)} & \text{drag, momentum and Basset} \end{cases} \tag{4.26}$$

The final coefficient depends on constant values (during time t):

$$F_{i,c} = \begin{cases} \frac{(m-\rho_f \Omega)\, g_i}{m} & \text{drag only} \\ \frac{(m-\rho_f \Omega)\, g_i}{m+M} & \text{drag and momentum} \\ \frac{(m-\rho_f \Omega)\, g_i + C_{i,Bas}}{m+M+\frac{4}{3}C_B\sqrt{dt}} & \text{drag, momentum and Basset} \end{cases} \tag{4.27}$$

Out of those coefficient the most important one is F_b as it can be used to define the particle relaxation time τ_{part}. This characteristic time is a measure of how fast a particle will react to flow variations, and it is given by the following definition:

$$\tau_{part} = \frac{1}{F_b} \tag{4.28}$$

It is thus changing with time.

To test the impact of each force component, let us consider isotropic particles falling unhindered in a stationary fluid ($U_i = 0$ and $dU_i = 0$). The settling velocity V_{set} can be defined as the maximum vertical velocity that the particles will reach ($dV_i = 0$). Using equations 4.24 and 4.28, it is given by the following equation (where it is assumed that this settling velocity is positive when particles sink, and positive when they float):

$$V_{set} = \frac{F_{z,c}}{F_b} = F_{z,c}\tau_{part} \tag{4.29a}$$

$$= \text{sign}\left(\rho_{s/f} - 1\right) \sqrt{\frac{2\left|\rho_{s/f} - 1\right|}{SC_D(\text{Re}_{set})}\left|\mathbf{g}\right|} \tag{4.29b}$$

With the value Re_{set} defined by:

$$\text{Re}_{set} = \frac{|V_{set}|\, D}{\nu} \tag{4.30}$$

And:

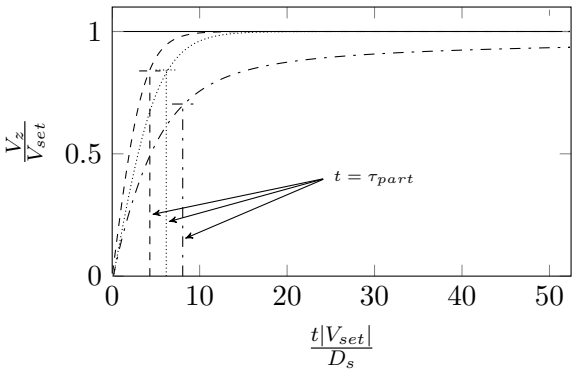
$$\rho_{s/f} = \frac{\rho_s}{\rho_f} \tag{4.31}$$

This equation shows that since the numerators of F_b and $F_{i,c}$ will cancel and $C_{i,Bas}$ is equal to 0 when $dU_i = 0$ and $dV_i = 0$, the settling velocity will be the same for all force scenarios. Solid particles were allowed to accelerate from rest to their settling velocity in a stationary fluid using the different force scenarios presented in equations 4.2, 4.4 and 4.5. A portion of the evolution of their vertical velocities are given in figure 4.1. Furthermore dimensionally speaking it is possible to rewrite the particle velocity and the particle relaxation time as functions of non-dimensional quantities:

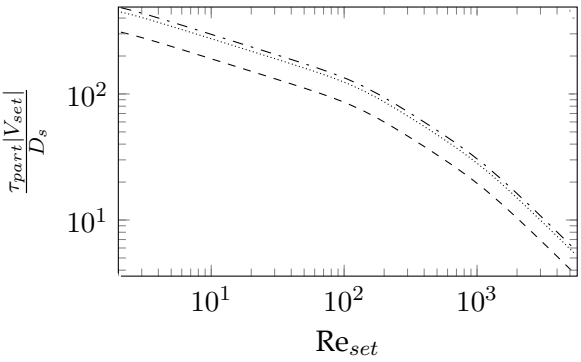
$$\frac{V_z}{V_{set}} = f\left(\rho_{s/f}, \frac{t\,|V_{set}|}{D}, \text{Re}_{set}\right) \tag{4.32a}$$

$$\frac{\tau_{part}\,|V_{set}|}{D} = f\left(\rho_{s/f}, \text{Re}_{set}\right) \tag{4.32b}$$

These values can be used to non-dimensionalise figure 4.1.



(a) Particle velocity, $\mathrm{Re}_{set} = 5700$



(b) Particle relaxation time

Figure 4.1: The evolution of the settling velocity and particle relaxation time (in dimensionless form) for spherical particles falling for one meter in a stationary fluid with $\rho_{s/f} = 1.13$. "——" is the maximal settling velocity, "- - -" is the velocity for model I, "·····" is the velocity for model II, "- · -" is the velocity for model III, see table 4.2.

Figure 4.1a shows that considering more components of the force reduces the acceleration of the solid particle (in this case $D_s = 0.02$ m, $\rho_s = 1129\,\mathrm{kg{\cdot}m^{-3}}$ and $\rho_f = 1000\,\mathrm{kg{\cdot}m^{-3}}$). It takes 3.7 s for a particle to settle 1 m if the only force, other than buoyancy, considered is the drag, but 3.78 s if the momentum is added and 4.23 s if the Basset history force is also added. Figure 4.1b shows the particle relaxation time for different Re_{set}. These calculations also allowed to calculate the relaxation time when the particle is at rest and when it has reached its settling velocity, these are shown in table 4.3. From the figure and the table it is visible that including all the components of the force increases the particle relaxation time, and therefore it means that particles will take long to respond to flow variations.

Table 4.3: The particle dimensionless particle relaxation time $\tau_{part}\,|V_{set}|\,/D_s$ calculated for settling velocities solved using the models presented in table 4.2. Here $\rho_{s/f} = 1.13$.

	Model I	Model II	Model III
$V_z = 0$	356	513	556
$t = \tau_{part}$	4.30	6.18	8.07
$V_z = V_{set}$	3.59	5.18	5.61

4.4 Testing the physical characteristics of solid bodies

To test the physical characteristics of the solid bodies the Basset history force and the buoyancy will be ignored. This is done to simplify calculations in order to make certain characteristics visible. This will be done by considering particles released in permanent Taylor eddies. These eddies solve the Navier-Stokes equations and their velocities are defined by:

$$U_x = -U_0 \sin\left(\frac{\pi}{\lambda_T}x\right)\cos\left(\frac{\pi}{\lambda_T}y\right) \tag{4.33a}$$

$$U_y = U_0 \cos\left(\frac{\pi}{\lambda_T}x\right)\sin\left(\frac{\pi}{\lambda_T}y\right) \tag{4.33b}$$

Where U_0 is characteristic velocity of the flow and λ_T is the diameter of a Taylor eddies. The acceleration of the flow is defined by:

$$\frac{dU_x}{dt} = \frac{\pi U_0^2}{2\lambda_T}\sin\left(\frac{2\pi}{\lambda_T}x\right) \tag{4.34a}$$

$$\frac{dU_y}{dt} = \frac{\pi U_0^2}{2\lambda_T}\sin\left(\frac{2\pi}{\lambda_T}y\right) \tag{4.34b}$$

The shape of the Taylor eddies is shown in figure 4.2.

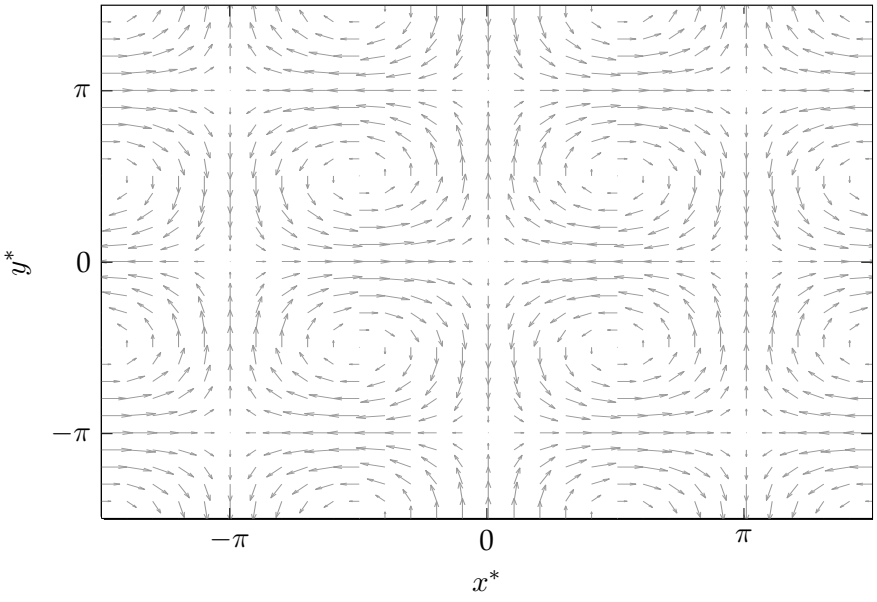


Figure 4.2: Typical shape of Taylor eddies.

Considering spherical particles transported by these eddies using only the drag force and the momentum (equation 4.4) it is possible to define 3 non-dimensional quantities using the Vaschy-Buckingham theorem:

$$A = \frac{2\rho_{s/f} + 1}{3} \tag{4.35a}$$

$$\mathrm{Re}_T = \frac{U_0 D_s}{\nu} \tag{4.35b}$$

$$\mathrm{St}_T = \frac{\pi D_s}{\lambda_T} \tag{4.35c}$$

Furthermore non-dimensional quantities can be defined through the following equations:

$$\mathbf{V}^* = \frac{\mathbf{V}}{U_0} \tag{4.36a}$$

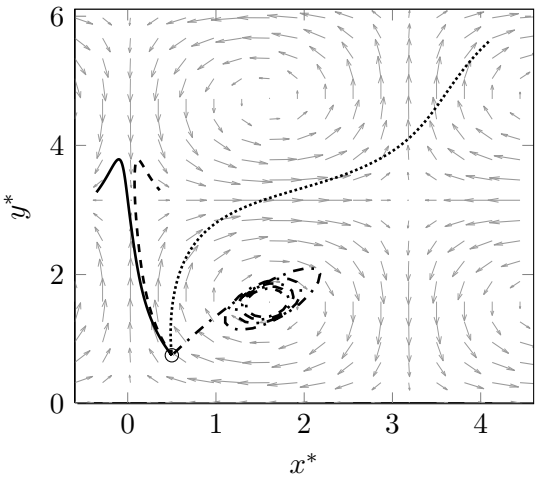
$$\mathbf{X}^* = \frac{2\pi\mathbf{X}}{\lambda_T} \tag{4.36b}$$

$$t^* = \frac{U_0 t}{2AD_s} \tag{4.36c}$$

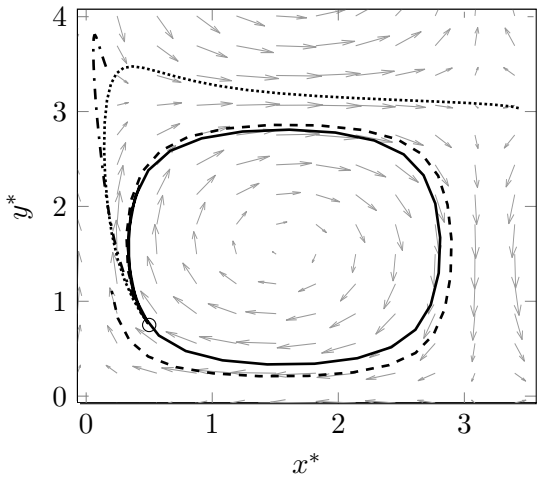
This therefore allows the following non-dimensional transport equation for spherical equation to be derived from equation 4.23b:

$$\frac{d\mathbf{V}^*}{dt^*} = \mathrm{St}_T \begin{pmatrix} \sin(2x^*) \\ \sin(2y^*) \end{pmatrix} + C_{D,sphere} \left| \begin{matrix} -\sin(x^*)\cos(y^*) - V_x^* \\ \cos(x^*)\sin(y^*) - V_y^* \end{matrix} \right| \begin{pmatrix} -\sin(x^*)\cos(y^*) - V_x^* \\ \cos(x^*)\sin(y^*) - V_y^* \end{pmatrix} \tag{4.37}$$

As a reminder, the drag coefficient C_D is a function of the particle Reynolds number of a sphere Re_s, which can be written in terms of Re_T. Using the two non-dimensional numbers that appear in equation 4.37, Re_T and St_T, simulations were done for different values. The particle trajectories within the turbulent eddies for a particle starting at point $(0.5, 0.75)$, which is well inside an eddy, are plotted in figure 4.3.



(a) $\mathrm{Re}_T = 1000$. —— $\mathrm{St}_T = 0.001$, - - - $\mathrm{St}_T = 0.01$, ····· $\mathrm{St}_T = 0.1$, – · – $\mathrm{St}_T = \pi$.



(b) $\mathrm{St}_T = 0.01$. —— $\mathrm{Re}_T = 0.01$, - - - $\mathrm{Re}_T = 1$, ····· $\mathrm{Re}_T = 100$, – · – $\mathrm{Re}_T = 10\,000$.

Figure 4.3: The transport of solid particles with different physical characteristics in Taylor eddies, see equation 4.37. Particles were released at point "– · –".

The two non-dimensional numbers Re_T and St_T represent two physical characteristics. Re_T is aratio between the inertial and viscous forces. St_T is a ratio between the size of the solid particles and the Taylor eddies. Figure 4.3 shows that if the particles are large in comparison the diameter of the Taylor eddies (typically $\mathrm{St}_T \gtrsim \pi$), then these eddies will not affect the transport of the particle. For example in figure 4.3a if $\mathrm{St}_T = \pi$ then the particle is transported to the center of the eddy, but as it is the same size as the particle this displacement is minimal. However for smaller St_T particles are ejected outside of the initial eddy, resulting in a large transport. The rapidity at which the particles are ejected is determined by the intensity of these eddies, through Re_T, as it is shown in figure 4.3b. From these simulations it is possible to conclude that the size of the solid bodies particles result in a filtering of certain turbulent structures in environmental flows.

Chapter 5

Fluid Velocities Model

Où le modèle pour décrire les vitesses du fluide à l'emplacement d'une particule Lagrangienne est défini. Cela commence par un bref aperçu des mathématiques stochastiques dans le domaine de la mécanique des fluides, avec en particulier la résolution du mouvement Brownien par Einstein. Le concept de marche aléatoire est ensuite introduit ainsi que le processus de Wiener. Finalement la notion d'intégrale stochastique est introduite, ainsi que le lemme d'Ito qui sert à résoudre ces intégrales. La deuxième section de ce chapitre démontre les étapes nécessaires pour développer un modèle Lagrangien stochastique permettant de prédire l'évolution dans le temps d'une particule de fluide dans un régime turbulent stationnaire, homogène et isotrope. En partant de cette base, le modèle Simplifié de Langevin est décrit, applicable à des régimes non homogènes, non stationnaires et non isotropes. Dans la troisième section, ce modèle est testé pour l'écoulement théorique d'une turbulence stationnaire, homogène et isotrope, ainsi que pour l'écoulement expérimental de la section 7.2.

5.1 A brief overview of stochastic modelling in fluid mechanics

The beginning of stochastic methods in fluid mechanics started with the resolution of Brownian motion (Gardiner, 2004). The botanist Robert Brown observed that pollen particles suspended in water were subject to irregular motion. As described by Einstein, these motions are the a result of very small fluid particles impacting the comparatively large pollen particles. Einstein then followed the reasoning that the motion of the fluid particles is so complex that the impact of the fluid can only be explained from a probabilistic point of view. He then introduced the hypotheses that the motion of each pollen particle is independent of the motion of the other particles and furthermore that the motion of a single particle recorded at two different times will also be independent, so long as those two times are sufficiently separated. This then allowed Einstein to realise that Brownian motion was equivalent to the problem of diffusion from a single point source, for which the solution was known. Therefore the number of particles per unit volume f at location X and time t, or the probability density function, is given by:

$$f\left(X,t\right)=\frac{N_p}{\sqrt{4\pi Dt}}\exp\left(-\frac{x^2}{4Dt}\right) \tag{5.1}$$

Where N_p is number of particles released at the source and D is known as the diffusion constant. This reasoning then lead to stochastic modelling of fluid mechanics. From this equation Einstein then calculated an expression for the root mean square value of the displacement to be $\sqrt{2Dt}$. This idea can be used to introduce the concept of random walk. From the initial hypotheses introduced by Einstein, it can derived that the motion of a particle over a time interval dt is independent of the history of the motion during the previous time steps. These processes belong to what are known as Markov processes, which are processes for which the future states (or future probability distributions) are definined by the present state of the system.Therefore, the displacement of a particle undergoing Brownian motion during the time interval dt can be modelled by the following equation:

$$dX_i=\xi\sqrt{2Ddt} \tag{5.2}$$

This formulation is known as random walk, where X_i represents the position of a particle at a time t, and therefore dX_i represents the displacement during a time interval dt. ξ is a random number, which is generated so that the mean of its distribution is equal to 0 and its standard deviation is equal to 1 (standard distribution). Therefore from a statistical point of view the displacement of particles during one time interval follows a distribution with zero mean and a standard a deviation equal to the root mean square of all possible displacements.

To understand the development of the stochastic model described in the following section, some further concepts of stochastic mathematics need to be described. The first is the Wiener process. This can be considered as a random walk process equivalent to a standard distribution. This process is not differentiable, but it is possible to observe incrementations of this process, W. The statistical mean of incrementations of the Wiener process is given by the following equation:

$$\langle W\rangle=0 \tag{5.3}$$

The symbol $\langle ...\rangle$ represents the first statistical moment:

$$\langle f(x)\rangle=\int_{-\infty}^{\infty}xf(x)dx \tag{5.4}$$

The standard deviation of the Wiener process can be considered as the autocorrelation of the this process:

$$\langle WW \rangle = 1 \tag{5.5}$$

Therefore using the concept of the Wiener process the Random Walk process described by equation 5.2 can be rewritten as:

$$dX_i = \sqrt{2D} dW_i \tag{5.6}$$

This then introduces the concept of stochastic integrals. If we have an arbitrary function $G(t)$ we define a stochastic integral as $\int_{t_0}^{t} G(s)dW(s)$. To solve for this equation it is useful to divide this equation into n subintervals, $t_0 \leq t_1 \leq ... \leq t_{n-1} \leq t$. In each of these interval the function G is assumed to be constant and equal to $G(\tau)$ where τ is a point chosen in between this interval, $t_{i-1} \leq \tau_i \leq t_i$. The integral can therefore be written as the limit of partial sums (Gardiner, 2004):

$$\int_{t_0}^{t} G(s)dW(s) \equiv \lim_{n \to +\infty} \sum_{i=1}^{n} G(\tau_i) \left[W(t_i) - W(t_{i-1}) \right] \tag{5.7}$$

However, the solution of the sum is dependent on the choice of the intermediate point τ_i. A common choice is to choose the intermediate point as $\tau_i = t_{i-1}$. From this formulation the Ito Stochastic integrals can be defined such that:

$$\lim_{n \to \infty} \left\langle \left[\sum_{i=1}^{n} G(t_{i-1}) \left[W(t_i) - W(t_{i-1}) \right] - \int_{t_0}^{t} G(s)dW(s) \right]^2 \right\rangle = 0 \tag{5.8}$$

Ito stochastic integrals are useful as they allow the following definitions:

$$\langle dW \rangle = 0 \tag{5.9a}$$
$$\langle dW dW \rangle = dt \tag{5.9b}$$

Or more generally:

$$\left\langle \int_{a_1}^{b_1} G(s)dW(s) \int_{a_2}^{b_2} H(s)dW(s) \right\rangle = \int_{a_2}^{b_1} G(s)H(s)ds \tag{5.10}$$

For $a1 \leq a2 \leq b1 \leq b2$.

5.2 The Simplified Langevin Model of turbulence

According to the terminology presented in chapter 2, the model for the fluid velocity chosen for the problem of the diffusion of algae particles in a coastal environment is a Lagrangian model. Therefore in the following development of the model, the fluid velocities will be written using a notation that

will differentiate the Eulerian velocities at a location in space and time $\mathbf{U}(\mathbf{x}, t)$ and the Lagrangian velocities for a fluid particle at a position in time $\mathbf{U}^L(t)$.

In Einstein model (equation 5.6) the particle velocities were not considered and did not exist (Wiener processes are not differentiable). However another approach to this problem would be to consider that the particles velocities can be modelled through a stochastic process (instead of particle positions). This was the approach considered by Langevin where the transport of the particles can be given by the following equations (Minier and Peirano, 2001):

$$dX_i(t) = U_i(t)^L dt \tag{5.11a}$$

$$dU_i^L(t) = -\frac{U_i^L(t)}{T}dt + \sqrt{K}dW_i(t) \tag{5.11b}$$

Where T is the Lagrangian integral time scale (the integral of the autocorrelation) of the fluid velocity and K is a diffusion constant. It should be noted that Langevin's equation can be made to correspond to Einstein's equation. The first part of equation 5.11b is known as the drift, and it represents the fact that fluid particles will follow largely the direction of the flow. The second part is the diffusive term, and in the flow it represents the fluctuations of each individual fluid particles from the overall flow due to turbulence. Therefore if we consider the turbulent intensities:

$$U_{rms,i} = \sqrt{\overline{U_i' U_i'}} \tag{5.12}$$

The diffusion constant of the Langevin equation can be set as:

$$K = \frac{2U_{rms,i}^2(\mathbf{X}, t)}{T} \tag{5.13}$$

As starting point let us consider the case of stationary homogeneous isotropic turbulence, with zero mean and a turbulent intensity defined by $U_{rms,i}$. Taking into account the turbulent fluctuations at the position of the fluid particle using Reynolds decomposition (see equation 3.8) it is possible to rewrite the evolution of the fluid velocities (Pope, 2004):

$$dU_i^L(t) = -\frac{U_i^L(t)}{T}dt + \sqrt{\frac{2U_{rms,i}^2(\mathbf{X}, t)}{T}}dW_i(t) \tag{5.14}$$

This equation is the Langevin equation. If it is considered that at a time t_0 the fluid particle velocity $U_i^L(t_0)$ is a random variable with zero mean and variance $U_{rms,i}$ then for $t > t_0$, $U_i^L(t)$ is a Markov process which can be described by a random variable for which it is known that $\left\langle U_i^L(t) \right\rangle = 0$ and $\left\langle U_i^L(t) U_j^L(t) \right\rangle = U_{rms,i}^2 \delta_{ij}$. The symbol δ_{ij} is a dirac, which is equal to 1 if $i = j$ and 0 otherwise. The autocovariance function is therefore defined by (Pope, 2004):

$$R^L(s) = \frac{\left\langle U_i^L(t+s) U_i^L(t) \right\rangle}{U_{rms,i}^2(\mathbf{X}, t)} \tag{5.15a}$$

$$= \exp\left(-\frac{|s|}{T}\right) \tag{5.15b}$$

This then allows the Lagrangian integral time scale to be defined by:

$$T = \int_0^\infty R^L(s)ds \tag{5.16}$$

If $s \ll T$ and because $dW_i(t)$ represents a Wiener process the fluid particle velocity at time $t + s$ is given by the following equation:

$$U_i^L(t+s) = U_i^L(t) - \frac{U_i^L(t)}{T}s + \xi\sqrt{\frac{2U_{rms,i}^2(\mathbf{X},t)s}{T}} \tag{5.17}$$

Where ξ is still a randomly generated number with mean equal to 0 and standard deviation equal to 1. The correlation of a fluid particle velocity component between two points in time can be defined by:

$$\mathcal{D}_i^L(s) = \left\langle \left[U_i^L(t+s) - U_i^L(t)\right]^2 \right\rangle \tag{5.18}$$

Using equation 5.17, and because $s/T \ll 1$ this correlation can be found to equal:

$$\mathcal{D}_i^L L(s) = \frac{2U_{rms,i}^2(\mathbf{X},t)s}{T} \tag{5.19}$$

From the Kolmogorov hypothesis, see section 3.2, it can be calculated that the correlation of the fluid velocity can be uniquely determined by the dissipation rate ε (if $s \gg \tau_s$). Therefore from dimensional analysis the correlation of a fluid velocity component between two points in time is:

$$\mathcal{D}_i(s) = C_0\varepsilon s \tag{5.20}$$

Where C_0 is a constant, which is typically set to equal 2.1, see Pope (2000). Comparing the correlation of the fluid velocity components as defined by Kolmogorov (equation 5.20) and the correlation of the fluid particle velocity components (equation 5.19) gives the following relation.

$$T = \frac{2U_{rms,i}^2(\mathbf{X},t)}{C_0\varepsilon} \tag{5.21}$$

Or using the definition for the turbulent kinetic energy (equation 3.12).

$$T = \frac{4}{3}\frac{k}{C_0\varepsilon} \tag{5.22}$$

Therefore the Langevin equation, defined by equation 5.14 can be rewritten as:

$$dU_i^L(t) = -\frac{3}{4}\frac{C_0\varepsilon}{k}U_i^L(t)dt + \sqrt{C_0\varepsilon}dW_i(t) \tag{5.23}$$

To extend this equation to inhomogeneous flows, modifications need to be applied to the Langevin equation above. Firstly, the velocity increment due to the mean pressure gradient (first terms in the right hand side of equation 3.3) need to be taken into account. Secondly, the fluid particle velocity needs to relax to the local Eulerian mean velocity. Finally, the drift coefficient needs to be modified to properly take into account for the rate of dissipation of the kinetic energy (in homogeneous turbulence this coefficient correspond to the value in equation 5.23 due to the forcing required to maintain homogeneous turbulence). Therefore, as defined in Pope (2004), the Simplified Langevin Model for turbulence in inhomogeneous turbulent flow is:

$$dU_i^L(t) = -\frac{1}{\rho_f}\frac{\partial \overline{P}}{\partial x_i}dt - \left(\frac{1}{2}+\frac{3}{4}C_0\right)\frac{\varepsilon}{k}\left[U_i^L(t)-\overline{U_i}\right]dt + \sqrt{C_0\varepsilon}dW_i(t) \tag{5.24}$$

In this equation all the mean flow components $\overline{P}$, $\overline{U_i}$, k and ε are evaluated at the fluid particle position $\mathbf{X_i}(t)$. These values require the use of another model. For the problem of algae transport in a coastal environment these will be defined with the use of a large Eulerian model that can take into account all the mean flow variation resulting from a complex bathymetry, tidal currents or wave breaking, using some of the models presented in chapter 3 for example. Furthermore the notation to show the fluid velocity in the Lagrangian sense, $U_i^L(t)$, will be dropped in the rest of the thesis as only the mean fluid velocities ($\overline{U_i}$) are found from Eulerian models. In addition, it should be restated that the development of equation 5.24 requires the time step to be $\tau_s \ll dt \ll T_t$, where T_t is the integral time scale. From estimation (5.22) and considering the modifications done above, this integral time scale is:

$$T_t = \frac{1}{\frac{1}{2}+\frac{3}{4}C_0}\frac{k}{\varepsilon} \tag{5.25}$$

This time scale is close to the characteristic time for the large turbulent eddies (τ_l in equation3.50c), and therefore will be referred to latter on as the turbulent characteristic time. Furthermore another notation for the Simplified Langevin Model is often used:

$$dU_i^L(t) = -\frac{1}{T_t}U_i^L(t)dt + C_i(t)dt + B_i(t)dW_i(t) \tag{5.26}$$

Where the coefficient C_i regroups the mean flow components:

$$C_i = -\frac{1}{\rho_f}\frac{\partial \overline{P}}{\partial x_i} + \frac{1}{T_t}\overline{U_i} \tag{5.27}$$

And the coefficient B_i is standard deviation of the stochastic term:

$$B_i = \sqrt{C_0\varepsilon} \tag{5.28}$$

The main interest in equation 5.24 is that averaging this equation will relax to the Reynolds equation (3.9b), as shown in Pope (2000). Another interesting point is through the definition:

$$\begin{aligned} U_i' \equiv & U_i^L(t) - \overline{U_i^L} \\ = & U_i^L(t) - \overline{U_i} \end{aligned} \tag{5.29}$$

The evolution of the Reynolds stresses can then be modelled. Let us assume that at the instant $t + dt$ the fluid velocity fluctuations have increased by dU_i'. Therefore the evolution of the Reynolds stresses are given, at the first order, by:

$$\begin{aligned}\frac{d\overline{U_i'U_j'}}{dt} =& \frac{\overline{\left(U_i' + dU_i'\right)\left(U_j' + dU_j'\right)} - \overline{U_i'U_j'}}{dt} \\ =& \frac{\overline{U_i'dU_j'}}{dt} + \frac{\overline{U_j'dU_i'}}{dt} + \frac{\overline{dU_i'dU_j'}}{dt}\end{aligned} \tag{5.30}$$

The first two terms of the equations are symmetrical. The mean evolution of the fluid velocity is:

$$\begin{aligned}\frac{d\overline{U_i}}{dt} =& \overline{\frac{dU_i}{dt}} \\ =& \overline{\frac{\partial U_i}{dt} + U_j\frac{\partial U_i}{\partial x_j}} \\ =& \frac{\partial \overline{U_i}}{\partial t} + \frac{\partial \overline{U_iU_j}}{\partial x_j}\end{aligned} \tag{5.31}$$

This is found using the continuity equation (3.4). Furthermore Reynolds decomposition can be used on equation 5.31:

$$\begin{aligned}\frac{d\overline{U_i}}{dt} =& \frac{\partial \overline{U_i}}{\partial t} + \frac{\partial}{\partial x_j}\left[\overline{\left(\overline{U_i} + U_i'\right)\left(\overline{U_j} + U_j'\right)}\right] \\ =& \frac{\partial \overline{U_i}}{\partial t} + \frac{\partial}{\partial x_j}\left(\overline{\overline{U_i}\,\overline{U_j} + U_i'U_j'}\right) \\ =& \frac{\partial \overline{U_i}}{\partial t} + \overline{U_j}\frac{\partial \overline{U_i}}{\partial x_j} + \frac{\partial \overline{U_i'U_j'}}{\partial x_j}\end{aligned} \tag{5.32}$$

Using this definition the evolution of the fluctuating fluid velocities can be rewritten as:

$$\begin{aligned}\frac{dU_i'}{dt} =& \frac{d}{dt}\left(U_i - \overline{U_i}\right) \\ =& \frac{dU_i}{dt} - \frac{\partial \overline{U_i}}{\partial t} - \overline{U_j}\frac{\partial \overline{U_i}}{\partial x_j} - U_j'\frac{\partial \overline{U_i}}{\partial x_j} \\ =& \frac{dU_i}{dt} - \frac{d\overline{U_i}}{dt} + \frac{\partial \overline{U_i'U_j'}}{\partial x_j} - U_j'\frac{\partial \overline{U_i}}{\partial x_j}\end{aligned} \tag{5.33}$$

Therefore the symmetric terms of equation 5.30 can be rewritten as:

$$\begin{aligned}\overline{\frac{U_i'dU_j'}{dt}} =& \overline{\frac{U_i'dU_j'}{dt}} \\ =& \overline{U_i'\left(\frac{dU_j}{dt} - \frac{d\overline{U_j}}{dt}\right)} + \overline{U_i'\frac{\partial \overline{U_i'U_j'}}{\partial x_j}} - \overline{U_i'U_j'\frac{\partial \overline{U_i}}{\partial x_j}} \\ =& \overline{U_i'\frac{(dU_j)'}{dt}} + \overline{U_i'}\frac{\partial \overline{U_i'U_j'}}{\partial x_j} - \overline{U_i'U_j'}\frac{\partial \overline{U_i}}{\partial x_j} \\ =& \overline{U_i'\frac{(dU_j)'}{dt}} + \mathcal{P}\end{aligned} \tag{5.34}$$

Where $\mathcal{P}$ is the production of turbulent kinetic energy (equation 3.18). In the case of stationary decaying homogeneous anisotropic turbulence it is equal to zero. Furthermore in this scenario there is no mean flow meaning that $d\overline{U_i} = 0$ and $(dU_i)' = dU_i$. Therefore using the Simplified Langevin Model for stationary decaying homogeneous anisotropic turbulence (equation 5.24 where $\overline{P} = 0$) to write dU_i, and the relations given in equations 5.30 and 5.34, one finds:

$$\begin{aligned}\frac{d\overline{U_i'U_j'}}{dt} =& -\frac{\overline{U_i'U_j'}}{T_t} + \sqrt{C_0\varepsilon}\overline{\frac{U_i'dW_j}{dt}} - \frac{\overline{U_j'U_i'}}{T_t} + \sqrt{C_0\varepsilon}\overline{\frac{U_j'dW_i}{dt}} \\ &+ \frac{\overline{U_i'U_j'}}{T_t^2}dt - \frac{\sqrt{C_0\varepsilon}}{T_t}\overline{U_i'dW_j} - \frac{\sqrt{C_0\varepsilon}}{T_t}\overline{U_j'dW_i} + C_0\varepsilon\overline{\frac{dW_idW_j}{dt}}\end{aligned} \tag{5.35}$$

If we recall that $dt \ll T_t$ and since $\overline{U_i'dW_j} = 0$ because U_i' and dW_i are independent then this equation simplifies to:

$$\frac{d\overline{U_i'U_j'}}{dt} = -\left(1 + \frac{3}{2}C_0\right)\frac{\varepsilon}{k}\overline{U_i'U_j'} + C_0\varepsilon\delta_{ij} \tag{5.36}$$

This is equivalent to Rotta's model (equation 3.48 in the absence of diffusion) provided we define:

$$C_R = 1 + \frac{3}{2}C_0 \tag{5.37}$$

Which for a value of $C_0 = 2.1$ will give $C_R = 4.15$.

The turbulence model presented here is called the Simplified Langevin Model because it is the simplest form of a larger group of stochastic turbulence model called Generalised Langevin Models. In the same fashion that the SLM is analogous to Rotta's model each GLM model can correspond to other Reynolds averaged models (Pope, 1994). However these models usually require more information of the Eulerian flow than is typically available in environmental flow and therefore prove inefficient for the problem of algae transport.

5.3 Testing the Simplified Langevin Model

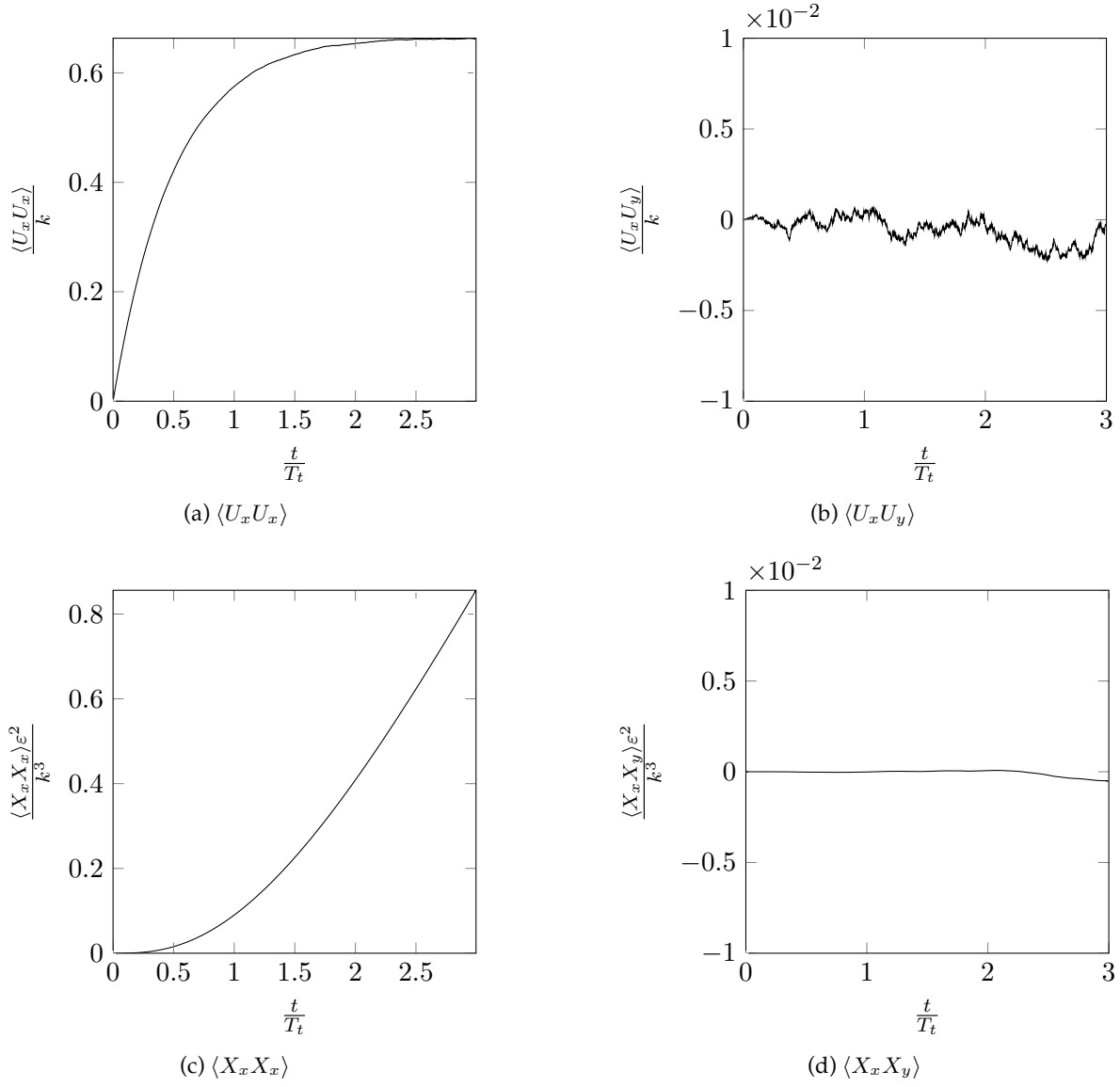
This model has been around for several years and it has been fairly well analysed, see for example Pope (2004). Nonetheless a few simple tests will be shown for fluid particles released in stationary homogeneous isotropic turbulence, thus the pressure gradient is zero. Remember however that the drift coefficient needs to be modified giving the following equation of motion for the fluid particles:

$$dX_i(t) = U_i(t)dt \tag{5.38a}$$

$$dU_i(t) = -\frac{U_i(t)}{T}dt + \sqrt{C_0\varepsilon}dW_i(t) \tag{5.38b}$$

$$T = T_t = \frac{1}{\frac{3}{4}C_0}\frac{k}{\varepsilon} \tag{5.38c}$$

The second moments for the velocity and the position of fluid particles are shown in figure 5.1. As areminder the second moments are the correlation of two fluid components, for example $\langle U_xU_x\rangle$ or $\langle U_xU_y\rangle$. In figure 5.1 only the moments along the first two components of direction are shown as turbulence is isotropic and stationary.



(a) $\langle U_x U_x \rangle$

(b) $\langle U_x U_y \rangle$

(c) $\langle X_x X_x \rangle$

(d) $\langle X_x X_y \rangle$

Figure 5.1: Second moments found for fluid particles released in stationary homogeneous isotropic turbulence: predictions of the Langevin model (5.38).

Figure 5.1 shows that the moment $\langle U_x U_x \rangle$ tends to a limit which is two thirds of the kinetic energy, as is expected from the definition of the turbulent kinetic energy (equation 3.12). Furthermore $\langle U_x U_y \rangle$ is close to zero (it would be zero with an infinite ammount of fluid particles released). This is also expected as it is a measure of the anisotropy, and the turbulence is isotropic. When looking at the moments for the position of the particle a quick calculation can be done by assuming that the evolution of the fluid velocities are almost zero (as there is no mean flow). The transport equation for the transport of fluid particles can be approximated as:

$$U_i(t)dt \simeq T_t \sqrt{C_0 \varepsilon} dW_i(t) \tag{5.39a}$$

$$dX_i = U_i dt \tag{5.39b}$$

Therefore the position of the particle is given by the following stochastic integral:

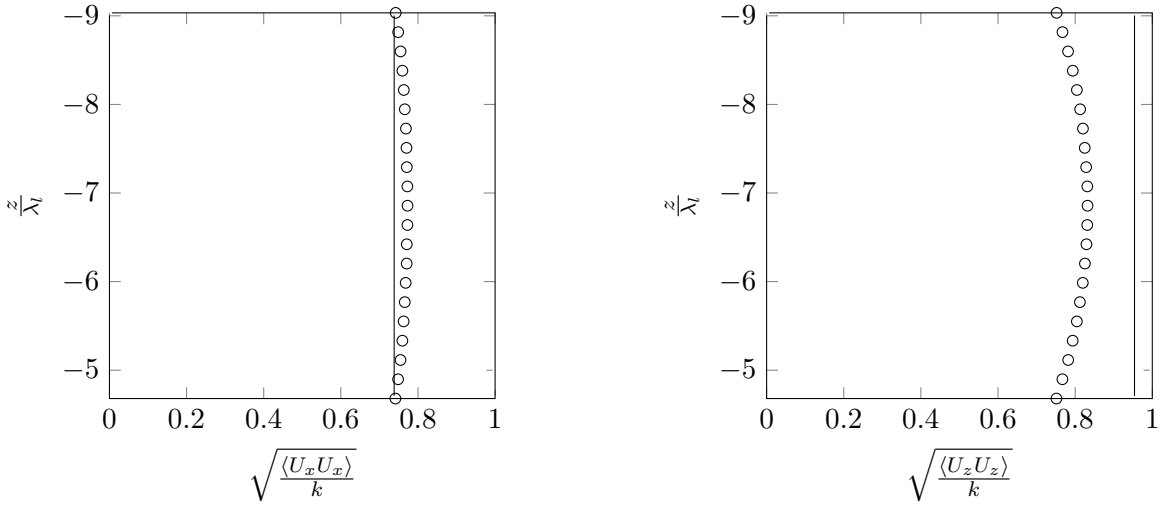
$$X_i = \int T_t \sqrt{C_0 \varepsilon} dW_i(t) \tag{5.40}$$

And therefore using Ito stochastic integrals (equation 5.8) this gives the following equation for the moments (through the definition in equation 5.10):

$$\begin{aligned}\langle X_i X_j \rangle =& \left\langle \int T_t \sqrt{C_0 \varepsilon} dW_i \int T_t \sqrt{C_0 \varepsilon} dW_j \right\rangle \\ =& T_t^2 C_0 \varepsilon \int dt \, \langle \xi_i \xi_j \rangle \\ \propto& T_t^2 C_0 \varepsilon t \delta_{ij} \end{aligned} \tag{5.41}$$

This explains why the second moment $\langle X_x X_x \rangle$ tends to a linear increase in time and $\langle X_x X_y \rangle$ is almost zero.

Furthermore, experimental measurements for a quasi-isotropic stationary turbulent flow are available through the experiment described in section 7.2. Fluid particles have been released in this regime, and the turbulent fluctuations were found to be approximately described by equations 7.4. We will now compare the results to the Simplified Langevin Model by observing the root mean square (rms) values of the velocities.



(a) $\langle U_x U_x \rangle$ (b) $\langle U_z U_z \rangle$

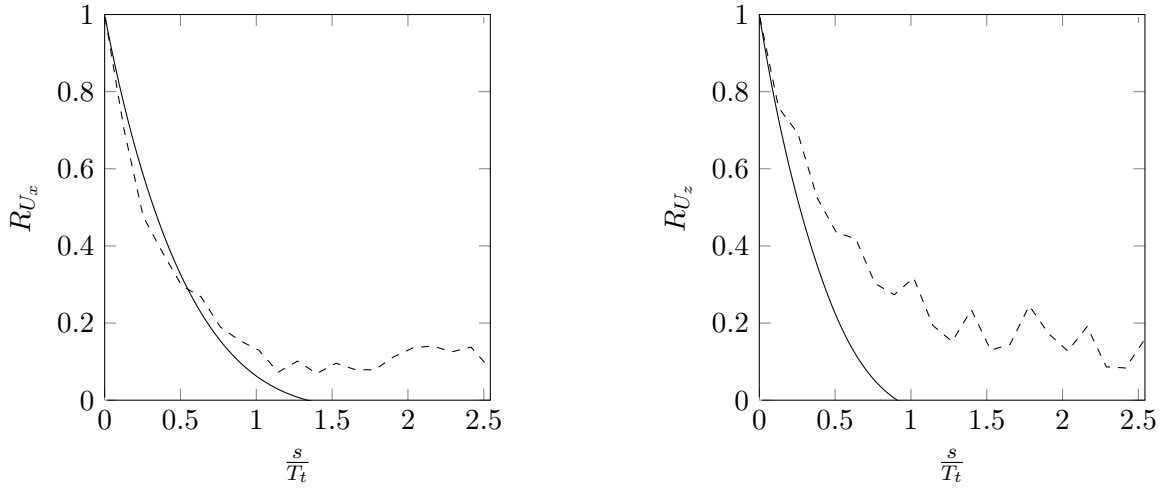
Figure 5.2: Second moments of fluid particle velocities in stationary quasi-isotropic grid turbulence (experiment in section 7.2). "——" shows the second moments found using the empirical formula 7.4 and "○" shows the moments found for fluid particles transported using the Langevin model (5.38).

As is expected, figure 5.2 shows that the Simplified Langevin Model cannot reproduce the velocity rms for the fluid particles in anisotropic turbulence. This is because it is a simple turbulence model, which assume a return to isotropy, which is not the case here. Other stochastic fluid velocities models could be applied to correspond to the problem (Pope, 1994, see), or some coefficients could be adjusted in the calculations of the characteristic turbulent time. Nonetheless this model gives a reasonable approximation of the fluid velocities rms values (with a better prediction for the horizontal values than the vertical values), and therefore this fluid velocities model will remain unchanged to be easily applicable to a wide variety of problems.

Another interesting characteristic is the autocorrelation of the fluid particle velocities. As a reminder the autocorrelation is defined as (equation 5.15a):

$$R_{U_i}(s) = \frac{\langle U_i(t+s)U_i(t)\rangle}{U^2_{rms,i}} \tag{5.42}$$

In figure 5.3, the autocorrelation of a numerical fluid particle transported in this turbulent regime is plotted against the autocorrelation of a point fixed in space found from the experimental results of section 7.2.



(a) R_{U_x} (b) R_{U_z}

Figure 5.3: The autocorrelation of the fluid velocities in stationary quasi-isotropic grid turbulence (experiment in section 7.2). "——" shows the normalised autocorrelations of numerical fluid particles transported using the Simplified Langevin Model and "- - -" shows the normalised autocorrelations of a point fixed in space found from the experimental results.

Figure 5.3 shows that the autocorrelation of a fluid particle is very similar to that of a recording fixed in space. There are some differences in the values of R_{U_i}, and especially R_{U_z}, but those occur because of the different nature of the velocities used to calculate the autocorrelations. In this figure the autocorrelation of the Lagrangian velocities found using the Simplified Langevin Model are compared to those found using the Eulerian velocities measured experimentally. The fact that differences are greater vertically results again from the fact that the Simplified Langevin Model cannot reproduce the turbulent regime. Nonetheless, if one was interested in recalibrating the coefficients of the Simplified Langevin Model (in particular constant C_0) to correspond to this particular case this figure could give a reasonable estimate of the Lagrangian integral timescale in the vertical direction.

As a reminder, from equation 5.16 the definition of an integral time scale is equal to the integral of the autocorrelation functions of the fluid velocities (as is plotted in figure 5.3). The stochastic model used supposes that the Lagrangian integral time scale is equal to T_t, however the values calculated from the numerical simulation gives a Lagrangian timescale of $0.39T_t$ horizontally and $0.31T_t$ vertically. But this is expected as the Simplified Langevin Model is applied, in this case, to a problem it cannot solve.

Furthermore using the experimental result of figure 5.3 the Eulerian time scales are given as $0.633T_t$ in the horizontal direction and $0.895T_t$ in the vertical direction. This indicates that the Eulerian and Lagrangian time scales are not equal. Although since in figure 5.3a, which corresponds to the autocorrelations of the horizontal velocities, the two curves correspond fairly closely (up to a certain point), and since the Simplified Langevin Model gives a good estimate of the horizontal turbulent velocities (see figure 5.2) it can be hypothesised that these two integral time scales are similar.

Chapter 6

Numerical Resolution

Où la méthode numérique utilisée pour résoudre le transport des algues en milieu côtier est développée. Cela commence par un descriptif des contraintes liées à la problématique diphasique, c'est-à-dire à l'interaction entre un corps solide et un fluide. Ensuite les contraintes numériques du modèle sont expliquées et une méthode numérique est proposée pour résoudre les équations régissant le transport des algues en milieu côtier. Pour finir les comportements asymptotiques de ce modèle sont expliqués.

6.1 Two-phase modelling

As shown in equation 4.24 from chapter 4 to model the particle transport one needs to know the turbulent fluid velocities at the position of the body. This is done through the use of a Lagrangian model on the fluid velocities, so that the large scale and the small scale of the flow can be modelled efficiently. The fluid velocity at the location of a particle will therefore be modelled using the Simplified Langevin Model (equation 5.24). However since the solid particle does not travel at the same velocity as the fluid a decorrelation occurs between the fluid particle and the solid particle. This was described in Csanady (1963) as the Crossing Trajectories Effect (CTE). The decorrelation between the fluid and the solid particles has two origins; it can be a result of external forces acting on the particle (for example gravity), but also the inertial properties of the solid particle. The decorrelation resulting from the inertial properties have not been well studied, and as such will be ignored in this thesis (it is assumed that modelling accurately the evolution of solid particles is more important) but this is clearly a place for future work on the subject. Nonetheless a method has been proposed in Minier and Peirano (2001) to take into account the decorrelation due to gravity, which is the only external force affecting the algae problematic. It is therefore assumed that the CTE result in a mean drift between the solid and fluid particles. This drift therefore changes the coefficients of the Simplified Langevin Model so that the modelled fluid velocity is the velocity seen by the particle $U_i^{(s)}$, as opposed to the actual fluid velocity U_i:

$$dU_i^{(s)} = -\frac{1}{T_i^{(s)}} U_i^{(s)} dt + C_i^{(s)} dt + B_i^{(s)} dW_i \tag{6.1}$$

Where the coefficients can have two forms, depending on whether the Crossing Trajectories Effects resulting from gravity is considered. The coefficient $T_i^{(s)}$ is the integral time scale defined by:

$$T_i^{(s)} = \begin{cases} T_t & \text{CTE ignored} \\ \dfrac{T_t}{\beta_i} & \text{CTE from gravity} \end{cases} \tag{6.2}$$

Where the coefficient β_i is a coefficient relating the seen integral time scale to the real integral time scale. The subscript i in this case represents directions parallel ($\parallel$) and perpendicular ($\perp$) to the mean drift between the fluid and solid particles:

$$\beta_\parallel = \sqrt{1 + 3T_{L/E}^2 \frac{\left|\overline{\mathbf{V}} - \overline{\mathbf{U}}\right|^2}{2k}} \tag{6.3a}$$

$$\beta_\perp = \sqrt{1 + 6T_{L/E}^2 \frac{\left|\overline{\mathbf{V}} - \overline{\mathbf{U}}\right|^2}{k}} \tag{6.3b}$$

$T_{L/E}$ is the ratio between the Lagrangian integral time scale, and the Eulerian integral time scale, which is assumed to be 1. This equation then shows that difference between the integral time scale seen by a solid particle an the real integral time scale of the fluid is function of the relative dimensionless mean drift between solid particles and fluid particles $\left|\overline{\mathbf{V}} - \overline{\mathbf{U}}\right| / \sqrt{k}$.

The coefficient $C_i^{(s)}$ in equation 6.1 regroups all of the relative mean flow components. Again for both cases it is given by:

$$C_i^{(s)} = \begin{cases} -\frac{1}{\rho_f}\frac{\partial \overline{P}}{\partial x_i} + \frac{1}{T_t}\overline{U_i} & \text{CTE ignored} \\ -\frac{1}{\rho_f}\frac{\partial \overline{P}}{\partial x_i} + \left(\overline{V_j} - \overline{U_j}\right)\frac{\partial \overline{U_i}}{\partial x_j} + \frac{1}{T_i^{(s)}}\overline{U_i} & \text{CTE from gravity} \end{cases} \tag{6.4}$$

Note the in equations 6.1 and 6.4 there is no summation over the repeated indices.

Finally the coefficient $B_i^{(s)}$ is the standard deviation of the stochastic term in equation 6.1, modelled for the different hypothesis of the Crossing Trajectories Effects:

$$B_i^{(s)} = \sqrt{\widetilde{C}_0 \varepsilon} \tag{6.5a}$$

$$\widetilde{C}_0 = \begin{cases} C_0 & \text{CTE ignored} \\ C_0 \text{ß}_i \frac{\widetilde{k}}{k} + \frac{2}{3}\left(\text{ß}_i \frac{\widetilde{k}}{k} - 1\right) & \text{CTE from gravity} \end{cases} \tag{6.5b}$$

Where the value $\widetilde{k}$ represents a modified turbulent kinetic energy:

$$\widetilde{k} = \frac{3}{2}\frac{\sum_{i=1}^{3} \text{ß}_i \overline{U_i' U_i'}}{\sum_{i=1}^{3} \text{ß}_i} \tag{6.6}$$

In the scenario where the Crossing Trajectories Effects are ignored equation 6.1 is equal to equation 5.24. This scenario is important because the CTE so far is only applied through the gravitational force. However this force is not applicable to two-dimensional horizontal problems, such as is often done in environmental flow, and furthermore it might require more information on the flow than is readily available.

The hypothesis that the Crossing Trajectories Effects is negligible implies that there is no decorrelation between the mean fluid velocity $\overline{U}_i$ and the mean solid body velocity $\overline{V}_i$. In the scope of a small time step this might be possible and therefore if the mean flow quantities ($\overline{\mathbf{U}}$, k and ε) are updated at every new position of the solid particle (and not of the fluid particle) these effect might be negligible. Furthermore if the spatial autocorrelation (following a travelling fluid particle) of the flow is the same as the temporal autocorrelation (at a fixed point in space) the crossing trajectories can also be neglected.

Therefore in most cases during this thesis the Crossing Trajectories Effects will be ignored, and as such it is assumed that the decorrelation between the fluid velocities and the solid body velocities are negligible during one time step. Nonetheless in the cases where the CTE should not be ignored the mean solid body velocity $\overline{V}_i$ will be calculated using the unhindered settling velocity, as defined by equation 4.29b.

6.2 Preliminary numerical considerations

Following the considerations given in the previous section the transport of solid particles in a turbulent flow can be modelled using a three step model:

$$dU_i^{(s)} = -\frac{1}{T_i^{(s)}} U_i^{(s)} dt + C_i^{(s)} dt + B_i^{(s)} dW_i \tag{6.7a}$$

$$dV_i = F_a dU_i^{(s)} + \frac{1}{\tau_{part}}\left(U_i^{(s)} - V_i\right) dt + F_{i,c} dt \tag{6.7b}$$

$$dX_i = V_i dt \tag{6.7c}$$

As is visible from this equation there are two characteristic times, the particle relaxation time τ_{part} and the integral time scale $T_i^{(s)}$ and dt is now considered as a numerical time step. These two characteristic times can be very limiting, as to solve the solid particle velocities explicitly one must satisfy $dt \sim \tau_{part}$, but to solve for the fluid particle velocities one must satisfy $dt \sim T_i^{(s)}$. However there is no reason why these two characteristic times would be of the same order, or even constant in space and time. It fact in any simulation the two times will have a range covering several orders and are almost always very different.

6.3 The exact integrator method

To circumvent this problem Peirano *et al.* (2006) have proposed a method for particles experiencing drag force only, and a similar approach will be to solve for this particle transport model in equations 6.7. As for an explicit resolution of these equations it is assumed that all the coefficients can be considered constant over the time interval $dt = t - t_0$. Therefore if F_a, τ_{part}, $F_{i,c}$, $T_i^{(s)}$, $C_i^{(s)}$ and $B_i^{(s)}$ are constant then there exists an analytical solution for the fluid velocity of the form (Peirano *et al.*, 2006):

$$U_i^{(s)}(t) = H_i(t) \exp\left(-\frac{t}{T_i^{(s)}}\right) \tag{6.8}$$

Where $H_i(t)$ is a function of time, and the derivative of the fluid velocity with respect to time is given by equation 6.7a:

$$dU_i^{(s)}(t) = -\frac{1}{T_i^{(s)}} U_i^{(s)} dt + dH_i(t) \exp\left(-\frac{t}{T_i^{(s)}}\right) \tag{6.9}$$

Thus, using equation 6.9 for the present problem, $H_i(t)$ is a stochastic process defined by:

$$dH_i(t) = \exp\left(\frac{t}{T_i^{(s)}}\right) \left[C_i^{(s)} dt + B_i^{(s)} dW_i(t)\right] \tag{6.10}$$

The solution for H_i over the interval dt is :

$$H_i(t) - H_i(t_0) = C_i^{(s)} T_i^{(s)} \left[\exp\left(\frac{t}{T_i^{(s)}}\right) - \exp\left(\frac{t_0}{T_i^{(s)}}\right)\right] + \int_{t_0}^{t} B_i^{(s)} \exp\left(\frac{s}{T_i^{(s)}}\right) dW_i(s) \tag{6.11}$$

This then gives the following equation for the fluid velocity at the location of the particle:

$$U_i^{(s)}(t) = \alpha_i U_i^{(s)}(t_0) + (1 - \alpha_i)\, C_i^{(s)} T_i^{(s)} + \gamma_i(t) \tag{6.12}$$

With:

$$\alpha_i = \exp\left(-\frac{dt}{T_i^{(s)}}\right) \tag{6.13}$$

Where γ_i is a stochastic integral equal to:

$$\gamma_i(t) = B_i^{(s)} \exp\left(-\frac{t}{T_i^{(s)}}\right) \int_{t_0}^{t} \exp\left(\frac{s}{T_i}\right) dW_i(s) \tag{6.14}$$

The same method can be applied to find the particle velocity from equation 6.7b, and the details of the calculations are shown in appendix A:

$$V_i(t) = \beta V_i(t_0) + (1-\beta)\left(C_i^{(s)} T_i^{(s)} + F_{i,c}\tau_{part}\right) + (\alpha_i - \beta)\,\check{C}_i\left(U_i^{(s)}(t_0) - C_i^{(s)} T_i^{(s)}\right) + \Gamma_i(t) \tag{6.15}$$

With:

$$\beta = \exp\left(-\frac{dt}{\tau_{part}}\right) \tag{6.16}$$

$$\check{C}_i = \frac{T_i^{(s)} - F_a\tau_{part}}{T_i^{(s)} - \tau_{part}} \tag{6.17}$$

Where Γ_i is a stochastic integral equal to:

$$\Gamma_i(t) = \check{C}_i\gamma_i(t) + B_i^{(s)}\left(F_a - \check{C}_i\right) \exp\left(-\frac{t}{\tau_{part}}\right) \int_{t_0}^{t} \exp\left(\frac{s}{\tau_{part}}\right) dW_i(s) \tag{6.18}$$

Finally to obtain the position of the solid particle at time t, a simple integration of the fluid velocity over the interval dt is performed:

$$\begin{aligned} X_i(t) = {} & X_i(t_0) + (1-\beta)\,\tau_{part} V_i(t_0) + \left[dt - (1-\beta)\,\tau_{part}\right]\left(C_i^{(s)} T_i^{(s)} + F_{i,c}\tau_{part}\right) \\ & + \check{C}_i\left(U_i^{(s)}(t_0) - C_i^{(s)} T_i^{(s)}\right)\left[(1-\alpha_i)\,T_i^{(s)} - (1-\beta)\,\tau_{part}\right] + \Phi_i(t) \end{aligned} \tag{6.19}$$

In this final equation the stochastic integral Φ_i is given by the following equation (see appendix A):

$$\begin{aligned} \Phi_i(t) = {} & -\check{C}_i T_i^{(s)}\gamma_i(t) - \tau_{part}\left[\Gamma_i(t) - \check{C}_i\gamma_i(t)\right] \\ & + B_i^{(s)}\left[\left(T_i^{(s)} - \tau_{part}\right)\check{C}_i + F_a\tau_{part}\right] \int_{t_0}^{t} dW_i(s) \end{aligned} \tag{6.20}$$

The three stochastic integrals, γ_i, Γ_i and Φ_i, developed here are dependent of each other. However since they are stochastic integrals of deterministic functions, they can each be modeled by a centered Gaussian random variable, a variable with zero mean (Peirano *et al.*, 2006). Furthermore it can be shown that a centered Gaussian vector can be expressed as the product of two matrices, the covariance matrix and a vector of independent standard random variables (zero mean and unitary standard deviation). Using the Cholesky decomposition and an appropriate random number generator these stochastic integrals can be modeled using the following equations:

$$\gamma_i = L_{11}\xi_{\gamma_i} \tag{6.21a}$$

$$\Gamma_i = L_{21}\xi_{\gamma_i} + L_{22}\xi_{\Gamma_i} \tag{6.21b}$$

$$\Phi_i = L_{31}\xi_{\gamma_i} + L_{32}\xi_{\Gamma_i} + L_{33}\xi_{\Phi_i} \tag{6.21c}$$

Where the ξ's are standard random variables and the coefficients L_{jk} are defined by:

$$L_{11} = \sqrt{\langle \gamma_i^2 \rangle} \tag{6.22a}$$

$$L_{21} = \frac{\langle \gamma_i \Gamma_i \rangle}{L_{11}} \tag{6.22b}$$

$$L_{22} = \sqrt{\langle \Gamma_i^2 \rangle - L_{21}^2} \tag{6.22c}$$

$$L_{31} = \frac{\langle \gamma_i \Phi_i \rangle}{L_{11}} \tag{6.22d}$$

$$L_{32} = \frac{\langle \Gamma_i \Phi_i \rangle - L_{21} L_{31}}{L_{22}} \tag{6.22e}$$

$$L_{33} = \sqrt{\langle \Phi_i^2 \rangle - L_{31}^2 - L_{32}^2} \tag{6.22f}$$

The covariances, $\langle \gamma_i^2 \rangle$, $\langle \Gamma_i \gamma_i \rangle$, *etc.*, are solved using the properties for stochastic integrals in Ito calculus (equation 5.10), where all the details of the calculations are given in appendix A:

$$\langle \gamma_i^2 \rangle = \left(1 - \alpha_i^2\right) B_i^{(s)\,2} \frac{T_i^{(s)}}{2} \tag{6.23a}$$

$$\langle \Gamma_i^2 \rangle = \left(B_i^{(s)} \check{C}_i\right)^2 \left[\left(1 - \alpha_i^2\right) \frac{T_i^{(s)}}{2} + \left(1 - \beta^2\right) \frac{\check{K}_i^2 \tau_{part}}{2} + 2\left(1 - \alpha_i \beta\right) \check{Q}_i \right] \tag{6.23b}$$

$$\begin{aligned} \langle \Phi_i^2 \rangle = \left(B_i^{(s)} \check{C}_i\right)^2 \Bigg\{ & \check{G}_i^2 dt + \left(1 - \alpha_i^2\right) \frac{T_i^{(s)\,3}}{2} + \left(1 - \beta^2\right) \frac{\check{K}_i^2 \tau_{part}^3}{2} \\ & - 2\check{G}_i \left[\left(1 - \alpha_i\right) T_i^{(s)\,2} + \left(1 - \beta\right) \check{K}_i \tau_{part}^2 \right] + 2\left(1 - \alpha_i \beta\right) \check{Q}_i T_i^{(s)} \tau_{part} \Bigg\} \end{aligned} \tag{6.23c}$$

$$\langle \gamma_i \Gamma_i \rangle = B_i^{(s)\,2} \check{C}_i \left[\left(1 - \alpha_i^2\right) \frac{T_i^{(s)}}{2} + \left(1 - \alpha_i \beta\right) \check{Q}_i \right] \tag{6.23d}$$

$$\langle \gamma_i \Phi_i \rangle = B_i^{(s)\,2} \check{C}_i \left[\left(1 - \alpha_i\right) \check{G}_i T_i^{(s)} - \left(1 - \alpha_i^2\right) \frac{T_i^{(s)\,2}}{2} - \left(1 - \alpha_i \beta\right) \check{Q}_i \tau_{part} \right] \tag{6.23e}$$

$$\begin{aligned} \langle \Gamma_i \Phi_i \rangle = \left(B_i^{(s)} \check{C}_i\right)^2 \Bigg\{ & \left[\left(1 - \alpha_i\right) T_i^{(s)} + \left(1 - \beta\right) \check{K}_i \tau_{part} \right] \check{G}_i - \left(1 - \alpha_i^2\right) \frac{T_i^{(s)\,2}}{2} \\ & - \left(1 - \beta^2\right) \frac{\check{K}_i^2 \tau_{part}^2}{2} - \left(1 - \alpha_i \beta\right) \check{K}_i T_i^{(s)} \tau_{part} \Bigg\} \end{aligned} \tag{6.23f}$$

With the following coefficients:

$$\check{K}_i = \frac{F_a}{\check{C}_i} - 1 \tag{6.24a}$$

$$\check{Q}_i = \frac{\check{K}_i T_i^{(s)} \tau_{part}}{T_i^{(s)} + \tau_{part}} \tag{6.24b}$$

$$\check{G}_i = T_i^{(s)} + \check{K}_i \tau_{part} \tag{6.24c}$$

It should be noted that $\check{G}_i \check{C}_i = T_i^{(s)}$ and that this model reduces to the model presented by Peirano *et al.* (2006) if the momentum and the Basset history force are ignored (*i.e.* $C_B = 0$, $C_{bas} = 0$, $F_a = 0$ and $M = 0$).

6.4 Asymptotic behaviour of the model

The main advantage of using this exact integrator method is that velocity components now become dependent on the exponential of the ratio between the numerical time step and a characteristic time (α_i and β, given by equations 6.13 and 6.16 respectively). The model therefore becomes more stable for extreme cases, such as when $dt \gg T_i^{(s)}$. Furthermore the following limit definitions are known for exponentials:

$$\lim_{x\to\infty} \exp(-x) = 0 \tag{6.25a}$$

$$\exp(-x) \underset{x\to 0}{\sim} 1 - x \tag{6.25b}$$

Using these limit definitions it is possible to define the behaviour of the model during extreme cases. Significant results will be shown, detailed calculations are presented in appendix B.

6.4.1 If $dt \gg T_i^{(s)}$

If the numerical time step dt is much larger than the integral time scales $T_i^{(s)}$ (i.e. $\alpha_i \to 0$), then according to equations 6.12, 6.21a, 6.22a and 6.23a the fluid velocity can be simplified to:

$$U_i^{(s)}(t) \to C_i^{(s)} T_i^{(s)} + B_i^{(s)} \sqrt{\frac{T_i^{(s)}}{2}} \xi_{\gamma_i} \tag{6.26}$$

This implies that the fluid velocities can be modelled with a term proportional to the mean flow and another proportional to the turbulent fluctuations. Simply put when the numerical time step dt is much larger than the integral time scale $T_i^{(s)}$ then all the turbulent fluctuations can be modelled as a white noise. According to equation 6.12, it can also be seen that the fluid particle forgets its initial velocity $U_i^{(s)}(t_0)$.

This is made more visible by looking at the simple case of of stationary homogeneous isotropic turbulence used in section 5.2 then for fluid particles ($V_i = U_i^{(s)} = U_i$) the coefficients become:

$$C_i^{(s)} = \frac{\overline{U_i}}{T} \tag{6.27a}$$

$$T_i^{(s)} = T \tag{6.27b}$$

$$B_i^{(s)} = \sqrt{C_0 \varepsilon} \tag{6.27c}$$

These are found from the relation given in equation 5.21, which means that the fluid velocity can be written as

$$\begin{aligned} U_i &\to \frac{\overline{U_i}}{T} T + \sqrt{\frac{C_0 \varepsilon T}{2}} \xi_{\gamma_i} \\ &= \overline{U_i} + U_{rms,i} \xi_{\gamma_i} \\ &= \overline{U_i} + U_i' \end{aligned} \tag{6.28}$$

Proving that the fluid velocities are modelled by a mean flow term and turbulent fluctuations simulated as a white noise.

6.4.2 If $dt \ll T_i^{(s)}$

If the numerical time step dt is much larger than the integral time scale $T_i^{(s)}$, then $\alpha_i \to 1$, and therefore from equations 6.12, 6.21a, 6.22a and 6.23a the fluid velocity can be simplified to:

$$U_i^{(s)}(t) \to U_i^{(s)}(t_0) + C_i^{(s)}dt + B_i^{(s)}\sqrt{dt} \tag{6.29}$$

Therefore the fluid velocities can be modelled using model similar Langevin's model for Brownian motion (equation 5.11b), which is expected as in this scenario the model is placed in a temporal frame of reference equal to the small turbulent eddies. However this means that the numerical time step is not much greater than the small scale of turbulence, which means that the turbulence model is not valid anymore (see chapter 5 for the development of the turbulence model). To be rigorous, when this is the case the turbulence model should be modelled through the following equation[1]:

$$U_i(t) = -\frac{1}{T_i}U_i(t)dt + C_i(t)dt + \Psi_i(t)dt \tag{6.30}$$

This equation implies that the small turbulent eddies are not modelled as a white noise, but through the following equation:

$$\Psi_i(t) = -\frac{1}{T_{\Psi_i}}\Psi_i(t)dt + B_{\Psi_i}(t)dW_i(t) \tag{6.31}$$

What this model does is to move the stochastic process up one level. This is the same reasoning as what was done to move from Einstein's stochastic model, which applied a random process to the position of a particle, to Langevin's stochastic model, which applied a random process to the velocity of a particle, and therefore was able to capture more information. What the model presented in equation 6.31 does, is to apply a random process to the acceleration of a fluid particle. This would require all the model constants (T_{Ψ_i} and B_{Ψ_i}) to be calibrated, and all the modelling consideration developed earlier (two-phase modelling and the exact integrator method) to be recalculated. Therefore for simplicity it is assumed that the numerical time step is always much larger than the characteristic time of the small turbulent eddies, i.e. $dt \gg \tau_s$, where τ_s is the characteristic time of the small turbulent eddies, as defined from the Kolmogorov hypothesis explained in chapter 3 and given by equation 3.49c.

6.4.3 If $dt \gg \tau_{part}$

In addition to the hypothesis that the numerical time step dt is much larger than the particle relaxation time τ_{part} (meaning that $\beta \to 0$) it can also assumed that the integral time scale $T_i^{(s)}$ is of the same order as the numerical time step. Under this hypothesis, using equations 6.15, 6.21b, 6.22b, 6.22c, 6.23b and 6.23d, the solid particle velocity tends to the following equation, where the assumption that $dt \sim T_i^{(s)}$ is used to make the equation more understandable:

$$V_i(t) \to U_i^{(s)}(t) + F_{i,c}\tau_{part} + \frac{B_i^{(s)}(F_a - 1)}{2}\sqrt{\tau_{part}}\xi_{\Gamma_i} \tag{6.32}$$

Therefore for this scenario the solid particle velocity will follow almost exactly the fluid velocity, the only differences are due to the external gravitational force and the momentum of the solid body

[1] J.-P. Minier, personal communication

(this is also true if $T_i^{(s)}$ is not of the same order as dt, see appendix B). This is to be expected as the particle relaxation time gives an information about the speed at which a solid particle responds to flow variations, and therefore when it is very small it responds almost instantly.

6.4.4 If $dt \ll \tau_{part}$

Again in this scenario, to ease the understanding of the solid particle velocity, it is assumed the numerical time step dt is of the same order as $T_i^{(s)}$. Therefore, using equations 6.15, 6.21b, 6.22b, 6.22c, 6.23b and 6.23d, the asymptotic solid particle velocity under the condition that the numerical time step dt is much smaller than the particle relaxation time τ_{part} (and therefore $\beta \to 1$) is:

$$V_i(t) \to V_i(t_0) + F_{i,c}dt + F_a dU_i^{(s)}(t_0) \tag{6.33}$$

Therefore in this limiting condition the solid particle velocity stays almost constant, with small variations resulting from the external buoyant forces and the momentum of the fluid. This is an expected solution, as a large particle relaxation time would imply that the particle would take very long to respond to flow variations, and therefore these would appear almost invisible to the particle.

Furthermore, for all limiting scenarios on $T_i^{(s)}$ and τ_{part} as well as the exact integrator model in general, it should be noted that there are a few cases when the model might be undetermined (see appendices A and B). However these cases are very specific and they are very unlikely to occur, but nonetheless these equations should be used with care.

Chapter 7

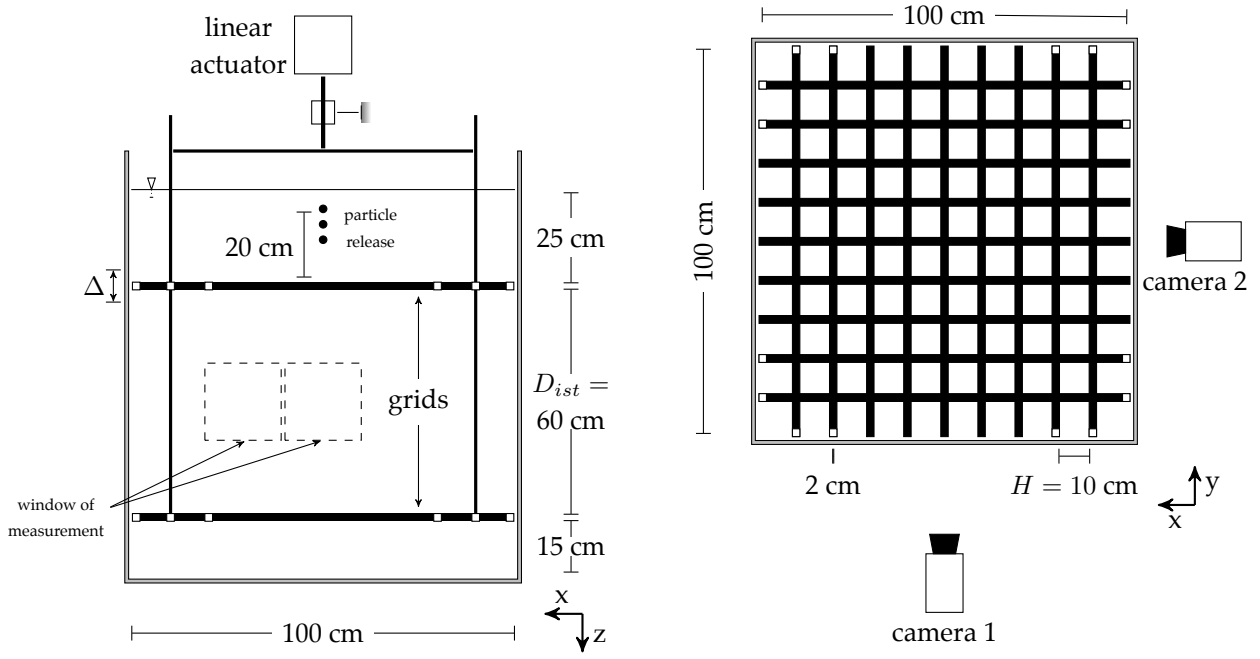
Particles Falling in Quasi-Homogeneous Turbulence

Où la première expérience servant à valider le modèle développé au chapitre 6 est décrite et analysée. Dans cette expérience, deux grilles oscillent en phase dans un fluide initialement stationnaire afin de créer une turbulence quasi-homogène. Cette turbulence a été quantifiée à l'aide de mesures PIV et LDV et un modèle empirique a été développé pour pouvoir étendre ces données au delà de la fenêtre de mesure. Ensuite des sphères de diamètres différents ont été lâchées dans deux fluides de densités différentes. Les trajectoires de ces sphères ont été enregistrées par deux caméras perpendiculaires. Un traitement d'image a ensuite été appliqué pour obtenir les vitesses de ces sphères. Les statistiques de ces vitesses ont été analysées, ce qui a permis de conclure qu'il est important de prendre en compte la traînée et la force de Basset, mais moins celle d'inertie. De plus la méthode pour prendre en compte les «Crossing Trajectories Effects» est appropriée pour ce cas où la gravité joue un rôle important, mais ces effets n'ont qu'un impact limité et ils peuvent ainsi être négligés pour les simulations en deux dimensions horizontales.

Plusieurs parties de ce chapitre sont issues du papier "Diffusion in grid turbulence of isotropic macro-particles using a Lagrangian stochastic method: theory and validation" par A. Joly, F. Moulin, D. Violeau, et D. Astruc soumis à "Physics of Fluids", (Joly et al., Physics of Fluids).

7.1 Experimental setup

The model presented in this thesis is subject to strong hypotheses, especially on the solid body dynamics. Therefore to test the accuracy of the model in predicting the behaviour of isotropic solid particles in turbulence, two experiments were conducted. For the first experiment particles of different sizes and relative densities where released in a quasi-homogeneous stationary turbulent regime. This regime was achieved by oscillating a pair of 1×1 m grids built with 2 cm thick square bars of mesh size $H = 10$ cm. The two grids were placed at a distance $D_{ist} = 60$ cm apart in a water tank, and were oscillated in phase at a frequency $f = 1.67$ Hz and a stroke $\Delta = 10$ cm.



(a) Side view

(b) Plan view

Figure 7.1: Scheme of the double-grid setup (the origin of the axis is located on the bottom right corner in the middle of the cross-section of the lower grid, and the x-axis is inversed). PIV measurement are recorded with camera 1, and particle trajectories using both cameras 1 and 2.

7.2 The turbulent regime

The turbulence generated by those grids was then quantified using Particle Image Velocimetry (PIV) and Two-Dimensional Laser Doppler Velocimetry (2D-LDV) measurements. These two techniques were chosen for the information on the turbulence they can provide. The PIV measurements were done for two 20×20 cm windows of measurement. One window in the center of the tank, with its center at $(50, 50, -30)$ cm, which is where the particles will be recorded, and the other window has its center placed at $(68, 50, -30)$ cm, which is closer to the edge of the tank, but this allows a comparison with the 2D-LDV results and check for the effect of the edge of the tank. A thousand images were recorded within a time interval of 1 s and an interburst of 10 ms with a spatial resolution of approximately 105 pixels/cm. The 2D-LDV measurements were recorded at $(65, 50, -30)$ cm at a frequency of 200 Hz for one hour with a laser beam diameter of 2.2 mm.

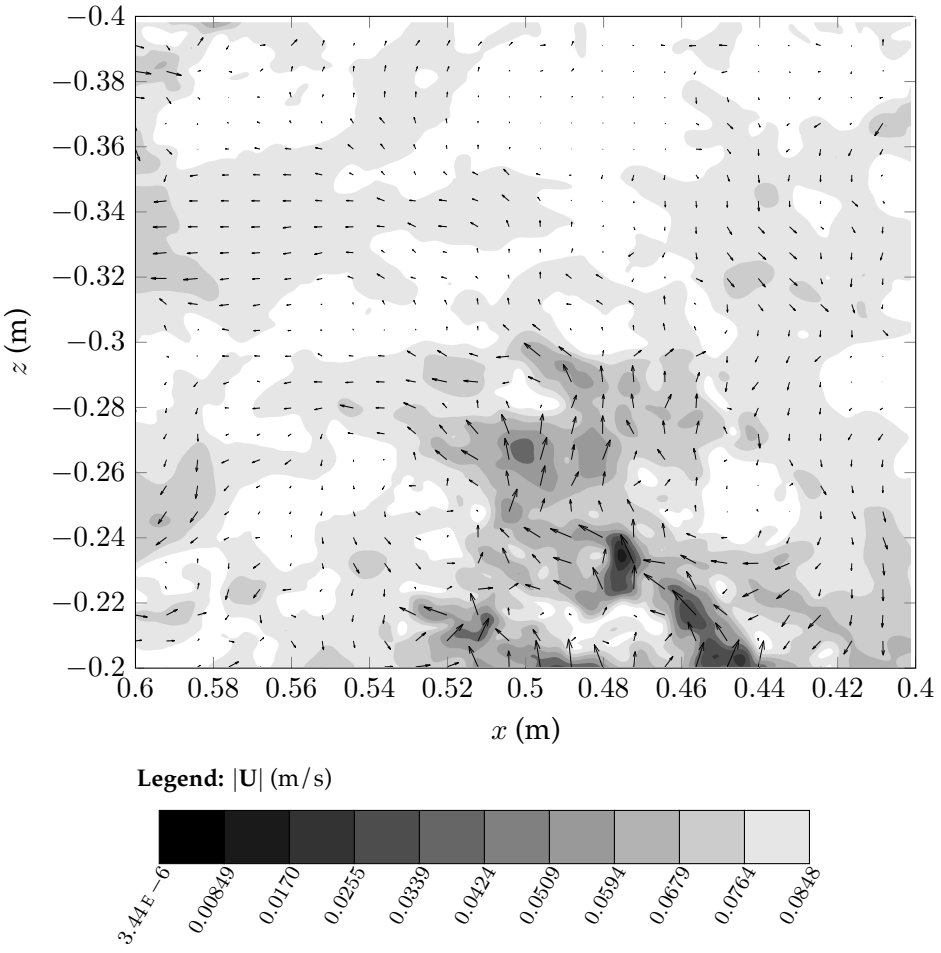


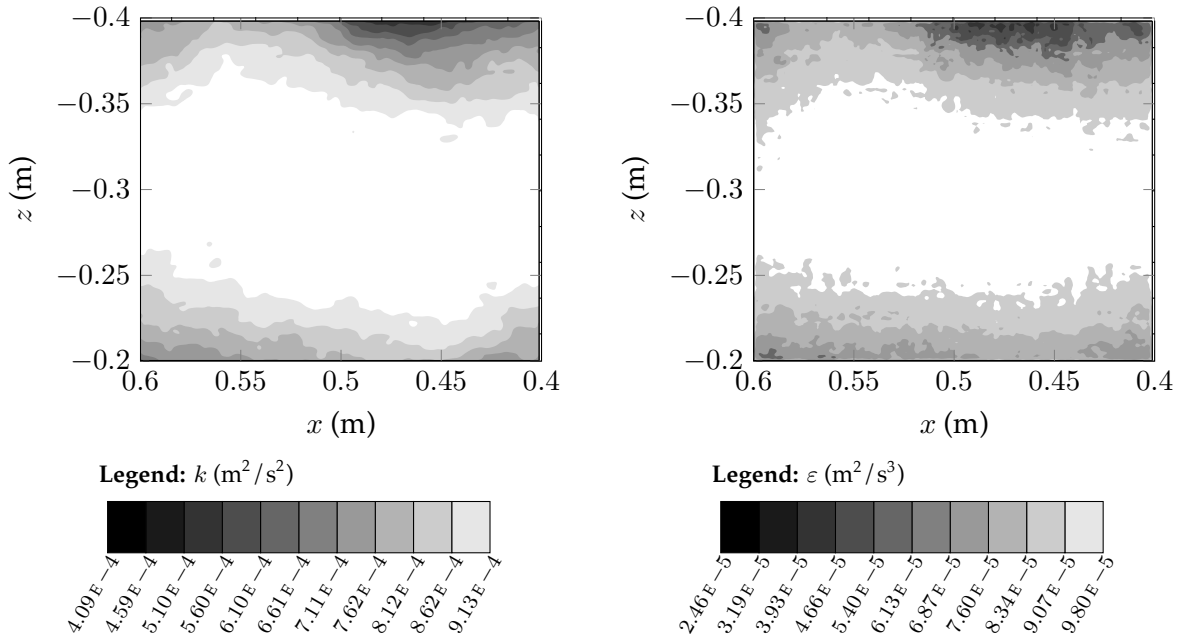
Figure 7.2: An instantaneous velocity field recorded using PIV in two grids generated turbulence oscillating in phase at $f = 1.67$ Hz and $\Delta = 10$ cm.

The PIV measurements give instantaneous velocity fields, such as the one presented in figure 7.2. From these velocity fields, the mean flow and the turbulent fluctuations can be calculated ($\overline{U_i}$ and U_i'). Yan *et al.* (2007) and Doron *et al.* (2001) give methods to calculate the kinetic turbulent energy, k, and its dissipation rate, ε, from a time series of those instantaneous planar velocity fields:

$$k = \frac{\overline{2U_x'^2 + U_z'^2}}{2} \tag{7.1}$$

$$\varepsilon = 3\nu \left[\overline{\left(\frac{\partial U_x}{\partial x}\right)^2} + \overline{\left(\frac{\partial U_z}{\partial x}\right)^2} + \overline{\left(\frac{\partial U_x}{\partial z}\right)^2} + \overline{\left(\frac{\partial U_z}{\partial z}\right)^2} + 2\overline{\left(\frac{\partial U_x}{\partial z}\frac{\partial U_z}{\partial x}\right)} + \frac{2}{3}\overline{\left(\frac{\partial U_x}{\partial x}\frac{\partial U_z}{\partial z}\right)} \right] \tag{7.2}$$

These can be found using the assumption that the turbulence is quasi-isotropic. This allows the turbulent properties required for particle transport generation to be known inside the window of measurement. Figure 7.3 shows the values calculated from the PIV measurements.



(a) Kinetic turbulent energy (k)

(b) Turbulent energy dissipation rate (ε)

Figure 7.3: The mean kinetic energy and its mean dissipation rate for two oscillating grid generated turbulence with $f = 1.67$ Hz and $\Delta = 10$ cm obtained from PIV measurements.

From the results of k and ε the mean Reynolds number of the turbulence inside the window of measurement can be calculated. As reminder it is in proportion to the ratio of the size large over the small turbulent eddies, and it can be calculated using the following equation:

$$R_t = \frac{k^2}{\varepsilon\nu} \tag{7.3}$$

Which for the current experiement is equal to about 6000. The effect of the edge of the tank was also tested, to verify the presence of mean flow. Table 7.1 summarizes the flow properties likely to be affected by the tank. From this table we see that some boundary effects can be observed. The mean velocities would suggest that there are some recirculation close to the edge of the tank, however as the particles are released in the center of the volume of measurement the mean flow velocity can be assumed to be equal to zero as they are an order under the velocity fluctuations. Furthermore in this table it also shows that the turbulence is slightly more isotropic in the center of the tank than at the edge, in accordance to intuition.

Table 7.1: Summary of flow characteristics for a grid oscillation amplitude of 10 cm and a frequency of 1.67 Hz.

position (cm)	$\overline{U_x}$ (m/s)	$\overline{U_z}$ (m/s)	$U_{rms,x}$ (m/s)	$U_{rms,z}$ (m/s)	$U_{rms,x}/U_{rms,z}$
$(65, 50, -30)$	-0.00220	-0.0125	0.0220	0.0302	0.729
$(50, 50, -30)$	-0.00158	-0.00423	0.0156	0.0196	0.795

Further measurements were done using 2D-LDV, although for a different grid oscillation frequency.

The comparison with a punctual PIV value in table 7.2 validates the values of the spatial PIV results. The same process was done in Al-Homoud and Hondzo (2007), and the difference ratios ($U_{rms,i,\text{PIV}}/U_{rms,i,\text{2D-LDV}}$) are also shown in table 7.2. Furthermore Al-Homoud and Hondzo (2007) calculated the anisotropy ratio ($U_{rms,x}/U_{rms,y}$) to be 1.05, whereas in this experiment it is 0.75.

Table 7.2: Comparison between Particle Image Velocimetry and Two Dimensional Laser Doppler Velocimetry measurements for a grid oscillation amplitude of 6 cm and a frequency of 2.63 Hz at position $(65, 50, -30)$ (the PIV data for an amplitude of 10 cm and a frequency of 1.67 Hz at the position of the LDV data were corrupted).

	$U_{rms,x}$ (m/s)	$U_{rms,z}$ (m/s)	k (m^2/s^2)
PIV	0.0113	0.0148	2.38×10^{-4}
2D-LDV	0.0103	0.0145	2.1×10^{-4}
$\frac{U_{rms,i,\text{PIV}}}{U_{rms,i,\text{2D-LDV}}}$	1.10	1.02	1.13
$\frac{U_{rms,i,\text{PIV}}}{U_{rms,i,\text{2D-LDV}}}$ in Al-Homoud and Hondzo (2007)	1.20	1.40	1.58

The fields in figure 7.3 are coarse, and for modelling purpose smooth empirical formulae have been developed as they can be extended outside of the window of measurement, to the point of release of the particles. In literature most studies of oscillating grids generated turbulence have been done for a single grid. These papers give empirical formulae for the spatial distribution of the root mean square of turbulent velocity fluctuations, as well as the kinetic turbulent energy and its dissipation rate (Al-Homoud and Hondzo, 2007; Cheng and Law, 2001; De Silva and Fernando, 1994; Holzner *et al.*, 2006). Using the crude assumption that the turbulent kinetic energy of the two grids can be added, an empirical formula can be developed for two grid generated turbulence, where a free parameter will to be adjusted to fit to the problem at hand:

$$U_{rms,x} = \sqrt{\overline{U_x'^2}} = U_{rms,y} = \theta_1 H^{\frac{1}{2}} \Delta^{\frac{3}{2}} f \left[z^{-2} + (D_{ist} - z)^{-2} \right]^{\frac{1}{2}} \tag{7.4a}$$

$$U_{rms,z} = \theta_2 H^{\frac{1}{2}} \Delta^{\frac{3}{2}} f \left[z^{-2} + (D_{ist} - z)^{-2} \right]^{\frac{1}{2}} \tag{7.4b}$$

$$k = \frac{1}{2} \left(2\theta_1^2 + \theta_2^2 \right) H \Delta^3 f^2 \left[z^{-2} + (D_{ist} - z)^{-2} \right] \tag{7.4c}$$

$$\varepsilon = \frac{\theta_3 U_{rms,x}^3}{D_{ist}} \tag{7.4d}$$

Where the rms subscript represents the root mean squared values of velocity, i.e. $U_{rms,i} = \sqrt{\overline{U_i^2}}$. These equations have been developed by assuming that the turbulent eddies are dependent on the mesh size of the grid, the frequency and the amplitude of the oscillations and that they decrease away from the grid.

From the measurements of the case where the grids are oscillating in phase at a frequency $f = 1.67$ Hz and stroke $\Delta = 10$ cm the constants have been estimated to be $\theta_1 = 0.202$, $\theta_2 = 0.261$ and $\theta_3 = 5.60$. This therefore gives the profiles in figure 7.4 for k and ε.

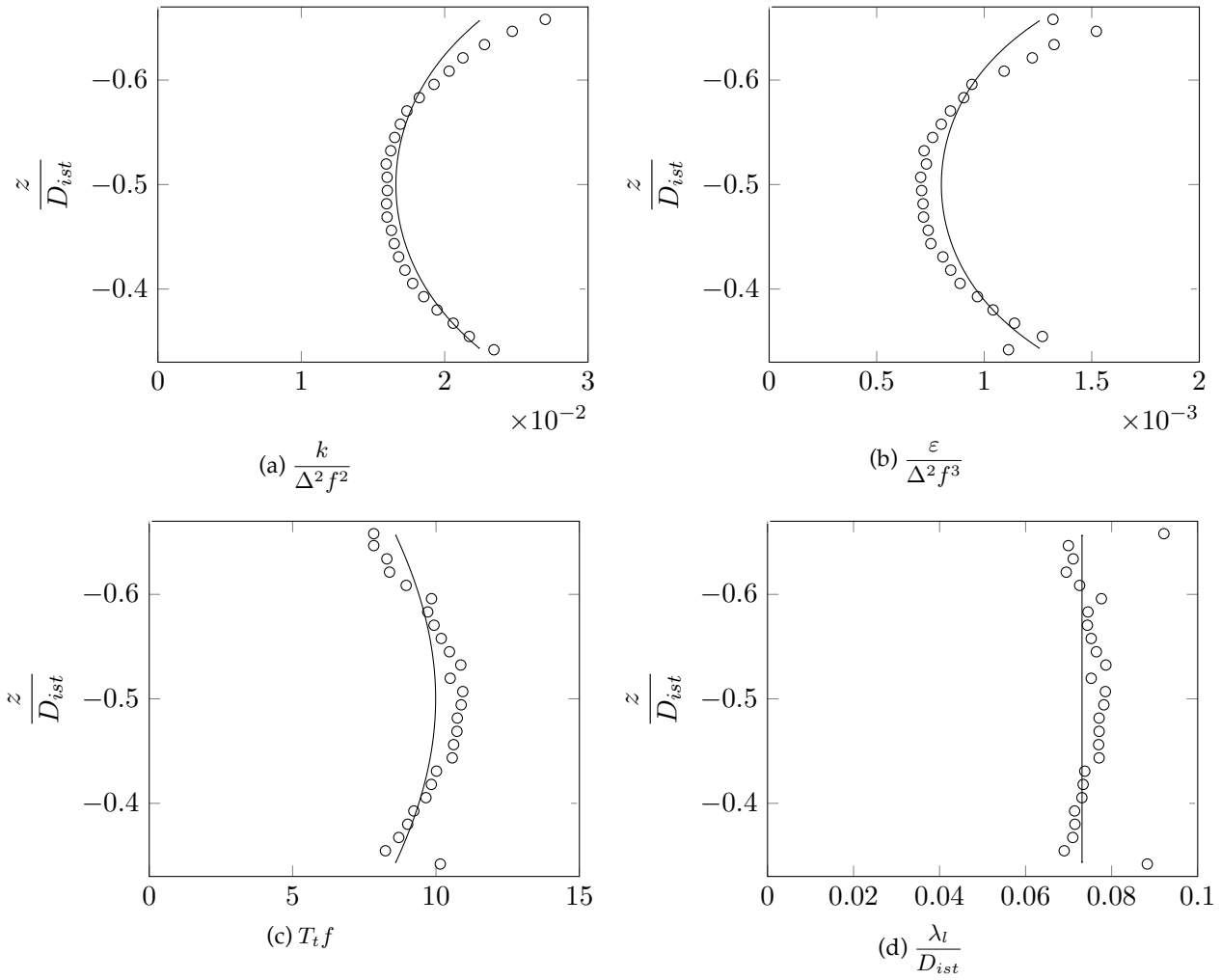


Figure 7.4: Non-dimensional vertical profiles for the kinetic turbulent energy k, its dissipation rate ε, the turbulence characteristic time T_t and the characteristic length of the large turbulent eddies λ_l. "○" is horizontally averaged experimental results and "——" is the empirical profile found using equations 7.4.

The two characteristic parameters of the turbulence are also given in figure 7.4 as they can be used to provide relationships between the turbulent flow and the particles released. These parameters are the turbulent characteristic time T_t from equation 5.25a and the characteristic size of the large turbulent eddies given equation 3.50a.

Equations 7.4, with the appropriate constants, allows therefore the mean turbulent flow properties to be reasonably estimated, which can then be inputed into the equations described in chapter 6 to predict particle transport. Furthermore using the empirical values for k and ε from equation 7.4 the ratio λ_l/D_{ist} is equal to a constant and interestingly for highly turbulent flows $D/\lambda_l \sim \tau_{part}/T_t$.

7.3 Particle tracking

Different spheres of Nylon Polyamide PA 6,6 (see table 7.3) were released 20 cm above the oscillating grids (see figure 7.1a). Two different fluids, of densities $\rho_f = 1000$ and 1084 kg/m^3, were used. For each run 25 particles were released in the experimental setup.

An updated Stokes number will also be introduced. Unlike the number of equation 2.2a which only compared the characteristic time of particles experiencing Stokes drag to the small turbulent eddies,

this number will show the impact of the turbulent eddies for settling particles using the characteristic time introduced in equations 4.28 and 5.25.

$$\mathrm{St}_{set} = \frac{\tau_{part}(\mathbf{V} = -V_{set}\mathbf{e_z})}{T_L} \tag{7.5}$$

This Stokes number uses the settling velocity V_{set} to calculate the particle relaxation time. As a reminder this velocity is the maximum velocity a body falling unhindered through the fluid can reach. It has been defined in chapter 4 by the following implicit formula:

$$V_{set} = \mathrm{sign}\left(\rho_{s/f} - 1\right)\sqrt{\frac{2\left|\rho_{s/f} - 1\right|}{SC_D(\mathrm{Re}_{set})}\left|\mathbf{g}\right|} \tag{7.6}$$

With:

$$\mathrm{Re}_{set} = \left|V_{set}\right| D/\nu \tag{7.7}$$

In table 7.3 the Stokes number is calculated using the settling velocities for each particle in a water of density $1000\ \mathrm{kg/m^3}$ and the mean turbulence characteristic time of figure 7.4.

Table 7.3: The diameters and densities of the Nylon Polyamide PA 6,6 particles.

Diameter D (mm)	Standard deviation of D (%)	Mean density ρ_s ($\mathrm{kg/m^3}$)	Standard deviation of ρ_s(%)	Stokes number St_{set}	Volume fraction of particles Ω_f
20	0.254	1129	0.0740	2.37	1.05×10^{-4}
10	0.508	1128	0.301	0.868	1.31×10^{-5}
5	1.02	1115	0.125	0.677	1.63×10^{-6}
2	2.54	1062	2.42	0.616	1.05×10^{-7}

Since for all the particles in table 7.3 the values for the Stokes number St_{set} is of the same order as one the turbulence effects and the particle properties need to be considered for all particle sizes. In addition since the Stokes number is greater for the larger particles, the properties of the bodies will have a greater effect. The settling velocities for all these particles released in waters of densities $\rho_f = 1000$ and $1085\ \mathrm{kg/m^3}$ are plotted in figure 7.5. Furthermore the values for the volume fraction number presented in this table indicate that the larger particles might affect the turbulence slightly, and that the one way fluid–particle coupling might be an over simplification.

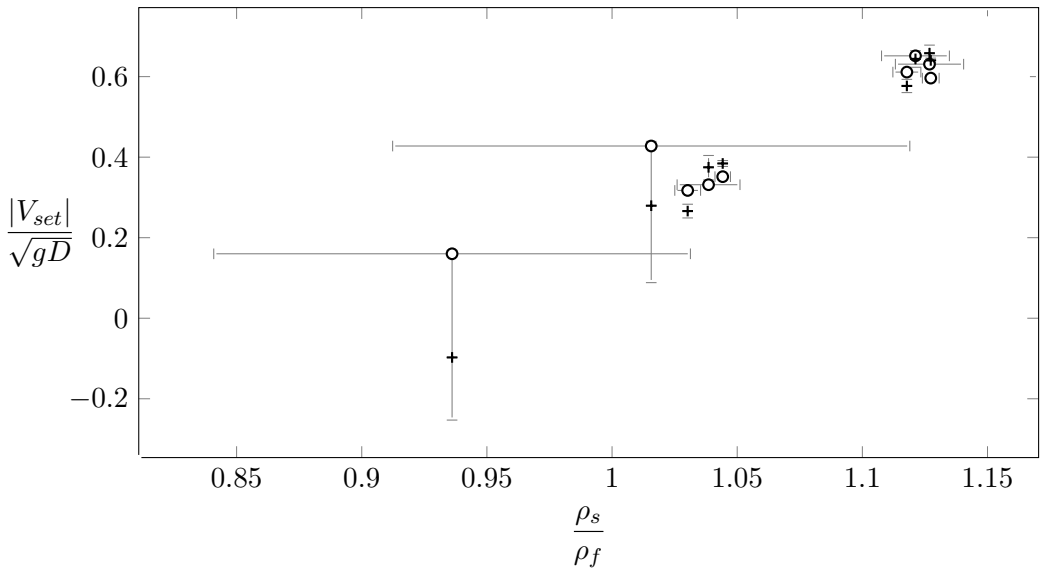


Figure 7.5: Dimensionless settling velocities for the particles described in table 7.3 and for fluid densities $\rho_f = 1000$ and 1084 kg/m^3. "+" is the analytical solution (equation 7.6) and "o" are the experimental measurements. "⊢⊣" are the 95% confidence interval error bars for the experimental density ratios and "⌶" are the 95% confidence interval error bars for the analytical velocities using these ratios.

The trajectories for the particles released into the flow described in section 7.1 were measured using two cameras placed perpendicularly to each other. The volume of measurement, located in the center of the two grids, had a shape close to a cube $20 \times 20 \times 20$ cm, but of a shape similar to the one presented in figure 7.6.

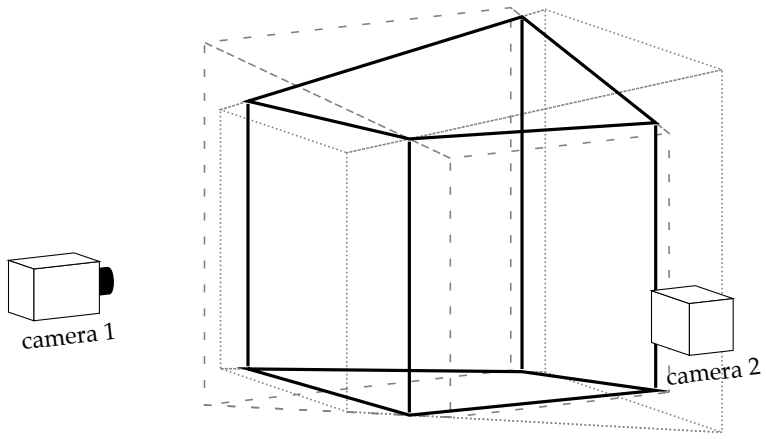


Figure 7.6: Volume of measurements for the two perpendicular cameras recording falling bodies. "⋯⋯" is the volume recorded by camera 1, "- - " is the volume recorded by camera 2 and "——" is the volume of measurement common in the two cameras.

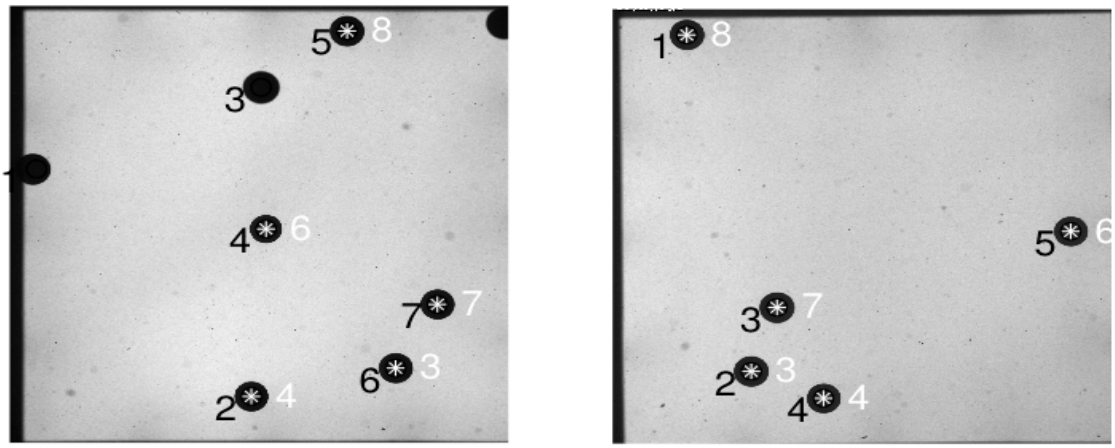
The shape of the volume of measurement described in figure 7.6 shows that a linear relationship needs to be assumed to convert particle position from pixel to millimetre (Cordeiro Fernandes, 2005), this relation is given by the following equation:

$$\text{Camera 1:} \quad \frac{X_x(mm)}{X_x(pixels)} = \alpha_y X_y(mm) + \beta_x \; ; \qquad \frac{X_{z_1}(mm)}{X_{z_1}(pixels)} = \alpha_y X_y(mm) + \beta_x \tag{7.8a}$$

$$\text{Camera 2:} \quad \frac{X_y(mm)}{X_y(pixels)} = \alpha_x X_x(mm) + \beta_y \; ; \qquad \frac{X_{z_2}(mm)}{X_{z_2}(pixels)} = \alpha_x X_x(mm) + \beta_y \tag{7.8b}$$

Obviously in equations 7.8, the particle position X_z should be equal in camera 1 and camera 2 ($X_{z_1} = X_{z_2}$). The coefficients α_i and β_i need to be calibrated by recording known positions of an object inside the volume of measurement, see appendix C.

Furthermore the shape and size of the volume recorded by a camera implies that particles seen by one camera might not be seen by the other, see figure 7.7 which shows an example of associated particles. The image processing necessary to obtain the position of the particles in pixels is given in appendix C.



(a) Camera 1 (b) Camera 2

Figure 7.7: Example of particles recorded for the two cameras. The number in black is a recognized particle in an image and the number in white, next to a white star, is a particle present in both cameras.

7.4 Model Validation

From these records of particle trajectories it is possible to obtain an estimate of the particle velocities looking at the displacement in between two recorded images. These particle velocities can be compared to the results obtained using the stochastic numerical model developed in chapter 6 (Equations 6.12, 6.15 and 6.19) where the mean flow characteristics are imputed from the empirical model presented in equations 7.4. The particle velocities will be compared through the probability density functions (pdf) of the horizontal and vertical velocities of particles present anywhere within the whole volume of measurement. The particles velocities are analysed, and not the positions of the particles, as the element of interest for this experiment is to observe the response of the model to a turbulent fluid velocity.

Furthermore the numerical model will be tested using different amount of information. The forces on the body will be tested for the three possible cases described in table 4.2 and in equations 4.25, 4.26 and 4.27, which are for the case where in addition to the buoyant forces only the drag force is taken into account, the drag and the momentum forces and the drag, momentum and Basset history forces. In addition there are two scenarios which will be tested to model the fluid velocities, which are given in equations 6.2, 6.4 and 6.5, and these involve the Crossing Trajectories Effect (CTE). The CTE will be

modelled in this turbulent flow regime by assuming that the mean velocity differences $\left|\overline{\mathbf{V}} - \overline{\mathbf{U}}\right|$ can be modelled using the settling velocity V_{set} as defined by equation 7.6, which means that the main drift is in the z direction, and using the $U_{rms,i}$ values given in equations 7.4a and 7.4b to solve for $\overline{U_i' U_i'}$. The impact of the CTE will be tested by comparing it to a case where it is ignored, meaning that the fluid velocity seen by a particle $U_i^{(s)}$ is equal to the fluid velocity U_i. The numerical model will be also compared to a model that is often used to predict the transport of particles in environmental flows, for example Issa *et al.* (2009) or Monti and Leuzzi (2010), which is a declination of the Brownian motion given in equation 5.2, which considers the flow velocity:

$$dX_i = \left[\overline{U_i} + \frac{C_\mu}{\sigma_c}\frac{\partial}{\partial x_i}\left(\frac{k^2}{\varepsilon}\right)\right]dt + \sqrt{2\frac{C_\mu}{\sigma_c}\frac{k^2}{\varepsilon}}dW_i \tag{7.9}$$

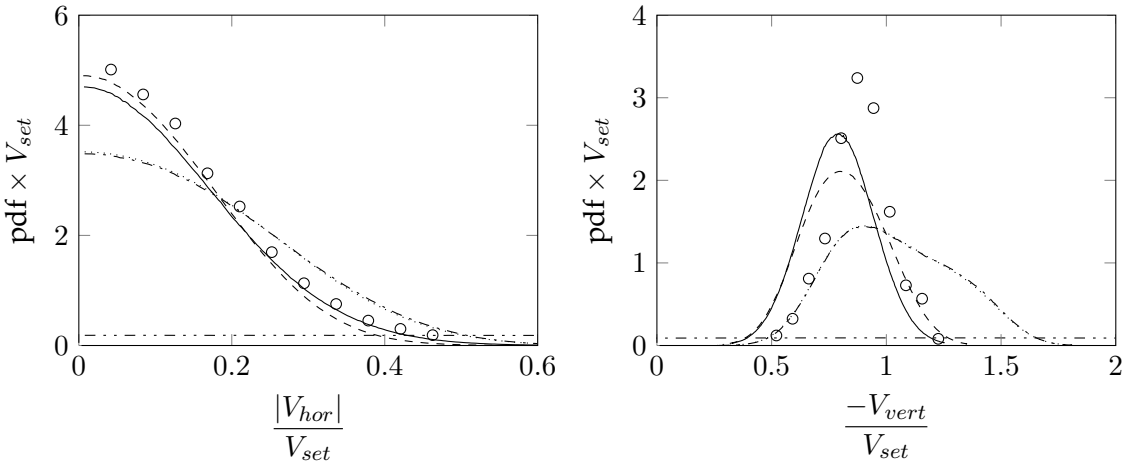
Where $C_\mu = 0.09$ and $\sigma_c = 0.72$, as was defined in Issa *et al.* (2009). It should be noted in this model that the physical properties of the solid particles are not taken into account, it is assumed that these bodies follow exactly the fluid, and that all of the turbulent fluctuations of the fluid velocity can be modelled as a white noise. All of the different modelled used are summarised in table 7.4.

Table 7.4: Summary of the different models compared and different forcing considered in the oscillating grid experiment.

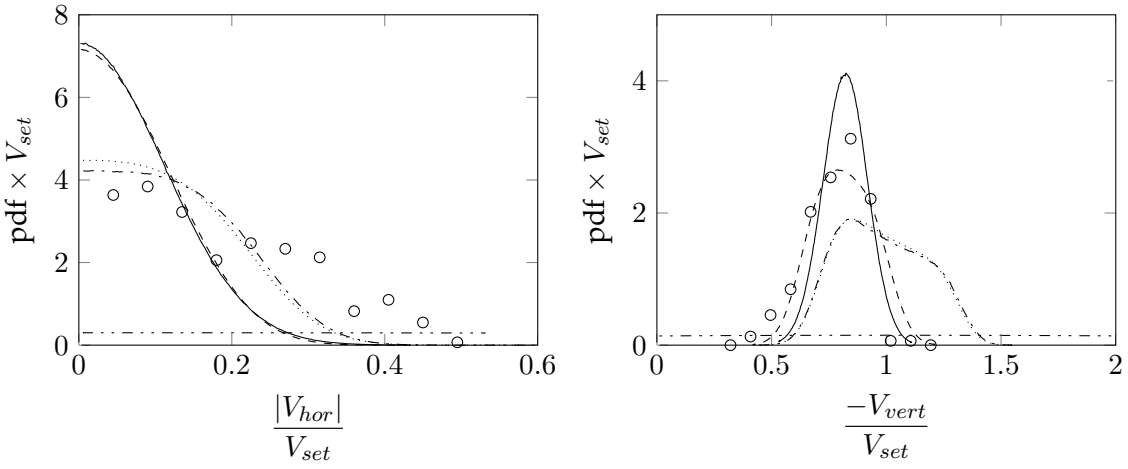
	Model I	Model II	Model III	Model IV	Brownian motion
Crossing Trajectories	yes	no	no	no	no
Basset	yes	yes	no	no	no
Momentum	yes	yes	yes	no	no
Drag	yes	yes	yes	yes	no
Source	eqns 4.5 & 6.1	eqn 4.5	eqn 4.4	eqn 4.2	eqn 7.9

The numerical particles released in the different simulations were initially released at rest, at the same release point as in the experiment, although in the experiment the particles were not exactly at rest when released.

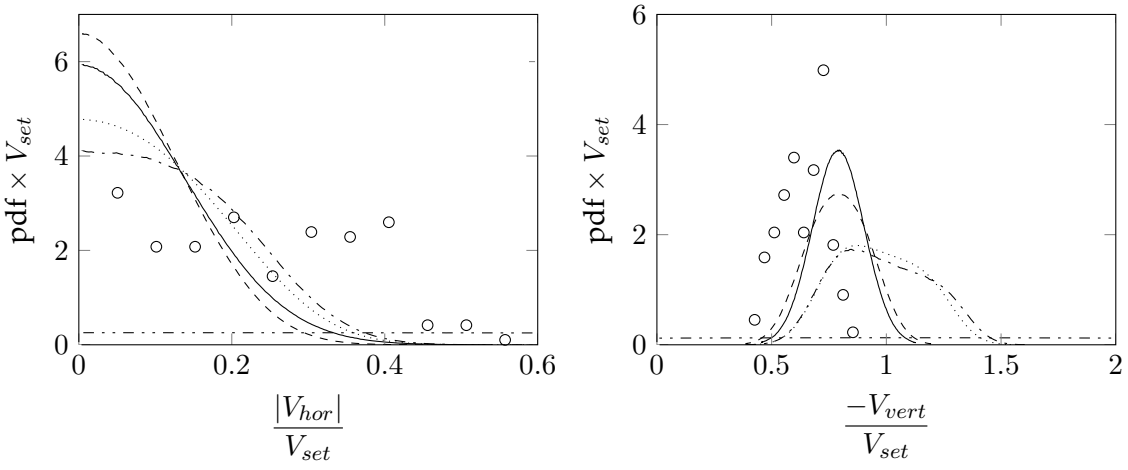
Figure 7.8 shows representative probability density functions (pdf) of the horizontal and vertical velocities. Each plot of this figure is associated to five characteristic numbers: D/λ_l which shows the ratio of the particle diameter D to the characteristic length of the large turbulent eddies λ_l, given by equation 3.50a, $\rho_{s/f} = \rho_s/\rho_f$ which gives the density ratio between the solid boy and the fluid, the Stokes number St_{set} given by equation 7.5, N_r which is the number of experimental velocity records and Re_{set} which is the particle Reynolds number for particles at settling velocity (equation 7.7). The pdf of the velocities are calculated using the velocity at every time step that a particles is present in the volume of measurement. N_r is then found using every recorded velocity along every trajectories of the particles. Only half of the horizontal velocity statistics are shown, as they are symmetrical around the mean velocity (here 0 m/s as there is no flow).



(a) $\frac{D}{\lambda_l} = 0.106$, $\rho_{s/f} = 1.12$, $\mathrm{St}_{set} = 1.52$, $N_r = 354$, $\mathrm{Re}_{set} = 620$



(b) $\frac{D}{\lambda_l} = 0.212$, $\rho_{s/f} = 1.13$, $\mathrm{St}_{set} = 2.06$, $N_r = 178$, $\mathrm{Re}_{set} = 2020$



(c) $\frac{D}{\lambda_l} = 0.424$, $\rho_{s/f} = 1.047$, $\mathrm{St}_{set} = 4.58$, $N_r = 105$, $\mathrm{Re}_{set} = 3450$

Figure 7.8: Probability density functions for particle velocities present inside the volume of measurement. "○" is the pdf for the experimental results, "——" is the pdf for model I, "- - -" is the pdf for model II, "·····" is the pdf for model III, '- - -" is the pdf for model IV and "- · · " is the pdf for Brownian motion. See table 7.4 for details on the models.

From figure 7.8 it is possible to conclude that for the force models I to IV the vertical displacement is driven by the buoyancy effects, as the vertical velocities are of the same order as the settling velocity. Conversely the horizontal velocities are smaller than the settling velocities, and therefore are driven by the turbulence. Secondly this figure shows that the simplification of the transport of isotropic particles in turbulence to Brownian motion (Issa *et al.*, 2009), as is done commonly for contaminant transport (Heemink, 1990; Monti and Leuzzi, 2010; Stijnen *et al.*, 2006), cannot model accurately the turbulent diffusion of these particles, and it overestimates greatly the diffusion (the dash-dot-dot lines in figure 7.8 are very flat curves).

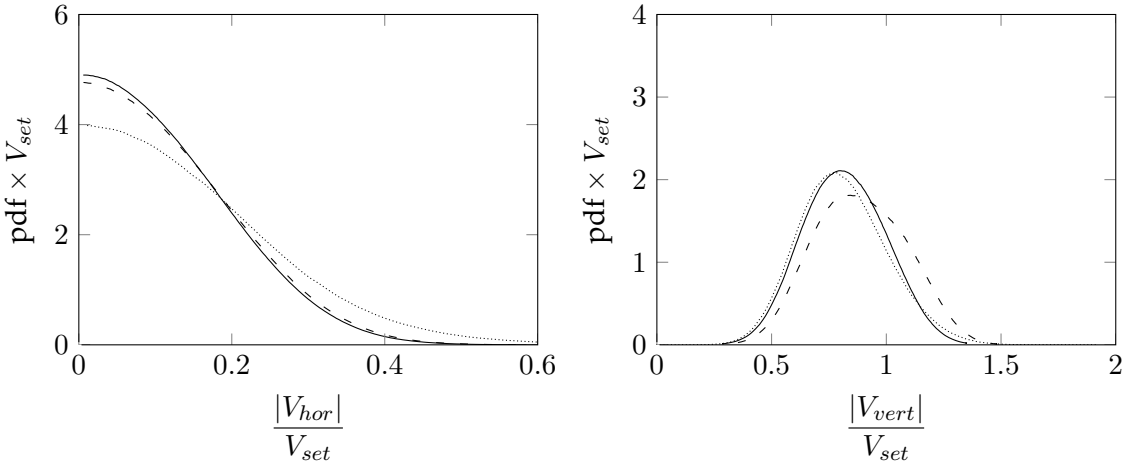
Furthermore the two particle transport models which ignore the Basset History force (the models III and IV in table 7.4), give very similar results, which would indicate that momentum and added mass of the body can be neglected, especially for small bodies. For both of these models the horizontal displacement statistics are fairly well modelled, but the vertical (settling) statistics are not modelled as accurately. However when the Basset History force (model II in table 7.4) is included the model shows very good correlation to the experimental results for small particles, but as particles become bigger the model looses accuracy. This is expected as the formulation of the Basset History force chosen is designed for small particles, and the bigger particles were modelled to test the limitations of the model. Furthermore for these large particles the hypothesis that the particles do not affect the flow might not be appropriate any more. Nonetheless, considering the Basset History force gives better probability density functions in the vertical direction, which is the main direction of motion of this problem.

In addition the Crossing Trajectories Effects mentioned by Csanady (1963) and accounted for in model I using the method proposed through equation 6.1 in Peirano *et al.* (2006) (see table 7.4) reduces the spread of velocity probability density functions shown in figure 7.8. This is expected because the crossing trajectories effects increases the decorrelation between the fluid and the solid particles, and this way a solid body does not follow completely the turbulent eddies and therefore are less diffused. Nevertheless the CTE has only affect slightly the standard deviation of the velocity pdf shown in figure 7.8. From this result, in two-dimensional horizontal simulations, the decorrelation between a solid body and a fluid particle due to gravity effects can be ignored. Nonetheless since the CTE from gravitational forces still have a visible impact on the pdfs shown in figure 7.8, the decorrelation occurring from inertial effects might not always be negligible and more research will need to be conducted in the future on those Crossing Trajectories Effects. However focusing on an accurate modelling of the solid body dynamics gives a reasonable estimates of the motion of solid particles as there are no great differences between the pdf of model I and II (only the height of the peak in the vertical velocity pdf, but not the location) and for the level of accuracy needed in the prediction of algae transport in a coastal environment CTE can be ignored, especially in two dimensional horizontal models.

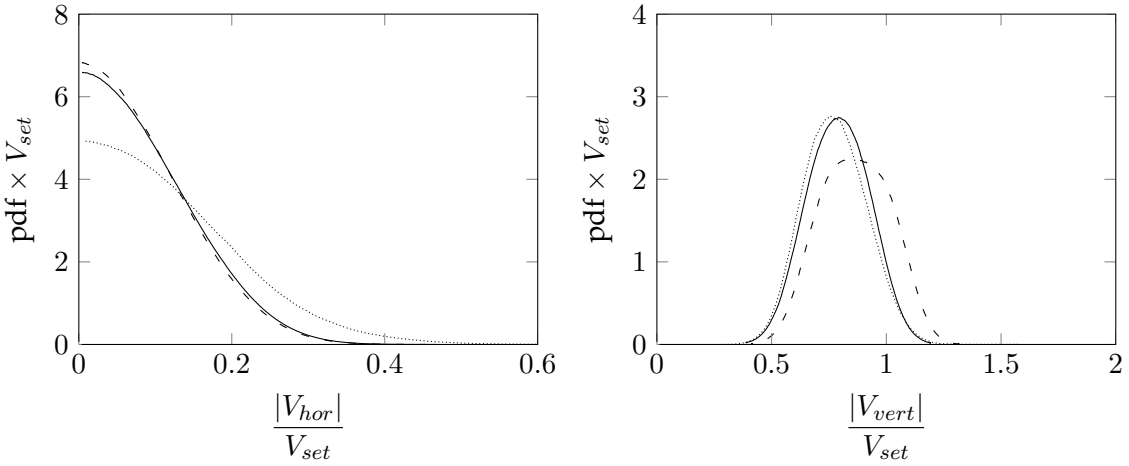
An other source of differences between experimental and numerical values could also originate from the relaxation time of the bodies at rest. This relaxation time represents the time a particle will forget the initial conditions. Solving equation 4.24 to calculate the settling motion of particles falling in a stationary fluid (without any turbulence), will give an estimate of the time a particle would take to settle from the point of release to the center of the volume of measurement see figure 7.1. This time will be named t_{set}, and it can be used to verify if a particle has forgotten the initial boundary conditions (i.e. the velocity at which it was released and the possible contacts with the oscillating grids). For the relaxation time of model II and the parameters of figure 7.8a $\tau_{part}(\mathbf{V}=0)/t_{set} = 0.571$. With the parameters of figure 7.8b $\tau_{part}(\mathbf{V}=0)/t_{set} = 3.27$ and for the parameters of figure 7.8c $\tau_{part}(\mathbf{V}=0)/t_{set} = 9.32$. These values should be analysed with care, as the relaxation decreases as the particle velocity increases, but nonetheless these values show that the smallest particles ($D/\lambda_l = 0.106$) are more likely to have forgotten the initial conditions at the point of release.

To verify this hypothesis numerical tests were done with the using model II. Particles were released at a known height, 10 cm below the center of the top oscillating grid. Large ($D/\lambda_l = 0.424$) and small ($D/\lambda_l = 0.106$) particles were released with different initial particle velocities $\mathbf{V_0}$: particles starting at rest, particles with an imposed initial vertical velocity equal to half the settling velocity and particles where the initial velocities are generated through a random distribution with a mean equal to zero

and a standard deviation equal to half the stroke Δ times the frequency f of grid oscillations, which could simulate the impact of the grids on the particles. Statistics are then plotted in figure 7.9.



(a) $\frac{D}{\lambda_l} = 0.106$, $\rho_{s/f} = 1.12$, $St_{set} = 1.52$



(b) $\frac{D}{\lambda_l} = 0.424$, $\rho_{s/f} = 1.047$, $St_{set} = 4.58$

Figure 7.9: Probability density functions for numerical particle velocities present inside the volume of measurement transported with different initial particle velocities $\mathbf{V_0}$. "—— " is the pdf for particles with $\mathbf{V_0} = 0$, "- - " is the pdf for particles with $V_{0,z} = \frac{1}{2}V_{set}$ and "····· " is the pdf for particles with $\langle \mathbf{V_0} \rangle = 0$ and $\langle \mathbf{V_0}^2 \rangle = \Delta f$.

Figure 7.9 shows that imposing an initial velocity distribution or an initial vertical settling velocity will modify the distribution of the velocities for both particles. This more visible for the large particles, which is expected, but it is still visible for small particles. This is probably because in the numerical simulations presented in figure 7.9 particles were released very close to the volume of measurement, as the empirical model for the mean flow characteristics (equations 7.4) cannot be applied much further above the volume of measurement.

Finally the finite size of the body has a filtering effect on the turbulence, as the turbulent eddies of size smaller then the particle will not affect the dispersion. This filtering effect is further emphasised by the inertial properties of the body as the particle relaxation time will limit the impact of the turbulent eddies. This is in accordance to what Yeo *et al.* (2010) has observed. This filtering process can be also observed in the numerical simulations. Figure 7.10 shows the difference in particle velocity statistics between solid particles modelled through model I (in table 7.4) and fluid particles transported using the empirical model presented in equations 7.4.

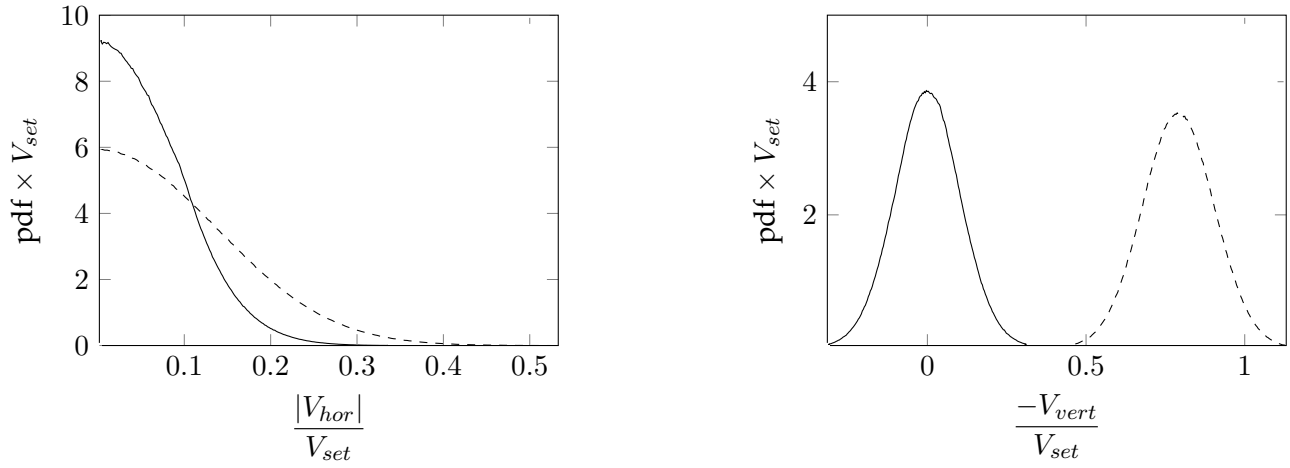


Figure 7.10: Particle statistics used to illustrate the filtering of turbulent eddies by solid particles."——" are statistics found for fluid particles and "- - -" are statistics found for solid particles defined by $D/\lambda_l = 0.106$, $\rho_{s/f} = 1.12$, $\mathrm{St}_{set} = 1.52$, $\mathrm{Re}_{set} = 620$ and modelled using model I.

In figure 7.10 it can be seen that the fluid particles do not have the same velocity probability density functions as the solid particles. Apart from the buoyant effects, which create a shift in vertical velocity pdf, the fluid velocities have a smaller width of diffusion. This can be explained through the filtering effect of the size of the particles. Because of their size the particles will only be transported with the larger turbulent eddies, which have more energy, and therefore diffuse more.

The correlation between the particle velocities and the fluid velocities can be calculated. These correlations can be calculated in a similar fashion to equation 5.15a:

$$R_{ij}\left(U_i, U_j, s\right) = \frac{\langle U_i(t)U_j(t+s)\rangle}{\langle U_i U_j\rangle} \tag{7.10a}$$

$$R_{ij}\left(V_i, V_j, s\right) = \frac{\langle V_i(t)V_j(t+s)\rangle}{\langle V_i V_j\rangle} \tag{7.10b}$$

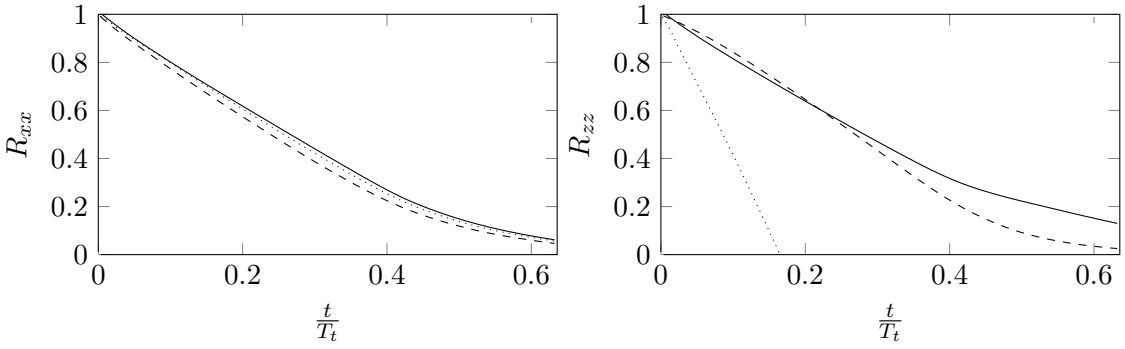
$$R_{ij}\left(U_i, V_j, s\right) = \frac{\langle U_i(t)V_j(t+s)\rangle}{\langle U_i V_j\rangle} \tag{7.10c}$$

The R_{xx} and R_{zz} correlation profiles found using these equations and following numerical particles released in the turbulent regime described by equations 7.4 are plotted in figure 7.11. Therefore U_i is given by equation 6.12 and V_i is given by equation 6.15.

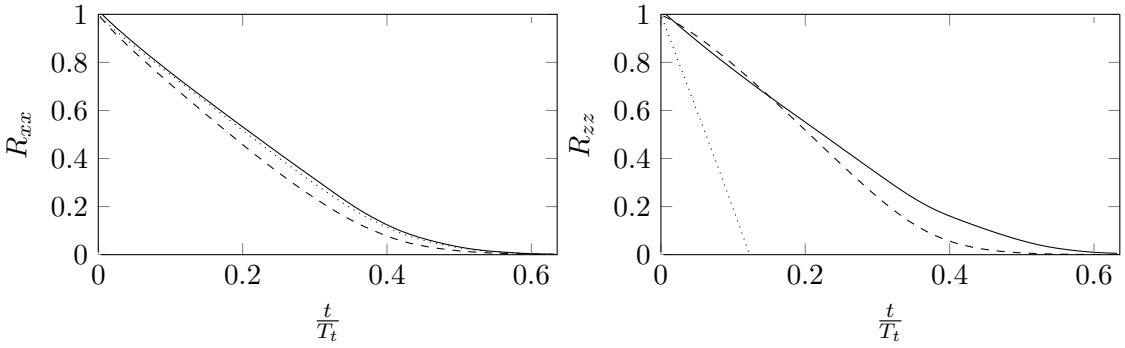
Figure 7.11 shows that the correlation between the fluid and the solid particle velocities decorrelates faster for larger particles. Furthermore, including the "Crossing Trajectories Effects" increases the rate at which the fluid velocities become decorrelated, while at the same time leaving the decorrelation rate of the solid particle velocities unchanged. This leads to a faster reduction of the correlation between the fluid and the solid particle velocities, which is the aim of including the "Crossing Trajectories Effect".

The autocorrelations plotted in figure 7.11 can be compared to those presented in figure 5.3 which followed fluid particles. The first thing noticeable is that the numerical values for the fluid velocities at the position of the solid particle decorrelate faster than for the fluid particles of figure 5.3, after $0.6T_t$ as opposed to $1.5T_t$. This difference is slightly bigger if "Crossing Trajectories Effects" are considered. Furthermore integrating the autocorrelation function of the fluid velocities gives an Lagrangian integral time scale equal to approximately $0.28T_t$ in both directions for the plots in figure 7.11a, and approximately $0.22T_t$ for those in figure 7.11b. This implies therefore that Lagrangian time scale for

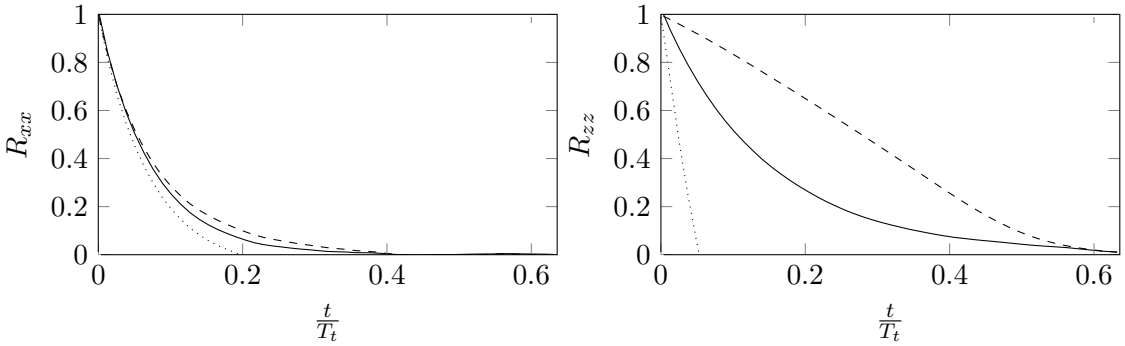
the fluid velocities following solid or fluid particles (figure 7.11 or 5.3) gives approximately the same values, that is unless CTE is taken into account. Integrating the autocorrelation functions for the fluid velocities of figure 7.11c gives characteristic time scales approximately equal to $0.075T_t$ in both directions. This is to be expected, as the CTE were taken into account by artificially reducing the modelled Lagrangian time scale T_l, through the use of $T_i^{(s)}$.



(a) $\frac{D}{\lambda_l} = 0.106$, $\rho_{s/f} = 1.12$, $\text{St}_{set} = 1.52$, $\text{Re}_{set} = 620$ solved using model II



(b) $\frac{D}{\lambda_l} = 0.424$, $\rho_{s/f} = 1.047$, $\text{St}_{set} = 4.58$, $\text{Re}_{set} = 3450$ solved using model II



(c) $\frac{D}{\lambda_l} = 0.106$, $\rho_{s/f} = 1.12$, $\text{St}_{set} = 1.52$, $\text{Re}_{set} = 620$ solved using model I

Figure 7.11: The correlation profiles of velocities for particles released in quasi-homogeneous turbulence. "——" plots $R_{ij}\left(U_i, U_j, s\right)$ from equation 7.10a, "- - -" plots $R_{ij}\left(V_i, V_j, s\right)$ from equation 7.10b and "·····" plots $R_{ij}\left(U_i, V_j, s\right)$ from equation 7.10b.

Finally this oscillating grid experiment allows the following conclusions to be done. A good modelling of the solid body dynamics is primordial. Out of these solid body dynamics the most important forces to consider (aside from the buoyant forces which are necessary to allow particles to settle) are the drag force and the Basset history force. The momentum of the body will however still be taken into account as it is one of the physical properties which can be adapted to correspond to that of

an algae. Furthermore the method proposed by Minier and Peirano (2001) to take into account the "Crossing Trajectories Effects" is appropriate for cases where the gravitational forces are important, as it increases the rate at which the correlation between fluid and solid particle velocities decreases. However even in this experiment the added accuracy due to the "Crossing Trajectories Effects" in the velocity statistics are only minimal (except on the vertical), and therefore it will be assumed that these effects can be neglected in two-dimensional horizontal simulations.

Chapter 8

Particles Released in a Partially Obstructed Channel

Où la deuxième expérience servant à valider le modèle développé dans le chapitre 6 est décrite et analysée. Dans cette expérience, des particules sont relâchées dans un canal partiellement obstrué par une digue perpendiculaire à ses parois. La vitesse du courant a été mesurée avec une tête ADV afin de caractériser la zone de recirculation à l'aval de la digue. Deux codes de calculs, Telemac-2D et OpenFoam, ont été utilisés pour obtenir les champs Eulériens des vitesses, de l'énergie cinétique turbulente et du taux de dissipation du fluide qui ont été comparés avec les mesures expérimentales. Ensuite des particules solides sphériques on été relâchées dans l'écoulement, et leur trajectoires ont été enregistrées à l'aide d'un caméra. Les deux simulations Eulériennes effectué avec Telemac-2D et OpenFoam ont été utilisées pour transporter des corps avec le modèle numérique du chapitre 6. La proportion et le temps de résidence moyen des corps entrant dans un quartier de la fenêtre de mesure de la caméra on été comparés. Il c'est avéré que Telemac-2D prédisait légèrement mieux le transport des corps. Ces simulations de courant ont donc été utilisées pour comparer la pertinence des différents modèles des du transport des corps. Bien que tous ces modèles produisent quasiment le même comportement du transport des corps, il est suggéré de prendre en compte toutes les composantes des forces dans une simulation d'un écoulement réel, car de faibles différences initiales peuvent avoir un grand impact sur une longue distance.

Plusieurs parties de ce chapitre sont issues du papier "Transport of isotropic particles in a partially obstructed channel flow : experiments and numerical modelling" par A. Joly, D. Violeau, F. Moulin, D. Astruc et C. Kassiotis soumis au "Journal of Hydraulic Research", (Joly et al., Journal of Hydraulic Research).

8.1 Experimental setup

This second experiment served to validate the behaviour of the model presented in chapter 6 in the case of a space-varying flow, and the validity of the coupling between a large-scale Eulerian flow model and a smaller scale stochastic Lagrangian particle transport model.

The flow configuration chosen is that of a partially obstructed open flat bed channel flow, which is a well documented configuration, see Ettema and Muste (2002), Tang *et al.* (2006) or Uijttewaal (2005). This flow has the advantage of having non homogeneous turbulence. In this experiment a fluid with a density of 1000 kg/m^3 and a flow rate of 0.5 m/s was imposed in a 2 m wide channel which was obstructed by a groyne 0.5 m long and 0.1 m thick. The water depth was imposed to be 0.3 m before the flow arrived at the groyne. The groyne was constructed high enough to stop overtopping. The experimental setup is described in figures 8.1 and 8.6. The Reynolds number was thus 10^6.

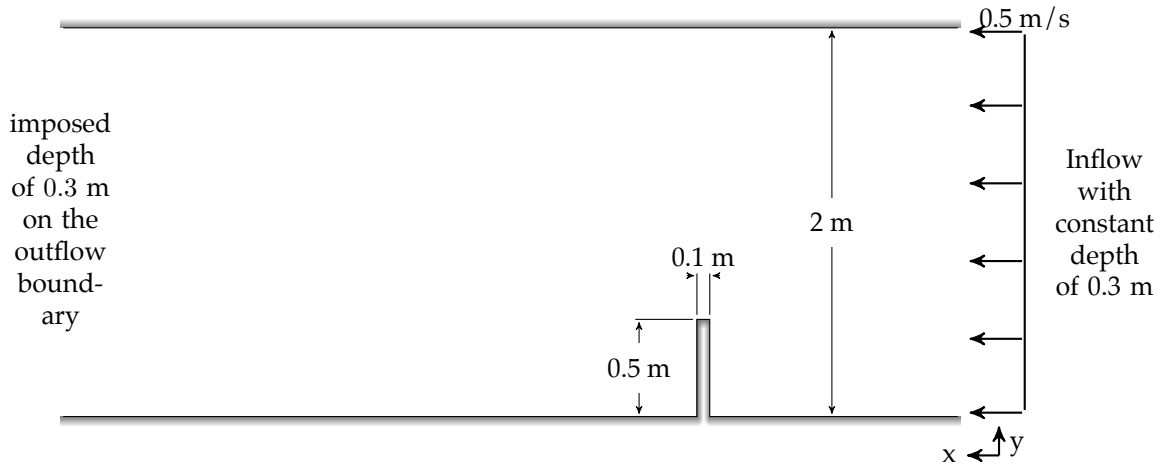


Figure 8.1: Experimental setup for a partially obstructed flat bed open channel flow (top view).

Ettema and Muste (2002) have conducted several partially obstructed flat bed open channel flow experiments and they have observed that generally the recirculation zone occurring after the groyne is of the order of 10-12 times the length of the groyne. This zone is of particular interest as it should trap particles released in the flow.

The water velocities were then recorded using a three-dimensional Acoustic Doppler Velocimetry head. A particle injector was designed to release a constant flow of spheres 6 mm in diameter and 2200 kg/m^3. Particles were released so that when entering the window of measurement they did not settle fully. The trajectories were recorded with a camera recording 14 images per second. It should be noted that a flat Plexiglas surface had to be placed just on the surface of the flow to provide undisturbed images. The obtained results are therefore only two dimensional. Parallax was also tested, and it was found to be negligible within the setup for the camera. Due to the difficulty of obtaining in situ measurements for real application, the experimental results will focus on the ability of the model to predict particles caught in the recirculation zone, so that the code can be used as a decision code for further real applications involving similar phenomenons. Since the particle transport model was already tested more thoroughly in chapter 7 in the case of zero-mean flow, the present test aims at investigating the ability of the model to deal with mean velocity gradients..

8.2 The flow regime

The velocities of the flow thus produced by the experimental set up shown in figure 8.1 were then recorded by placing an Acoustic Doppler Velocimetry head in the flow at different location and height. Using these velocity results the recirculation zone for the problem can be determined. Figure 8.2

shows the streamlines of this flow.

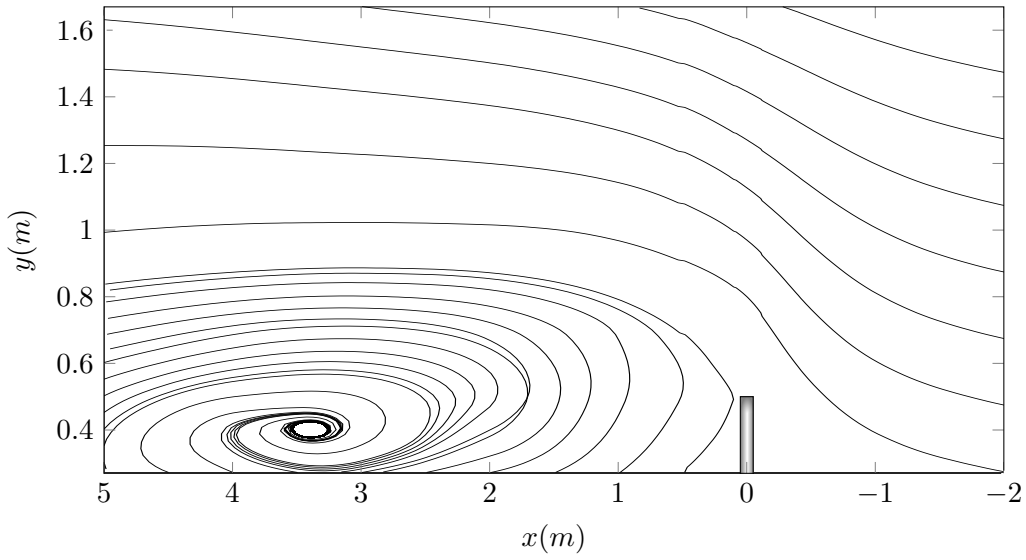


Figure 8.2: The streamlines for the flow defined by the experimental set up shown in figure 8.1.

Figure 8.2 can be used to find an estimate of the recirculation zone behind the groyne. From this figure it can be estimated to be just above 5 metres (the experimental measurements did not provide information at a distance greater than 5 metres after the groyne). This is in accordance to Ettema and Muste (2002), which estimated such flow patterns to be 10-12 times the length of the groyne, which in this case means it should be between 5 and 6 meters.

This flow was also simulated using two different Eulerian numerical flow models. A simulation was done using Telemac-2D, which solves the shallow-water equations with a depth-averaged k-ε closure using a finite elements method (Hervouet, 2007). This code is useful for large coastal flows as it can deal with tidal flats and it was designed for industrial needs. Another simulation was done using OpenFoam, which solves the two-dimensional Navier-Stokes equations with a k-ε closure using a finite volumes method (Open CFD, 2011). This code is more academic and should give better velocity profiles.

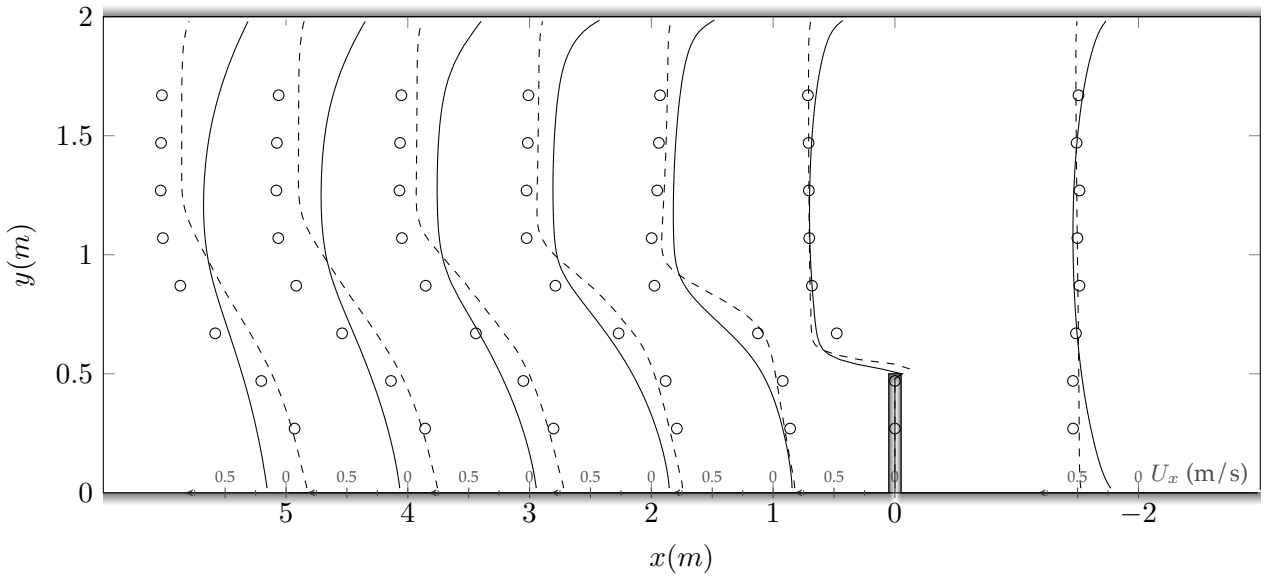


Figure 8.3: Profiles of the horizontal velocity plotted at different locations along the canal. The small axis mark on top of the x-axis represent the values of velocity magnitude. "○" are experimental results, "——" are results found using Telemac-2D and "- - -" are results found using OpenFoam.

Figure 8.3 shows selected horizontal velocity profiles. These profiles are plotted on their location along the x-axis. The scale of the velocities are set so that its zero value is situated on the x coordinate of the profile (the axes for the velocities U_x are drawn above the x-axis for each profile). It can be seen in this figure that both numerical models give reasonable velocity profiles, although they seem to be too diffusive, and they underestimate the size of the recirculation region. OpenFoam seems to model more accurately the velocities along the edge of the canal, and as such it gives a better estimate of the size of the recirculation zone. In addition it should be noted that the flow rate between the experimental and the numerical results do not seem to agree down stream of the groyne, which would indicate some imprecision in the experimental measurement.

These two codes will also be compared for the turbulent kinetic energy k and its dissipation rate ε, as these two flow characteristics are responsible for the diffusive behaviour of solid particles. However care should be done to observe the turbulent velocities with and ADV head as the recording rate needs to be small enough to observe all the turbulent structures, and the number of samples need to be large enough to reduce the error (Chanson, 2008). In this experiment velocity data were recorded at a rate of 50 Hz for 2 minutes, which means that 6000 samples were recorded, which should be sufficient as the characteristic time for the small turbulent eddies can be estimated $\tau_s = 0.02$ s and for the large turbulent eddies $\tau_l = 7$ s, see chapter 3. Therefore the turbulent kinetic energy can be calculated from experimental measurements, but the spatial resolution was not fine enough to calculate its dissipation rate. The selected profiles in the canal for k and ε using both numerical models as well as the experimental data for the turbulent kinetic energy are given in figures 8.4 and 8.5 respectively.

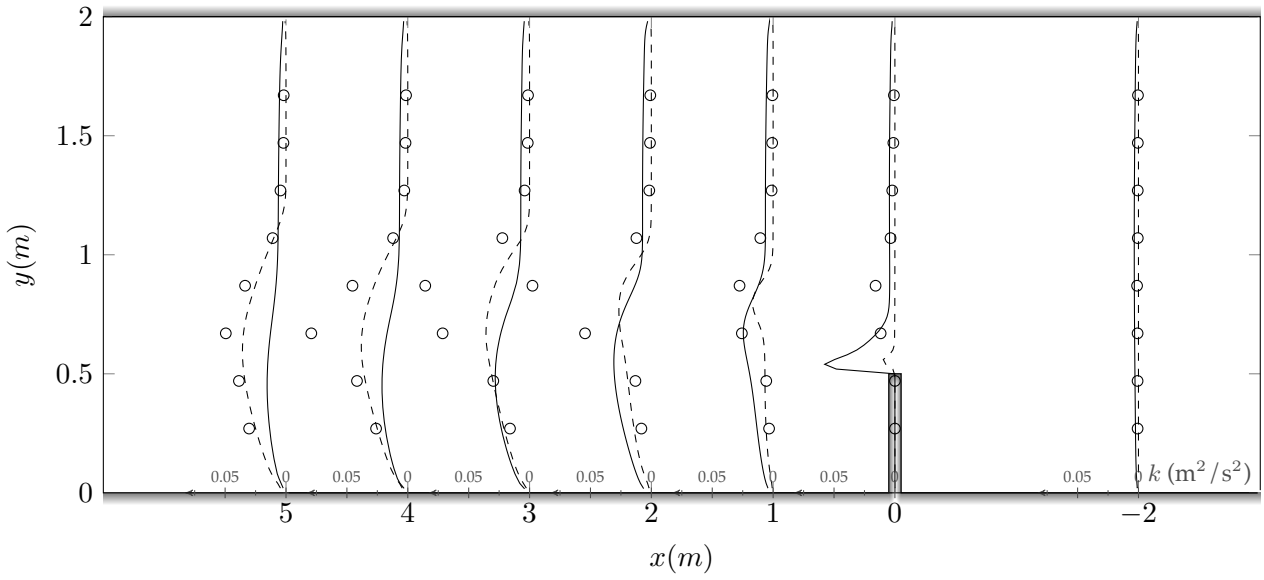


Figure 8.4: Profiles of the turbulent kinetic energy (TKE) plotted at different locations along the canal. The small axis mark on top of the x-axis represent the values of TKE. "○" are experimental results, "——" are results found using Telemac-2D and "- - -" are results found using OpenFoam.

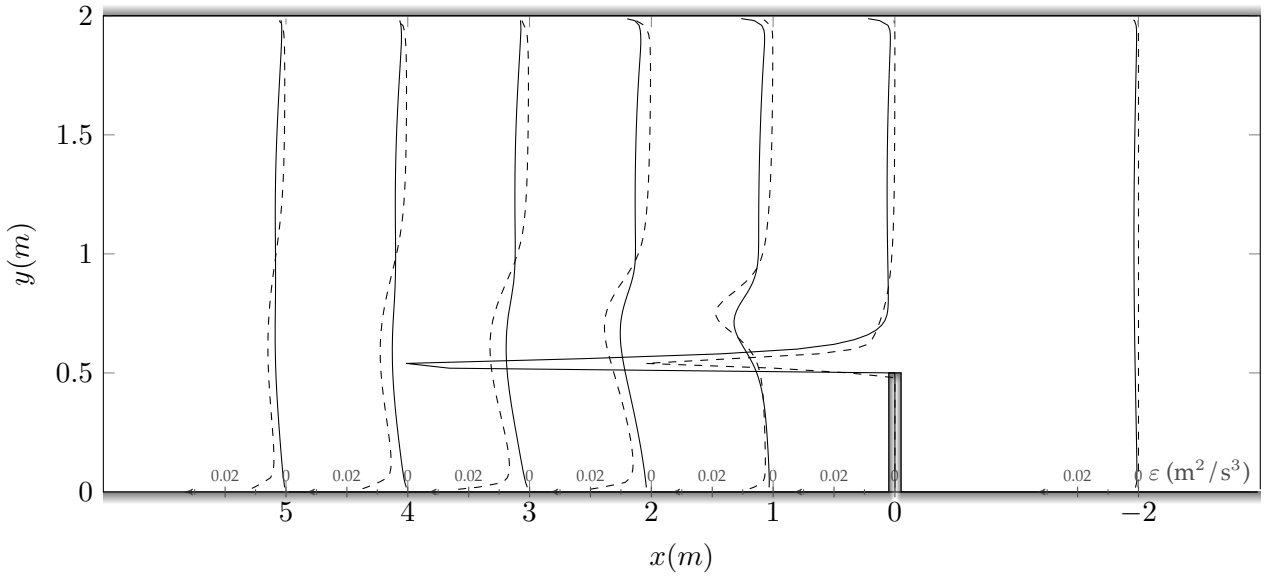


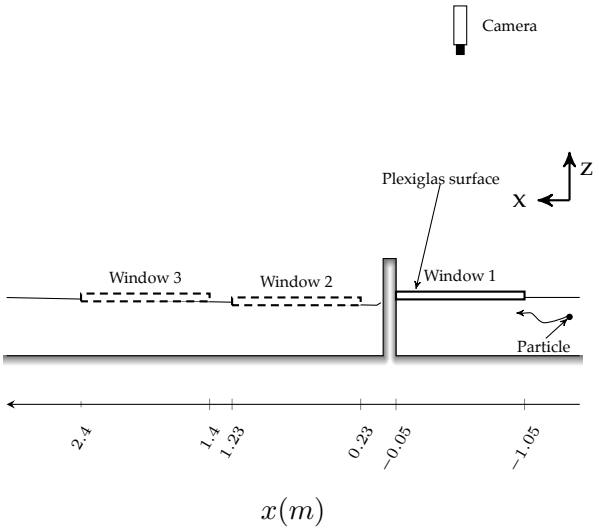
Figure 8.5: Profiles of the turbulent kinetic energy dissipation rate plotted at different locations along the canal. The small axis mark on top of the x-axis represent the values of the energy dissipation. "○" are experimental results, "——" are results found using Telemac-2D and "- - -" are results found using OpenFoam.

Figure 8.4 shows that both numerical models have more difficulties calculating the kinetic energy at the edge of the recirculation zone. Telemac-2D seems to estimate the turbulent kinetic energy directly after the groyne more accurately (looking at the experimental data placed just above the groyne), but further downstream OpenFoam gives better values. The numerical values for the dissipation rate are plotted in figure 8.5. Telemac-2D seems to find much more dissipation directly after the groyne.

The Eulerian mean velocity, turbulent kinetic energy and dissipation rate fields will be inputed into equations 6.12, 6.15 and 6.19 to transport numerical particles. The trajectories of these particles will be compared to experimental data of particles released into this flow.

8.3 Particle tracking

Spheres 6 mm in diameter (D_s) and of density $\rho_s = 2200$ kg·m^{-3} were released in the flow one at a time at fixed intervals (about 1 Hz). This was done to ensure that particles would not affect each other's motion. Several particles were released at different positions in the flow. These positions are drawn on figures 8.10 to 8.13. To record the trajectories of these particles a camera was placed above the flow to record particles entering a window of measurement, see figure 8.6. The horizontal coordinate system was chosen as in figure 8.10. The recorded images were then processed using the method described in appendix C.



(a) Schematic diagram (side view)

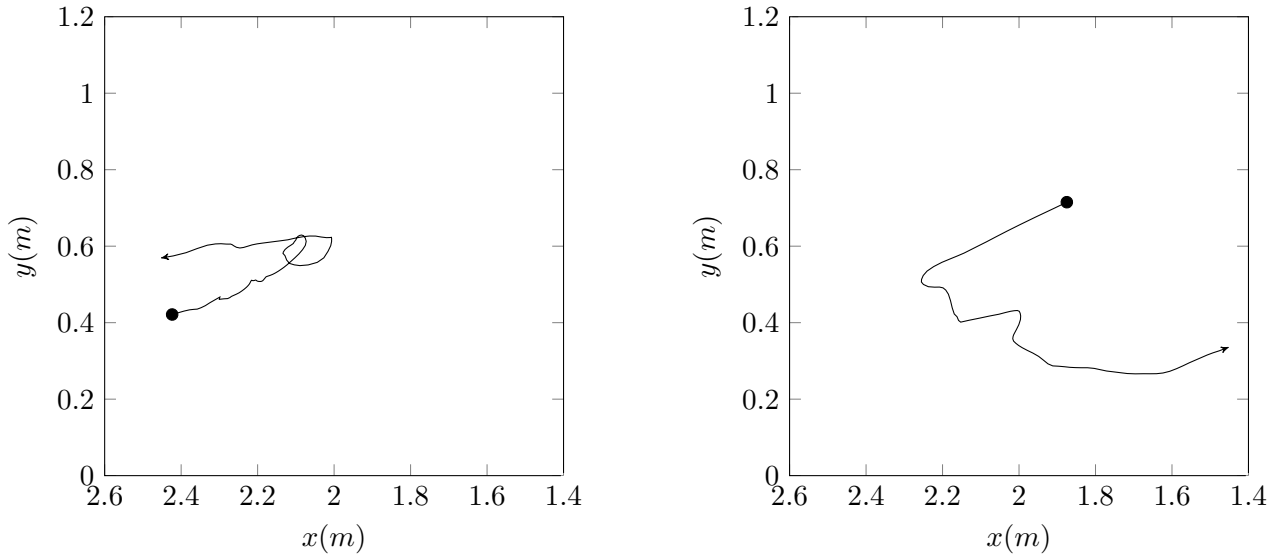


(b) Photograph

Figure 8.6: Experimental setup to record the particle trajectories.

In the numerical simulations, the solid boundaries were treated in such a way that particles whose path in one time step crossed a solid boundary was stopped just before the boundary, but still within the domain. This was done to stop particles exiting the domain through a solid boundary and to simulate the fact that the fluid velocities decrease towards a solid boundary. The method used for a triangular mesh (which was used in both Telemac-2D and OpenFoam) is described in appendix D.

The real particles released in the flow are then recorded using the camera when they enter a window of measurement. From each recorded image it is possible to obtain the position of a particle, and a time series of such images gives the trajectories of each particle. Two typical particle trajectories recorded by the camera placed at the position of the window of measurement 3 are plotted in figure 8.7.



(a) *Particle released at position (0.98,0.5) and recorded in window 3*

(b) *Particle released at position (0.175,0.4) and recorded in window 3*

Figure 8.7: Typical particle trajectories. The axes are the same as those presented in figure 8.6.

It should be noted, however, that it was difficult to obtain full trajectories of particles entering and leaving the window of measurement downstream of the groyne, as its presence lead to a generation of vortices, and entrainment of air bubbles, which would disturb the images recorded by the camera, see figure 8.8. These meant that particles were often hidden by air bubbles or vortices, and in some cases uncertain particles were ignored to stop bogus particles impacting the results. This is why the plotted trajectories in figure 8.7 do not start and finish at the edges of the window of measurement. Nonetheless, this process meant that experimental particles had their trajectories divided into segments, and these particles were counted several times.

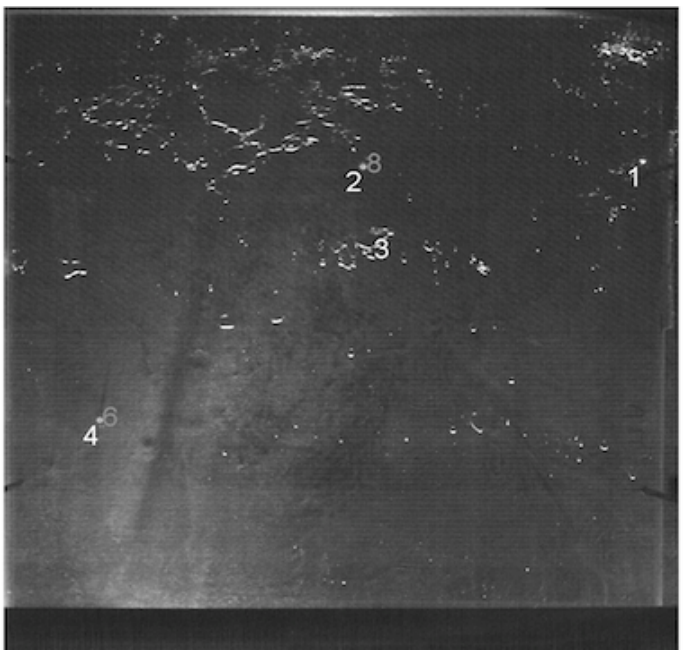


Figure 8.8: A disturbed image recorded by the camera due to the air entrainment. The number in white shows the number of objects recognised as particles and the number in light grey shows actual solid bodies.

To analyse the trajectories of the particles, the window of measurements are then divided into four quadrants. From the recorded particle trajectories we can observe the proportion of particles released into the flow entering each quadrant of the window of measurement, and the mean time of residence inside this quadrant. The same thing was done for the artificial particles in the simulations. These results are plotted in figures 8.10 to 8.13, where for each quadrant the value of interest is plotted along a line going from the inner most corner to the outter most corner. The length scales for these values are chosen in such a way that the maximum value is placed on the outer most corner. The points plotted for each quadrant are then linked together to form an area. An annotated example is found in figure 8.9.

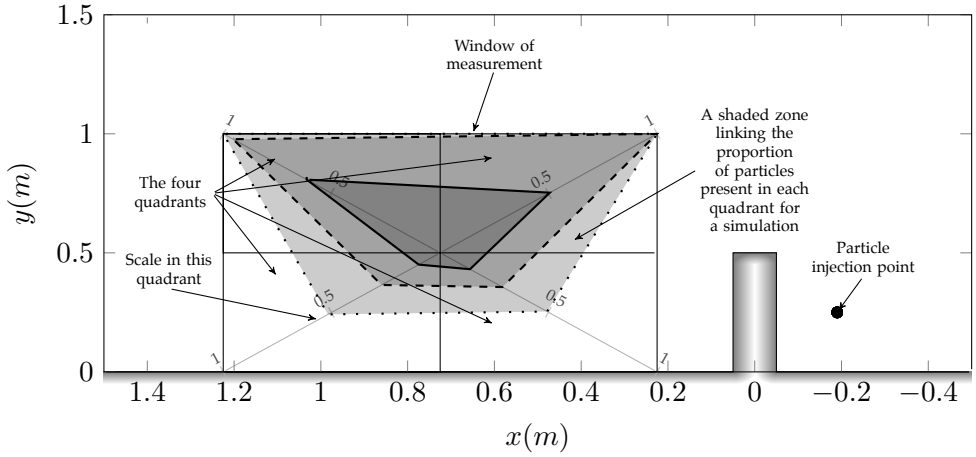


Figure 8.9: An annotated example to explain how the proportion of particles entering each quadrant of a window of measurement are presented. " ▭ " shows the experimental measurements, " ▭ " shows the measurements using Telemac-2D and " ▭ " shows the measurements using OpenFoam.

Figures 8.10 and 8.11 plot the presence in different windows of particles transported in the experiment, and in the numerical simulations considering the drag, momentum and Basset History forces (but ignoring the "Crossing Trajectories Effects"). This is the definition of model II given in table 8.2 [1], but using two different Eulerian mean flow models (Telemac-2D and OpenFoam). In figure 8.10 the proportion of particles entering a quadrant are plotted. This is done by dividing the number of different particles entering a quadrant by the total number of articles released into the flow. In figure 8.11 the mean particle residence time inside a quadrant is plotted. This residence time is found by adding the time each particle spends in a quadrant and dividing it by the total number of particles that entered this quadrant.

Figures 8.10 and 8.11 show that the two Eulerian models prove fairly effective in their ability to predict the entrapment of particles, as in general there is an acceptable correlation between numerical and experimental results in the number of particles entering each quadrant. For the windows of measurement placed downstream of the groyne, the number of particles recorded in the experiment are much lower. This is because the images were severely affected by the generation of vortices after the dike, and the position of a particle would be lost for a few images, see figure 8.8. This means that one particle can be accounted for multiple times. Furthermore particles leaving the window of measurement, and entering again will also be accounted for more than once. In addition, figure 8.10 indicates that particle trajectories calculated using OpenFoam, seem to experience greater dispersion.

The generation of vortices also has an effect on the experimental estimation of the residence times inside a quadrant, because the number of particles inside a quadrant is overestimated and part of the trajectories were hidden. Nonetheless the shape of the area composing the time of residence inside

[1] The same nomenclature as chapter 7 is used.

the quadrants seem to agree for both numerical models. The only drawback would be that Telemac-2D seems to slow down particles near solid boundaries, and therefore increase the time of residence in the quadrants close to a solid boundary.

This can be seen also by looking at the ratios between the values of N_{prop} and t_{res} in the two top quadrants and the two bottom quadrants. These ratios, shown in table 8.1, show that the shape of the overall shaded areas of figures 8.10 and 8.11 are generally similar in the experimental and the numerical results.

Table 8.1: Ratios of the proportion (N_{prop}) and the mean time of residence (t_{res}) of particles present in the top and bottom half of the window of measurement.

		top right over top left		bottom right over bottom left	
		N_{prop}	t_{res} (s)	N_{prop}	t_{res} (s)
window 1; release = (−1.3,0.19)	experiment	0.000	0.000	1.06	0.758
	Telemac-2D	0.008	0.405	1.01	0.890
	OpenFoam	0.000	0.000	1.00	1.49
window 2; release = (0.175,0.45)	experiment	1.26	1.77	1.37	0.934
	Telemac-2D	1.12	1.65	1.61	1.85
	OpenFoam	1.00	1.46	0.852	1.57
window 3; release = (0.175,0.45)	experiment	0.988	0.748	1.18	1.04
	Telemac-2D	1.13	1.18	1.31	0.982
	OpenFoam	1.12	1.24	1.08	1.18
window 2; release = (0.98,0.55)	experiment	0.821	1.07	1.39	0.444
	Telemac-2D	1.05	1.16	1.07	1.73
	OpenFoam	1.00	1.05	0.954	1.65

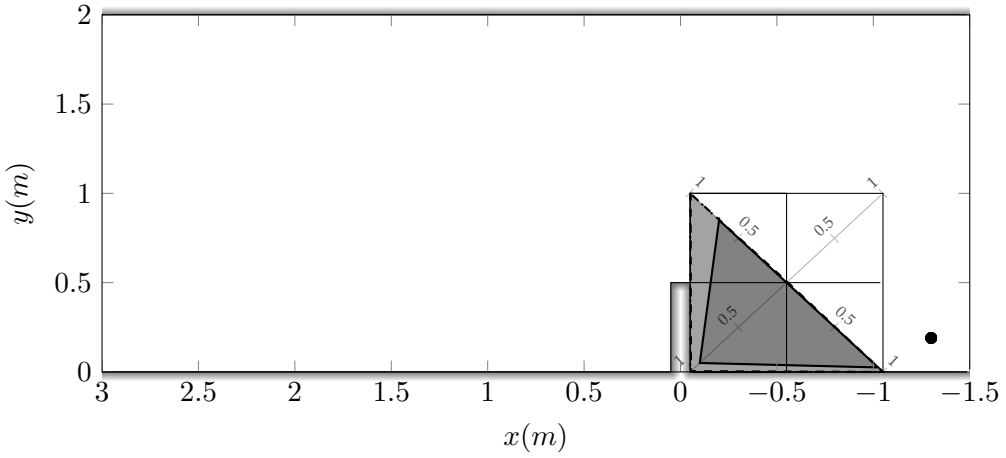
Finally, because in figures 8.10 and 8.11 Telemac-2D seems to be in better accordance to experimental results, when focusing on the shape of the shaded areas plotted in the windows of measurement, the effects of the force components of the solid body dynamics will be tested using Telemac-2D, even if OpenFoam predicted the fluid velocities more accurately. Figures 8.12 and 8.13 plots the influence of each particle transport model, summarised in table 8.2.

Table 8.2: Summary of the different models compared and different forcing considered in the partially obstructed channel experiment[2].

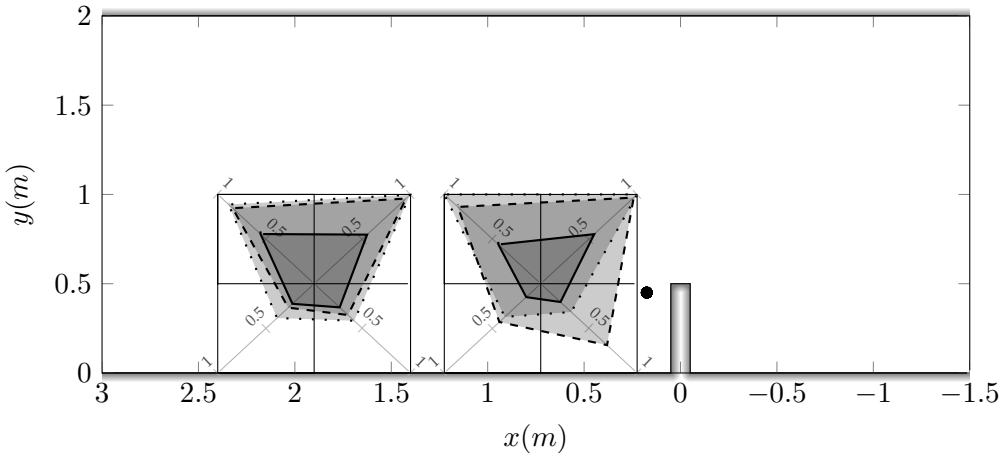
	Model II	Model III	Model IV
Basset	yes	no	no
Momentum	yes	yes	no
Drag	yes	yes	yes
Source	eqns 4.5 & 5.24	eqns 4.4 & 5.24	eqns 4.2 & 5.24

The numerical particles released in the different simulations were initially released at rest, at the same release points as in the experiment, although in the experiment the particles were not exactly at rest when released, they had a small initial vertical velocity.

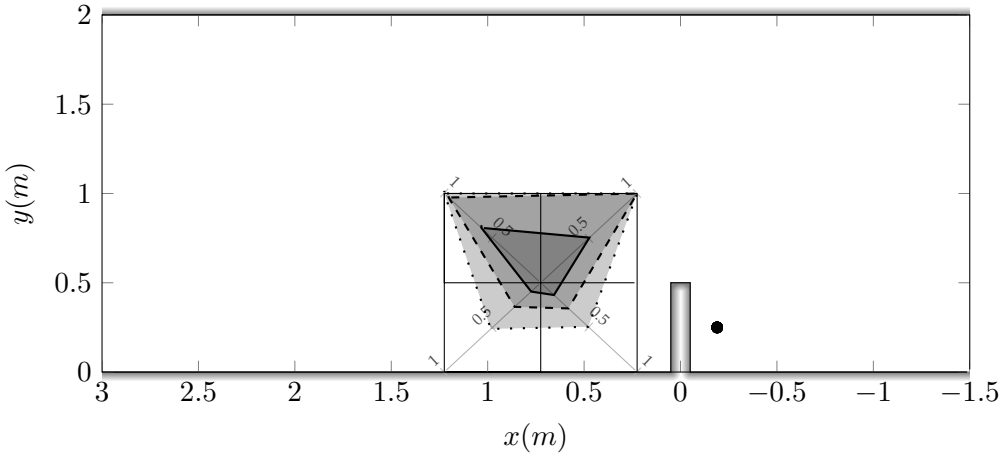
[2]Model I presented in table 7.4 is not used as the model taking into account the "Crossing Trajectories Effects" has hardly any effect in 2D horizontal particle transport models.



(a) *Particles released at point* $(-1.3, 0.19)$ *m*

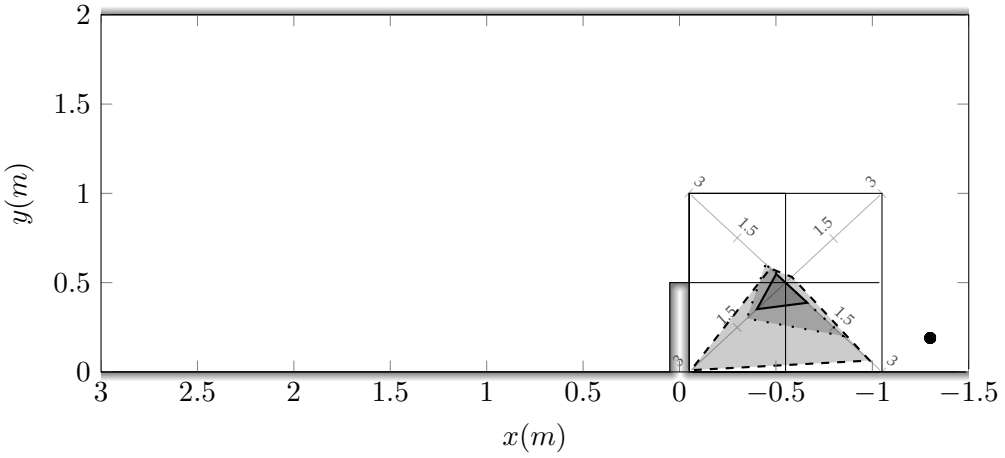


(b) *Particles released at point* $(0.175, 0.45)$ *m*

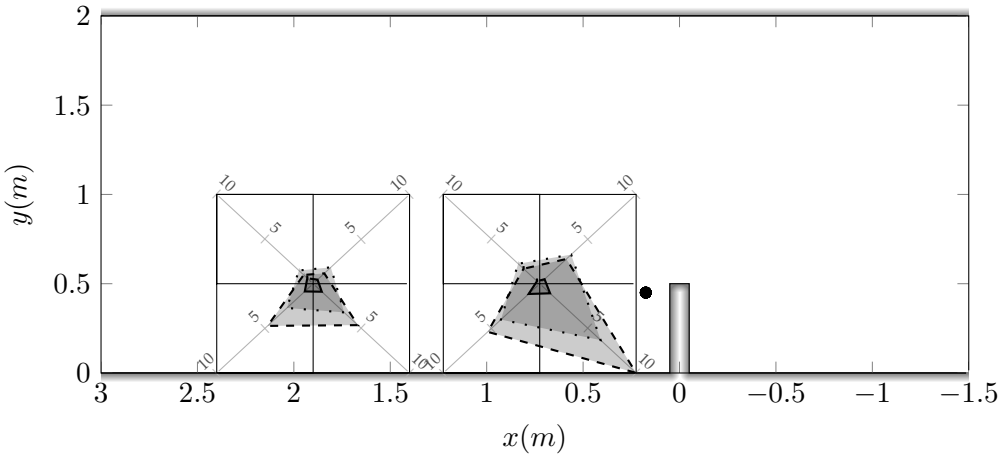


(c) *Particles released at point* $(-0.19, 0.25)$ *m*

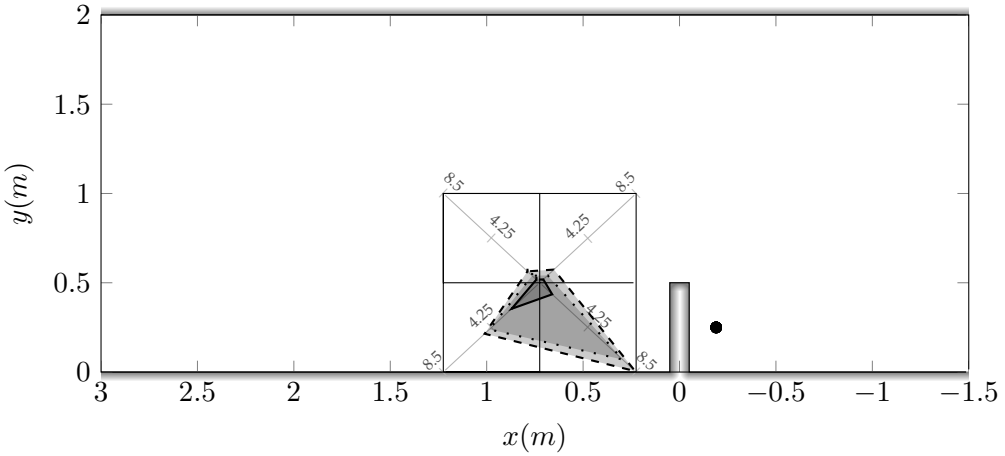
Figure 8.10: Partially obstructed channel experiment: proportion of released particles entering a quadrant of the window of measurement for various locations of release. " ▭ " shows the experimental measurements, " ▭ " shows the computational results (CR) using Telemac-2D and " ▭ " shows the CR using OpenFoam. Simulations are done using model II of table 8.2.



(a) *Particles released at point* $(-1.3, 0.19)$ *m*

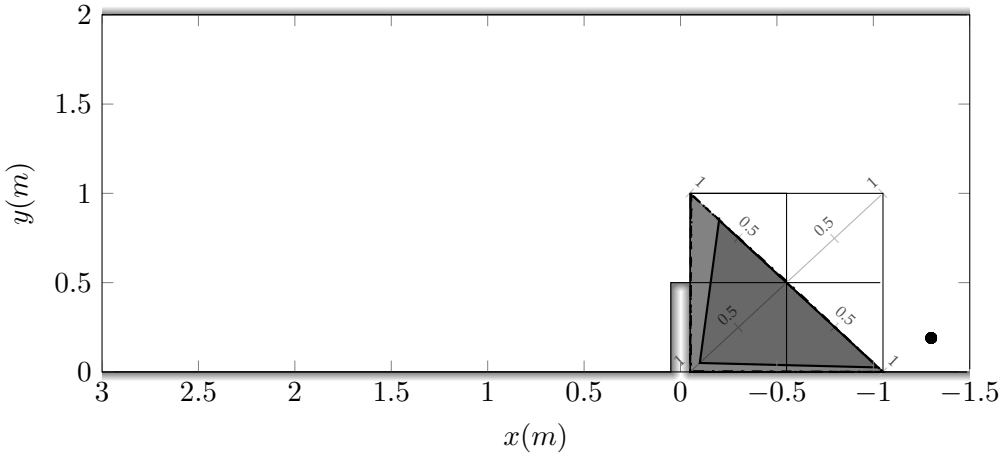


(b) *Particles released at point* $(0.175, 0.45)$ *m*

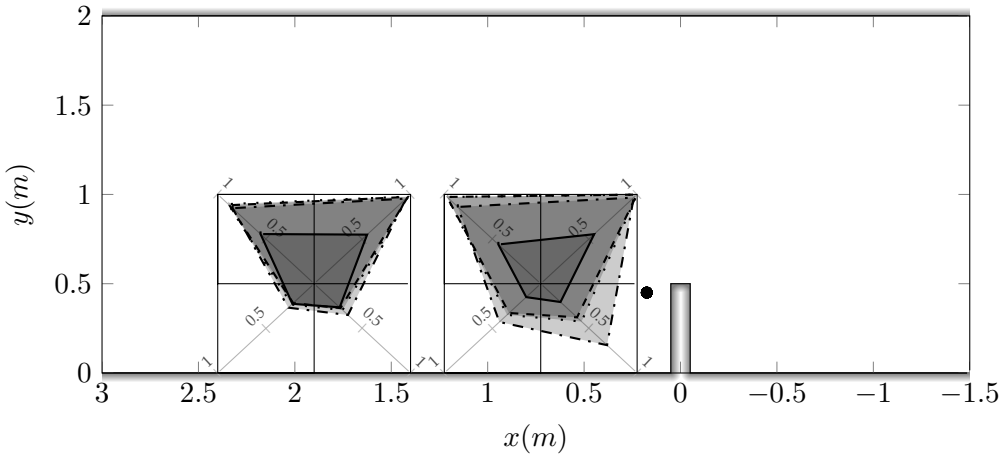


(c) *Particles released at point* $(-0.19, 0.25)$ *m*

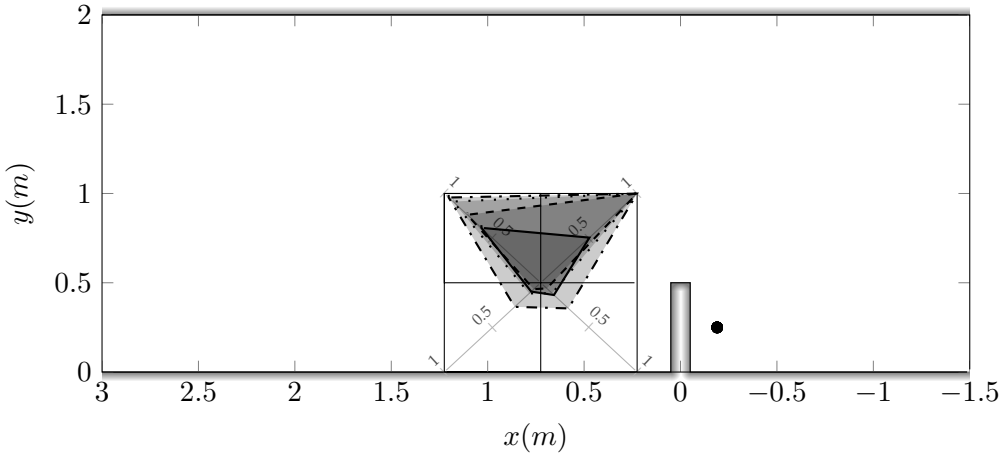
Figure 8.11: Partially obstructed channel experiment: mean particles residence time inside a quadrant of the window of measurement for various locations of release. The time is given in seconds. " ▭ " shows the experimental measurements, " ▭ " shows the CR using Telemac-2D and " ▭ " shows the CR using OpenFoam. Simulations are done using model II of table 8.2.



(a) *Particles released at point* (−1.3,0.19) *m*

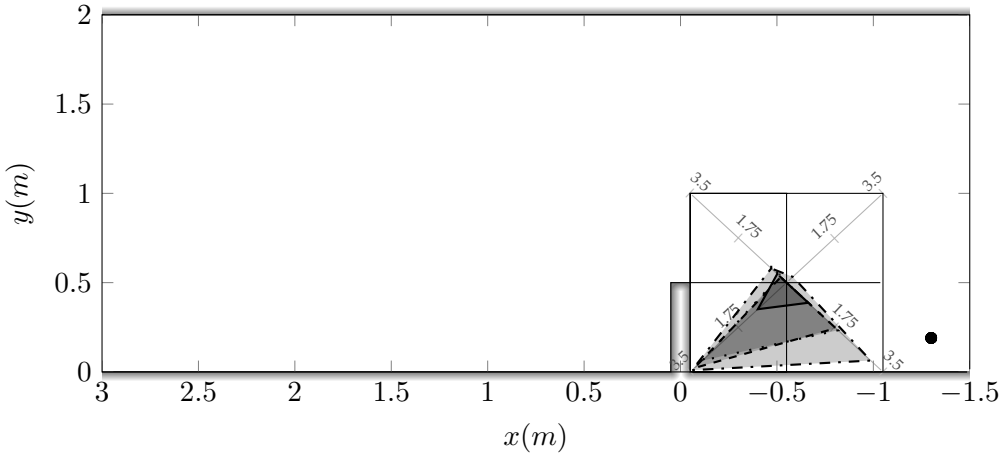


(b) *Particles released at point* (0.175,0.45) *m*

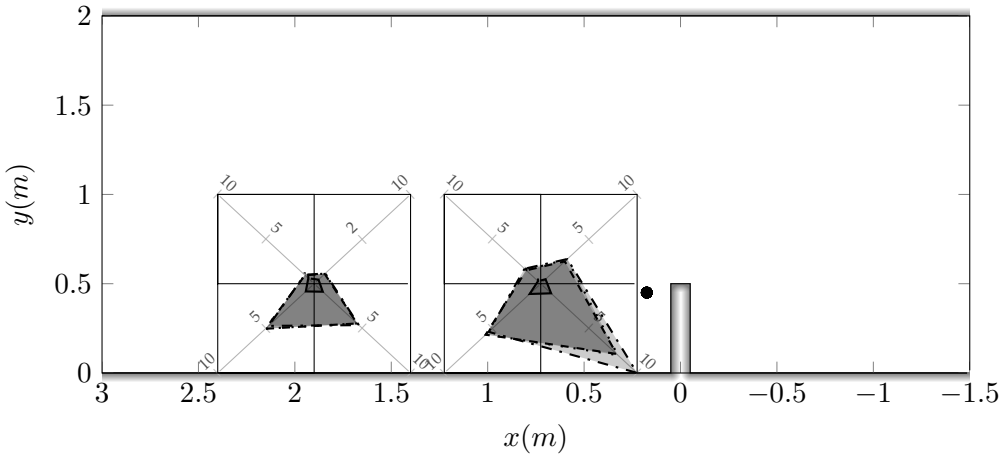


(c) *Particles released at point* (−0.19,0.25) *m*

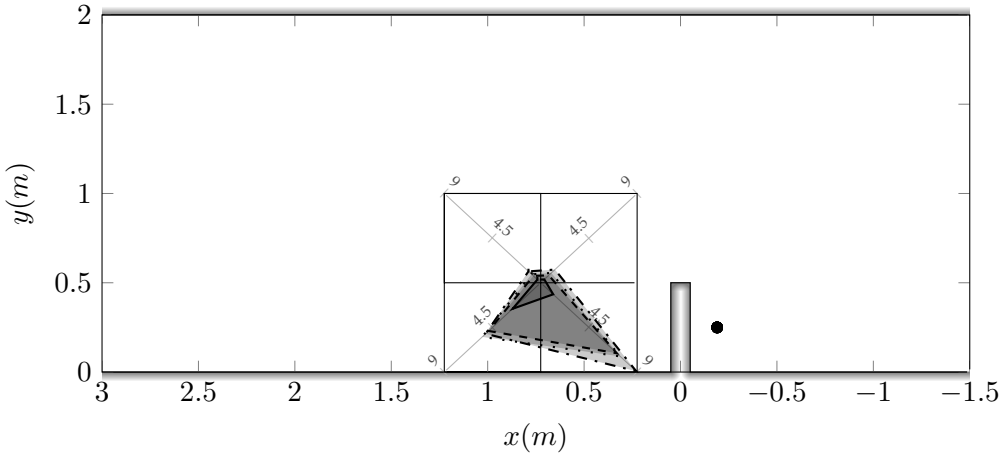
Figure 8.12: Partially obstructed channel: proportion of released particles entering a quadrant of the window of measurement for various locations of release. " ▭ " shows the experimental measurements, " ▭ " shows the CR using model IV, " ▭ " shows the CR using model III and " ▭ " shows the CR using model II. The flow is simulated using Telemac-2D and a description of the particle transport models can be found in table 8.2.



(a) *Particles released at point* $(-1.3, 0.19)$ *m*



(b) *Particles released at point* $(0.175, 0.45)$ *m*



(c) *Particles released at point* $(-0.19, 0.25)$ *m*

Figure 8.13: Partially obstructed channel: mean particles residence time inside a quadrant of the window of measurement for various locations of release. Time is given in seconds. " ▭ " shows the experimental measurements, " ▭ " shows the CR using model IV, " ▭ " shows the CR using model III and " ▭ " shows the CR using model II. The flow is simulated using Telemac-2D and a description of the particle transport models can be found in table 8.2.

Figures 8.12 and 8.13 show that the results found using the different models are very similar. This is because the particles chosen in these simulations are small, and the amount of information extracted from those simulations is very coarse. The plots of the model using all the force components (equation 4.5) shows slightly better results, but it is hardly visible. However, in chapter 7 it was proven that the particle velocities are better predicted with a more complete particle transport model. This means that in real, more complex flows, a complete force model should still be considered, as the particles will be transported over a large area, where minute early differences can become more apparent later on in the simulations. Furthermore having more information present in the model can make it adaptable to real inertial particle, as we will show in chapter 9.

Finally this partially obstructed channel experiment allows the following conclusions. The coupling between an Eulerian mean flow model and the Lagrangian particle transport model works, and it is effective in predicting particles trapped by a recirculation zone. It also shows that a good prediction of the turbulent kinetic energy k and its dissipation rate ε is just as critical as the mean flow velocities $\mathbf{U}$ when considering solid particle transport. In addition for a very coarse demand in results, for example in this experiment the aim was to find if particles could be trapped in a recirculation zone, then going into great details when modelling the solid body dynamics might be unnecessary. Nonetheless for real problems it is still recommended to take into account all force components.

Chapter 9

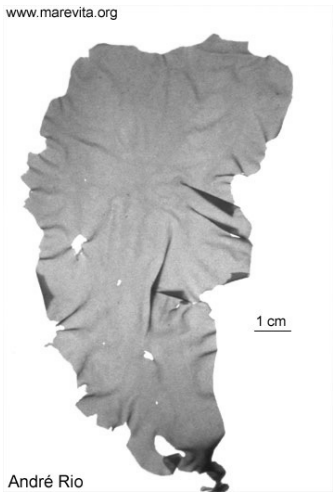
Real Life Applications

Où sont données les étapes nécessaires pour appliquer le modèle de transport de particules développé dans les chapitres précédents (voir les chapitres 4 à 6) à la problématique du transport d'algues aux alentours de la centrale nucléaire de Paluel. La première étape est de modifier les coefficients des caractéristiques mécaniques des corps pour correspondre à une algue. Ceci est fait en modifiant les coefficients de masse ajoutée et de traînée selon les valeurs données dans Gaylord et al. *(1994). Ces valeurs sont ensuite comparées aux valeurs d'un corps sphérique ayant le même volume que les algues prises en compte.*

Ensuite le cas d'une problématique réelle est décrit, à savoir le chenal d'amenée de la centrale de Paluel. La simulation de l'écoulement est expliquée, et différents modèles de transport des particules sont appliqués. Les modèles de transport de particules arrivent assez bien reproduire les observations concernant le mode de remplissage du chenal d'amenée de la centrale, mais n'arrivent pas à reproduire le bon taux de remplissage de chaque pompe. Plusieurs voies sont suggérées pour améliorer ce résultat.

9.1 Information on the type of algae considered

Figure 2.1 in the introduction presented the fact that the main algae causing a problem are known as Ulva. These algae have a very weak grip on the sea bed and are therefore easily carried by a current. They are only slightly denser than water, around $1050\,\mathrm{kg/m^3}$. These alga are very thin, two cells thick (therefore about $50\ \mu$m), but characteristic length in the order of 5 cm, see figure 9.1.



(a) Ulva scandinavica[1]



(b) Iridaea Flaccida[2]

Figure 9.1: Example of algae.

Because of their size the inertial properties of such particles can be very significant. However since these algal particles are transported over a large distance and because they can fold over it can be assumed that their orientation will only play a minor part in their transport, and it is assumed that they can be modelled similarly as spheres. However there are a few modifications that can be done to correspond better to their specificities. Firstly the algae will be considered as disks that are 5 cm in diameter (D_a) and $50\ \mu$m in thickness (t_a) . For modelling purpose it will be assumed that they can be folded and will resemble a sphere when transported by the flow. Therefore the inertial properties of an alga will be normalised using the maximum projected area (Gaylord *et al.*, 1994). This means that the the Reynolds number , the surface area and the volume used to find the drag coefficient and added mass tensor are defined by:

$$\mathrm{Re}_a = \frac{|\mathbf{U}-\mathbf{V}|\,D_a}{\nu} \tag{9.1a}$$

$$S_a = \frac{\pi D_a^2}{4} \tag{9.1b}$$

$$\Omega_a = S_a t_a \tag{9.1c}$$

Gaylord *et al.* (1994) provide experimental values for the drag coefficient and added mass tensor of three algae of different shape. Out of these algae Iridaea Flaccida is the closest in shape to the Ulvas. These experimental values will be linked to the values for a sphere, such as given by Almedeij (2008), in figure 9.2.

[1]source: http://www.marevita.org
[2]source: Gaylord *et al.* (1994)

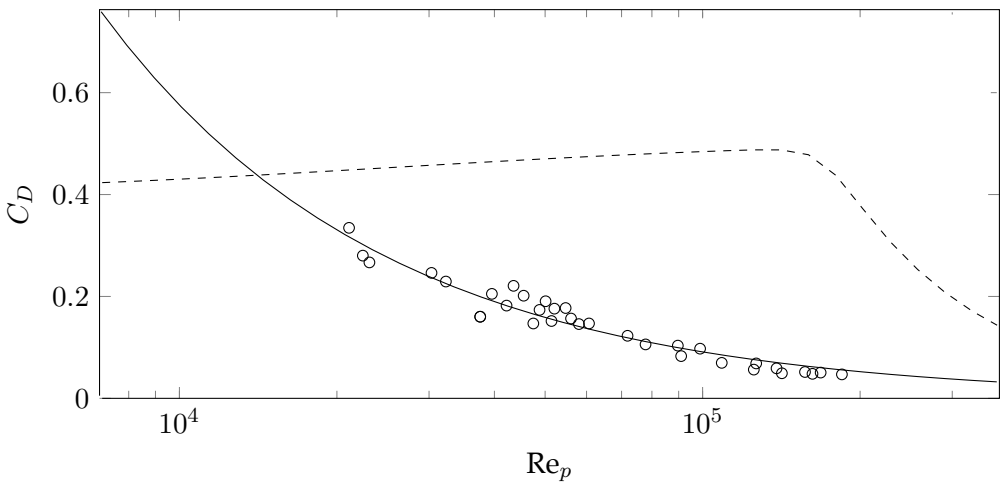


Figure 9.2: The drag coefficient for an Iridaea flaccida. "○" represents the experimental values given in Gaylord *et al.* (1994), "——" represents the best fit line of those values and "- - -" represents the empirical formula for a sphere given by Almedeij (2008).

Figure 9.2 shows that the drag coefficient of an algae particle is lower than that of a sphere for high particle Reynolds number. However it should be noted that the lowest value of the Reynolds number from the experimental data is still rather high (around 2×10^5). This is why the best fit line of the experimental drag coefficient increases rapidly after the known values. In order to stop the model from overestimating the drag coefficient it is assumed that for the particle Reynolds number at the intersection of the best fit line and the spherical drag coefficient ($\mathrm{Re} = 14073$ in figure 9.2) and under, the value for the drag coefficient should be that of a sphere, but calculated with the properties of an alga. The drag coefficient for an algae is therefore given in the following equation:

$$C_{D,a} = \begin{cases} \exp\left(6.822121 - 0.800627 \ln\left(\mathrm{Re}\right)\right) & \text{if } \mathrm{Re} > 14073 \\ C_{D,sphere}\left(\mathrm{Re}_a\right) & \text{if } \mathrm{Re} < 14073 \end{cases} \tag{9.2}$$

Where $C_{D,sphere}$ is given by equation 9.6, described later on. In the same paper by Gaylord *et al.* (1994) an estimate of the added mass constant is given for the same alga (it is simplified to an isotropic body, see equation 4.19):

$$M = M_a = 3.57 \rho_f \Omega_a \tag{9.3}$$

As a reminder the added mass constant of a sphere is $\rho_f \Omega / 2$, therefore algae particles are more dependant on momentum effects than spheres, but are less influenced by drag forces.

9.2 Applying the model to represent algae particles

The response of an algae particle will be analysed in comparison to that of a sphere of equivalent volume. A sphere of equivalent volume is given by defining the diameter through the following equation:

$$D_s = \left(\frac{3 \pi D_a^2 t_a}{2} \right)^{\frac{1}{3}} \tag{9.4}$$

The other physical properties are defined in the same way as in section 4.2:

$$\mathrm{Re}_s = \frac{|\mathbf{U} - \mathbf{V}|\, D_s}{\nu} \tag{9.5a}$$

$$S_s = \frac{\pi D_s^2}{4} \tag{9.5b}$$

$$\Omega_s = \frac{\pi D_s^3}{6} \tag{9.5c}$$

With the drag coefficient given by the equation given in Almedeij (2008), which was also given previously in chapter 4:

$$C_{D,sphere} = \left[\frac{1}{(\varphi_1 + \varphi_2)^{-1} + (\varphi_3)^{-1}} + \varphi_4\right]^{1/10} \tag{9.6a}$$

$$\varphi_1 = (24\mathrm{Re}_s^{-1})^{10} + (21\mathrm{Re}_s^{-0,67})^{10} + (4\mathrm{Re}_s^{-0,33})^{10} + (0,4)^{10} \tag{9.6b}$$

$$\varphi_2 = \frac{1}{(0,148\mathrm{Re}_s^{0,11})^{-10} + (0,5)^{-10}} \tag{9.6c}$$

$$\varphi_3 = (1,57 \times 10^8 \mathrm{Re}_s^{-1,625})^{10} \tag{9.6d}$$

$$\varphi_4 = \frac{1}{(6 \times 10^{-17}\mathrm{Re}_s^{2,63})^{-10} + (0,2)^{-10}} \tag{9.6e}$$

The first test done is for free falling particles. Both particles were allowed to accelerate from rest for 1 second. The evolution of the of their falling velocities are given in figure 9.3. In this figure the falling velocities are non-dimensionalised using the settling velocity V_{set} defined in equation 4.29b.

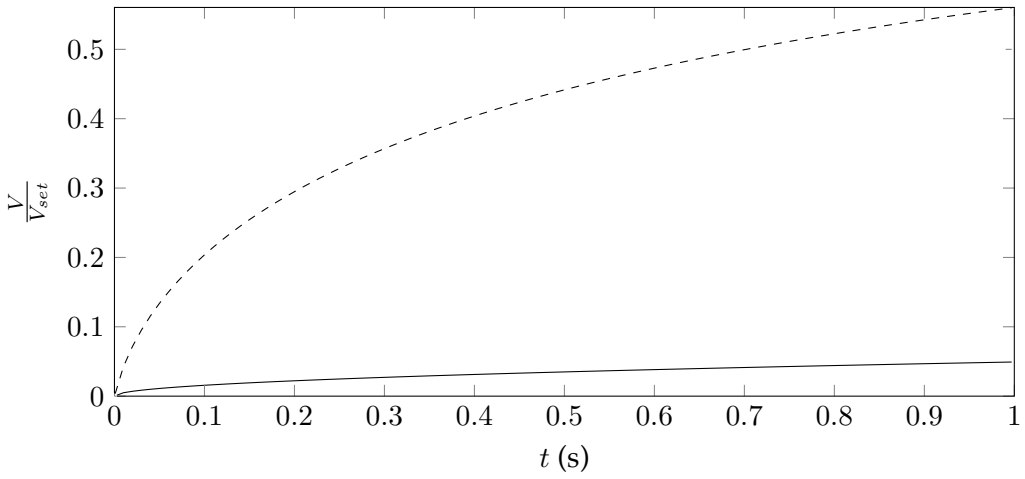


Figure 9.3: Comparison between a free falling alga and a sphere of equivalent volume. "——" represents the alga and "- - -" represents the sphere.

From figure 9.3 it is visible that an alga particle takes much more time than a sphere to attain its maximal settling velocity. Furthermore from equation 4.29b these settling velocities can be calculated to be 0.0436 m/s for a sphere and 0.00232 m/s for an alga. From those values it is possible to conclude that an alga will take much longer to adapt to flow variations from an initial state than a sphere.

The second test done by releasing particles in permanent Taylor eddies. These eddies are defined in section 4.4 and solve for the Navier-Stokes equations. A fluid particle, an algae and a sphere of equivalent volume were released in these eddies at the same position and with an initial velocity equal to the fluid velocity. Their trajectories are plotted in figure 9.4.

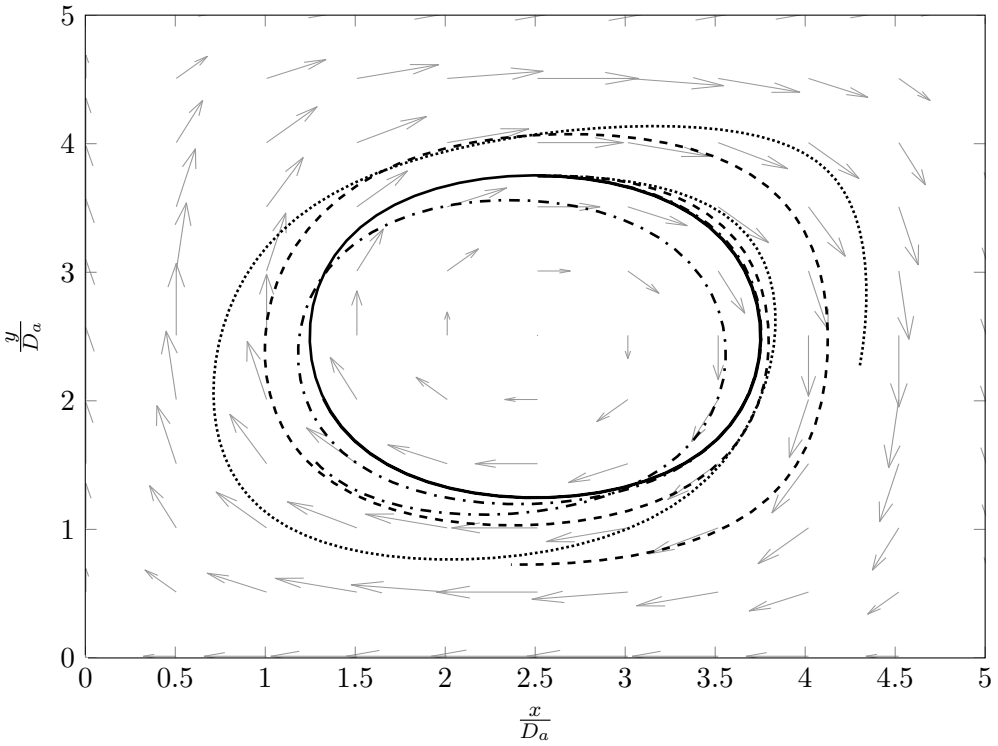


Figure 9.4: Trajectories of different bodies released in Taylor eddies. "——" is a fluid particle, "- - -" is an alga particle, "·····" is a sphere of equivalent volume as the alga and "-··-" is a sphere with the same diameter as the alga.

Figure 9.4 shows that alga particles will stay stuck in a turbulent eddy longer than a sphere of equivalent volume, but less than a sphere with the same diameter. Therefore even though an alga might take longer to accelerate than a sphere it will also follow more closely the turbulent fluctuations of a fluid, and therefore it can be expected to diffuse more.

9.3 Application around a real bathymetry

Using all the coefficients and consideration presented in section 9.1 algae particles will be released in a real bathymetry. A real bathymetry therefore implies that the simulations of the transport of particles will be much longer then for the experiments of chapters 7 and 8. There are also several other flow characteristics that need to be considered. For example the bathymetry can produce rapid changes in flow patterns, and the time step needs to be chosen so that the displacement of one particle during that time step can respond to the mean flow variations. Furthermore, the scale of the problem requires effects such as the tides to be taken into account. These tides will create a variation in mean flows, and therefore the Basset history force can become very important. The effect of the tides can result in the deposition of particles on tidal flats, and these particle need to be taken into account properly. Deposited particles need to forget all the previous forcing applied onto it and stay in their position until the tide rises again to reintroduce them into the flow. The flow around a real bathymetry can also experience additional forcing due to the action of the waves. Furthermore the waves can increase the diffusion of particles on the free-surface, but since algae particles are slightly denser than water these effects will be ignored, even when the water depth is very small, such as around tidal flats.

9.4 Description of the problematic around Paluel

The real problematic that was chosen to test the model is that of the flow around the Paluel nuclear power station, which situated along the Normandy coast of northern France. Due to the increase and mass depositions of algal bloom along the french coast of Brittany and Normandy in the last decades, for reasons explained in chapter 2, EDF has been interested in causes that can lead these algal blooms to clog the filter before the pumps providing access to cool water, with aims maximise production. Observations have lead to the conclusion that the presence of algae in the coastal water is most critical when the wind blows from the north west, as the resulting waves, in combination to a rising tide can create a zone of recirculation. Algae particles will be trapped and will accumulate in this recirculation zone, but as the tide reverses these particles will be released as a block into the channel leading to the pumps of the nuclear power station. Figure 9.5 shows the bathymetry around the Paluel power plant, with the position of the pumps represented.

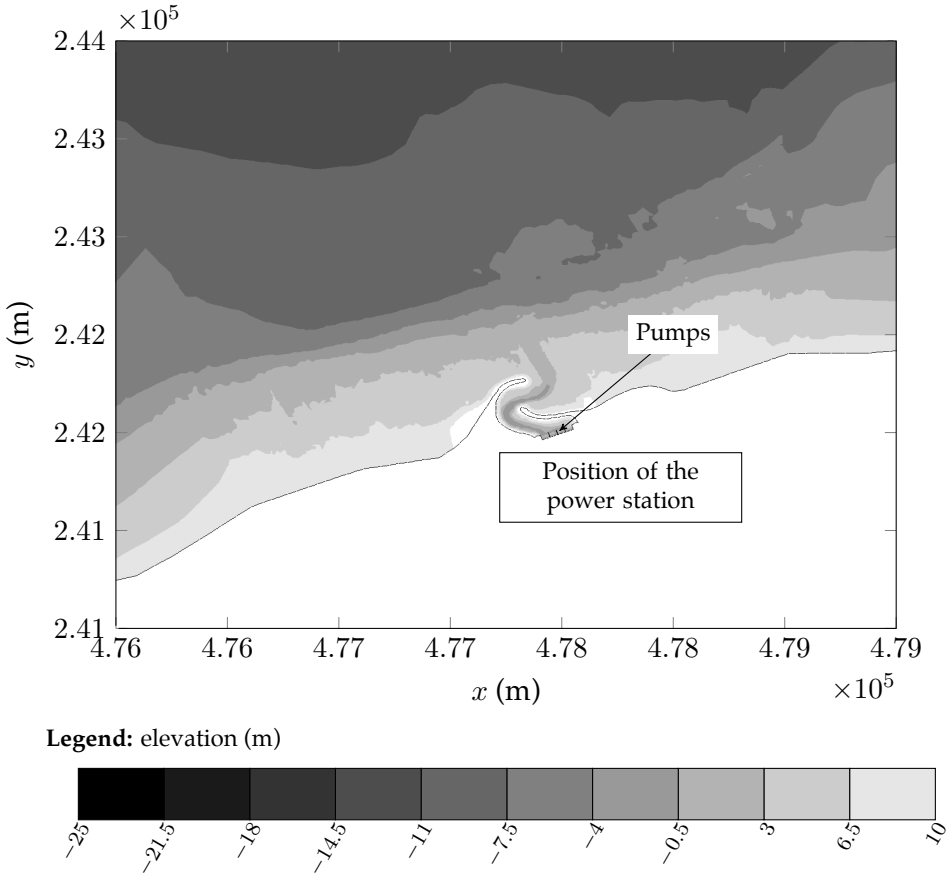


Figure 9.5: The bathymetry around the Paluel power station.

The flow in this bathymetry was then modelled using the industrial code Telemac-2D. This code is a finite element solver of the shallow water equations. The shallow water equations used are similar to equations 3.28 presented in chapter 3, but the external forcing are taken into account:

$$\frac{\partial h}{\partial t} + \frac{\partial h U_i}{\partial x_i} = 0 \tag{9.7a}$$

$$\frac{\partial \overline{U_i}}{\partial t} + \overline{U_j}\frac{\partial \overline{U_i}}{\partial x_j} = -g\frac{\partial \eta}{\partial x_i} + \frac{1}{h}\frac{\partial}{\partial x_j}\left[h\left(\nu + \nu_T\right)\left(\frac{\partial \overline{U_i}}{\partial x_j} + \frac{\partial \overline{U_j}}{\partial x_i}\right)\right] + \frac{1}{h}\frac{\partial R_{ij}}{\partial x_j} + C_{or,i} + F_{bo,i} + F_{wi,i} \tag{9.7b}$$

Where:

- R_{ij} is the radiation stress tensor, which will be used later to include the effect of the waves.
- $C_{or,i}$ represents the effect of Coriolis, and it is given by equation:

$$\mathbf{C_{or}} = h 2 f_e \sin\left(L_{at}\right)\begin{pmatrix} -U_y \\ U_x \end{pmatrix} \tag{9.8}$$

  Where f_e is the earth's self rotation frequency and L_{at} is the latitude.

- $F_{bo,i}$ is the bottom friction forces given by equation:

$$F_{bo,i} = \frac{S_{bo} u_*^2}{|\mathbf{U}|} U_i \tag{9.9}$$

  Where S_{bo} is the local slope of the bottom and u_* is the bottom shear velocity.

- $F_{wi,i}$ is the wind friction forces given by equation:

$$F_{wi,i} = a_w \left|\mathbf{U_w}\right| U_{w,i} \tag{9.10}$$

  Where a_w is a dimensionless wind friction coefficient and $\mathbf{U_w}$ is the wind velocity vector ten meters above the sea surface.

Equations 9.7 are then closed using a depth-averaged k-ε turbulence model described in equations 3.29. The values thus found for k and ε are then used in equations 9.7 through the usual relation for the eddy viscosity:

$$\nu_T = C_\mu \frac{k^2}{\varepsilon} \tag{9.11}$$

The tides are taken into account by imposing height and velocity constraints along the water boundaries. The waves on the other hand are taken into account through the radiation stresses. These radiations stresses are calculated using the computational code called Tomawac (Benoit *et al.*, 1996). Tomawac is a third generation model solving the equations governing the spectral wave action density $\vartheta(\mathbf{x}, \mathbf{k_w})$. The wave action density is a function of a two-dimensional position vector $\mathbf{x}$ and a two dimensional wave number vector $\mathbf{k_w}$ (with length $2\pi/\lambda_w$, where λ_w is the wavelength). This spectral density is given by the following equation (for example see: Komen *et al.*, 1994):

$$\frac{\partial \vartheta}{\partial t} + \frac{\partial}{\partial x_i}\left(\vartheta V_{w,i}\right) + \frac{\partial}{\partial k_{w,i}}\left(\vartheta V_{w,i}\right) = \sum_{i=1}^{6} Q_i \tag{9.12}$$

Where $\mathbf{V_w}$ is a four dimensional vector given by:

$$\mathbf{V_w} = \left(\frac{d\mathbf{x}}{dt}, \frac{d\mathbf{k_w}}{dt} \right) \tag{9.13}$$

The components of the vector are given by the following equations:

$$\frac{dx_i}{dt} = \frac{C_g}{|\mathbf{k_w}|} k_{w,i} + U_i \tag{9.14a}$$

$$\frac{dk_{w,i}}{dt} = \frac{\partial \sigma_w}{\partial h} \frac{\partial h}{\partial x_i} - k_{w,j} \frac{\partial U_i}{\partial x_j} \tag{9.14b}$$

Where C_g is the wave group velocity, h is the water depth and $\mathbf{U}$ is the depth averaged fluid velocity. The last two variables can be unsteady in Tomawac, when waves are propagated in areas where tidal effects are considered. σ_w is the relative angular wave frequency, meaning that it is observed in a frame moving with the current at a speed $\mathbf{U}$. It is given by the following equation:

$$\sigma_w = \omega - k_{w,i} U_i \tag{9.15}$$

ω is the absolute angular wave frequency, ($\omega = 2\pi/T_w$, with T_w being the wave period). Linear wave theory gives the following expressions:

$$C_g = \frac{n_w \sigma_w}{|\mathbf{k_w}|} \tag{9.16a}$$

$$\sigma_w^2 = g\,|\mathbf{k_w}| \tanh\left(|\mathbf{k_w}|\, h\right) \tag{9.16b}$$

$$n_w = \frac{1}{2}\left[1 + \frac{2\,|\mathbf{k_w}|\, h}{\sinh\left(2\,|\mathbf{k_w}|\, h\right)}\right] \tag{9.16c}$$

Furthermore the six terms of equation 9.12 labelled Q_i represent the effect of the following physical phenomena:

- Q_1: input of energy from the wind
- Q_2: dissipation due to white capping
- Q_3: non-linear four-wave interactions (also known as "quadruplet" interactions)
- Q_4: dissipation due to bottom friction
- Q_5: dissipation due to depth-induced breaking in shallow water areas
- Q_6: non-linear three-wave interactions in shallow water (also known as "triplet' or "triad" interactions

The term Q_1 is a source term, the terms Q_2, Q_4 and Q_5 are sink terms (that depend on the local wind velocity, bathymetry and wave spectrum). The terms Q_3 and Q_6 are responsible for the redistribution of energy within the wave spectrum. The models for the terms Q_i's are complex, and readers is advised to look up Benoit *et al.* (1996) for more information. Tomawac produces, amongst other results, the radiation stresses through the following relation:

$$R_{ij} = -\frac{g}{2\pi h}\int\int\left[\frac{1}{|\mathbf{k_w}|^2}k_{w,i}k_{w,j} + \left(1-\frac{1}{2n_w}\right)\delta_{ij}\right]C_g^2\vartheta dk_{w,i}dk_{w,j} \tag{9.17}$$

The integrals of R_{ij} runs over the whole spectrum of energy. These radiation stresses can then be inserted in equation 9.7. The waves therefore affect the currents, whereas the mean currents and water depth affect the wave propagation through equations 9.14. Therefore the fluid velocity along a coastline is calculated in three stages. Firstly the mean currents of the flow are found without considering the effect of the waves. This current are then used to modify the wave propagation and the radiation stresses are calculated. Finally the radiation stresses are used to recalculate the current along the coastline. The wave-current is stopped at this stage the radiation stresses induced current will not modify greatly the wave propagation[3].

More details on the methods used by the Telemac-2D and Tomawac industrial code can be found in Hervouet (2007) and Benoit *et al.* (1996) respectively [4], while a more complete description of how this code was used to solve the flows around the Paluel power station and an brief overview of the validations are given in Issa *et al.* (2009).

Figure 9.6 shows the importance of including radiation stresses in the numerical simulations. In this figure the velocity vectors show that when the effect of the waves is taken into account through the radiation stresses a recirculation zone west of the power station channel appears during flood tide. This was also observed in situ, and especially during high risk events (Issa, 2008). What was therefore concluded was that algae particles can be trapped in this zone and accumulate. Then, when the tide reverses (during ebb tide), a high concentration of algae is released towards the pumps. It is this high concentration of algae entering the channel towards the pumps that can result in clogging.

9.5 Transport patterns

There the flow around the Paluel power station was then solved using Telemac-2D in combination with Tomawac, where the domain considered was meshed 7 kilometres west of the power station, 15 kilometres east and 7 kilometres into the sea. The elements of the mesh are 5 metres wide around the pumps, 10 metres wide in the channel leading to the pumps, 15 metres wide around the power station and 500 meters wide along the maritime boundaries. The simulations were then done using a 2 second time step for the duration of three tides, where the first tide is used to let the flow be established (Issa and Rougé, 2007). A time step of 2 second was chosen to verify the CFL conditions[5].

To test the effects of algae in the flow around the Paluel power station, numerical simulations of particles released into the flow calculated using Telemac-2D were done using different particle transport models, see chapter 6. The flow was simulated for a mean tide (with a tide coefficient of 75, with 1 m waves propagating at a frequency of 0.11 and direction 125° and 2500 particles were released.

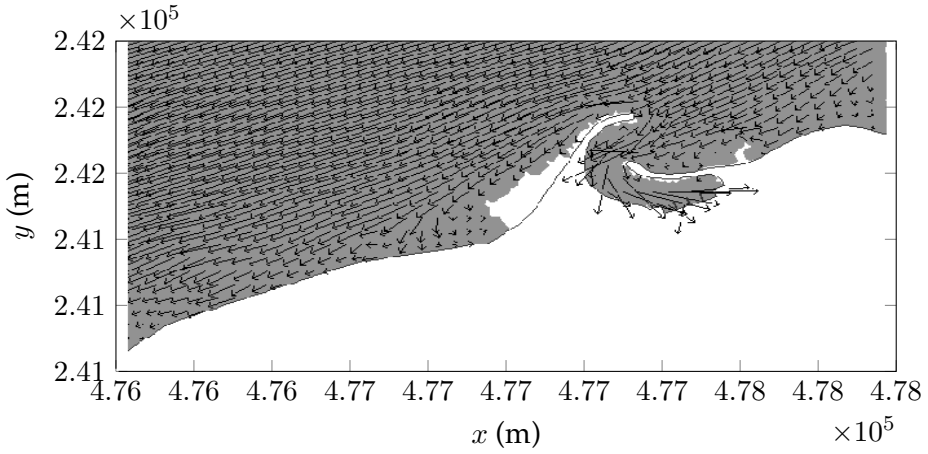
The numerical particles were released one hour before low tide in the center of the recirculation zone, uniformly in a 50×50 m area centred around (476823 m,241652 m), using the same axis as on figure 9.5. This was done to ensure that particles fill up the whole recirculation area before the tide reverses and the are transported towards the pumps. The released particles were then transported in the triangular finite element mesh used by the Telemac-2D simulations in the same way as the simulations of chapter 8 and using the method described in appendix D.

The different particle models used are summarised in tables 9.1, where the same nomenclature as chapters 7 and 8 is used.

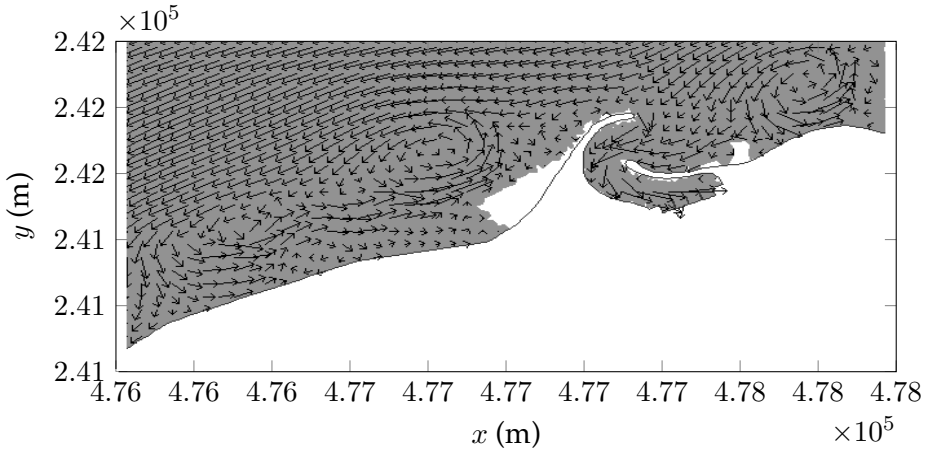
[3] A real coupling of both Telemac-2D and Tomawac is possible, but for the simulations around the Paluel power station this method is sufficient.

[4] Both codes can be distributed to private and public user: www.opentelemac.org

[5] The CFL number is a ratio between the fluid velocity multiplied by the time and the length scale (for example the size of an element of the mesh). CFL conditions states that this number should be smaller than one.



(a) Simulation without any radiation stresses



(b) Simulation with radiation stresses calculated from north west (125°) waves with a wave height of 1 m and a frequency 0.11 Hz

Figure 9.6: Two vector plots of the velocities around the Paluel power station to show the importance of including the radiation stresses. The velocities are shown one hour before the high tide (at time HT-1h). The white regions represent tidal flats, as calculated in Telemac-2D.

The simulations were first tested for spheres with the same diameter as the algae described in section 9.1, but using the different solid body dynamics models described in chapter 4 (Models II to IV). This was done to verify the impact of the different force components on the motion of solid bodies in a real flow. These bodies were then compared to Model V, which is a simulation similar to model II, but with a sphere chosen so that its volume is the same as an algae particle, see section 9.2. Model VI is a simulation done with algae particles, as they are defined in section 9.1. Finally Model VII is a simulation where the particles follow exactly the mean flow velocities, and Brownian motion used in model VIII is a simple dispersive model (see equation 7.9 in chapter 7). These last two models are used as references as they are the simplest two models used in environmental flows. For example Brownian motion used in Issa *et al.* (2009) or Monti and Leuzzi (2010).

Figures 9.7 to 9.13 shows the evolution of particles transported using the models described in table 9.1. The first thing that should be noted is the particles in all models undergo the transport pattern expected. The particles are trapped in the recirculation zone that occurs as a result of the waves, and as the tide reverses the particles are released towards the channel preceding the pumps. Looking at the evolution from figure 9.7, where particles follow exactly the mean flow properties, to figure 9.8 where the dispersion is modelled using a simple turbulence model, it can be seen that considering the turbulence of the fluid is necessary to have particles enter the channel. Figure 9.9 is the first model which considers solid body dynamics, and it shows that including solid body dynamics increases the

Table 9.1: Summary of the different models compared and different forcing considered for particles released around the Paluel power station[6]. SLM means the Simplified Langevin Model, see chapter 5.

	Basset	Momentum	Drag	Turbulence model[7]	Body & size
Model II	yes	yes	yes	SLM	sphere; $D_s = 5$ cm
Model III	no	yes	yes	SLM	sphere; $D_s = 5$ cm
Model IV	no	no	yes	SLM	sphere; $D_s = 5$ cm
Model V	yes	yes	yes	SLM	sphere; D_s =eqn 9.4
Model VI	yes	yes	yes	SLM	Algae; $D_a = 5$ cm
Model VII	no	no	no	none	fluid particle
Model VIII	no	no	no	Brownian motion	fluid particle

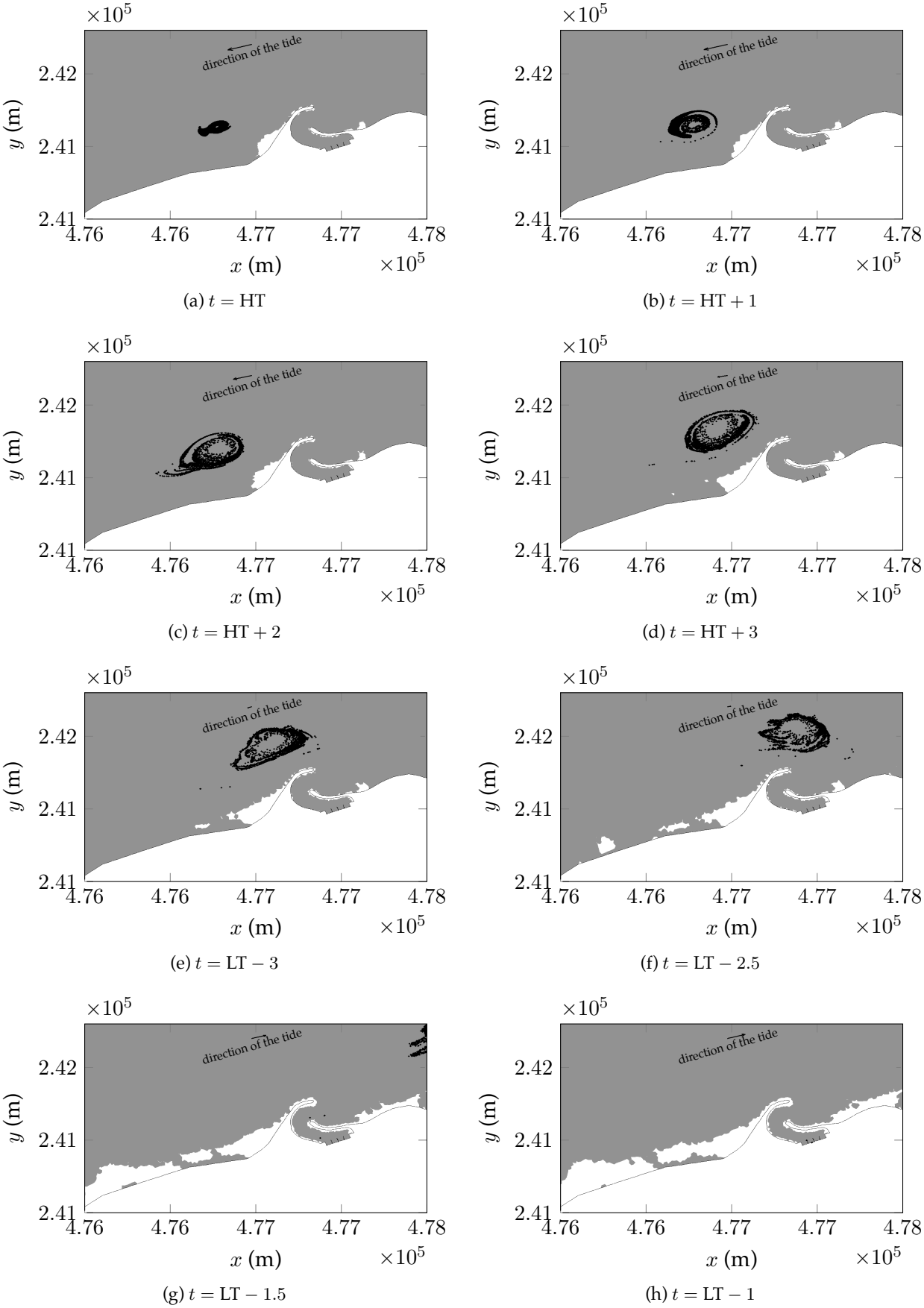
effect of the mean flow pattern on the motion of the particles, as the particles fill up the recirculation zone more completely. However the particles enter the channel in a single line. Figure 9.10 shows that adding the momentum of the bodies to the solid body dynamics increases the dispersion of the bodies so that particles fill up the recirculation zone more uniformly and they enter the channel in a less organised manner. Figure 9.11 shows that the final addition of the Basset History force to the particle transport model tightens the area covered by the particles.

Looking at figures 9.11 to 9.13 shows that modifying the characteristics of the solid bodies to apply to algae, by considering a sphere with an equivalent volume or changing the physical characteristics, tends to increase the overall diffusive effects, as the area covered by the particles is more uniform. However the area covered by the particles is slightly smaller than for spherical that have the same diameter as the algae particles. Besides these considerations adapting the model to correspond to algae particles does not change greatly the transport pattern of the particles.

Therefore figures 9.7 to 9.13 allows to conclude that considering only the mean velocities of the flow is sufficient to verify if particles can be trapped into the recirculation zone that appears west of the power station. However it is important to consider diffusive effects to have particles enter the channel. Furthermore every information that can be applied to the solid body dynamics model modifies the transport pattern and therefore it is important to include as much information as possible when modelling the particle transport.

[6]Model I presented in table 7.4 is not used as the model taking into account the "Crossing Trajectories Effects" has hardly any effect in 2D horizontal particle transport models.

[7]See chapter 5.



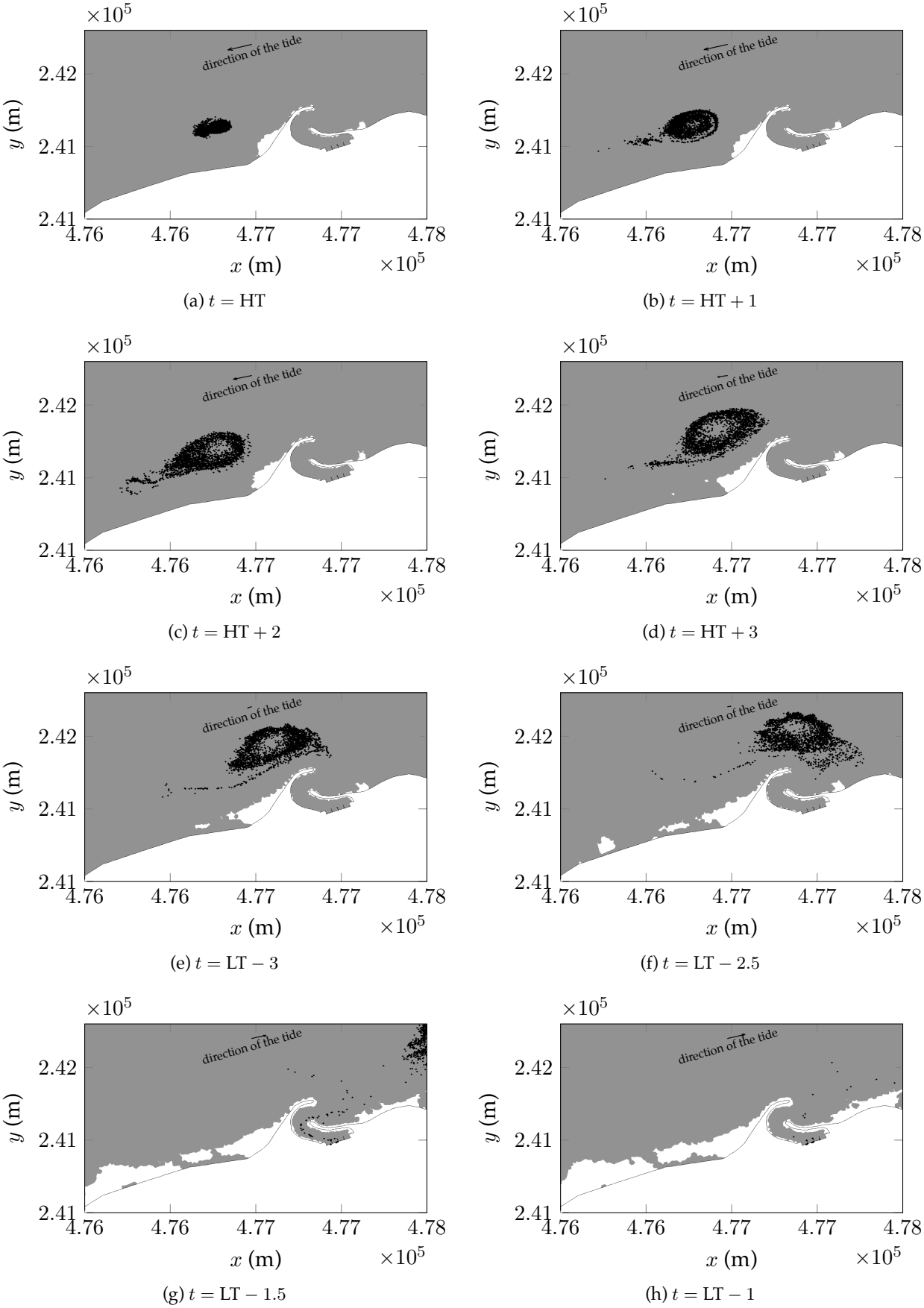
(a) $t = \text{HT}$ (b) $t = \text{HT} + 1$

(c) $t = \text{HT} + 2$ (d) $t = \text{HT} + 3$

(e) $t = \text{LT} - 3$ (f) $t = \text{LT} - 2.5$

(g) $t = \text{LT} - 1.5$ (h) $t = \text{LT} - 1$

Figure 9.7: Particles transported in the flow around Paluel using fluid trajectories (Model VII). LT is the time of the Low Tide and HT is the time of the High Tide. The white regions show the tidal flats.



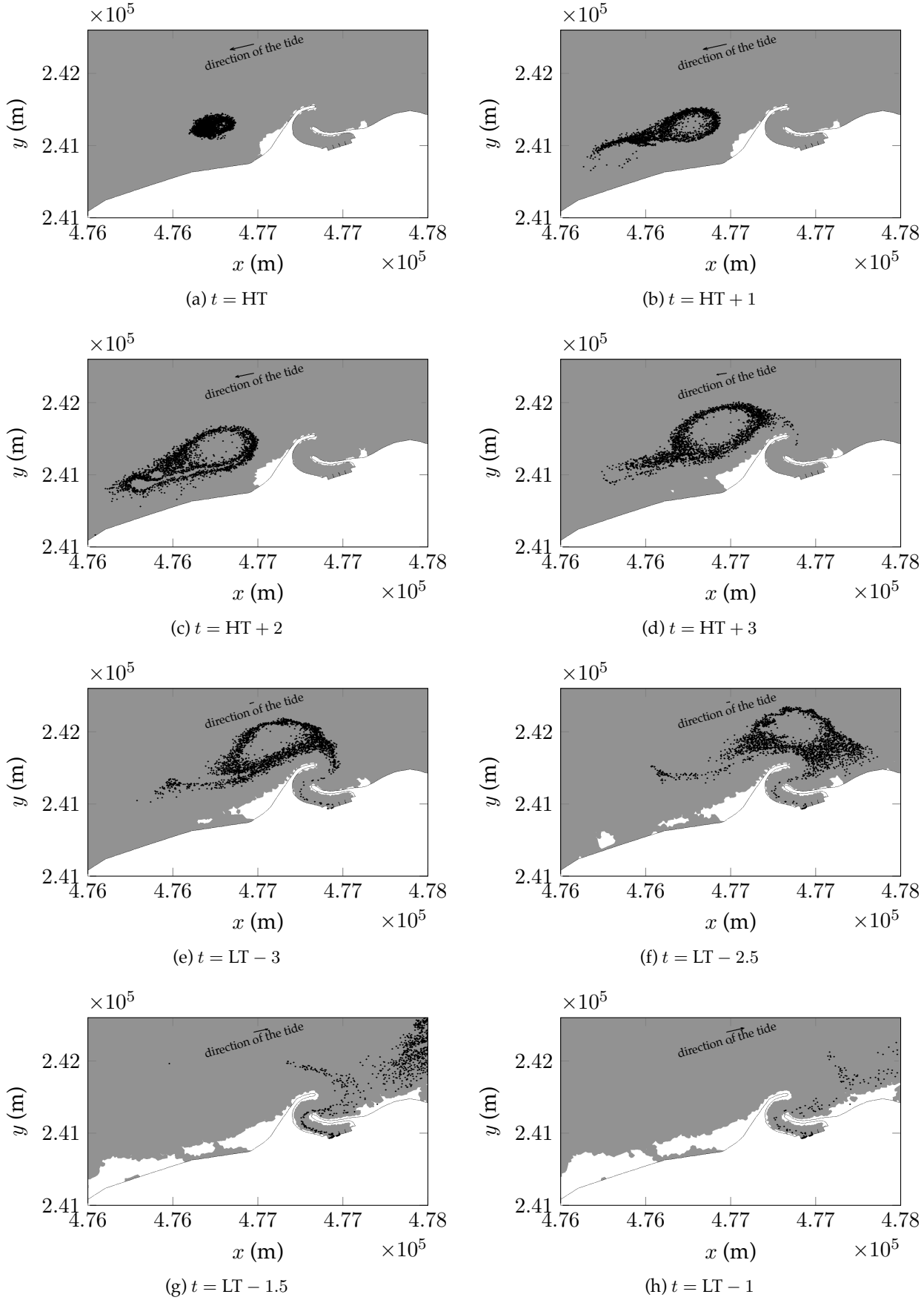
(a) $t = \text{HT}$ (b) $t = \text{HT} + 1$

(c) $t = \text{HT} + 2$ (d) $t = \text{HT} + 3$

(e) $t = \text{LT} - 3$ (f) $t = \text{LT} - 2.5$

(g) $t = \text{LT} - 1.5$ (h) $t = \text{LT} - 1$

Figure 9.8: Particles transported in the flow around Paluel using model VIII. LT is the time of the Low Tide and HT is the time of the High Tide. The white regions show the tidal flats.



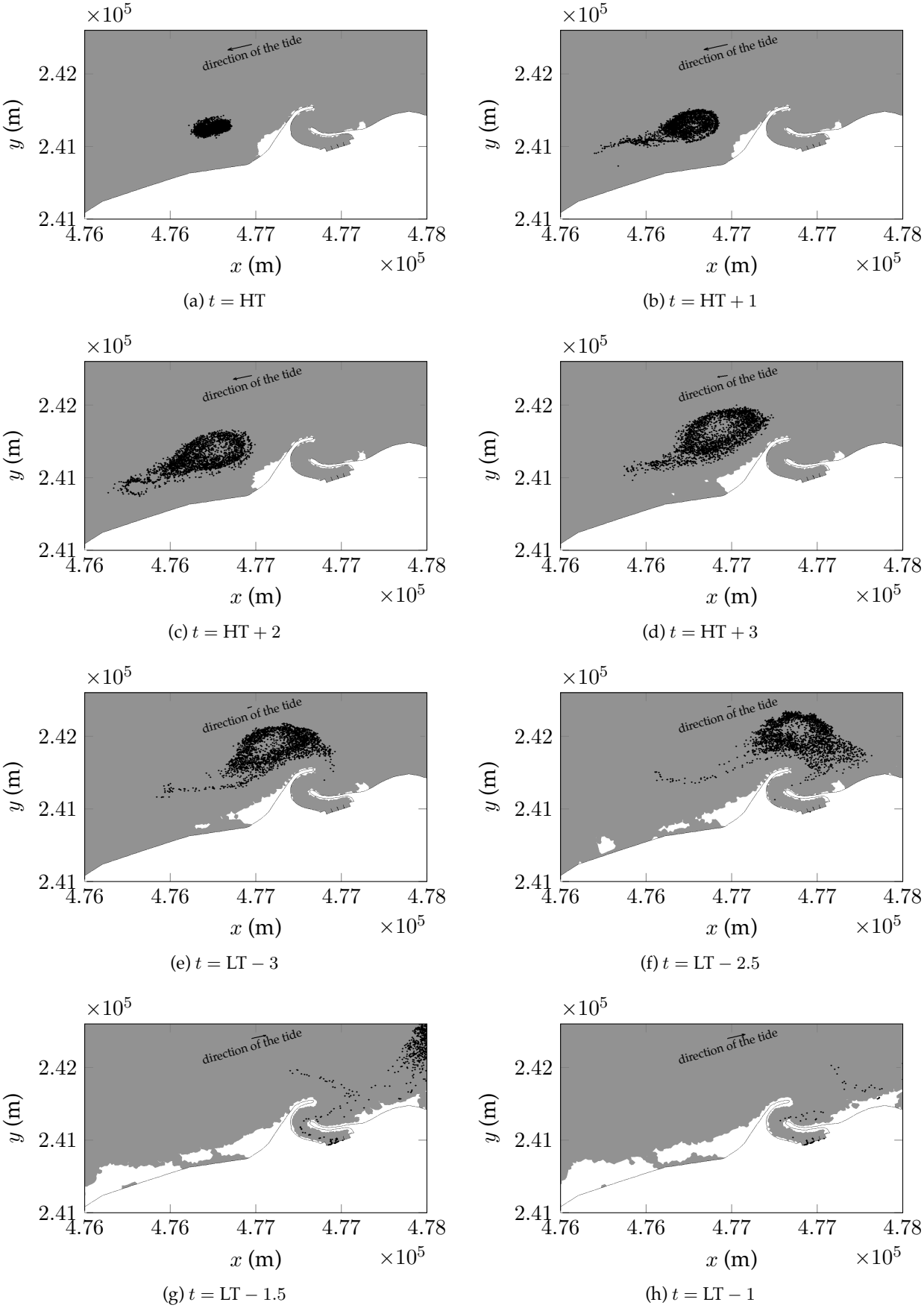
(a) $t = \text{HT}$ (b) $t = \text{HT} + 1$

(c) $t = \text{HT} + 2$ (d) $t = \text{HT} + 3$

(e) $t = \text{LT} - 3$ (f) $t = \text{LT} - 2.5$

(g) $t = \text{LT} - 1.5$ (h) $t = \text{LT} - 1$

Figure 9.9: Particles transported in the flow around Paluel using Langevin equation, model IV. LT is the time of the Low Tide and HT is the time of the High Tide. The white regions show the tidal flats.



(a) $t = \text{HT}$

(b) $t = \text{HT} + 1$

(c) $t = \text{HT} + 2$

(d) $t = \text{HT} + 3$

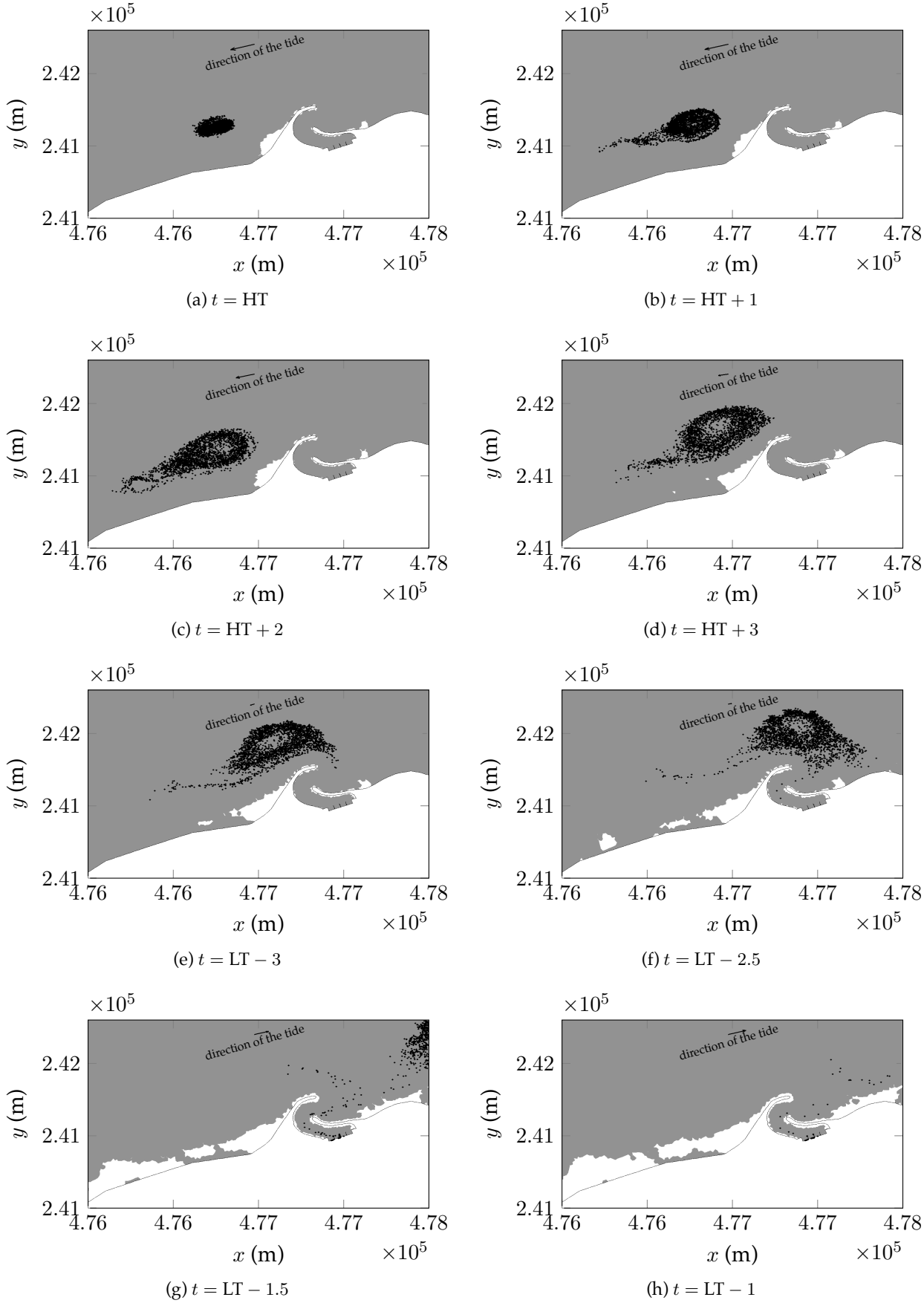
(e) $t = \text{LT} - 3$

(f) $t = \text{LT} - 2.5$

(g) $t = \text{LT} - 1.5$

(h) $t = \text{LT} - 1$

Figure 9.10: Particles transported in the flow around Paluel using Langevin equation, model III. LT is the time of the Low Tide and HT is the time of the High Tide. The white regions show the tidal flats.



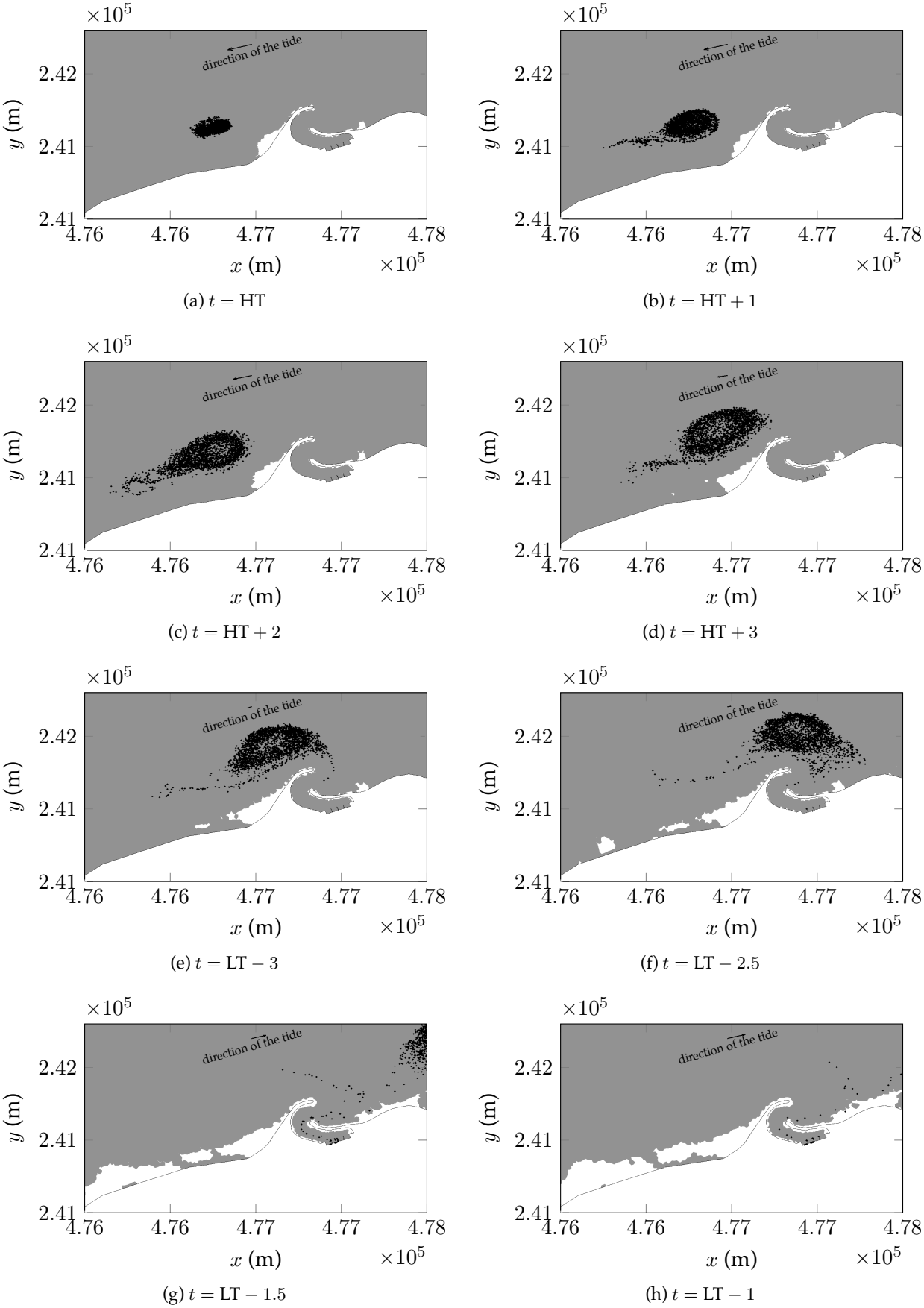
(a) $t = \text{HT}$ (b) $t = \text{HT} + 1$

(c) $t = \text{HT} + 2$ (d) $t = \text{HT} + 3$

(e) $t = \text{LT} - 3$ (f) $t = \text{LT} - 2.5$

(g) $t = \text{LT} - 1.5$ (h) $t = \text{LT} - 1$

Figure 9.11: Particles transported in the flow around Paluel using Langevin equation, model II. LT is the time of the Low Tide and HT is the time of the High Tide. The white regions show the tidal flats.



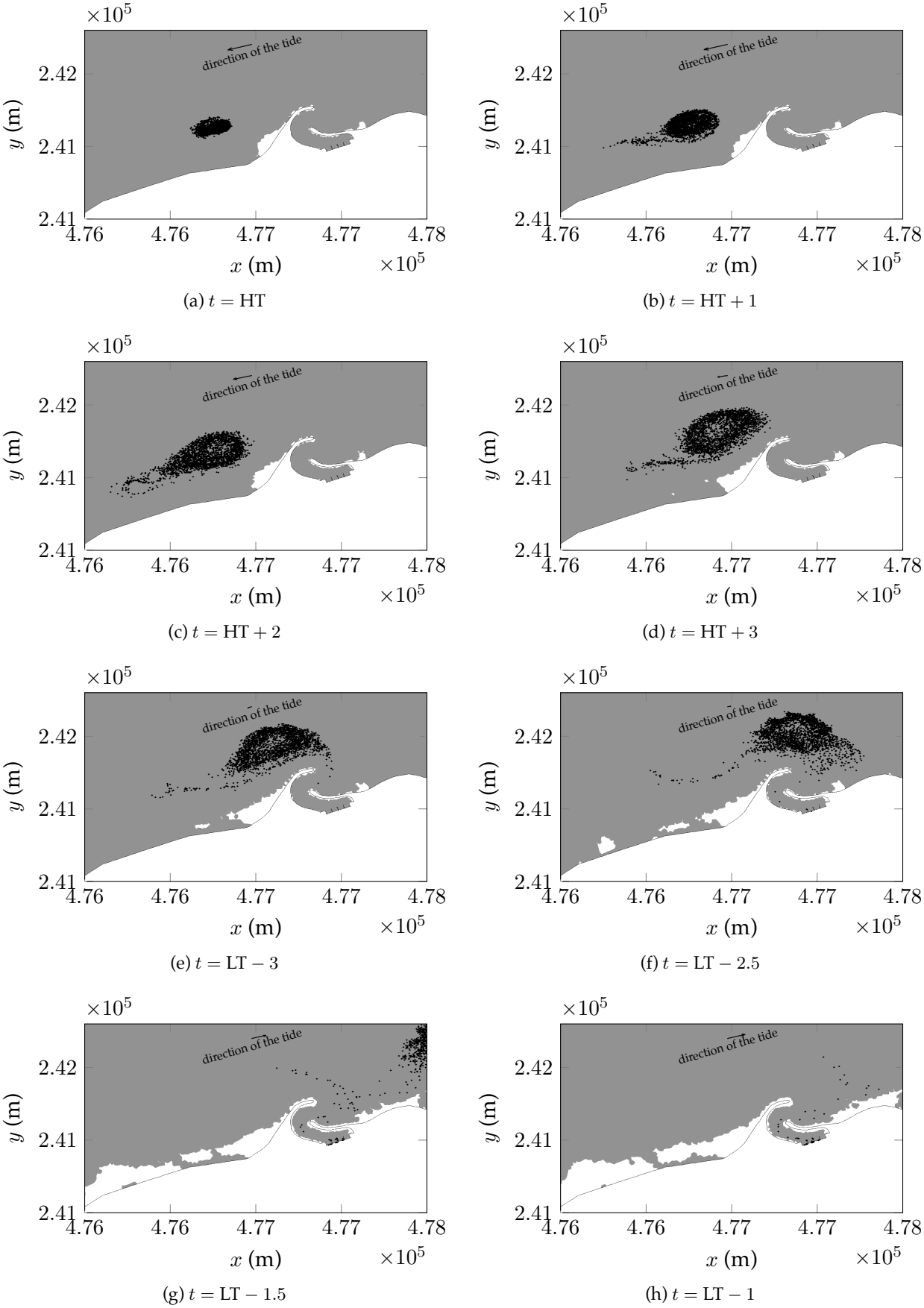
(a) $t = \text{HT}$ (b) $t = \text{HT} + 1$

(c) $t = \text{HT} + 2$ (d) $t = \text{HT} + 3$

(e) $t = \text{LT} - 3$ (f) $t = \text{LT} - 2.5$

(g) $t = \text{LT} - 1.5$ (h) $t = \text{LT} - 1$

Figure 9.12: Particles transported in the flow around Paluel using Langevin equation, model V. LT is the time of the Low Tide and HT is the time of the High Tide. The white regions show the tidal flats.



(a) $t = \text{HT}$ (b) $t = \text{HT} + 1$

(c) $t = \text{HT} + 2$ (d) $t = \text{HT} + 3$

(e) $t = \text{LT} - 3$ (f) $t = \text{LT} - 2.5$

(g) $t = \text{LT} - 1.5$ (h) $t = \text{LT} - 1$

Figure 9.13: Particles transported in the flow around Paluel using Langevin equation, model VI. LT is the time of the Low Tide and HT is the time of the High Tide. The white regions show the tidal flats.

9.6 Particles exiting the domain

The transport patterns of the previous sections have shown that modifying the physical characteristics of the transported particles change visibly the transport pattern of the particles (figures 9.7 to 9.12), but it is difficult to analyse the significances of these different transport pattern. The main interest in this problem was to have a method that could be used to predict the clogging of the pumps of the Paluel power station. Therefore to differentiate the relevance of the different particle transport models an analysis of the particles exiting the domain will be done. The pumps of the Paluel power station a number, ranging from one to four, and will be numbered west to east, see figure 9.14.

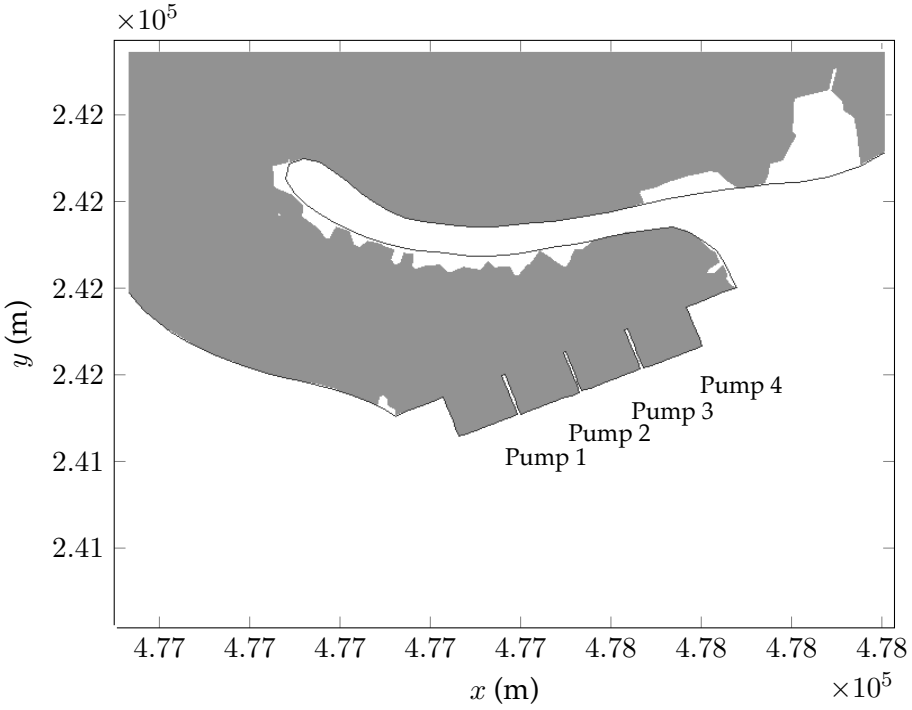
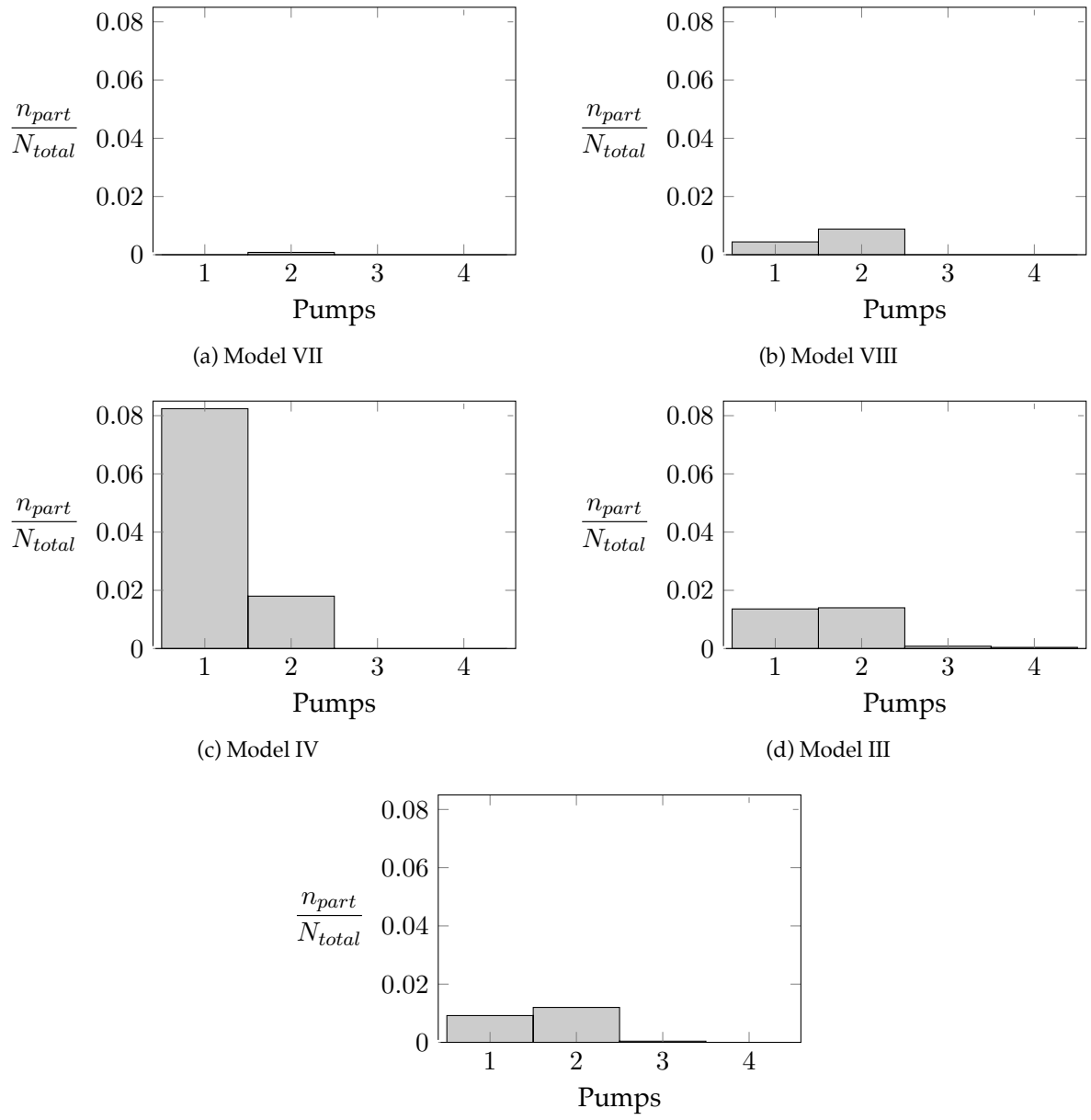


Figure 9.14: Description of the pumps[8]used by the Paluel power station.

In situ observations by EDF have lead to the conclusion that the pumps 3 and 4 are the most at risk (Travade and Guerin, 2004). Figures 9.15 and 9.16 show the number of particles exiting the domain of calculations through each pump. Figure 9.15 shows the evolution of how particles exit the simulation model when additional information on the behaviour of particles is added to the model. Figure 9.15a shows the values for particles following the mean flow (model VII), figure 9.15b shows how adding a simple turbulence model (model VIII) increases the amount of particles entering the pumps, which is in accordance to what is said in section 9.5. Figure 9.15c shows that adding the drag coefficient to the particle transport model (model IV) increases even more the amount of particles entering the pumps, but these particles enter mostly pump 1. Adding even more information to the solid body dynamics, figures 9.15d and 9.15e (model III and II), reduces the amount of particles entering the model to a value closer to the value of the brownian motion model, but it also increases the mixing of the particles within the channel, as particles enter the first to pumps more uniformly.

[8]Technically, each pump is doubled.



(a) Model VII

(b) Model VIII

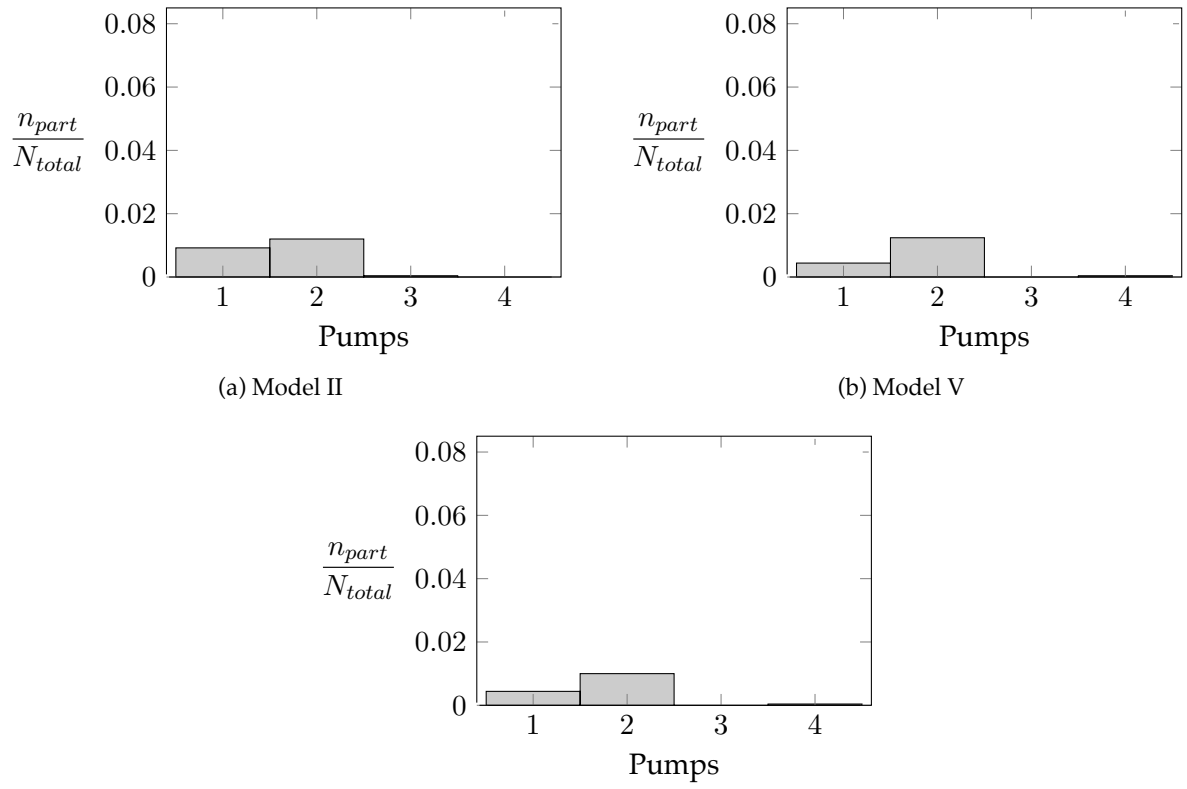
(c) Model IV

(d) Model III

(e) Model II

Figure 9.15: Bar plots of the number of particles entering each pumps, for different solid body dynamics models. n_{part} are the number of particles entering a pump and N_{total} is the total number of particles released.

Figure 9.16 shows the evolution of how particles exit the domain when the body is modified to correspond to algae particles. Figure 9.16a is the same as figure 9.15e, and it shows how spherical particles with the same diameter as the algae (model II) exit the domain. In figure 9.16b spherical particles are still carried, but these particles have the same volume as the algae (model V). Modifying the diameter of the transported particle so that the volume corresponds to that of an algae reduces the amount of particles entering through pump 1. In figure 9.16c, particles are made to correspond to algae particles (model VI) by modifying the solid body dynamics through the considerations presented in section 9.1, also increases the difference between the particles entering pump 1 and 2, but it does so less than the bodies transported in figure 9.16b.



(a) Model II

(b) Model V

(c) Model VI

Figure 9.16: Bar plots of the number of particles entering each pumps, for different solid body shape or size. n_{part} are the number of particles entering a pump and N_{total} is the total number of particles released.

No solid particle transport model in figures 9.15 or 9.16 is able to predict that the two most affected pumps are pumps 3 and 4, as was observed in situ by Travade and Guerin (2004). There are four possible reasons why this might be the case.

Firstly the position at which the particles exit the domain is very dependent on the point of release, however there are no in situ data, only observations, on how the particles are distributed into the recirculation zone. A better method would have been to release the algae particles further west of the power station so that the tidal currents transport the particles towards the recirculation zone in a more natural fashion. This method was not done, so that the transport pattern of the particles in the current could be more visible.

The second reason, and most important, why the simulation do not find that pump 3 and 4 are those subject to the highest risk of clogging might result from three-dimensional effects. The flow simulations were done in two dimensions, but the algae particles are not distributed uniformly along the water column, and are more likely to travel along the bed. In addition the pumps of the power station do not pump the water along the whole water column, but around the surface of the flow. This difference in level might explain why in the observations pumps 3 and 4 are the most at risk, as particles might arrive towards pumps 1 and 2 along the sea bed, and then get lifted off the bed, towards the free-surface and the enter pumps 3 and 4.

The third reason why none of the models presented in figures 9.15 and 9.16 cannot predict accurately the risk to pumps 3 and 4 could be because the mixing regime inside the channel is not accurately predicted. Inside the channel the flow model was only calibrated by observing the mean flow velocities, however no calibration or measurement were done on the turbulent kinetic energy or its dissipation rate (Rougé and Luck, 2006). Furthermore no velocity measurements were done just around the pumps, and therefore the velocity around the pumps might be off. Figure 9.17 for example shows

that some of velocity vectors would go through the walls separating the pumps, and suggests that some measurements of the flow velocities around the entrance of the pumps might be necessary to calibrate the velocity profiles in this area. Nonetheless the test case of chapter 8 tends to indicate that Telemac-2D gives reasonable approximations to the flow velocities.

The final reason why the pumps 3 and 4 were not found to be the most at risk is because the clogging was only tested for one scenario of tides and waves. This scenario is suspected to be the one most favourable to algae clogging, but it might not be the one that affects the two eastern pumps the most.

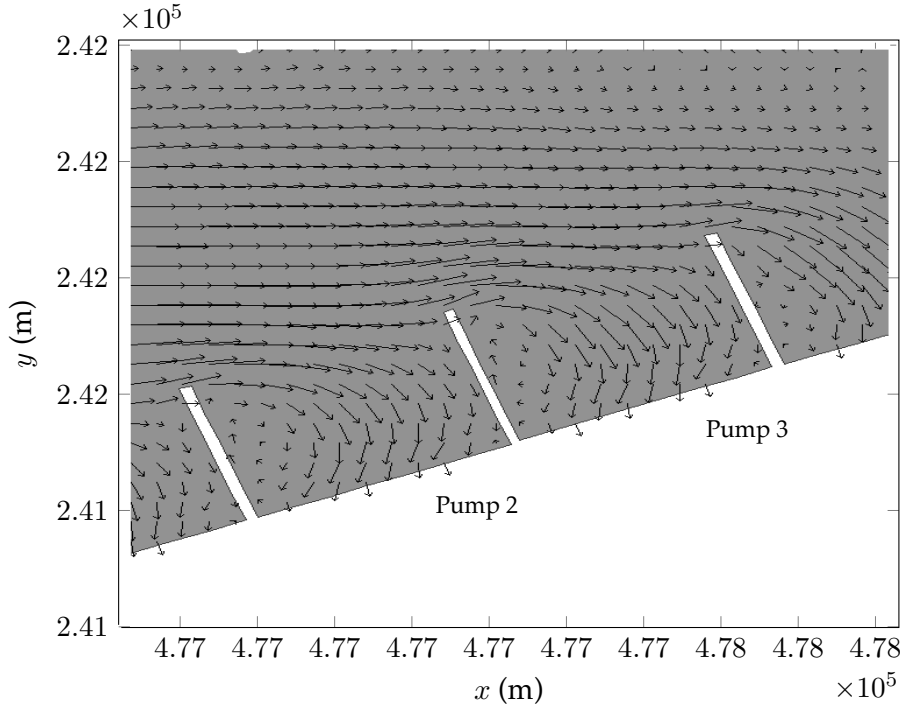


Figure 9.17: Fluid velocity vectors around the pumps of the Paluel power station.

Nonetheless figures 9.15 and 9.16 show that considering the diffusion due to turbulence and the solid body dynamics to the transport of particles increases the amount of particles that enter the channel and exit the domain through the pumps. Figure 9.15 shows that refining the forces acting on the solid bodies tends to shift the mean location at which the particles exit the domain towards the eastern pumps. This effect is then further emphasized when the particles considered are spheres with a volume equivalent to an alga or an alga modelled using the considerations presented in section 9.1.

The mean location at which the particles exit the domain can be calculated by weighting each pump number with the number of particles exiting through it and the total number of particles exiting the domain. This gives the following equation:

$$E_{xit} = \frac{\sum_{i_p=1}^{4} i_p n_{part,i_p}}{\sum_{i_p=1}^{4} n_{part,i_p}} \tag{9.18}$$

Where E_{xit} is mean location at which the particles exit the domain, i_p is the pump number and n_{part,i_p} is the number of particles exiting the domain through pump i_p. The mean location at which the particles exit the domain for the different particle transport models model is given in figure 9.18.

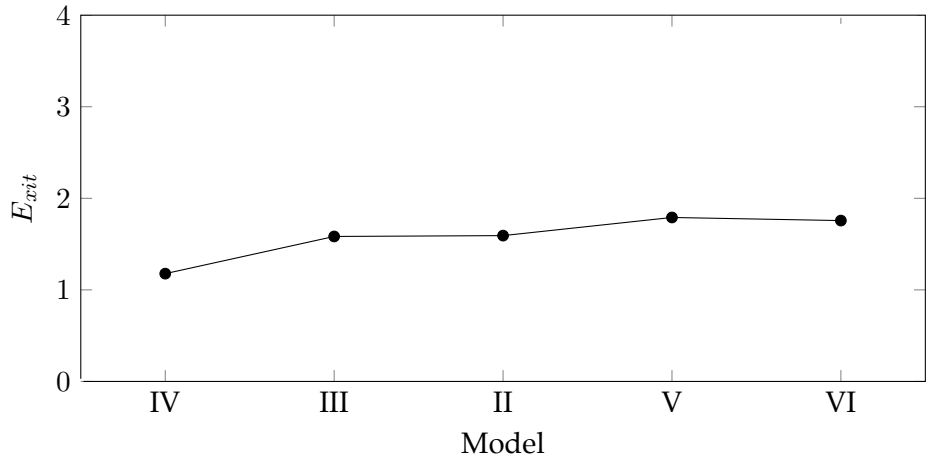
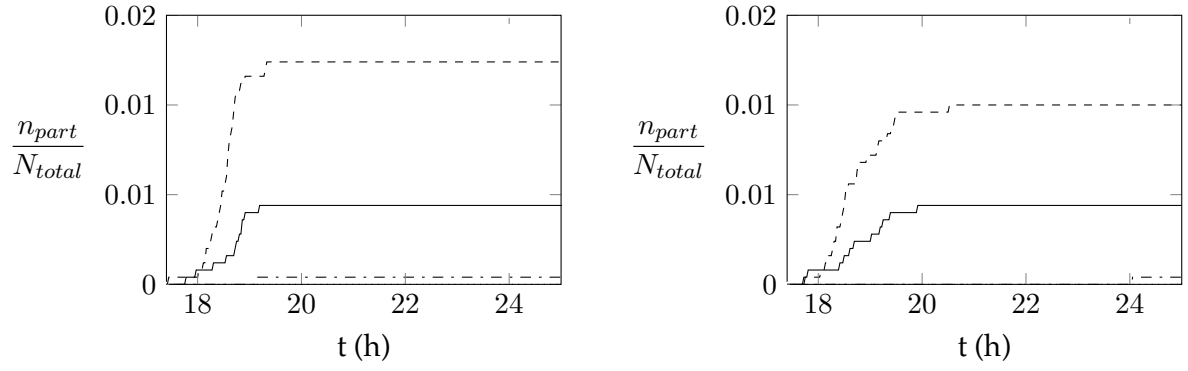


Figure 9.18: Mean location at which the particles exit the domain for different particle transport model, see equation 9.18. Models VII and VIII are not shown, because not enough particles exit the domain.

Figure 9.18 therefore shows that including the more information on the solid body dynamics, shifts the mean location at which the particles exit the domain towards the east, and therefore closer to the observations. What this implies is that including all of the relevant information on the solid body dynamics is necessary to have the particles mix properly within the channel, although this is still limited by the degree of accuracy of the channel flow. Furthermore the small difference between model V and model VI suggest that more research might be necessary on mechanical characteristics of an alga, particularly on the drag coefficient at low particle Reynolds number (see figure 9.2).

The final interesting criteria is to look a how fast the particles fill up the pumps. Figure 9.19 shows the cumulative number of particles entering the channel in time, for the two models that are made to resemble alga particles, as they are those that correspond the most to the observations.



(a) Model V

(b) Model VI

Figure 9.19: Cumulative number of particles entering each pumps for models considering different particles. "——" shows the number of particles entering pump 1, "- - -" shows the number of particles entering pump 2, "·····" shows the number of particles entering pump 3 (for both cases it is equal to zero) and "-·-" shows the number of particles entering pump 4.

The information figure 9.19 shows is that when an effort is made to have the transported particles resemble an algae the difference between the rate at which the pump 1 and pump 2 fill up is greater. This then leads to the hypothesis that if the point of release of the particles, the fluid velocities in the

channel were modified and the three-dimensional effects were taken into account so that the particles exited the domain in a way resembling the observations, algae particles would enter the channel in a tighter group than spheres with the same volumes, and therefore would be more likely to cause problems.

In conclusion the simulations around the Paluel power station show that the particle transport model developed in this thesis can be applied to environmental flows fairly easily. It also underlines the importance of an understanding of how much information is required from a simulation to adapt the particle transport model to the problematic. For example if for the problem of the Paluel power station the only information that was required was to understand under what conditions particles can get trapped west of the power station then using only the mean flows will be necessary. However if one is interested in seeing if particles can enter the pumps then some body dynamics would need to be applied, as well as a turbulence model. It might be necessary also to test different conditions of release o the particles. If the information required was to understand exactly how the particles enter the pumps, then a complete description of the solid dynamics, as well as modifications so that the body corresponds to an algae, will be necessary. However this will also require several other steps, such as a more complete calibration of the flow regime in the channel as well as research on how particles enter the recirculation zone. Furthermore three dimensional effects of the flow will need to be taken into account, and this will require other considerations on the particle transport model, such as how algae particles will be transported along the bed.

Table 9.2: The computational times of the different particle transport models on a HP Workstation Z600. The simulations are done for three tides, where the first tide is used to let the flow become established. Particles are then released after this first tide.

Model	Computational time	Percentage increase in time per particle (%)
No particles	17 h 50 m	-
Model VII	18 h 30 m	0.0015
Model VIII	18 h 30 m	0.0015
Model IV	18 h 30 m	0.0015
Model III	18 h 30 m	0.0015
Model II	18 h 30 m	0.0015
Model V	18 h 30 m	0.0015
Model VI	18 h 30 m	0.0015

Finally the different computational times for different particle transport models are shown in table 9.2. One can see in this table that the increase in computational time caused by releasing 2500 particles into the flow is rather small, around 4%, regardless of the particle transport model used.

Chapter 10

Conclusion

Le modèle développé dans ce mémoire a été testé sur trois cas tests. Premièrement un test simple a été fait dans lequel des corps sphériques ont été relâchés dans une turbulence stationnaire quasi-homogène. De ces expériences il peut être conclu qu'il est nécessaire d'avoir une bonne description des propriétés dynamiques des corps pour prédire les vitesses de ces corps dans ce régime turbulent. Dans un deuxième temps, des particules sphériques ont été relâchées dans un écoulement en canal partiellement obstrué. Il a ainsi été prouvé que le modèle arrive à prédire de façon satisfaisante la proportion de corps se trouvant capturée par la zone de recirculation située derrière une digue. Cependant pour ce type d'information il n'est pas nécessaire de modéliser la dynamique des corps solides avec une grande précision. Dans le dernier cas test des particules, ressemblant à des algues, ont été relâchées dans un écoulement réel aux alentours de la centrale de Paluel. Il a ainsi été trouvé qu'il n'est pas nécessaire de prendre en compte toutes les forces agissant sur le transport des corps pour obtenir un mode de transport qui semble proche de la réalité. Cependant, pour vérifier si des particules peuvent rentrer dans le canal d'amenée de la centrale il est nécessaire de prendre en compte une description complète des forces agissant sur les propriétés dynamiques des corps. Finalement la combinaison du modèle Eulérien de courant et du modèle Lagrangien de transport des corps n'arrive pas à prédire précisément quelles pompes de la centrale sont le plus touchées, et une étude plus approfondie serait nécessaire.

Le modèle développé permet ainsi de modéliser des particules proches des algues dans un écoulement côtier complexe. Il se différencie ainsi des modèles de transport de particules disponible dans la littérature par la possibilité de prendre en compte de larges écoulements naturels, le degré d'information sur la dynamique des corps et la taille et la forme des particules modélisées.

Cependant il reste encore quelques perspectives d'améliorations. Il semble surtout nécessaire d'approfondir le comportement des corps en trois dimensions, ainsi que le surcroit de décorrélation entre la vitesse moyenne des corps et du fluide liée aux effets inertiels des corps.

Néanmoins ce modèle de transport de particules peut-être utilisé pour prédire le transport d'algues en suivant les quelques conseils suivants. Premièrement il est important d'avoir une bonne prédiction des valeurs caractéristiques moyennes de l'écoulement. Ensuite il est important de savoir quel degré d'information l'utilisateur veut obtenir de la simulation, car il peut être possible d'ignorer certaines composantes des propriétés dynamique des corps. Il est aussi important d'utiliser un pas de temps suffisamment petit pour qu'une particule subisse toutes les variations moyennes de l'écoulement. Finalement l'utilisateur devrait comprendre quel type de corps doit être relâchés et comment prendre en compte chaque composante des forces caractérisant la dynamique des corps.

10.1 Conclusion on the validity of the model

This thesis aimed to develop a particle transport model that could be used in combination with a environmental flow model to predict the motion of algae particles along the coast line. In order to do so a three step stochastic model was developed, see equations 6.7. In the first step the turbulent fluid velocities at the location of the body are modelled using a Lagrangian model described in chapter 5, and extended in chapter 6. This model requires the mean fluid velocities, the turbulent kinetic energy and its dissipation rate at the location of the particle to be known, and therefore this requires a large Eulerian mean flow model to be applied. Because of the hypothesis on the size and concentration of bodies developed in chapter 2, the coupling between this large Eulerian mean flow model and the stochastic Lagrangian model needs only to be done from the Eulerian model to the Lagrangian model. Using these turbulent fluid velocities the transport of the solid particle can be calculated. Details on the forces required to predict the motion of a solid particle can be found in chapter 4, and a description of how to extend this model to algae particles can be found in section 9.1.

The resolution of the particles transport model, as defined by equations 6.7, can be difficult to solve explicitly as the equations governing the fluid and the solid body velocities are subjected to strong constraints on the numerical time step. A method is therefore proposed in chapter 6 to limit those constraints on the numerical time step.

This model was then applied to three test cases. Firstly it was applied to spherical particles released in quasi-isotropic turbulence generated by a pair of oscillating grids (see chapter 7). In this model the effects of different force components were tested, as well as the "Crossing Trajectories Effect". This effect represents the increased decorrelation between a solid particle's mean velocity and that of the mean surrounding fluid's velocity, due to the velocity differences (a solid particle will not remain inside a turbulent eddy during the whole duration of the eddy). Most of the decorrelation occurs from external forces, and a method was used to take into account those effects resulting from the gravitational forces. This experiment brought to light that a good description of the forces acting on the solid particles is necessary to predict the solid particle velocities. Furthermore it also showed that the "Crossing Trajectories Effect" resulting from the gravitational forces only have a little effect on the horizontal solid particle velocities.

The second test case, described in chapter 8, released particles in a non-homogeneous mean flow. This was done by releasing particles in a partially obstructed channel. The groyne, which was used to obstruct partially the flow, created a recirculation zone behind. The objective of this test case was therefore to test the coupling between the large Eulerian flow model and the stochastic Lagrangian solid particle transport model. The result show that this model is able to predict that particles will be trapped into the recirculation zone. The correspondence between the experimental and the numerical results on the proportion of particles entering a zone of interest, as well as the mean time of residence inside that zone are adequate, but not great. However it was difficult to obtain great experimental results as the groyne obstructing generated a lot vortices, distorting the recordings of particle trajectories. Furthermore it can be concluded from this experimental test case that considering all of the force components in the particle transport model might not be necessary to predict if particles will be trapped in a recirculation zone.

The final test case was for a real environmental flow (see chapter 9). The aim was to simulate the motion of algae around a nuclear power station. In order to do so a large Eulerian flow model was developed. This model included the effect of the bathymetry, the tide and waves. The simulations of particle transport in this problematic show that the particle transport model is fairly effective in predicting the entrapment of particles inside a recirculation zone. Furthermore the different particle transport models, considering different force components, particle shape and size have different visible effects on how particles enter the channel leading to the nuclear power station. From these results it can be concluded that in real flow simulations, it is important to include a good description of the body of interest. However these simulations then proved limited when trying to predict precisely which of the pumps used by the Paluel power station were most at risk, and it suggested to model

the flow in three dimensions, and recalibrate the flow regime inside the channel to improve those results.

10.2 Strong points of the model

The model was developed for a specific type of problem. Its aim was to provide tools to predict the transport of algae particles along the coastline. To do so the simulation of the transport of particles was separated into two different modelling steps. In the first stage of the simulations, the mean flow around the coastline of interest is found using a large Eulerian model. The model suggested is to use Telemac-2D, as it is an industrial code specifically designed for this purpose. It uses finite elements to solve the shallow water equations, and it can take into account the effect of the tides, and through the use of Tomawac the radiation stresses occurring from the wave breaking. Tomawac is a third generation model solving the equations governing the spectral wave action density, and it is distributed as part of the Telemac system. A large Eleurian model is used so that a solution to the general governing flow can be found fast, but while at the same time remaining descriptive enough to take into account all of the large scale effects that can impact the transport of algae particles. To link the large scale variations to the small scale variations that affect the transport of algae particle this Eulerian flow model is coupled to stochastic Lagrangian particle model. This is the second step of the simulations. Once the mean flow characteristics have been calculated using the large Eulerian flow model, the pertinent information is extracted and used to calculate the turbulent fluid velocities at the position of a solid body. These turbulent fluid velocities are then used to calculate the transport of particles by considering a wide range of physical characteristics on the shape and size of the particle and applying the relevant force components of the solid body dynamics.

This coupling between a large Eulerian flow model and a stochastic Lagrangian particle transport model is one of the strong points of this model. Through this coupling it can take into account large complex flows while at the same time considering enough information on the solid body dynamics, shape and size to have a realistic transport of such particles, and differentiate different type of solid particles. This differentiates the model to DNS particle transport models (for example: Uhlmann, 2008), which provide a complete description of the forces acting on a solid body in the flow, but cannot be applied to large scale particle transport model.

Furthermore the use of a large scale Eulerian flow model allows the deposition and reinsertion of solid particles on tidal flats to be taken into account, allowing a process specific to algae transport to be considered.

The detailed description of the solid body dynamics is a second strong point of this particle transport model as it can provides short term responses to flow variations. This could not be done in models designed specifically for the transport of algae particles in large coastal flows, such as the models described in Salomonsen *et al.* (1999) and Donaghay and Osborn (1997) which focused on the evolution of populations of algae particle over the course of several days or weeks.

Furthermore in this model an efficient method has been developed to take into account complex forces such as the Basset history force and the turbulence using a fixed time step. This allows a detailed description of the solid body dynamics to apply to a wide range of physical problems. This is particularly important as several particle transport model in environmental flows limit themselves to modelling particles as fluid particles experiencing turbulent diffusion through a simple turbulence model, for example Monti and Leuzzi (2010), Issa *et al.* (2009), Heemink (1990) or Stijnen *et al.* (2006).

In addition this model can be applied to large, non spherical (but still isotropic) particles. This is a strong point as the size of the particle filters the smaller scales of turbulence. Furthermore the constants used to model the solid body dynamics can be modified to apply to large spheres or algae (although the bodies still need to be considered isotropic), making the model easily adaptable to different bodies. Therefore through the hypothesis applied on the solid body dynamics to correspond to the specificities of the algae, this transport model differentiates itself from other models that include

a detailed description of the surrounding flow and the solid body dynamics. Example of such models can be found for aerosols models, such as those presented in Csanady (1963), Minier and Peirano (2001) or Sawford and Guest (1991), or for air bubbles transport model, for example see Yeo *et al.* (2010).

Finally the model developed in chapter 6 has been constructed in such a way that the degree of information on the solid body dynamics, size and shape is modulable. This means that simplifications can easily be made to the particle transport model, allowing simulations to be as efficient as possible for the problem considered.

10.3 Limitations and perspectives

Nonetheless the particle transport model developed in this thesis has a few limitations. The first limitation is linked to the two dimensional modelling. As the numerical test case of chapter 9 brought to light, some of the problems considered in environmental flows will require three dimensional effects to be considered. To adapt the problem to three dimensional effects is slightly more complex to solving for the flow using a three dimensional Eulerian model, and taking into account the gravitational effects in the particle transport problem, as described in chapter 9. Besides, some additional particle transport modelling characteristics will need to be analysed. For example no attempt has been made in this thesis to consider the bed load transport or the additional surface diffusion resulting from wave breaking.

The second limitation of the particle transport model developed in this thesis is its consideration of "Crossing Trajectories Effects". In this thesis the only method used to take into account the "Crossing Trajectories Effects" was using the method developed in Minier and Peirano (2001). This method only considered the increased decorrelation between the solid particle velocities and the fluid velocities that resulted from the mean velocity differences between the solid particles and the surrounding fluid created by external forces, such as the acceleration due to gravity. However mean velocity differences between a solid particle and the surrounding fluid can result also from the inertial properties of this solid body. Therefore some additional research is recommended on the impact of the inertial properties of solid bodies on the "Crossing Trajectories Effects". An improved modelling of the "Crossing Trajectories Effects" with the inertial properties of the solid bodies will probably only impact particles transported in regions were the mean fluid flow changes rapidly, as normally in environmental flows particles are transported over long distance, and it can be readily assumed that there will not be a large difference between the mean particle velocities and the mean fluid velocities.

The final limitation of particle transport model is linked to the precision of the fluid modelling around each specific particles. This model was developed to be used easily in combination with environmental flow Eulerian models. These models typically do not require a more refined turbulence model than the k-ε model, and the differences in turbulent velocities are not known over length scale equal to the size of the solid body. Because of this limitation particles have to be assumed to be irrotational and the Basset History force are calculated under the assumption that the solid bodies are small. This is reinforced by the fact that the turbulent fluid velocities at the position of a solid body are also limited by the stochastic fluid velocity model applied, refer to Pope (2000) for more information. Nonetheless this limitation will not affect greatly simulations in environmental flows, but it can explain some of the differences between the experimental and numerical results presented in chapter 7.

To summarize, the perspective for improvement of this solid particle transport model should focus on the three dimensional particle transport and on the inertial "Crossing trajectories Effect".

10.4 Advices to use the model

Before using the particle transport model developed in this thesis to particles transported in an environmental flow one should ensure that the Eulerian flow model provides the correct mean flow characteristics. For example in the simulations around the Paluel power station, had the radiation stresses not been taken into account, the recirculation zone west of the power station would not have been modelled, and the diffusion of solid particles would not have been modelled accurately. Furthermore these simulations point out the limitations of the flow model in the channel before pumps and it suggest that this model should be modified to consider three dimensional effects and possibly a recalibration of the fluid velocities.

Secondly the user of the code should know how much information they want from the simulations. It is not always necessary to go as deep as the Basset History force, when considering solid body dynamics. For example in the partially obstructed channel experiment, described in chapter 8, the only information that was required was if particles could get trapped in the recirculation zone, and it has been shown that a particle transport model that only went as far as the drag forces gave similar results to a model that considered all the force components up to the Basset History force.

Thirdly the time step should be chosen with care. Even though the exact integrator method developed in chapter 6 to solve for the particle transport model is subject to weak constraints on the numerical time step, the displacement of a solid particle during one time step should be small enough that a particle can see all of the fluid variations. This is why it is recommended to set the time step of the numerical solid particle transport model using CFL conditions.

Finally the solid body dynamics, size and shape considered should be understood. The trickiest force component of the solid body dynamics model is the Basset history force. This force is found in the model developed in this thesis by summing an integrand over a certain time interval. This time interval is divided into a number of sub steps. It is recommended that those sub steps are set to the same value as the numerical stochastic time step, and that the time interval over which the integrand is summed is about a hundred stochastic time steps long. Furthermore this model gives very different values according to the physical characteristics of the body, such as the size and density. In addition the modifications that can be done to apply the model to algae has been set to correspond to a certain type of algae (see chapter 9), and should not be used by default.

Appendix A

Calculations relative to the exact integrator model

Où les étapes de calculs nécessaires pour développer l'intégrateur exact du modèle stochastique (chapitre 6) sont présentées.

A.1 The three steps solid particle transport model

From all the considerations presented in chapters 4, 5 and 6 a three step particle transport model was developed:

$$dU_i^{(s)} = -\frac{1}{T_i^{(s)}} U_i^{(s)} dt + C_i^{(s)} dt + B_i^{(s)} dW_i \tag{A.1a}$$

$$dV_i = F_a dU_i^{(s)} + \frac{1}{\tau_{part}} \left(U_i^{(s)} - V_i \right) dt + F_{i,c} dt \tag{A.1b}$$

$$dX_i = V_i dt \tag{A.1c}$$

This model is subject to strong constraints on the time step dt because of $T_i^{(s)}$ and τ_{part}. Therefore a method is needed to solve these equations. As for an explicit resolution of these equations it is assumed that all the coefficients can be considered constant over the time interval $dt = t - t_0$. Therefore if F_a, τ_{part}, $F_{i,c}$, $T_i^{(s)}$, $C_i^{(s)}$ and $B_i^{(s)}$ are constant then there exists an analytical solution for the motion of solid isotropic bodies

A.2 Analytical solution for the fluid velocities

Since all the coefficient of the governing equation A.1a are fixed then there should exist a solution for the fluid velocity seen by the solid body $U_i^{(s)}$ with the form:

$$U_i^{(s)}(t) = H_i(t) \exp\left(-\frac{t}{T_i^{(s)}} \right) \tag{A.2}$$

This then gives:

$$\begin{aligned} dU_i^{(s)}(t) &= -\frac{1}{T_i^{(s)}} H_i(t) \exp\left(-\frac{t}{T_i^{(s)}} \right) dt + dH_i(t) \exp\left(-\frac{t}{T_i^{(s)}} \right) \\ &= -\frac{1}{T_i^{(s)}} U_i^{(s)} dt + dH_i(t) \exp\left(-\frac{t}{T_i^{(s)}} \right) \end{aligned} \tag{A.3}$$

And therefore:

$$dH_i(t) = \exp\left(\frac{t}{T_i^{(s)}} \right) \left[C_i^{(s)} dt + B_i^{(s)} dW_i(t) \right] \tag{A.4}$$

A solution for H_i can then be calculated by integrating over the interval $dt = t - t_0$.

$$\begin{aligned} \int_{t_0}^{t} dH_i(s) &= \int_{t_0}^{t} C_i^{(s)} \exp\left(\frac{s}{T_i^{(s)}} \right) ds + \int_{t_0}^{t} B_i^{(s)} \exp\left(\frac{s}{T_i^{(s)}} \right) dW_i(s) \\ [H_i(s)]_{t_0}^{t} &= C_i^{(s)} T_i^{(s)} \left[\exp\left(\frac{s}{T_i^{(s)}} \right) \right]_{t_0}^{t} + \int_{t_0}^{t} B_i^{(s)} \exp\left(\frac{s}{T_i^{(s)}} \right) dW_i(s) \\ H_i(t) - H_i(t_0) &= C_i^{(s)} T_i^{(s)} \left[\exp\left(\frac{t}{T_i^{(s)}} \right) - \exp\left(\frac{t_0}{T_i^{(s)}} \right) \right] + \int_{t_0}^{t} B_i^{(s)} \exp\left(\frac{s}{T_i^{(s)}} \right) dW_i(s) \end{aligned} \tag{A.5}$$

Using equation A.2, a solution for $H_i(t_0)$ can be calculated:

$$H_i(t_0) = U_i^{(s)}(t_0) \exp\left(\frac{t_0}{T_i^{(s)}}\right) \tag{A.6}$$

Therefore equations A.5 and A.6 can be used to solve equation A.2:

$$\begin{aligned} U_i^{(s)}(t) =& \left\{ U_i^{(s)}(t_0) \exp\left(\frac{t_0}{T_i^{(s)}}\right) + C_i^{(s)} T_i^{(s)} \left[\exp\left(\frac{t}{T_i^{(s)}}\right) - \exp\left(\frac{t_0}{T_i^{(s)}}\right) \right] \right. \\ & \left. + \int_{t_0}^{t} B_i^{(s)} \exp\left(\frac{s}{T_i^{(s)}}\right) dW_i(s) \right\} \exp\left(-\frac{t}{T_i^{(s)}}\right) \\ =& U_i^{(s)}(t_0) \exp\left(-\frac{dt}{T_i^{(s)}}\right) + C_i^{(s)} T_i^{(s)} \left[1 - \exp\left(-\frac{dt}{T_i^{(s)}}\right) \right] + \gamma_i(t) \end{aligned} \tag{A.7}$$

Or, if we define:

$$\alpha_i = \exp\left(-\frac{dt}{T_i^{(s)}}\right) \tag{A.8}$$

Then:

$$U_i^{(s)}(t) = \alpha_i U_i^{(s)}(t_0) + (1 - \alpha_i)\, C_i^{(s)} T_i^{(s)} + \gamma_i(t) \tag{A.9}$$

Where the stochastic integral γ_i is:

$$\gamma_i(t) = B_i^{(s)} \exp\left(-\frac{t}{T_i^{(s)}}\right) \int_{t_0}^{t} \exp\left(\frac{s}{T_i^{(s)}}\right) dW_i(s) \tag{A.10}$$

A.3 Analytical solution for the solid particle velocities

If equation A.1a is used in place of $dU_i^{(s)}(t)$ in equation A.1b then:

$$dV_i(t) = F_a \left[-\frac{1}{T_i^{(s)}} U_i^{(s)} dt + C_i^{(s)} dt + B_i^{(s)} dW_i(t) \right] + \frac{1}{\tau_{part}} \left(U_i^{(s)}(t) - V_i(t) \right) dt + F_{i,c} dt \tag{A.11}$$

Then, as in for fluid velocities, a solution should exist under the following form:

$$V_i(t) = H_i(t) \exp\left(-\frac{t}{\tau_{part}}\right) \tag{A.12}$$

Therefore, the differential of V_i is given by:

$$\begin{aligned} dV_i(t) =& -\frac{1}{\tau_{part}} H_i(t) \exp\left(-\frac{t}{\tau_{part}}\right) dt + dH_i(t) \exp\left(-\frac{t}{\tau_{part}}\right) \\ =& -\frac{1}{\tau_{part}} V_i(t) dt + dH_i(t) \exp\left(-\frac{t}{\tau_{part}}\right) \end{aligned} \tag{A.13}$$

Which gives the following expression for $dH_i(t)$:

$$\begin{aligned} dH_i(t) \exp\left(-\frac{t}{\tau_{part}}\right) =& F_a \left[-\frac{1}{T_i^{(s)}} U_i^{(s)} dt + C_i^{(s)} dt + B_i^{(s)} dW_i(t)\right] + \frac{1}{\tau_{part}} U_i^{(s)}(t) dt + F_{i,c} dt \\ =& \left(\frac{1}{\tau_{part}} - \frac{F_a}{T_i^{(s)}}\right) U_i^{(s)}(t_0) \exp\left(-\frac{dt}{T_i^{(s)}}\right) dt + \left(\frac{1}{\tau_{part}} - \frac{F_a}{T_i^{(s)}}\right) C_i T_i dt \\ & - \left(\frac{1}{\tau_{part}} - \frac{F_a}{T_i^{(s)}}\right) C_i^{(s)} T_i^{(s)} \exp\left(-\frac{dt}{T_i^{(s)}}\right) dt + \left(F_a C_i^{(s)} + F_{i,c}\right) dt \\ & + \left(\frac{1}{\tau_{part}} - \frac{F_a}{T_i^{(s)}}\right) \gamma_i dt + F_a B_i^{(s)} dW_i(t) \end{aligned} \tag{A.14}$$

The following notations can be used:

$$\check{C} = \frac{1}{\tau_{part}} - \frac{F_a}{T_i^{(s)}} = \frac{T_i^{(s)} - F_a \tau_{part}}{T_i^{(s)} \tau_{part}} \tag{A.15}$$

$$K_i = \frac{1}{\tau_{part}} - \frac{1}{T_i^{(s)}} = \frac{T_i^{(s)} - \tau_{part}}{T_i^{(s)} \tau_{part}} \tag{A.16}$$

dH_i can therefore be written as (recall that $dt = t - t_0$):

$$\begin{aligned} dH_i(t) =& \left(\check{C} U_i^{(s)}(t_0) - \check{C} C_i^{(s)} T_i^{(s)}\right) \exp\left(K_i t + \frac{t_0}{T_i^{(s)}}\right) dt \\ & + \left(\check{C} C_i^{(s)} T_i^{(s)} + F_a C_i^{(s)} + F_{i,c}\right) \exp\left(\frac{t}{\tau_{part}}\right) dt \\ & + \check{C} \gamma_i \exp\left(\frac{t}{\tau_{part}}\right) dt + F_a B_i^{(s)} \exp\left(\frac{t}{\tau_{part}}\right) dW_i(t) \end{aligned} \tag{A.17}$$

A solution can therefore be calculated by integrating on the interval $dt = t - t_0$:

$$\begin{aligned} \int_{t_0}^{t} dH_i(s) =& \left(\check{C} U_i^{(s)}(t_0) - \check{C} C_i^{(s)} T_i^{(s)}\right) \int_{t_0}^{t} \exp\left(K_i s + \frac{t_0}{T_i^{(s)}}\right) ds \\ & + \left(\check{C} C_i^{(s)} T_i^{(s)} + F_a C_i^{(s)} + F_{i,c}\right) \int_{t_0}^{t} \exp\left(\frac{s}{\tau_{part}}\right) ds \\ & + \check{C} \int_{t_0}^{t} \gamma_i \exp\left(\frac{s}{\tau_{part}}\right) ds + F_a B_i^{(s)} \int_{t_0}^{t} \exp\left(\frac{s}{\tau_{part}}\right) dW_i(s) \end{aligned} \tag{A.18}$$

Therefore:

$$
\begin{aligned}
\left[H_i(s)\right]_{t_0}^{t} = &\left(\check{C}U_i^{(s)}(t_0) - \check{C}C_i^{(s)}T_i^{(s)}\right)\left[\frac{1}{K_i}\exp\left(K_i s + \frac{t_0}{T_i^{(s)}}\right)\right]_{t_0}^{t} \\
&+ \left(\check{C}C_i^{(s)}T_i^{(s)} + F_a C_i^{(s)} + F_{i,c}\right)\left[\tau_{part}\exp\left(\frac{s}{\tau_{part}}\right)\right]_{t_0}^{t} \\
&+ \check{C}\int_{t_0}^{t}\gamma_i\exp\left(\frac{s}{\tau_{part}}\right)ds + F_a B_i^{(s)}\int_{t_0}^{t}\exp\left(\frac{s}{\tau_{part}}\right)dW_i(s)
\end{aligned} \tag{A.19}
$$

Using the definition of $V_i(t)$ given previously (equation A.12) it is possible to conclude that $H_i(t_0) = V_i(t_0)\exp\left(t_0/\tau_{part}\right)$, and therefore:

$$
\begin{aligned}
H_i(t) = &V_i(t_0)\exp\left(\frac{t_0}{\tau_{part}}\right) \\
&+ \frac{1}{K_i}\left(\check{C}U_i^{(s)}(t_0) - \check{C}C_i^{(s)}T_i^{(s)}\right)\left[\exp\left(\frac{t}{\tau_{part}} - \frac{t}{T_i^{(s)}} + \frac{t_0}{T_i^{(s)}}\right) - \exp\left(\frac{t_0}{\tau_{part}} - \frac{t_0}{T_i^{(s)}} + \frac{t_0}{T_i^{(s)}}\right)\right] \\
&+ \tau_{part}\left(\check{C}C_i^{(s)}T_i^{(s)} + F_a C_i^{(s)} + F_{i,c}\right)\left[\exp\left(\frac{t}{\tau_{part}}\right) - \exp\left(\frac{t_0}{\tau_{part}}\right)\right] \\
&+ \check{C}\int_{t_0}^{t}\gamma_i\exp\left(\frac{s}{\tau_{part}}\right)ds + F_a B_i^{(s)}\int_{t_0}^{t}\exp\left(\frac{s}{\tau_{part}}\right)dW_i(s)
\end{aligned} \tag{A.20}
$$

If this definition of $H_i(t)$ is used in equation A.12, and after rearrangements:

$$
\begin{aligned}
V_i(t) = &V_i(t_0)\exp\left(-\frac{dt}{\tau_{part}}\right) + \frac{1}{K_i}\left(\check{C}U_i^{(s)}(t_0) - \check{C}C_i^{(s)}T_i^{(s)}\right)\left[\exp\left(-\frac{dt}{T_i^{(s)}}\right) - \exp\left(-\frac{dt}{\tau_{part}}\right)\right] \\
&+ \tau_{part}\left(\check{C}C_i^{(s)}T_i^{(s)} + F_a C_i^{(s)} + F_{i,c}\right)\left[1 - \exp\left(-\frac{dt}{\tau_{part}}\right)\right] \\
&+ \check{C}\exp\left(-\frac{t}{\tau_{part}}\right)\int_{t_0}^{t}\gamma_i\exp\left(\frac{s}{\tau_{part}}\right)ds \\
&+ F_a B_i^{(s)}\exp\left(-\frac{t}{\tau_{part}}\right)\int_{t_0}^{t}\exp\left(\frac{s}{\tau_{part}}\right)dW_i(s)
\end{aligned} \tag{A.21}
$$

If we define:

$$
\beta = \exp\left(-\frac{dt}{\tau_{part}}\right) \tag{A.22}
$$

Then the exact integrator for the solid particle velocities, with α_i defined in equation A.8, is:

$$
\begin{aligned}
V_i(t) = &\beta V_i(t_0) + (1-\beta)\left(C_i^{(s)}T_i^{(s)} + F_{i,c}\tau_{part}\right) \\
&+ (\alpha_i - \beta)\check{C}_i\left(U_i^{(s)}(t_0) - C_i^{(s)}T_i^{(s)}\right) \\
&+ \Gamma_i
\end{aligned} \tag{A.23}
$$

With:

$$\begin{aligned}\check{C}_i =& \frac{\check{C}}{K_i} \\ =& \frac{T_i^{(s)} - F_a\tau_{part}}{T_i^{(s)} - \tau_{part}}\end{aligned} \tag{A.24}$$

However it should be noted that $\check{C}_i$ (and therefore $V_i(t)$) is undefined if $T_i^{(s)} = \tau_{part}$, but these values have no reason to be equal. Nonetheless in computer programming a limiter should be applied (eg: $\min(T_i^{(s)} - \tau_{part}, 10^{-6})$) just in case.

The stochastic integral Γ_i defined by:

$$\Gamma_i = \check{C}\exp\left(-\frac{t}{\tau_{part}}\right)\int_{t_0}^{t}\gamma_i\exp\left(\frac{s}{\tau_{part}}\right)ds + F_aB_i^{(s)}\exp\left(-\frac{t}{\tau_{part}}\right)\int_{t_0}^{t}\exp\left(\frac{s}{\tau_{part}}\right)dW_i(s) \tag{A.25}$$

Inserting the definition for γ_i in Γ_i, the stochastic integral of V_i becomes:

$$\begin{aligned}\Gamma_i =& \check{C}\exp\left(-\frac{t}{\tau_{part}}\right)\int_{t_0}^{t}B_i^{(s)}\exp\left(-\frac{s}{T_i^{(s)}}\right)\int_{t_0}^{t}\exp\left(\frac{s}{T_i^{(s)}}\right)dW_i(s)\exp\left(\frac{s}{\tau_{part}}\right)ds \\ &+ F_aB_i^{(s)}\exp\left(-\frac{t}{\tau_{part}}\right)\int_{t_0}^{t}\exp\left(\frac{s}{\tau_{part}}\right)dW_i(s)\end{aligned} \tag{A.26}$$

Using integration by parts Γ_i can be rewritten as:

$$\begin{aligned}\Gamma_i =& B_i^{(s)}\check{C}_i\exp\left(-\frac{t}{T_i^{(s)}}\right)\int_{t_0}^{t}\exp\left(\frac{s}{T_i^{(s)}}\right)dW_i(s) \\ &+ B_i^{(s)}\left(F_a - \check{C}_i\right)\exp\left(-\frac{t}{\tau_{part}}\right)\int_{t_0}^{t}\exp\left(\frac{s}{\tau_{part}}\right)dW_i(s) \\ =& \check{C}_i\gamma_i\left(t\right) + B_i^{(s)}\left(F_a - \check{C}_i\right)\exp\left(-\frac{t}{\tau_{part}}\right)\int_{t_0}^{t}\exp\left(\frac{s}{\tau_{part}}\right)dW_i(s)\end{aligned} \tag{A.27}$$

A.4 Analytical solution for the position of the body

Using the definition for the displacement of the bodies given by equation A.1c, a solution can be found by integrating $dX_i(t)$ over the interval $dt = t - t_0$:

$$\begin{aligned}X_i(t) - X_i(t_0) =& V_i(t_0)\int_{t_0}^{t}\exp\left(-\frac{ds}{\tau_{part}}\right)ds \\ &+ \left(C_i^{(s)}T_i^{(s)} + F_{i,c}\tau_{part}\right)\left[\int_{t_0}^{t}ds - \int_{t_0}^{t}\exp\left(-\frac{ds}{\tau_{part}}\right)ds\right] \\ &+ \check{C}_i\left(U_i^{(s)}(t_0) - C_i^{(s)}T_i^{(s)}\right)\left[\int_{t_0}^{t}\exp\left(-\frac{ds}{T_i^{(s)}}\right)ds - \int_{t_0}^{t}\exp\left(-\frac{ds}{\tau_{part}}\right)ds\right] \\ &+ \int_{t_0}^{t}\Gamma_i ds\end{aligned} \tag{A.28}$$

Using the following integral:

$$\begin{aligned}\int_{t_0}^{t}\exp\left(-\frac{ds}{Const.}\right)ds=&\int_{t_0}^{t}\exp\left(-\frac{s}{Const.}\right)\exp\left(\frac{t_0}{Const.}\right)ds\\ =&Const.\left[1-\exp\left(-\frac{dt}{Const.}\right)\right]\end{aligned}\tag{A.29}$$

The solution to $X_i(t)$ can be found by:

$$\begin{aligned}X_i(t)=&X_i(t_0)+V_i(t_0)\tau_{part}\left[1-\exp\left(-\frac{dt}{\tau_{part}}\right)\right]\\&+\left(C_i^{(s)}T_i^{(s)}+F_{i,c}\tau_{part}\right)\left\{dt-\tau_{part}\left[1-\exp\left(-\frac{dt}{\tau_{part}}\right)\right]\right\}\\&+\check{C}_i\left(U_i^{(s)}(t_0)-C_i^{(s)}T_i^{(s)}\right)\left\{T_i^{(s)}\left[1-\exp\left(-\frac{dt}{T_i^{(s)}}\right)\right]-\tau_{part}\left[1-\exp\left(-\frac{dt}{\tau_{part}}\right)\right]\right\}\\&+\Phi_i\end{aligned}\tag{A.30}$$

Or using the α_i and β notation:

$$\begin{aligned}X_i(t)=&X_i(t_0)+(1-\beta)\,\tau_{part}V_i(t_0)+\left[dt-(1-\beta)\,\tau_{part}\right]\left(C_i^{(s)}T_i^{(s)}+F_{i,c}\tau_{part}\right)\\&+\check{C}_i\left(U_i^{(s)}(t_0)-C_i^{(s)}T_i^{(s)}\right)\left[(1-\alpha_i)\,T_i^{(s)}-(1-\beta)\,\tau_{part}\right]\\&+\Phi_i\end{aligned}\tag{A.31}$$

Where Φ_i is a stochastic integral defined by:

$$\begin{aligned}\Phi_i=&\int_{t_0}^{t}\Gamma_i ds\\=&\int_{t_0}^{t}B_i^{(s)}\check{C}_i\exp\left(-\frac{s}{T_i^{(s)}}\right)\int_{t_0}^{t}\exp\left(\frac{s}{T_i^{(s)}}\right)dW_i(s)ds\\&+\int_{t_0}^{t}B_i^{(s)}\left(F_a-\check{C}_i\right)\exp\left(-\frac{s}{\tau_{part}}\right)\int_{t_0}^{t}\exp\left(\frac{s}{\tau_{part}}\right)dW_i(s)ds\end{aligned}\tag{A.32}$$

Integration by parts can again be used to rearrange this integral:

$$\begin{aligned}\Phi_i=&\left(B_i^{(s)}T_i^{(s)}\check{C}_i+F_aB_i^{(s)}\tau_{part}-B_i^{(s)}\check{C}_i\tau_{part}\right)\int_{t_0}^{t}dW_i(s)\\&-B_i^{(s)}\check{C}_iT_i^{(s)}\exp\left(-\frac{t}{T_i^{(s)}}\right)\int_{t_0}^{t}\exp\left(\frac{s}{T_i^{(s)}}\right)dW_i(s)\\&-B_i^{(s)}\left(F_a-\check{C}_i\right)\tau_{part}\exp\left(-\frac{t}{\tau_{part}}\right)\int_{t_0}^{t}\exp\left(\frac{s}{\tau_{part}}\right)dW_i(s)\\=&-\check{C}_iT_i^{(s)}\gamma_i\left(t\right)-\tau_{part}\left[\Gamma_i-\check{C}_i\gamma_i\left(t\right)\right]\\&+B_i^{(s)}\left[\left(T_i^{(s)}-\tau_{part}\right)\check{C}_i+F_a\tau_{part}\right]\int_{t_0}^{t}dW_i(s)\end{aligned}\tag{A.33}$$

A.5 Solving the stochastic integrals

The are therefore three stochastic integrals:

$$\gamma_i(t) = B_i^{(s)} \exp\left(-\frac{t}{T_i^{(s)}}\right) \int_{t_0}^{t} \exp\left(\frac{s}{T_i^{(s)}}\right) dW_i(s) \tag{A.34a}$$

$$\begin{aligned}\Gamma_i(t) =& B_i^{(s)} \check{C}_i \exp\left(-\frac{t}{T_i^{(s)}}\right) \int_{t_0}^{t} \exp\left(\frac{s}{T_i^{(s)}}\right) dW_i(s) \\ &+ B_i^{(s)} \left(F_a - \check{C}_i\right) \exp\left(-\frac{t}{\tau_{part}}\right) \int_{t_0}^{t} \exp\left(\frac{s}{\tau_{part}}\right) dW_i(s)\end{aligned} \tag{A.34b}$$

$$\begin{aligned}\Phi_i(t) =& B_i^{(s)} \left[\left(T_i^{(s)} - \tau_{part}\right) \check{C}_i + F_a \tau_{part}\right] \int_{t_0}^{t} dW_i(s) \\ &- B_i^{(s)} \check{C}_i T_i^{(s)} \exp\left(-\frac{t}{T_i^{(s)}}\right) \int_{t_0}^{t} \exp\left(\frac{s}{T_i^{(s)}}\right) dW_i(s) \\ &- B_i^{(s)} \left(F_a - \check{C}_i\right) \tau_{part} \exp\left(-\frac{t}{\tau_{part}}\right) \int_{t_0}^{t} \exp\left(\frac{s}{\tau_{part}}\right) dW_i(s)\end{aligned} \tag{A.34c}$$

Each integral can be modelled as a dependent centred Gaussian integral (Peirano *et al.*, 2006). This property allows the implies the following definition:

$$\begin{pmatrix} \gamma_i \\ \Gamma_i \\ \Phi_i \end{pmatrix} = \mathbf{L} \begin{pmatrix} \xi_{\gamma_i} \\ \xi_{\Gamma_i} \\ \xi_{\Phi_i} \end{pmatrix} \tag{A.35}$$

Where each ξ_i corresponds to an independent random variable with 0 mean and a standard deviation equal to 1. The matrix $\mathbf{L}$ is defined by:

$$\mathbf{L}\mathbf{L}^{\mathbf{T}} = \mathbf{\Sigma} \tag{A.36}$$

Where $\mathbf{\Sigma}$ is the covariance matrix defined as:

$$\Sigma_{ij} = \text{cov}\left(\varkappa_i, \varkappa_j\right) \tag{A.37}$$

Therefore $\mathbf{L}\mathbf{L}^{\mathbf{T}}$ is equal to:

$$\begin{aligned}\begin{pmatrix} L_{11} & 0 & 0 \\ L_{21} & L_{22} & 0 \\ L_{31} & L_{32} & L_{33} \end{pmatrix} \begin{pmatrix} L_{11} & L_{21} & L_{31} \\ 0 & L_{22} & L_{32} \\ 0 & 0 & L_{33} \end{pmatrix} &= \begin{pmatrix} \text{cov}\left(\gamma_i, \gamma_i\right) & \text{cov}\left(\gamma_i, \Gamma_i\right) & \text{cov}\left(\gamma_i, \Phi_i\right) \\ \text{cov}\left(\Gamma_i, \gamma_i\right) & \text{cov}\left(\Gamma_i, \Gamma_i\right) & \text{cov}\left(\Gamma_i, \Phi_i\right) \\ \text{cov}\left(\Phi_i, \gamma_i\right) & \text{cov}\left(\Phi_i, \Gamma_i\right) & \text{cov}\left(\Phi_i, \Phi_i\right) \end{pmatrix} \\ &\equiv \begin{pmatrix} \langle\gamma_i\gamma_i\rangle - \langle\gamma_i\rangle\langle\gamma_i\rangle & \langle\gamma_i\Gamma_i\rangle - \langle\gamma_i\rangle\langle\Gamma_i\rangle & \langle\gamma_i\Phi_i\rangle - \langle\gamma_i\rangle\langle\Phi_i\rangle \\ \langle\Gamma_i\gamma_i\rangle - \langle\Gamma_i\rangle\langle\gamma_i\rangle & \langle\Gamma_i\Gamma_i\rangle - \langle\Gamma_i\rangle\langle\Gamma_i\rangle & \langle\Gamma_i\Phi_i\rangle - \langle\Gamma_i\rangle\langle\Phi_i\rangle \\ \langle\Phi_i\gamma_i\rangle - \langle\Phi_i\rangle\langle\gamma_i\rangle & \langle\Phi_i\Gamma_i\rangle - \langle\Phi_i\rangle\langle\Gamma_i\rangle & \langle\Phi_i\Phi_i\rangle - \langle\Phi_i\rangle\langle\Phi_i\rangle \end{pmatrix} \\ &= \begin{pmatrix} \langle\gamma_i^2\rangle & \langle\gamma_i\Gamma_i\rangle & \langle\gamma_i\Phi_i\rangle \\ \langle\gamma_i\Gamma_i\rangle & \langle\Gamma_i^2\rangle & \langle\Gamma_i\Phi_i\rangle \\ \langle\gamma_i\Phi_i\rangle & \langle\Gamma_i\Phi_i\rangle & \langle\Phi_i^2\rangle \end{pmatrix}\end{aligned} \tag{A.38}$$

And so each coefficient of the matrix **L** is defined as:

$$L_{11}^2 = \langle \gamma_i^2 \rangle \quad \Rightarrow \quad L_{11} = \sqrt{\langle \gamma_i^2 \rangle} \tag{A.39a}$$

$$L_{11}L_{21} = \langle \Gamma_i \gamma_i \rangle \quad \Rightarrow \quad L_{21} = \frac{\langle \gamma_i \Gamma_i \rangle}{L_{11}} \tag{A.39b}$$

$$L_{11}L_{31} = \langle \gamma_i \Phi_i \rangle \quad \Rightarrow \quad L_{31} = \frac{\langle \gamma_i \Phi_i \rangle}{L_{11}} \tag{A.39c}$$

$$L_{21}^2 + L_{22}^2 = \langle \Gamma_i^2 \rangle \quad \Rightarrow \quad L_{22} = \sqrt{\langle \Gamma_i^2 \rangle - L_{21}^2} \tag{A.39d}$$

$$L_{21}L_{31} + L_{22}L_{32} = \langle \Gamma_i \Phi_i \rangle \quad \Rightarrow \quad L_{32} = \frac{\langle \Gamma_i \Phi_i \rangle - L_{21}L_{31}}{L_{22}} \tag{A.39e}$$

$$L_{31}^2 + L_{32}^2 + L_{33}^2 = \langle \Phi_i^2 \rangle \quad \Rightarrow \quad L_{33} = \sqrt{\langle \Phi_i^2 \rangle - L_{31}^2 - L_{32}^2} \tag{A.39f}$$

The covariance are the defined by the following equations (using Ito integrals):

$$\begin{aligned}
\langle \gamma_i^2 \rangle =& \left\langle B_i^{(s)} \exp\left(-\frac{t}{T_i^{(s)}}\right) \int_{t_0}^{t} \exp\left(\frac{s}{T_i^{(s)}}\right) dW_i(s) B_i^{(s)} \exp\left(-\frac{t}{T_i^{(s)}}\right) \int_{t_0}^{t} \exp\left(\frac{s}{T_i^{(s)}}\right) dW_i(s) \right\rangle \\
=& B_i^{(s)\,2} \exp\left(-\frac{2t}{T_i^{(s)}}\right) \int_{t_0}^{t} \exp\left(\frac{2s}{T_i^{(s)}}\right) ds \\
=& B_i^{(s)\,2} \exp\left(-\frac{2t}{T_i^{(s)}}\right) \frac{T_i^{(s)}}{2} \left[\exp\left(\frac{2s}{T_i^{(s)}}\right)\right]_{t_0}^{t} \\
=& \frac{B_i^{(s)\,2} T_i^{(s)}}{2} \left[\exp\left(\frac{2t}{T_i^{(s)}} - \frac{2t}{T_i^{(s)}}\right) - \exp\left(\frac{2t_0}{T_i^{(s)}} - \frac{2t}{T_i^{(s)}}\right)\right] \\
=& \frac{B_i^{(s)\,2} T_i^{(s)}}{2} \left[1 - \exp\left(-\frac{2dt}{T_i^{(s)}}\right)\right] \\
=& \left(1 - \alpha_i^2\right) B_i^{(s)\,2} \frac{T_i^{(s)}}{2}
\end{aligned} \tag{A.40}$$

From this the following rule can be defined for Ito stochastic integrals:

$$\begin{aligned}
\exp\left(-\frac{2t}{Const.}\right) & \left\langle \int_{t_0}^{t} \exp\left(\frac{s}{Const.}\right) dW_i(s) \int_{t_0}^{t} \exp\left(\frac{s}{Const.}\right) dW_i(s) \right\rangle \\
&= \exp\left(-\frac{2t}{Const.}\right) \int_{t_0}^{t} \exp\left(\frac{2s}{Const.}\right) ds \\
&= \exp\left(-\frac{2t}{Const.}\right) \frac{Const.}{2} \left[\exp\left(\frac{2s}{Const.}\right)\right]_{t_0}^{t} \\
&= \exp\left(-\frac{2t}{Const.}\right) \frac{Const.}{2} \left[\exp\left(\frac{2t}{Const.}\right) - \exp\left(\frac{2t_0}{Const.}\right)\right] \\
&= \frac{Const.}{2} \left[\exp\left(\frac{2t}{Const.} - \frac{2t}{Const.}\right) - \exp\left(\frac{2t_0}{Const.} - \frac{2t}{Const.}\right)\right] \\
&= \frac{Const.}{2} \left[1 - \exp\left(-\frac{2dt}{Const.}\right)\right]
\end{aligned} \tag{A.41}$$

For the following quantities the intermediates calculations relating to equation A.41 will not be given:

$$\begin{aligned}\left\langle \Gamma_i^2 \right\rangle =& \left\langle \left[B_i^{(s)} \check{C}_i \exp\left(-\frac{t}{T_i^{(s)}}\right) \int_{t_0}^{t} \exp\left(\frac{s}{T_i^{(s)}}\right) dW_i(s) \right.\right. \\ & \left. + B_i^{(s)} \left(F_a - \check{C}_i\right) \exp\left(-\frac{t}{\tau_{part}}\right) \int_{t_0}^{t} \exp\left(\frac{s}{\tau_{part}}\right) dW_i(s) \right] \\ & \left[B_i^{(s)} \check{C}_i \exp\left(-\frac{t}{T_i^{(s)}}\right) \int_{t_0}^{t} \exp\left(\frac{s}{T_i^{(s)}}\right) dW_i(s) \right. \\ & \left.\left. + B_i^{(s)} \left(F_a - \check{C}_i\right) \exp\left(-\frac{t}{\tau_{part}}\right) \int_{t_0}^{t} \exp\left(\frac{s}{\tau_{part}}\right) dW_i(s) \right] \right\rangle \\ =& \left(B_i^{(s)} \check{C}_i\right)^2 \exp\left(-\frac{2t}{T_i^{(s)}}\right) \left\langle \int_{t_0}^{t} \exp\left(\frac{s}{T_i^{(s)}}\right) dW_i(s) \int_{t_0}^{t} \exp\left(\frac{s}{T_i^{(s)}}\right) dW_i(s) \right\rangle \\ & + 2 B_i^{(s)\,2} \check{C}_i \left(F_a - \check{C}_i\right) \exp\left(-\frac{t}{T_i^{(s)}} - \frac{t}{\tau_{part}}\right) \left\langle \int_{t_0}^{t} \exp\left(\frac{s}{T_i^{(s)}}\right) dW_i(s) \int_{t_0}^{t} \exp\left(\frac{s}{\tau_{part}}\right) dW_i(s) \right\rangle \\ & + B_i^{(s)\,2} \left(F_a - \check{C}_i\right)^2 \exp\left(-\frac{2t}{\tau_{part}}\right) \left\langle \int_{t_0}^{t} \exp\left(\frac{s}{\tau_{part}}\right) dW_i(s) \int_{t_0}^{t} \exp\left(\frac{s}{\tau_{part}}\right) dW_i(s) \right\rangle \end{aligned} \tag{A.42}$$

Thus:

$$\begin{aligned}\left\langle \Gamma_i^2 \right\rangle =& \left(B_i^{(s)} \check{C}_i\right)^2 \frac{T_i^{(s)}}{2} \left[1 - \exp\left(-\frac{2dt}{T_i^{(s)}}\right)\right] \\ & + 2 B_i^{(s)\,2} \check{C}_i \left(F_a - \check{C}_i\right) \frac{T_i^{(s)} \tau_{part}}{T_i^{(s)} + \tau_{part}} \left[1 - \exp\left(\frac{dt}{\tau_{part}}\right) \exp\left(\frac{dt}{T_i^{(s)}}\right)\right] \\ & + B_i^{(s)\,2} \left(F_a - \check{C}_i\right)^2 \frac{\tau_{part}}{2} \left[1 - \exp\left(-\frac{2dt}{\tau_{part}}\right)\right] \end{aligned} \tag{A.43}$$

If in addition to α_i and β the two following constants are defined:

$$\check{K}_i = \frac{F_a}{\check{C}_i} - 1 \tag{A.44}$$

$$\check{Q}_i = \check{K}_i \frac{T_i^{(s)} \tau_{part}}{T_i^{(s)} + \tau_{part}} \tag{A.45}$$

The covariance $\left\langle \Gamma_i^2 \right\rangle$ can then be further simplified:

$$\left\langle \Gamma_i^2 \right\rangle = \left(B_i^{(s)} \check{C}_i\right)^2 \left[\left(1 - \alpha_i^2\right) \frac{T_i^{(s)}}{2} + \left(1 - \beta^2\right) \frac{\check{K}_i^2 \tau_{part}}{2} + 2 \left(1 - \alpha_i \beta\right) \check{Q}_i \right] \tag{A.46}$$

The following calculations follow the same logic:

$$\begin{aligned}\left\langle \Phi_i^2 \right\rangle = \Bigg\langle \Bigg\{ & B_i^{(s)} \left[\left(T_i^{(s)} - \tau_{part} \right) \check{C}_i + F_a \tau_{part} \right] \int_{t_0}^{t} dW_i(s) \\ & - B_i^{(s)} \check{C}_i T_i^{(s)} \exp\left(-\frac{t}{T_i^{(s)}} \right) \int_{t_0}^{t} \exp\left(\frac{s}{T_i^{(s)}} \right) dW_i(s) \\ & - B_i^{(s)} \left(F_a - \check{C}_i \right) \tau_{part} \exp\left(-\frac{t}{\tau_{part}} \right) \int_{t_0}^{t} \exp\left(\frac{s}{\tau_{part}} \right) dW_i(s) \Bigg\} \\ & \Bigg\{ B_i^{(s)} \left[\left(T_i^{(s)} - \tau_{part} \right) \check{C}_i + F_a \tau_{part} \right] \int_{t_0}^{t} dW_i(s) \\ & - B_i^{(s)} \check{C}_i T_i^{(s)} \exp\left(-\frac{t}{T_i^{(s)}} \right) \int_{t_0}^{t} \exp\left(\frac{s}{T_i^{(s)}} \right) dW_i(s) \\ & - B_i^{(s)} \left(F_a - \check{C}_i \right) \tau_{part} \exp\left(-\frac{t}{\tau_{part}} \right) \int_{t_0}^{t} \exp\left(\frac{s}{\tau_{part}} \right) dW_i(s) \Bigg\} \Bigg\rangle \end{aligned} \tag{A.47}$$

Hence:

$$\begin{aligned}\left\langle \Phi_i^2 \right\rangle = & B_i^{(s)\,2} \left[\left(T_i^{(s)} - \tau_{part} \right) \check{C}_i + F_a \tau_{part} \right]^2 \left\langle \int_{t_0}^{t} dW_i(s) \int_{t_0}^{t} dW_i(s) \right\rangle \\ & - 2 B_i^{(s)\,2} \left[\left(T_i^{(s)} - \tau_{part} \right) \check{C}_i + F_a \tau_{part} \right] \check{C}_i T_i^{(s)} \exp\left(-\frac{t}{T_i^{(s)}} \right) \left\langle \int_{t_0}^{t} dW_i(s) \int_{t_0}^{t} \exp\left(\frac{s}{T_i^{(s)}} \right) dW_i(s) \right\rangle \\ & - 2 B_i^{(s)\,2} \left[\left(T_i^{(s)} - \tau_{part} \right) \check{C}_i + F_a \tau_{part} \right] \left(F_a - \check{C}_i \right) \tau_{part} \exp\left(-\frac{t}{\tau_{part}} \right) \\ & \times \left\langle \int_{t_0}^{t} dW_i(s) \int_{t_0}^{t} \exp\left(\frac{s}{\tau_{part}} \right) dW_i(s) \right\rangle \\ & + B_i^{(s)\,2} \check{C}_i^2 T_i^{(s)\,2} \exp\left(-\frac{2t}{T_i^{(s)}} \right) \left\langle \int_{t_0}^{t} \exp\left(\frac{s}{T_i^{(s)}} \right) dW_i(s) \int_{t_0}^{t} \exp\left(\frac{s}{T_i^{(s)}} \right) dW_i(s) \right\rangle \\ & + 2 B_i^{(s)\,2} \check{C}_i T_i^{(s)} \left(F_a - \check{C}_i \right) \tau_{part} \exp\left(-\frac{t}{T_i^{(s)}} \right) \exp\left(-\frac{t}{\tau_{part}} \right) \\ & \times \left\langle \int_{t_0}^{t} \exp\left(\frac{s}{T_i^{(s)}} \right) dW_i(s) \int_{t_0}^{t} \exp\left(\frac{s}{\tau_{part}} \right) dW_i(s) \right\rangle + B_i^{(s)\,2} \left(F_a - \check{C}_i \right)^2 \tau_{part}^2 \exp\left(-\frac{2t}{\tau_{part}} \right) \\ & \times \left\langle \int_{t_0}^{t} \exp\left(\frac{s}{\tau_{part}} \right) dW_i(s) \int_{t_0}^{t} \exp\left(\frac{s}{\tau_{part}} \right) dW_i(s) \right\rangle \end{aligned} \tag{A.48}$$

Thus:

$$\begin{aligned}\left\langle \Phi_i^2 \right\rangle = & B_i^{(s)\,2} \left[\left(T_i^{(s)} - \tau_{part} \right) \check{C}_i + F_a \tau_{part} \right]^2 dt \\ & - 2 B_i^{(s)\,2} \left[\left(T_i^{(s)} - \tau_{part} \right) \check{C}_i + F_a \tau_{part} \right] \check{C}_i T_i^{(s)\,2} \left[1 - \exp\left(-\frac{dt}{T_i^{(s)}} \right) \right] \\ & - 2 B_i^{(s)\,2} \left[\left(T_i^{(s)} - \tau_{part} \right) \check{C}_i + F_a \tau_{part} \right] \left(F_a - \check{C}_i \right) \tau_{part}^2 \left[1 - \exp\left(-\frac{dt}{\tau_{part}} \right) \right] \\ & + B_i^{(s)\,2} \check{C}_i^2 \frac{T_i^{(s)\,3}}{2} \left[1 - \exp\left(-\frac{2dt}{T_i^{(s)}} \right) \right] \\ & + 2 B_i^{(s)\,2} \check{C}_i \left(F_a - \check{C}_i \right) \frac{T_i^{(s)\,2} \tau_{part}^2}{T_i^{(s)} + \tau_{part}} \left[1 - \exp\left(\frac{dt}{\tau_{part}} \right) \exp\left(\frac{dt}{T_i^{(s)}} \right) \right] \\ & + B_i^{(s)\,2} \left(F_a - \check{C}_i \right)^2 \frac{\tau_{part}^3}{2} \left[1 - \exp\left(-\frac{2dt}{\tau_{part}} \right) \right] \end{aligned} \tag{A.49}$$

If the next constant is defined:

$$\begin{aligned}\check{G}_i =& \frac{\left(T_i^{(s)} - \tau_{part}\right)\check{C}_i + F_a\tau_{part}}{\check{C}_i} \\ =& T_i^{(s)} + \check{K}_i\tau_{part}\end{aligned} \tag{A.50}$$

This then gives the following equation for $\left\langle \Phi_i^2 \right\rangle$:

$$\begin{aligned}\left\langle \Phi_i^2 \right\rangle =& B_i^{(s)\,2}\check{C}_i^2 \left\{ \check{G}_i^2 dt + \left(1-\alpha_i^2\right)\frac{T_i^{(s)\,3}}{2} + \left(1-\beta^2\right)\frac{\check{K}_i^2\tau_{part}^3}{2} \right. \\ & \left. -2\check{G}_i\left[\left(1-\alpha_i\right)T_i^{(s)\,2} + \left(1-\beta\right)\check{K}_i\tau_{part}^2\right] + 2\left(1-\alpha_i\beta\right)\check{Q}_i T_i^{(s)}\tau_{part} \right\}\end{aligned} \tag{A.51}$$

All the constant useful for simplification purposes have now been defined, therefore the following calculations are given without further explanations.

$$\begin{aligned}\left\langle \gamma_i\Gamma_i \right\rangle =& \left\langle B_i^{(s)}\exp\left(-\frac{t}{T_i^{(s)}}\right)\int_{t_0}^{t}\exp\left(\frac{s}{T_i^{(s)}}\right)dW_i(s)\left[B_i^{(s)}\check{C}_i\exp\left(-\frac{t}{T_i^{(s)}}\right)\int_{t_0}^{t}\exp\left(\frac{s}{T_i^{(s)}}\right)dW_i(s)\right.\right. \\ & \left.\left. + B_i^{(s)}\left(F_a-\check{C}_i\right)\exp\left(-\frac{t}{\tau_{part}}\right)\int_{t_0}^{t}\exp\left(\frac{s}{\tau_{part}}\right)dW_i(s)\right]\right\rangle\end{aligned} \tag{A.52}$$

Hence:

$$\begin{aligned}\left\langle \gamma_i\Gamma_i \right\rangle =& B_i^{(s)\,2}\check{C}_i\exp\left(-\frac{2t}{T_i^{(s)}}\right)\left\langle\int_{t_0}^{t}\exp\left(\frac{s}{T_i^{(s)}}\right)dW_i(s)\int_{t_0}^{t}\exp\left(\frac{s}{T_i^{(s)}}\right)dW_i(s)\right\rangle \\ & + B_i^{(s)\,2}\left(F_a-\check{C}_i\right)\exp\left(-\frac{t}{T_i^{(s)}}\right)\exp\left(-\frac{t}{\tau_{part}}\right) \\ & \times\left\langle\int_{t_0}^{t}\exp\left(\frac{s}{T_i^{(s)}}\right)dW_i(s)\int_{t_0}^{t}\exp\left(-\frac{t}{\tau_{part}}\right)dW_i(s)\right\rangle\end{aligned} \tag{A.53}$$

Thus:

$$\begin{aligned}\left\langle \gamma_i\Gamma_i \right\rangle =& B_i^{(s)\,2}\check{C}_i\frac{T_i^{(s)}}{2}\left[1-\exp\left(-\frac{2dt}{T_i^{(s)}}\right)\right] \\ & + B_i^{(s)\,2}\left(F_a-\check{C}_i\right)\frac{T_i^{(s)}\tau_{part}}{T_i^{(s)}+\tau_{part}}\left[1-\exp\left(-\frac{dt}{\tau_{part}}\right)\exp\left(\frac{-dt}{T_i^{(s)}}\right)\right]\end{aligned} \tag{A.54}$$

Therefore:

$$\left\langle \gamma_i\Gamma_i \right\rangle = B_i^{(s)\,2}\check{C}_i\left[\left(1-\alpha_i^2\right)\frac{T_i^{(s)}}{2} + \left(1-\alpha_i\beta\right)\check{Q}_i\right] \tag{A.55}$$

And:

$$\begin{aligned}\langle\gamma_i\Phi_i\rangle =& \left\langle B_i^{(s)}\exp\left(-\frac{t}{T_i^{(s)}}\right)\int_{t_0}^{t}\exp\left(\frac{s}{T_i^{(s)}}\right)dW_i(s)\right.\\ &\left[B_i^{(s)}\left[\left(T_i^{(s)}-\tau_{part}\right)\check{C}_i+F_a\tau_{part}\right]\int_{t_0}^{t}dW_i(s)\right.\\ &-B_i^{(s)}\check{C}_iT_i^{(s)}\exp\left(-\frac{t}{T_i^{(s)}}\right)\int_{t_0}^{t}\exp\left(\frac{s}{T_i^{(s)}}\right)dW_i(s)\\ &\left.\left.-B_i^{(s)}\left(F_a-\check{C}_i\right)\tau_{part}\exp\left(-\frac{t}{\tau_{part}}\right)\int_{t_0}^{t}\exp\left(\frac{s}{\tau_{part}}\right)dW_i(s)\right]\right\rangle \end{aligned} \tag{A.56}$$

Which gives:

$$\begin{aligned}\langle\gamma_i\Phi_i\rangle =&B_i^{(s)\,2}\left[\left(T_i^{(s)}-\tau_{part}\right)\check{C}_i+F_a\tau_{part}\right]\exp\left(-\frac{t}{T_i^{(s)}}\right)\left\langle\int_{t_0}^{t}\exp\left(\frac{s}{T_i^{(s)}}\right)dW_i(s)\int_{t_0}^{t}dW_i(s)\right\rangle\\ &-B_i^{(s)\,2}\check{C}_iT_i^{(s)}\exp\left(-\frac{2t}{T_i^{(s)}}\right)\left\langle\int_{t_0}^{t}\exp\left(\frac{s}{T_i^{(s)}}\right)dW_i(s)\int_{t_0}^{t}\exp\left(\frac{s}{T_i^{(s)}}\right)dW_i(s)\right\rangle\\ &-B_i^{(s)\,2}\left(F_a-\check{C}_i\right)\tau_{part}\exp\left(-\frac{t}{T_i^{(s)}}\right)\exp\left(-\frac{t}{\tau_{part}}\right)\\ &\times\left\langle\int_{t_0}^{t}\exp\left(\frac{s}{T_i^{(s)}}\right)dW_i(s)\int_{t_0}^{t}\exp\left(\frac{s}{\tau_{part}}\right)dW_i(s)\right\rangle \end{aligned} \tag{A.57}$$

Hence:

$$\langle\gamma_i\Phi_i\rangle =B_i^{(s)\,2}\left[\left(T_i^{(s)}-\tau_{part}\right)\check{C}_i+F_a\tau_{part}\right]T_i^{(s)}\left[1-\exp\left(-\frac{dt}{T_i^{(s)}}\right)\right] \tag{A.58}$$

$$\begin{aligned}&-B_i^{(s)\,2}\check{C}_i\frac{T_i^{(s)\,2}}{2}\left[1-\exp\left(-\frac{2dt}{T_i^{(s)}}\right)\right]\\ &-B_i^{(s)\,2}\left(F_a-\check{C}_i\right)\tau_{part}\frac{T_i^{(s)}\tau_{part}}{T_i^{(s)}+\tau_{part}}\left[1-\exp\left(-\frac{dt}{\tau_{part}}\right)\exp\left(-\frac{dt}{T_i^{(s)}}\right)\right]\end{aligned} \tag{A.59}$$

Therefore:

$$\langle\gamma_i\Phi_i\rangle =B_i^{(s)\,2}\check{C}_i\left[\left(1-\alpha_i\right)\check{G}_iT_i^{(s)}-\left(1-\alpha_i^2\right)\frac{T_i^{(s)\,2}}{2}-\left(1-\alpha_i\beta\right)\check{Q}_i\tau_{part}\right] \tag{A.60}$$

Finally:

$$\begin{aligned}\langle\Gamma_i\Phi_i\rangle =& \left\langle\left[B_i^{(s)}\check{C}_i\exp\left(-\frac{t}{T_i^{(s)}}\right)\int_{t_0}^{t}\exp\left(\frac{s}{T_i^{(s)}}\right)dW_i(s)\right.\right.\\ &\left.+B_i^{(s)}\left(F_a-\check{C}_i\right)\exp\left(-\frac{t}{\tau_{part}}\right)\int_{t_0}^{t}\exp\left(\frac{s}{\tau_{part}}\right)dW_i(s)\right]\\ &\left[B_i^{(s)}\left[\left(T_i^{(s)}-\tau_{part}\right)\check{C}_i+F_a\tau_{part}\right]\int_{t_0}^{t}dW_i(s)\right.\\ &-B_i^{(s)}\check{C}_iT_i^{(s)}\exp\left(-\frac{t}{T_i^{(s)}}\right)\int_{t_0}^{t}\exp\left(\frac{s}{T_i^{(s)}}\right)dW_i(s)\\ &\left.\left.-B_i^{(s)}\left(F_a-\check{C}_i\right)\tau_{part}\exp\left(-\frac{t}{\tau_{part}}\right)\int_{t_0}^{t}\exp\left(\frac{s}{\tau_{part}}\right)dW_i(s)\right]\right\rangle \end{aligned} \tag{A.61}$$

Thus:

$$\begin{aligned}\langle \Gamma_i \Phi_i \rangle =& B_i^{(s)\,2} \check{C}_i \left[\left(T_i^{(s)} - \tau_{part} \right) \check{C}_i + F_a \tau_{part} \right] \exp\left(-\frac{t}{T_i^{(s)}} \right) \left\langle \int_{t_0}^{t} \exp\left(\frac{s}{T_i^{(s)}} \right) dW_i(s) \int_{t_0}^{t} dW_i(s) \right\rangle \\ & - B_i^{(s)\,2} \check{C}_i^2 T_i^{(s)} \exp\left(-\frac{2t}{T_i^{(s)}} \right) \left\langle \int_{t_0}^{t} \exp\left(\frac{s}{T_i^{(s)}} \right) dW_i(s) \int_{t_0}^{t} \exp\left(\frac{s}{T_i^{(s)}} \right) dW_i(s) \right\rangle \\ & - B_i^{(s)\,2} \check{C}_i \left(F_a - \check{C}_i \right) \tau_{part} \exp\left(-\frac{t}{T_i^{(s)}} \right) \exp\left(-\frac{t}{\tau_{part}} \right) \\ & \times \left\langle \int_{t_0}^{t} \exp\left(\frac{s}{T_i^{(s)}} \right) dW_i(s) \int_{t_0}^{t} \exp\left(\frac{s}{\tau_{part}} \right) dW_i(s) \right\rangle \\ & + B_i^{(s)\,2} \left(F_a - \check{C}_i \right) \left[\left(T_i^{(s)} - \tau_{part} \right) \check{C}_i + F_a \tau_{part} \right] \exp\left(-\frac{t}{\tau_{part}} \right) \\ & \times \left\langle \int_{t_0}^{t} \exp\left(\frac{s}{\tau_{part}} \right) dW_i(s) \int_{t_0}^{t} dW_i(s) \right\rangle - B_i^{(s)\,2} \check{C}_i \left(F_a - \check{C}_i \right) T_i^{(s)} \exp\left(-\frac{t}{T_i^{(s)}} \right) \exp\left(-\frac{t}{\tau_{part}} \right) \\ & \times \left\langle \int_{t_0}^{t} \exp\left(\frac{s}{T_i^{(s)}} \right) dW_i(s) \int_{t_0}^{t} \exp\left(\frac{s}{\tau_{part}} \right) dW_i(s) \right\rangle - B_i^{(s)\,2} \left(F_a - \check{C}_i \right)^2 \tau_{part} \exp\left(-\frac{2t}{\tau_{part}} \right) \\ & \times \left\langle \int_{t_0}^{t} \exp\left(\frac{s}{\tau_{part}} \right) dW_i(s) \int_{t_0}^{t} \exp\left(\frac{s}{\tau_{part}} \right) dW_i(s) \right\rangle \end{aligned} \tag{A.62}$$

Which gives:

$$\begin{aligned}\langle \Gamma_i \Phi_i \rangle =& B_i^{(s)\,2} \check{C}_i \left[\left(T_i^{(s)} - \tau_{part} \right) \check{C}_i + F_a \tau_{part} \right] T_i^{(s)} \left[1 - \exp\left(-\frac{dt}{T_i^{(s)}} \right) \right] \\ & - B_i^{(s)\,2} \check{C}_i^2 \frac{T_i^{(s)\,2}}{2} \left[1 - \exp\left(-\frac{2dt}{T_i^{(s)}} \right) \right] \\ & - B_i^{(s)\,2} \check{C}_i \left(F_a - \check{C}_i \right) \tau_{part} \frac{T_i^{(s)} \tau_{part}}{T_i^{(s)} + \tau_{part}} \left[1 - \exp\left(-\frac{dt}{\tau_{part}} \right) \exp\left(-\frac{dt}{T_i^{(s)}} \right) \right] \\ & + B_i^{(s)\,2} \left(F_a - \check{C}_i \right) \left[\left(T_i^{(s)} - \tau_{part} \right) \check{C}_i + F_a \tau_{part} \right] \tau_{part} \left[1 - \exp\left(-\frac{dt}{\tau_{part}} \right) \right] \\ & - B_i^{(s)\,2} \check{C}_i \left(F_a - \check{C}_i \right) T_i^{(s)} \frac{T_i^{(s)} \tau_{part}}{T_i^{(s)} + \tau_{part}} \left[1 - \exp\left(-\frac{dt}{\tau_{part}} \right) \exp\left(-\frac{dt}{T_i^{(s)}} \right) \right] \\ & - B_i^{(s)\,2} \left(F_a - \check{C}_i \right)^2 \frac{\tau_{part}^2}{2} \left[1 - \exp\left(-\frac{2dt}{\tau_{part}} \right) \right] \end{aligned} \tag{A.63}$$

Therefore:

$$\begin{aligned}\langle \Gamma_i \Phi_i \rangle =& B_i^{(s)\,2} \check{C}_i^2 \left\{ \left[\left(1 - \alpha_i \right) T_i^{(s)} + \left(1 - \beta \right) \check{K}_i \tau_{part} \right] \check{G}_i - \left(1 - \alpha_i^2 \right) \frac{T_i^{(s)\,2}}{2} \right. \\ & \left. - \left(1 - \beta^2 \right) \frac{\check{K}_i^2 \tau_{part}^2}{2} - \left(1 - \alpha_i \beta \right) \check{K}_i T_i^{(s)} \tau_{part} \right\} \end{aligned} \tag{A.64}$$

Because of the definitions for $\check{K}_i$, $\check{Q}_i$ and $\check{G}_i$ (given in equations A.44, A.45 and A.50 respectively) all of the covariances are undefined if $T_i^{(s)} = F_a \tau_{part}$. Furthermore to use this model the time interval dt is set to equal the numerical time step dt.

Appendix B

Asymptotic behaviour of the exact integrator model

Où les calculs nécessaires pour décrire le comportement assymptotique du modèle de transport de corps solides résolu avec un integrateur exact sont présentés.

The aim of the exact integrator model, developed in appendix A and presented in chapter 6 is given by the following equations:

$$U_i^{(s)}(t) = \alpha_i U_i^{(s)}(t_0) + (1-\alpha_i)\, C_i^{(s)} T_i^{(s)} + \gamma_i(t) \tag{B.1a}$$

$$V_i(t) = \beta V_i(t_0) + (1-\beta)\left(C_i^{(s)} T_i^{(s)} + F_{i,c}\tau_{part}\right) + (\alpha_i - \beta)\,\check{C}_i\left(U_i^{(s)}(t_0) - C_i^{(s)} T_i^{(s)}\right) + \Gamma_i(t) \tag{B.1b}$$

$$\begin{aligned} X_i(t) = {} & X_i(t_0) + (1-\beta)\,\tau_{part} V_i(t_0) + \left[dt - (1-\beta)\,\tau_{part}\right]\left(C_i^{(s)} T_i^{(s)} + F_{i,c}\tau_{part}\right) \\ & + \check{C}_i\left(U_i^{(s)}(t_0) - C_i^{(s)} T_i^{(s)}\right)\left[(1-\alpha_i)\, T_i^{(s)} - (1-\beta)\,\tau_{part}\right] + \Phi_i(t) \end{aligned} \tag{B.1c}$$

With the following coefficients:

$$\alpha_i = \exp\left(-\frac{dt}{T_i^{(s)}}\right) \tag{B.2a}$$

$$\beta = \exp\left(-\frac{dt}{\tau_{part}}\right) \tag{B.2b}$$

$$\check{C}_i = \frac{T_i^{(s)} - F_a \tau_{part}}{T_i^{(s)} - \tau_{part}} \tag{B.2c}$$

An the stochastic integrals $\gamma_i(t)$, $\Gamma_i(t)$ and $\Phi_i(t)$ are modelled using the following equations:

$$\gamma_i = L_{11}\xi_{\gamma_i} \tag{B.3a}$$

$$\Gamma_i = L_{21}\xi_{\gamma_i} + L_{22}\xi_{\Gamma_i} \tag{B.3b}$$

$$\Phi_i = L_{31}\xi_{\gamma_i} + L_{32}\xi_{\Gamma_i} + L_{33}\xi_{\Phi_i} \tag{B.3c}$$

With the components of the matrix **L** given by:

$$L_{11} = \sqrt{\langle \gamma_i^2 \rangle} \tag{B.4a}$$

$$L_{21} = \frac{\langle \gamma_i \Gamma_i \rangle}{L_{11}} \tag{B.4b}$$

$$L_{22} = \sqrt{\langle \Gamma_i^2 \rangle - L_{21}^2} \tag{B.4c}$$

$$L_{31} = \frac{\langle \gamma_i \Phi_i \rangle}{L_{11}} \tag{B.4d}$$

$$L_{32} = \frac{\langle \Gamma_i \Phi_i \rangle - L_{21} L_{31}}{L_{22}} \tag{B.4e}$$

$$L_{33} = \sqrt{\langle \Phi_i^2 \rangle - L_{31}^2 - L_{32}^2} \tag{B.4f}$$

And the covariances are modelled through the following equations:

$$\left\langle \gamma_i^2 \right\rangle = \left(1-\alpha_i^2\right) B_i^{(s)\,2} \frac{T_i^{(s)}}{2} \tag{B.5a}$$

$$\left\langle \Gamma_i^2 \right\rangle = \left(B_i^{(s)} \check{C}_i\right)^2 \left[\left(1-\alpha_i^2\right) \frac{T_i^{(s)}}{2} + \left(1-\beta^2\right) \frac{\check{K}_i^2 \tau_{part}}{2} + 2\left(1-\alpha_i\beta\right) \check{Q}_i \right] \tag{B.5b}$$

$$\begin{aligned} \left\langle \Phi_i^2 \right\rangle = \left(B_i^{(s)} \check{C}_i\right)^2 \Bigg\{ & \check{G}_i^2 dt + \left(1-\alpha_i^2\right) \frac{T_i^{(s)\,3}}{2} + \left(1-\beta^2\right) \frac{\check{K}_i^2 \tau_{part}^3}{2} \\ & - 2\check{G}_i \left[\left(1-\alpha_i\right) T_i^{(s)\,2} + \left(1-\beta\right) \check{K}_i \tau_{part}^2 \right] + 2\left(1-\alpha_i\beta\right) \check{Q}_i T_i^{(s)} \tau_{part} \Big\} \end{aligned} \tag{B.5c}$$

$$\left\langle \gamma_i \Gamma_i \right\rangle = B_i^{(s)\,2} \check{C}_i \left[\left(1-\alpha_i^2\right) \frac{T_i^{(s)}}{2} + \left(1-\alpha_i\beta\right) \check{Q}_i \right] \tag{B.5d}$$

$$\left\langle \gamma_i \Phi_i \right\rangle = B_i^{(s)\,2} \check{C}_i \left[\left(1-\alpha_i\right) \check{G}_i T_i^{(s)} - \left(1-\alpha_i^2\right) \frac{T_i^{(s)\,2}}{2} - \left(1-\alpha_i\beta\right) \check{Q}_i \tau_{part} \right] \tag{B.5e}$$

$$\begin{aligned} \left\langle \Gamma_i \Phi_i \right\rangle = \left(B_i^{(s)} \check{C}_i\right)^2 \Bigg\{ & \left[\left(1-\alpha_i\right) T_i^{(s)} + \left(1-\beta\right) \check{K}_i \tau_{part} \right] \check{G}_i - \left(1-\alpha_i^2\right) \frac{T_i^{(s)\,2}}{2} \\ & - \left(1-\beta^2\right) \frac{\check{K}_i^2 \tau_{part}^2}{2} - \left(1-\alpha_i\beta\right) \check{K}_i T_i^{(s)} \tau_{part} \Bigg\} \end{aligned} \tag{B.5f}$$

With the following coefficients:

$$\check{K}_i = \frac{F_a}{\check{C}_i} - 1 \tag{B.6a}$$

$$\check{Q}_i = \frac{\check{K}_i T_i^{(s)} \tau_{part}}{T_i^{(s)} + \tau_{part}} \tag{B.6b}$$

$$\check{G}_i = T_i^{(s)} + \check{K}_i \tau_{part} \tag{B.6c}$$

Furthermore it can be shown that $\check{G}_i \check{C}_i = T_i^{(s)}$.

The exact integrator was to develop so that the particle transport model is less dependent on the time step, thanks to the asymptotic behaviour of the exponents α_i and β. In this appendix we will present the asymptotic behaviour of the exact integrator model for different ration between the numerical time step dt and the characteristic times $T_i^{(s)}$ and τ_{part}.

B.1 For a time step dt much larger than the integral time scale $T_i^{(s)}$

For this scenario the following simplifications can be done:

$$\frac{dt}{T_i^{(s)}} \to \infty \tag{B.7a}$$

$$\alpha_i \to 0 \tag{B.7b}$$

From the simplifications B.7 the covariances are given by:

$$\begin{aligned} \left\langle \gamma_i^2 \right\rangle &= \left(1-\alpha_i^2\right) B_i^{(s)\,2} \frac{T_i^{(s)}}{2} \\ &\to \frac{B_i^{(s)\,2} T_i^{(s)}}{2} \end{aligned} \tag{B.8}$$

$$\begin{aligned}\left\langle \Gamma_i^2 \right\rangle =& \left(B_i^{(s)}\check{C}_i\right)^2 \left[\left(1-\alpha_i^2\right)\frac{T_i^{(s)}}{2} + \left(1-\beta^2\right)\frac{\check{K}_i^2\tau_{part}}{2} + 2\left(1-\alpha_i\beta\right)\check{Q}_i\right] \\ \rightarrow& \left(B_i^{(s)}\check{C}_i\right)^2 \left[\frac{T_i^{(s)}}{2} + \left(1-\beta^2\right)\frac{\check{K}_i^2\tau_{part}}{2} + 2\check{Q}_i\right] \end{aligned} \tag{B.9}$$

And:

$$\begin{aligned}\left\langle \Phi_i^2 \right\rangle =& B_i^{(s)\,2}\check{C}_i^2 \Bigg\{ \check{G}_i^2 dt + \left(1-\alpha_i^2\right)\frac{T_i^{(s)\,3}}{2} + \left(1-\beta^2\right)\frac{\check{K}_i^2\tau_{part}^3}{2} \\ & -2\check{G}_i\left[\left(1-\alpha_i\right)T_i^{(s)\,2} + \left(1-\beta\right)\check{K}_i\tau_{part}^2\right] + 2\left(1-\alpha_i\beta\right)\check{Q}_i T_i^{(s)}\tau_{part} \Bigg\} \\ \rightarrow& B_i^{(s)\,2}T_i^{(s)\,2}dt + B_i^{(s)\,2}\check{C}_i^2 \Bigg\{ \frac{T_i^{(s)\,3}}{2} + \left(1-\beta^2\right)\frac{\check{K}_i^2\tau_{part}^3}{2} \\ & -2\check{G}_i\left[T_i^{(s)\,2} + \left(1-\beta\right)\check{K}_i\tau_{part}^2\right] + 2\check{Q}_i T_i^{(s)}\tau_{part} \Bigg\} \end{aligned} \tag{B.10}$$

However $T_i^{(s)\,2}dt$ might not be defined, but it should tend to 0 as usually dt is fixed and this scenario occurs when $T_i^{(s)\,2}dt$ is very small:

$$\begin{aligned}\left\langle \gamma_i\Gamma_i \right\rangle =& B_i^{(s)\,2}\check{C}_i \left[\left(1-\alpha_i^2\right)\frac{T_i^{(s)}}{2} + \left(1-\alpha_i\beta\right)\check{Q}_i\right] \\ \rightarrow& B_i^{(s)\,2}\check{C}_i\left(\frac{T_i^{(s)}}{2} + \check{Q}_i\right) \end{aligned} \tag{B.11}$$

$$\begin{aligned}\left\langle \gamma_i\Phi_i \right\rangle =& B_i^{(s)\,2}\check{C}_i \left[\left(1-\alpha_i\right)\check{G}_i T_i^{(s)} - \left(1-\alpha_i^2\right)\frac{T_i^{(s)\,2}}{2} - \left(1-\alpha_i\beta\right)\check{Q}_i\tau_{part}\right] \\ \rightarrow& B_i^{(s)\,2}\check{C}_i\left(\check{G}_i T_i^{(s)} - \frac{T_i^{(s)\,2}}{2} - \check{Q}_i\tau_{part}\right) \end{aligned} \tag{B.12}$$

$$\begin{aligned}\left\langle \Gamma_i\Phi_i \right\rangle =& B_i^{(s)\,2}\check{C}_i^2 \Bigg\{ \left[\left(1-\alpha_i\right)T_i^{(s)} + \left(1-\beta\right)\check{K}_i\tau_{part}\right]\check{G}_i - \left(1-\alpha_i^2\right)\frac{T_i^{(s)\,2}}{2} \\ & - \left(1-\beta^2\right)\frac{\check{K}_i^2\tau_{part}^2}{2} - \left(1-\alpha_i\beta\right)\check{K}_i T_i^{(s)}\tau_{part} \Bigg\} \\ \rightarrow& B_i^{(s)\,2}\check{C}_i^2 \Bigg\{ \left[T_i^{(s)} + \left(1-\beta\right)\check{K}_i\tau_{part}\right]\check{G}_i - \frac{T_i^{(s)\,2}}{2} \\ & - \left(1-\beta^2\right)\frac{\check{K}_i^2\tau_{part}^2}{2} - \check{K}_i T_i^{(s)}\tau_{part} \Bigg\} \end{aligned} \tag{B.13}$$

These covariances imply the coefficients of matrix $\mathbf{L}$ can be determined (assuming that $T_i^{(s)\,2}dt \rightarrow 0$), and therefore stochastic integrals can be defined. The fluid velocity however is modelled as:

$$\begin{aligned} U_i^{(s)}(t) =& \alpha_i U_i^{(s)}(t_0) + \left(1-\alpha_i\right)C_i^{(s)}T_i^{(s)} + \gamma_i(t) \\ \rightarrow& C_i^{(s)}T_i^{(s)} + \gamma_i(t) \end{aligned} \tag{B.14}$$

Which using equation B.8 is:

$$U_i^{(s)}(t) = C_i^{(s)} T_i^{(s)} + \sqrt{\frac{B_i^{(s)\,2} T_i^{(s)}}{2}} \xi_{\gamma_i} \tag{B.15}$$

Therefore the fluid velocity is modelled through a mean flow component and a random variable. The solid body velocity is given by:

$$\begin{aligned} V_i(t) =& \beta V_i(t_0) + (1-\beta)\left(C_i^{(s)} T_i^{(s)} + F_{i,c}\tau_{part}\right) \\ &+ (\alpha_i - \beta)\,\check{C}_i\left(U_i^{(s)}(t_0) - C_i^{(s)} T_i^{(s)}\right) \\ &+ \Gamma_i \end{aligned} \tag{B.16}$$

Hence:

$$\begin{aligned} V_i(t) \rightarrow& \beta V_i(t_0) + (1-\beta)\left(C_i^{(s)} T_i^{(s)} + F_{i,c}\tau_{part}\right) \\ &+ \beta\check{C}_i\left(U_i^{(s)}(t_0) - C_i^{(s)} T_i^{(s)}\right) \\ &+ \Gamma_i \end{aligned} \tag{B.17}$$

And the position of the bodies is given by:

$$\begin{aligned} X_i(t) =& X_i(t_0) + (1-\beta)\,\tau_{part} V_i(t_0) + \left[dt - (1-\beta)\,\tau_{part}\right]\left(C_i^{(s)} T_i^{(s)} + F_{i,c}\tau_{part}\right) \\ &+ \check{C}_i\left(U_i^{(s)}(t_0) - C_i^{(s)} T_i^{(s)}\right)\left[(1-\alpha_i)\,T_i^{(s)} - (1-\beta)\,\tau_{part}\right] \\ &+ \Phi_i \end{aligned} \tag{B.18}$$

Hence:

$$\begin{aligned} X_i(t) \rightarrow& X_i(t_0) + (1-\beta)\,\tau_{part} V_i(t_0) + \left[dt - (1-\beta)\,\tau_{part}\right]\left(C_i^{(s)} T_i^{(s)} + F_{i,c}\tau_{part}\right) \\ &+ \check{C}_i\left(U_i^{(s)}(t_0) - C_i^{(s)} T_i^{(s)}\right)\left[T_i^{(s)} - (1-\beta)\,\tau_{part}\right] \\ &+ \Phi_i \end{aligned} \tag{B.19}$$

Which is again determined only if $T_i^{(s)} dt$ can be determined.

B.2 For a time step dt much smaller than the integral time scale $T_i^{(s)}$

For this scenario the following simplifications can be done:

$$\frac{dt}{T_i^{(s)}} \rightarrow 0 \tag{B.20a}$$

$$\alpha_i \rightarrow 1 \tag{B.20b}$$

Therefore the covariances are given by:

$$\begin{aligned}\left\langle \gamma_i^2 \right\rangle &= \left(1-\alpha_i^2\right) B_i^{(s)\,2} \frac{T_i^{(s)}}{2} \\ &\rightarrow B_i^{(s)\,2} dt\end{aligned} \tag{B.21}$$

And:

$$\begin{aligned}\left\langle \Gamma_i^2 \right\rangle &= \left(B_i^{(s)} \check{C}_i\right)^2 \left[\left(1-\alpha_i^2\right) \frac{T_i^{(s)}}{2} + \left(1-\beta^2\right) \frac{\check{K}_i^2 \tau_{part}}{2} + 2\left(1-\alpha_i\beta\right) \check{Q}_i\right] \\ &\rightarrow \left(B_i^{(s)} \check{C}_i\right)^2 \left\{dt + \left(1-\beta^2\right) \frac{\check{K}_i^2 \tau_{part}}{2} + 2\left[1-\beta+\frac{dt}{T_i^{(s)}}\beta\right] \check{Q}_i\right\}\end{aligned} \tag{B.22}$$

The following can be defined:

$$\begin{aligned}\frac{dt}{T_i^{(s)}} \check{Q}_i =& \frac{dt}{T_i^{(s)}} \frac{T_i^{(s)} \tau_{part}}{T_i^{(s)} + \tau_{part}} \left(\frac{T_i^{(s)} - \tau_{part}}{T_i^{(s)} - F_a \tau_{part}} F_a - 1\right) \\ =& dt \frac{\tau_{part}}{T_i^{(s)} + \tau_{part}} \frac{T_i^{(s)}\left(1-F_a\right)}{T_i^{(s)} - F_a \tau_{part}}\end{aligned} \tag{B.23}$$

Which is 0 if $\tau_{part} \gg T_i^{(s)}$or $\tau_{part} \ll T_i^{(s)}$. If $\tau_{part} \sim T_i^{(s)}$ than this is proportional to dt, and therefore since it is still determined this scenario is ignored. Therefore:

$$\left\langle \Gamma_i^2 \right\rangle \rightarrow \left(B_i^{(s)} \check{C}_i\right)^2 \left[dt + \left(1-\beta^2\right) \frac{\check{K}_i^2 \tau_{part}}{2} + 2\left(1-\beta\right) \check{Q}_i\right] \tag{B.24}$$

And:

$$\begin{aligned}\left\langle \Phi_i^2 \right\rangle =& B_i^{(s)\,2} \check{C}_i^2 \left\{\check{G}_i^2 dt + \left(1-\alpha_i^2\right) \frac{T_i^{(s)\,3}}{2} + \left(1-\beta^2\right) \frac{\check{K}_i^2 \tau_{part}^3}{2}\right. \\ & \left. -2\check{G}_i \left[\left(1-\alpha_i\right) T_i^{(s)\,2} + \left(1-\beta\right) \check{K}_i \tau_{part}^2\right] + 2\left(1-\alpha_i\beta\right) \check{Q}_i T_i^{(s)} \tau_{part}\right\}\end{aligned} \tag{B.25}$$

Hence:

$$\begin{aligned}\left\langle \Phi_i^2 \right\rangle \rightarrow & B_i^{(s)\,2} \check{C}_i^2 \left\{\left(\check{G}_i^2 + T_i^{(s)\,2}\right) dt + \left(1-\beta^2\right) \frac{\check{K}_i^2 \tau_{part}^3}{2}\right. \\ & \left. -2\check{G}_i \left[T_i^{(s)}\, dt + \left(1-\beta\right) \check{K}_i \tau_{part}^2\right] + 2\left[1-\beta+\frac{dt}{T_i^{(s)}}\beta\right] \check{Q}_i T_i^{(s)} \tau_{part}\right\}\end{aligned} \tag{B.26}$$

In this covariance $T_i^{(s)} dt$ appears and therefore it might be undetermined. We also have:

$$\begin{aligned}\left\langle \gamma_i \Gamma_i \right\rangle =& B_i^{(s)\,2} \check{C}_i \left[\left(1-\alpha_i^2\right) \frac{T_i^{(s)}}{2} + \left(1-\alpha_i\beta\right) \check{Q}_i\right] \\ \rightarrow & B_i^{(s)\,2} \check{C}_i \left[dt + \left(1-\beta\right) \check{Q}_i\right]\end{aligned} \tag{B.27}$$

And:

$$\begin{aligned}\langle \gamma_i \Phi_i \rangle =& B_i^{(s)\,2} \check{C}_i \left[(1-\alpha_i)\, \check{G}_i T_i^{(s)} - \left(1-\alpha_i^2\right) \frac{T_i^{(s)\,2}}{2} - (1-\alpha_i\beta)\, \check{Q}_i \tau_{part} \right] \\ \rightarrow& B_i^{(s)\,2} \check{C}_i \left\{ \left(\check{G}_i - T_i^{(s)}\right) dt - \left(1-\beta+\frac{dt}{T_i^{(s)}}\beta\right) \check{Q}_i \tau_{part} \right\} \end{aligned} \tag{B.28}$$

Since $\check{G}_i - T_i^{(s)} = \check{K}_i \tau_{part}$ this covariance might only be undetermined if $\tau_{part} \sim T_i^{(s)}$. We can also write:

$$\begin{aligned}\langle \Gamma_i \Phi_i \rangle =& B_i^{(s)\,2} \check{C}_i^2 \left\{ \left[(1-\alpha_i)\, T_i^{(s)} + (1-\beta)\, \check{K}_i \tau_{part} \right] \check{G}_i - \left(1-\alpha_i^2\right) \frac{T_i^{(s)\,2}}{2} \right. \\ & \left. - \left(1-\beta^2\right) \frac{\check{K}_i^2 \tau_{part}^2}{2} - (1-\alpha_i\beta)\, \check{K}_i T_i^{(s)} \tau_{part} \right\} \end{aligned} \tag{B.29}$$

And thus:

$$\begin{aligned}\langle \Gamma_i \Phi_i \rangle \rightarrow& B_i^{(s)\,2} \check{C}_i^2 \left\{ \left[\check{G}_i - T_i^{(s)} \right] dt + (1-\beta)\, \check{K}_i \tau_{part} dt \right. \\ & \left. - \left(1-\beta^2\right) \frac{\check{K}_i^2 \tau_{part}^2}{2} - \left[1-\beta+\frac{dt}{T_i^{(s)}}\beta \right] \check{K}_i T_i^{(s)} \tau_{part} \right\} \end{aligned} \tag{B.30}$$

Again this covariance might be undetermined only if $\tau_{part} \sim T_i^{(s)}$. The only coefficient of matrix **L** that might be undetermined are therefore L_{31}, L_{31} or L_{31}, because they are dependent on $\langle \gamma_i \Phi_i \rangle$, $\langle \Gamma_i \Phi_i \rangle$ and $\left\langle \Phi_i^2 \right\rangle$. This then implies that the stochastic integral Φ_i could be undetermined. Still, the fluid velocities becomes can be simplified to:

$$\begin{aligned} U_i^{(s)}(t) =& \alpha_i U_i^{(s)}(t_0) + (1-\alpha_i)\, C_i^{(s)} T_i^{(s)} + \gamma_i(t) \\ \rightarrow& U_i^{(s)}(t_0) + C_i^{(s)} dt + B_i^{(s)} \sqrt{dt} \xi_{\gamma_i} \end{aligned} \tag{B.31}$$

And therefore it appears that the fluid velocities can be modelled using the Langevin model. This is because in this case the temporal frame of reference is placed around the small turbulent eddies, and therefore in this case dt is not much greater than the small scales of turbulence τ_p, which means that the turbulence model is not valid any more.

The solid particle velocity is given by:

$$\begin{aligned} V_i(t) =& \beta V_i(t_0) + (1-\beta) \left(C_i^{(s)} T_i^{(s)} + F_{i,c} \tau_{part} \right) \\ & + (\alpha_i - \beta)\, \check{C}_i \left(U_i^{(s)}(t_0) - C_i^{(s)} T_i^{(s)} \right) \\ & + \Gamma_i \\ \rightarrow& \beta V_i(t_0) + (1-\beta) \left(C_i^{(s)} T_i^{(s)} + F_{i,c} \tau_{part} \right) \\ & + (1-\beta)\, \check{C}_i \left(U_i^{(s)}(t_0) - C_i^{(s)} T_i^{(s)} \right) + \check{C}_i C_i^{(s)} dt \\ & + \Gamma_i \end{aligned} \tag{B.32}$$

And the position of the body is given by:

$$\begin{aligned} X_i(t) =& X_i(t_0) + (1-\beta)\,\tau_{part} V_i(t_0) + \left[dt - (1-\beta)\,\tau_{part}\right]\left(C_i^{(s)} T_i^{(s)} + F_{i,c}\tau_{part}\right) \\ &+ \check{C}_i\left(U_i^{(s)}(t_0) - C_i^{(s)} T_i^{(s)}\right)\left[(1-\alpha_i)\,T_i^{(s)} - (1-\beta)\,\tau_{part}\right] \\ &+ \Phi_i \\ \rightarrow& X_i(t_0) + (1-\beta)\,\tau_{part} V_i(t_0) + \left[dt - (1-\beta)\,\tau_{part}\right]\left(C_i^{(s)} T_i^{(s)} + F_{i,c}\tau_{part}\right) \\ &+ \check{C}_i\left(U_i^{(s)}(t_0) - C_i^{(s)} T_i^{(s)}\right)\left[dt - (1-\beta)\,\tau_{part}\right] \\ &+ \Phi_i \end{aligned} \tag{B.33}$$

Because of Φ_i, the position of the body is only determined if $T_i^{(s)} dt$ can be determined.

B.3 For a time step dt much larger than the particle relaxation time τ_{part}

For this scenario the following simplifications can be done:

$$\frac{dt}{\tau_{part}} \rightarrow \infty \tag{B.34a}$$

$$\beta \rightarrow 0 \tag{B.34b}$$

The covariance $\left\langle \gamma_i^2 \right\rangle$ remains unchanged, as it is independent of β. However the remaining covariances are equal to:

$$\begin{aligned} \left\langle \Gamma_i^2 \right\rangle =& \left(B_i^{(s)}\check{C}_i\right)^2 \left[\left(1-\alpha_i^2\right)\frac{T_i^{(s)}}{2} + \left(1-\beta^2\right)\frac{\check{K}_i^2\tau_{part}}{2} + 2\left(1-\alpha_i\beta\right)\check{Q}_i\right] \\ \rightarrow& \check{C}_i^2\left\langle \gamma_i^2 \right\rangle + \left(B_i^{(s)}\check{C}_i\right)^2\left[\frac{\check{K}_i^2\tau_{part}}{2} + 2\check{Q}_i\right] \end{aligned} \tag{B.35}$$

And:

$$\begin{aligned} \left\langle \Phi_i^2 \right\rangle =& B_i^{(s)\,2}\check{C}_i^2 \left\{ \check{G}_i^2 dt + \left(1-\alpha_i^2\right)\frac{T_i^{(s)\,3}}{2} + \left(1-\beta^2\right)\frac{\check{K}_i^2\tau_{part}^3}{2} \right. \\ & \left. -2\check{G}_i\left[(1-\alpha_i)\,T_i^{(s)\,2} + (1-\beta)\,\check{K}_i\tau_{part}^2\right] + 2\left(1-\alpha_i\beta\right)\check{Q}_i T_i^{(s)}\tau_{part}\right\} \\ \rightarrow& B_i^{(s)\,2}\check{C}_i^2 \left\{ \check{G}_i^2 dt + \left(1-\alpha_i^2\right)\frac{T_i^{(s)\,3}}{2} + \frac{\check{K}_i^2\tau_{part}^3}{2} \right. \\ & \left. -2\check{G}_i\left[(1-\alpha_i)\,T_i^{(s)\,2} + \check{K}_i\tau_{part}^2\right] + 2\check{Q}_i T_i^{(s)}\tau_{part}\right\} \end{aligned} \tag{B.36}$$

Since $\check{G}_i\check{C}_i = T_i^{(s)}$ the covariance $\left\langle \Phi_i^2 \right\rangle$ can be determined for all values of τ_{part}. The final covariances can the be written as:

$$\begin{aligned} \left\langle \gamma_i\Gamma_i \right\rangle =& B_i^{(s)\,2}\check{C}_i\left[\left(1-\alpha_i^2\right)\frac{T_i^{(s)}}{2} + \left(1-\alpha_i\beta\right)\check{Q}_i\right] \\ \rightarrow& \check{C}_i\left\langle \gamma_i^2 \right\rangle + B_i^{(s)\,2}\check{C}_i\check{Q}_i \end{aligned} \tag{B.37}$$

And:

$$\begin{aligned}\langle \gamma_i \Phi_i \rangle =& B_i^{(s)\,2} \check{C}_i \left[(1-\alpha_i)\, \check{G}_i T_i^{(s)} - \left(1-\alpha_i^2\right) \frac{T_i^{(s)\,2}}{2} - (1-\alpha_i\beta)\, \check{Q}_i \tau_{part} \right] \\ \rightarrow& B_i^{(s)\,2} \check{C}_i \left[(1-\alpha_i)\, \check{G}_i T_i^{(s)} - \check{Q}_i \tau_{part} \right] - \check{C}_i \left\langle \gamma_i^2 \right\rangle \end{aligned} \tag{B.38}$$

Finally:

$$\begin{aligned}\langle \Gamma_i \Phi_i \rangle =& B_i^{(s)\,2} \check{C}_i^2 \left\{ \left[(1-\alpha_i)\, T_i^{(s)} + (1-\beta)\, \check{K}_i \tau_{part} \right] \check{G}_i - \left(1-\alpha_i^2\right) \frac{T_i^{(s)\,2}}{2} \right. \\ & \left. - \left(1-\beta^2\right) \frac{\check{K}_i^2 \tau_{part}^2}{2} - (1-\alpha_i\beta)\, \check{K}_i T_i^{(s)} \tau_{part} \right\} \\ \rightarrow& B_i^{(s)\,2} \check{C}_i^2 \left\{ \left[(1-\alpha_i)\, T_i^{(s)} + \check{K}_i \tau_{part} \right] \check{G}_i - \left(1-\alpha_i^2\right) \frac{T_i^{(s)\,2}}{2} \right. \\ & \left. - \frac{\check{K}_i^2 \tau_{part}^2}{2} - \check{K}_i T_i^{(s)} \tau_{part} \right\} \end{aligned} \tag{B.39}$$

For matrix **L**, the coefficient L_{11} remains unchanged, and there are two significant results:

$$\begin{aligned} L_{21} =& \frac{\langle \gamma_i \Gamma_i \rangle}{L_{11}} \\ \rightarrow& \check{C}_i \sqrt{\left\langle \gamma_i^2 \right\rangle} + \frac{B_i^{(s)\,2} \check{C}_i \check{Q}_i}{\sqrt{\left\langle \gamma_i^2 \right\rangle}} \\ \rightarrow& L_{11} + \left(\check{C}_i - 1\right) L_{11} + \frac{B_i^{(s)\,2} \check{C}_i \check{Q}_i}{L_{11}} \end{aligned} \tag{B.40}$$

And:

$$\begin{aligned} L_{22} =& \sqrt{\left\langle \Gamma_i^2 \right\rangle - L_{21}^2} \\ \rightarrow& \left[\left(B_i^{(s)} \check{C}_i\right)^2 \frac{\check{K}_i^2 \tau_{part}}{2} - \frac{B_i^{(s)\,4} \check{C}_i^2 \check{Q}_i^2}{\left\langle \gamma_i^2 \right\rangle} \right]^{\frac{1}{2}} \end{aligned} \tag{B.41}$$

The others coefficient of the matrix **L** are all defined, but they are less significant, and therefore they will not be presented. Since L_{11} remains unchanged, γ_i is also unchanged. The following conclusions can be done on Γ_i:

$$\begin{aligned} \Gamma_i =& L_{21} \xi_{\gamma_i} + L_{22} \xi_{\Gamma_i} \\ \rightarrow& \gamma_i + \left[\left(\check{C}_i - 1\right) L_{11} + \frac{B_i^{(s)\,2} \check{C}_i \check{Q}_i}{L_{11}} \right] \xi_{\gamma_i} \\ & + \left[\left(B_i^{(s)} \check{C}_i\right)^2 \frac{\check{K}_i^2 \tau_{part}}{2} - \frac{B_i^{(s)\,4} \check{C}_i^2 \check{Q}_i^2}{L_{11}^2} \right]^{\frac{1}{2}} \xi_{\Gamma_i} \end{aligned} \tag{B.42}$$

The final stochastic integral Φ_i is determined, as L_{31}, L_{32} and L_{33} are all determined. Furthermore the fluid velocity $U_i^{(s)}$ will remain unchanged, and the solid body velocity is given by:

$$\begin{aligned}
V_i(t) =&\beta V_i(t_0) + (1-\beta)\left(C_i^{(s)}T_i^{(s)} + F_{i,c}\tau_{part}\right)\\
&+ (\alpha_i - \beta)\check{C}_i\left(U_i^{(s)}(t_0) - C_i^{(s)}T_i^{(s)}\right)\\
&+ \Gamma_i\\
\rightarrow&\alpha_i U_i^{(s)}(t_0) - \alpha_i C_i^{(s)}T_i^{(s)} + C_i^{(s)}T_i^{(s)} + \gamma_i\\
&+ \alpha_i\left(\check{C}_i - 1\right)U_i^{(s)}(t_0) - \alpha_i\left(\check{C}_i - 1\right)C_i^{(s)}T_i^{(s)}\\
&+ F_{i,c}\tau_{part} + \left[\left(\check{C}_i - 1\right)L_{11} + \frac{B_i^{(s)\,2}\check{C}_i\check{Q}_i}{L_{11}}\right]\xi_{\gamma_i}\\
&+ \left[\left(B_i^{(s)}\check{C}_i\right)^2\frac{\check{K}_i^2\tau_{part}}{2} - \frac{B_i^{(s)\,4}\check{C}_i^2\check{Q}_i^2}{L_{11}^2}\right]^{\frac{1}{2}}\xi_{\Gamma_i}\\
\rightarrow&U_i^{(s)}(t) + F_{i,c}\tau_{part} + f\left(F_a, T_i^{(s)}, \tau_{part}\right)
\end{aligned} \tag{B.43}$$

Therefore the particle will advance at a velocity close to the fluid velocity, with minor differences linked to the momentum and buoyancy effects of the particle. Furthermore assuming that $T_i^{(s)}$ is of the same order as dt will make the equation easier to understand:

$$T_i^{(s)} \gg \tau_{part} \tag{B.44a}$$

$$\begin{aligned}
\check{C}_i =&\frac{T_i^{(s)} - F_a\tau_{part}}{T_i^{(s)} - \tau_{part}}\\
\rightarrow&1
\end{aligned} \tag{B.44b}$$

$$\begin{aligned}
\check{K}_i =&\frac{F_a}{\check{C}_i} - 1\\
\rightarrow&F_a - 1
\end{aligned} \tag{B.44c}$$

$$\begin{aligned}
\check{Q}_i =&\check{K}_i\frac{T_i^{(s)}\tau_{part}}{T_i^{(s)} + \tau_{part}}\\
\rightarrow&\left(F_a - 1\right)\tau_{part}
\end{aligned} \tag{B.44d}$$

Using these simplifications the velocity of the solid particle becomes:

$$V_i(t) \rightarrow U_i^{(s)}(t) + F_{i,c}\tau_{part} + \frac{B_i^{(s)}\left(F_a - 1\right)}{2}\sqrt{\tau_{part}}\xi_{\Gamma_i} \tag{B.45}$$

The position of the particle is given by:

$$\begin{aligned}
X_i(t) =&X_i(t_0) + (1-\beta)\tau_{part}V_i(t_0) + \left[dt - (1-\beta)\tau_{part}\right]\left(C_i^{(s)}T_i^{(s)} + F_{i,c}\tau_{part}\right)\\
&+ \check{C}_i\left(U_i^{(s)}(t_0) - C_i^{(s)}T_i^{(s)}\right)\left[(1-\alpha_i)T_i^{(s)} - (1-\beta)\tau_{part}\right]\\
&+ \Phi_i\\
\rightarrow&X_i(t_0) + \tau_{part}V_i(t_0) + \left(C_i^{(s)}T_i^{(s)} + F_{i,c}\tau_{part}\right)dt\\
&+ \check{C}_i\left(U_i^{(s)}(t_0) - C_i^{(s)}T_i^{(s)}\right)\left[(1-\alpha_i)T_i^{(s)} - \tau_{part}\right]\\
&+ \Phi_i
\end{aligned} \tag{B.46}$$

There is multiple of $dt\tau_{part}$ that appears, but since this scenario could only occurs for very small τ_{part}, it can be assumed that the position of the particle can always be determined.

B.4 For a time step dt much smaller than the particle relaxation time τ_{part}

For this scenario the following simplifications can be done:

$$\frac{dt}{\tau_{part}} \to 0 \tag{B.47a}$$

$$\beta \to 1 \tag{B.47b}$$

The covariance $\langle \gamma_i^2 \rangle$ remains unchanged, as it is independent of β. However the remaining covariances are equal to:

$$\begin{aligned}
\langle \Gamma_i^2 \rangle &= \left(B_i^{(s)} \check{C}_i\right)^2 \left[\left(1-\alpha_i^2\right)\frac{T_i^{(s)}}{2} + \left(1-\beta^2\right)\frac{\check{K}_i^2 \tau_{part}}{2} + 2\left(1-\alpha_i\beta\right)\check{Q}_i\right] \\
&\to \left(B_i^{(s)} \check{C}_i\right)^2 \left[\left(1-\alpha_i^2\right)\frac{T_i^{(s)}}{2} + \check{K}_i^2 dt + 2\left(1-\alpha_i+\alpha_i\frac{dt}{\tau_{part}}\right)\check{Q}_i\right] \\
&\to \check{C}_i^2 \langle \gamma_i^2 \rangle + \left(B_i^{(s)} \check{C}_i\right)^2 \left[\check{K}_i^2 dt + 2\left(1-\alpha_i+\alpha_i\frac{dt}{\tau_{part}}\right)\check{Q}_i\right]
\end{aligned} \tag{B.48}$$

The following can be defined:

$$\check{K}_i dt = \frac{T_i^{(s)}\left(1-F_a\right)}{T_i^{(s)} - F_a \tau_{part}} dt \tag{B.49}$$

And:

$$\begin{aligned}
\frac{dt}{\tau_{part}}\check{Q}_i =& \frac{dt}{\tau_{part}} \frac{T_i^{(s)}\tau_{part}}{T_i^{(s)}+\tau_{part}} \frac{T_i^{(s)}\left(1-F_a\right)}{T_i^{(s)} - F_a\tau_{part}} \\
=& dt \frac{T_i^{(s)}}{T_i^{(s)}+\tau_{part}} \frac{T_i^{(s)}\left(1-F_a\right)}{T_i^{(s)} - F_a\tau_{part}}
\end{aligned} \tag{B.50}$$

Both of these variables can be determined for all values of $T_i^{(s)}$ and τ_{part}, and therefore $\langle \Gamma_i^2 \rangle$ as well. Furthermore:

$$\begin{aligned}
\langle \Phi_i^2 \rangle =& B_i^{(s)\,2} \check{C}_i^2 \left\{ \check{G}_i^2 dt + \left(1-\alpha_i^2\right)\frac{T_i^{(s)\,3}}{2} + \left(1-\beta^2\right)\frac{\check{K}_i^2\tau_{part}^3}{2} \right. \\
& \left. -2\check{G}_i\left[\left(1-\alpha_i\right)T_i^{(s)\,2} + \left(1-\beta\right)\check{K}_i\tau_{part}^2\right] + 2\left(1-\alpha_i\beta\right)\check{Q}_i T_i^{(s)}\tau_{part} \right\} \\
\to & B_i^{(s)\,2} \check{C}_i^2 \left\{ \check{G}_i^2 dt + \left(1-\alpha_i^2\right)\frac{T_i^{(s)\,3}}{2} + \check{K}_i^2\tau_{part}^2 dt \right. \\
& \left. -2\check{G}_i\left[\left(1-\alpha_i\right)T_i^{(s)\,2} + \check{K}_i\tau_{part} dt\right] + 2\left(1-\alpha_i+\alpha_i\frac{dt}{\tau_{part}}\right)\check{Q}_i T_i^{(s)}\tau_{part} \right\}
\end{aligned} \tag{B.51}$$

However if $\tau_{part}dt$ is undetermined than $\langle \Phi_i^2 \rangle$ is also undetermined. Inaddition:

$$\begin{aligned}
\langle \gamma_i \Gamma_i \rangle =& B_i^{(s)\,2} \check{C}_i \left[\left(1-\alpha_i^2\right)\frac{T_i^{(s)}}{2} + \left(1-\alpha_i\beta\right)\check{Q}_i\right] \\
\to & \check{C}_i \langle \gamma_i^2 \rangle + B_i^{(s)\,2} \check{C}_i \left(1-\alpha_i+\alpha_i\frac{dt}{\tau_{part}}\right)\check{Q}_i
\end{aligned} \tag{B.52}$$

This covariance is therefore determined. Furthermore $\langle \gamma_i \Phi_i \rangle$ is given by:

$$\begin{aligned}\langle \gamma_i \Phi_i \rangle =& B_i^{(s)\,2} \check{C}_i \left[(1-\alpha_i)\, \check{G}_i T_i^{(s)} - \left(1-\alpha_i^2\right) \frac{T_i^{(s)\,2}}{2} - (1-\alpha_i \beta)\, \check{Q}_i \tau_{part} \right] \\ \rightarrow & B_i^{(s)\,2} \check{C}_i \left[(1-\alpha_i)\, \check{G}_i T_i^{(s)} - \left(1-\alpha_i^2\right) \frac{T_i^{(s)\,2}}{2} - (1-\alpha_i)\, \check{Q}_i \tau_{part} - \alpha_i \check{Q}_i dt \right]\end{aligned} \tag{B.53}$$

Because of $\check{Q}_i dt$ this covariance could also be undetermined. Finally:

$$\begin{aligned}\langle \Gamma_i \Phi_i \rangle =& B_i^{(s)\,2} \check{C}_i^2 \left\{ \left[(1-\alpha_i)\, T_i^{(s)} + (1-\beta)\, \check{K}_i \tau_{part} \right] \check{G}_i - \left(1-\alpha_i^2\right) \frac{T_i^{(s)\,2}}{2} \right. \\ & \left. - \left(1-\beta^2\right) \frac{\check{K}_i^2 \tau_{part}^2}{2} - (1-\alpha_i \beta)\, \check{K}_i T_i^{(s)} \tau_{part} \right\} \\ \rightarrow & B_i^{(s)\,2} \check{C}_i^2 \left\{ \left[(1-\alpha_i)\, T_i^{(s)} + \check{K}_i dt \right] \check{G}_i - \left(1-\alpha_i^2\right) \frac{T_i^{(s)\,2}}{2} \right. \\ & \left. - \check{K}_i^2 \tau_{part} dt - (1-\alpha_i)\, \check{K}_i T_i^{(s)} \tau_{part} - \alpha_i \check{K}_i T_i^{(s)} dt \right\}\end{aligned} \tag{B.54}$$

This covariance could also be undetermined.

For the coefficients of matrix **L**, the first coefficient L_{11} will remain unchanged, and the two following coefficients give significant results:

$$\begin{aligned}L_{21} =& \frac{\langle \gamma_i \Gamma_i \rangle}{L_{11}} \\ \rightarrow & \check{C}_i \sqrt{\langle \gamma_i^2 \rangle} + \frac{B_i^{(s)\,2} \check{C}_i \left(1-\alpha_i+\alpha_i \frac{dt}{\tau_{part}}\right) \check{Q}_i}{\sqrt{\langle \gamma_i^2 \rangle}} \\ \rightarrow & \check{C}_i L_{11} + \frac{B_i^{(s)\,2} \check{C}_i \left(1-\alpha_i+\alpha_i \frac{dt}{\tau_{part}}\right) \check{Q}_i}{L_{11}}\end{aligned} \tag{B.55}$$

And:

$$\begin{aligned}L_{22} =& \sqrt{\langle \Gamma_i^2 \rangle - L_{21}^2} \\ \rightarrow & \left[\left(B_i^{(s)} \check{C}_i\right)^2 \check{K}_i^2 dt + \frac{B_i^{(s)\,4} \check{C}_i^2 \left(1-\alpha_i+\alpha_i \frac{dt}{\tau_{part}}\right)^2 \check{Q}_i^2}{L_{11}^2} \right]^{\frac{1}{2}}\end{aligned} \tag{B.56}$$

The coefficients L_{31}, L_{32} and L_{33} could however be undetermined, because of the covariances that are required to calculate them.

The stochastic integral γ_i will remain unchanged, however Γ_i can be written as:

$$
\begin{aligned}
\Gamma_i =& L_{21}\xi_{\gamma_i} + L_{22}\xi_{\Gamma_i} \\
\rightarrow& \left[\check{C}_i L_{11} + \frac{B_i^{(s)\,2}\check{C}_i\left(1-\alpha_i+\alpha_i\frac{dt}{\tau_{part}}\right)\check{Q}_i}{L_{11}}\right]\xi_{\gamma_i} \\
&+\left[\left(B_i^{(s)}\check{C}_i\right)^2\check{K}_i^2 dt + \frac{B_i^{(s)\,4}\check{C}_i^2\left(1-\alpha_i+\alpha_i\frac{dt}{\tau_{part}}\right)^2\check{Q}_i^2}{L_{11}^2}\right]^{\frac{1}{2}}\xi_{\Gamma_i} \\
\rightarrow& \check{C}_i\gamma_i + \frac{B_i^{(s)\,2}\check{C}_i\left(1-\alpha_i+\alpha_i\frac{dt}{\tau_{part}}\right)\check{Q}_i}{L_{11}}\xi_{\gamma_i} \\
&+\left[\left(B_i^{(s)}\check{C}_i\right)^2\check{K}_i^2 dt - \frac{B_i^{(s)\,2}\check{C}_i\left(1-\alpha_i+\alpha_i\frac{dt}{\tau_{part}}\right)\check{Q}_i}{L_{11}}\right]\xi_{\Gamma_i}
\end{aligned}
\tag{B.57}
$$

In addition the integral Φ_i might be undetermined, because L_{31}, L_{32} and L_{33} are only determined if $dt\tau_{part}$ is determined.

Furthermore the fluid velocity $U_i^{(s)}$ will remain unchanged, whereas the solid body velocity is given by:

$$
\begin{aligned}
V_i(t) =& \beta V_i(t_0) + (1-\beta)\left(C_i^{(s)}T_i^{(s)} + F_{i,c}\tau_{part}\right) \\
&+ (\alpha_i-\beta)\check{C}_i\left(U_i^{(s)}(t_0) - C_i^{(s)}T_i^{(s)}\right) \\
&+ \Gamma_i \\
\rightarrow& V_i(t_0) + F_{i,c}dt \\
&+ \check{C}_i\left(U_i^{(s)}(t) - U_i^{(s)}(t_0)\right) \\
&+ \frac{B_i^{(s)\,2}\check{C}_i\left(1-\alpha_i+\alpha_i\frac{dt}{\tau_{part}}\right)\check{Q}_i}{L_{11}}\xi_{\gamma_i} \\
&+\left[\left(B_i^{(s)}\check{C}_i\right)^2\check{K}_i^2 dt - \frac{B_i^{(s)\,2}\check{C}_i\left(1-\alpha_i+\alpha_i\frac{dt}{\tau_{part}}\right)\check{Q}_i}{L_{11}}\right]\xi_{\Gamma_i} \\
\rightarrow& V_i(t_0) + F_{i,c}dt + \check{C}_i dU_i^{(s)}(t_0) + f\left(F_a, T_i^{(s)}, \tau_{part}\right)
\end{aligned}
\tag{B.58}
$$

Therefore the particle velocity will be determined mostly through the external buoyant forces, and with slight differences resulting from the momentum of the fluid. In addition assuming that $T_i^{(s)}$ is of the same order as dt will make the equation easier to understand:

$$
T_i^{(s)} \ll \tau_{part} \tag{B.59a}
$$

$$
\begin{aligned}
\check{C}_i =& \frac{T_i^{(s)} - F_a\tau_{part}}{-\tau_{part}} \\
\rightarrow& F_a
\end{aligned}
\tag{B.59b}
$$

$$
\begin{aligned}
\check{K}_i =& \frac{F_a}{\check{C}_i} - 1 \\
\rightarrow& 0
\end{aligned}
\tag{B.59c}
$$

$$
\begin{aligned}
\check{Q}_i =& \check{K}_i\frac{T_i^{(s)}\tau_{part}}{T_i^{(s)} + \tau_{part}} \\
\rightarrow& 0
\end{aligned}
\tag{B.59d}
$$

Which gives the following expression for the solid particle velocity:

$$V_i(t) \rightarrow V_i(t_0) + F_{i,c}dt + F_a dU_i^{(s)}(t_0) \tag{B.60}$$

The position of a solid particle is given by:

$$\begin{aligned} X_i(t) =& X_i(t_0) + (1-\beta)\,\tau_{part} V_i(t_0) + \left[dt - (1-\beta)\,\tau_{part}\right]\left(C_i^{(s)} T_i^{(s)} + F_{i,c}\tau_{part}\right) \\ &+ \check{C}_i\left(U_i^{(s)}(t_0) - C_i^{(s)} T_i^{(s)}\right)\left[(1-\alpha_i)\,T_i^{(s)} - (1-\beta)\,\tau_{part}\right] \\ &+ \Phi_i \\ \rightarrow& X_i(t_0) + V_i(t_0)dt \\ &+ \check{C}_i\left(U_i^{(s)}(t_0) - C_i^{(s)} T_i^{(s)}\right)\left[(1-\alpha_i)\,T_i^{(s)} - dt\right] \\ &+ \Phi_i \end{aligned} \tag{B.61}$$

Therefore $X_i(t)$ is determined only if Φ_i is also determined, which requires $dt\tau_{part}$ to be determined.

Appendix C

Video particle tracking image processing

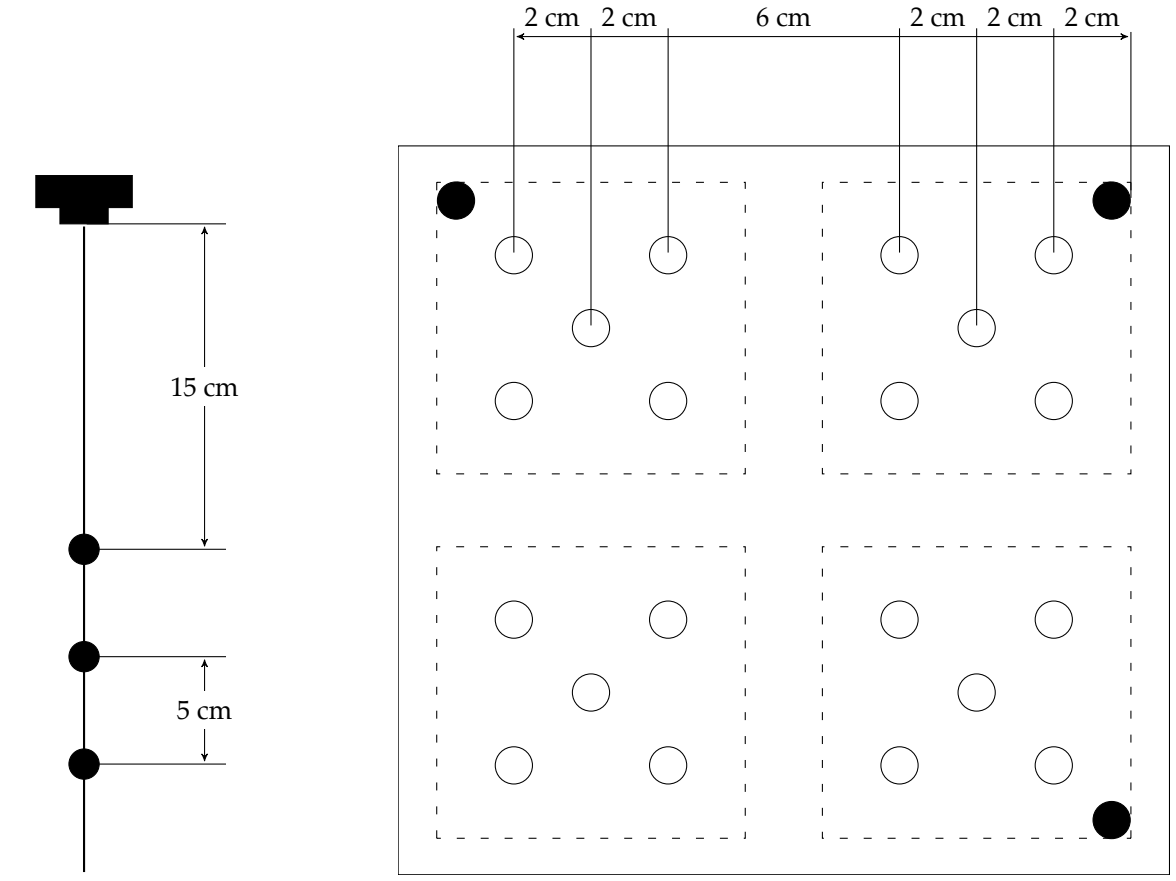
Où sont expliquées les étapes du traitement des images nécessaires pour obtenir la trajectoire des particules en milimètres, pour les expériences des chapitres 7 et 8.

C.1 Methodology for the image processing

The image processing of images recorded by two perpendicular cameras is done in three stages. Firstly a calibration is necessary to correct for the parallax of the cameras. The images are then processed to obtain the positions of each recorded particle in millimetres. Finally the third process links the particles recorded in one camera to the particles recorded in the other, so that the three-dimensional position of the particles can be given in millimetres.

C.1.1 Calibrating the camera fields

The oscillating grids experiment described in chapter 7 was set up so that the two cameras were placed perpendicular to two neighbouring sides of the water tank in such a way that the cameras were placed at the same level, and that the recorded volume was the less deformed possible. Nonetheless the volume observed is not cubic (because of the parallax of the cameras) and a set of calibrations were done so that the constants allowing a conversion from pixels to millimetres could be done inside the volume of measurements. This was done by placing a fishing wire with spherical weights attached at different locations within the volume of measurement, see figure C.1.



(a) Fishing wire (b) Position of the fishing wire

Figure C.1: The tools used to calibrate the cameras of the oscillating grids experiment. The fishing wire (a) is placed in the holes of the plate, represented in figure (b) by the white circles. The plate was fixed on the top oscillating grid with screws, the black circles in figure (b). Therefore spherical weights attached to fishing wire, the black circles of figure (a), enter the volume of measurement with a known position.

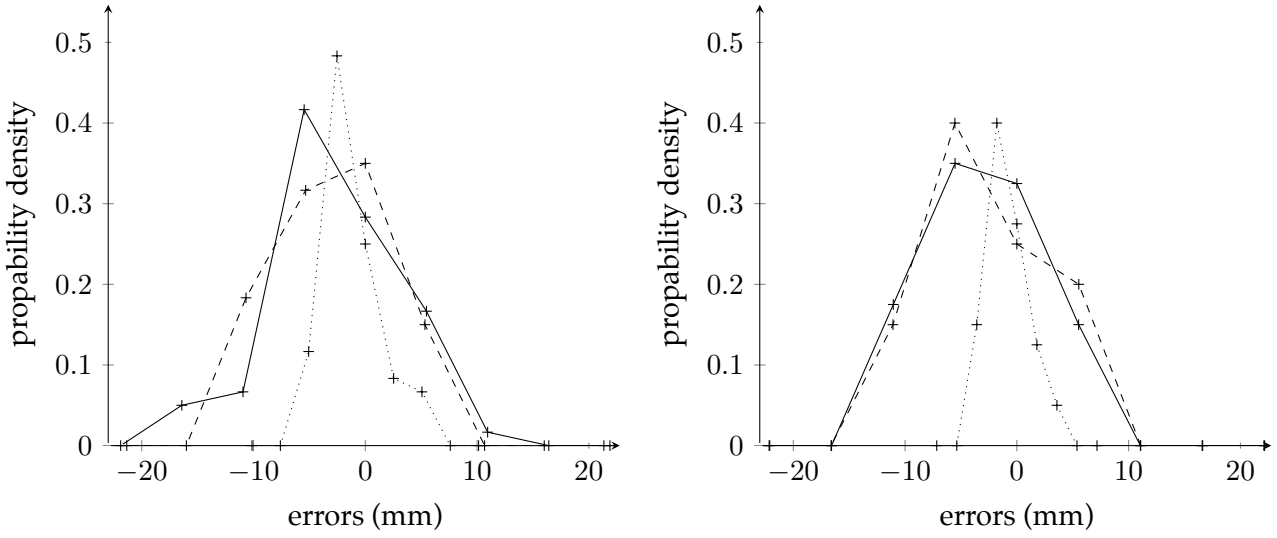
Since the position of the weights placed on the fishing wire are known, and the cameras records

these positions in pixels (see section C.1.2), then the constants of the relationship linking pixels to millimetres defined in Cordeiro Fernandes (2005) can be known:

$$\text{Camera 1:} \quad \frac{X_x(mm)}{X_x(pixels)} = \alpha_x X_y(mm) + \beta_x \; ; \qquad \frac{X_{z_1}(mm)}{X_{z_1}(pixels)} = \alpha_{z_1} X_y(mm) + \beta_{z_1} \tag{C.1a}$$

$$\text{Camera 2:} \quad \frac{X_y(mm)}{X_y(pixels)} = \alpha_y X_x(mm) + \beta_y \; ; \qquad \frac{X_{z_2}(mm)}{X_{z_2}(pixels)} = \alpha_{z_2} X_x(mm) + \beta_{z_2} \tag{C.1b}$$

This calibration allows to find the maximum difference in level of the two cameras, $X_{z_1}(pixels)$ and $X_{z_2}(pixels)$, which can be used to link the position of the particles seen by the two cameras (see section C.1.3), as well as the distribution of the errors between the real positions in millimetres and those calculated from equations C.1, see figure C.2.



(a) $\rho_f = 1000$ kg·m^{-3} (b) $\rho_f = 1084$ kg·m^{-3}

Figure C.2: Probability density functions of the errors on the positions of the fishing weights after the transform given by equations C.1. "—+—" errors along the x-axis, "- + -" errors along the y-axis and "· · + · ·" errors along the z-axis.

For the partially obstructed channel experiment described in chapter 8, only one camera was used, as the volume of measurement is very shallow, and therefore it is reduced to a two dimensional problem. This means that only one camera is used, and the parallax of this camera can be neglected ($\simeq 0.5\%$). Nonetheless the equations C.1 can also be used and the camera calibration was done by placing a uniform dot pattern at two different heights into the window of measurement. Therefore to convert the positions from pixels to millimetres using a linear relation in one the following relation is used:

$$\frac{X_x(mm)}{X_x(pixels)} = \alpha_{z_1} X_{z_1}(mm) + \beta_x \tag{C.2a}$$

$$\frac{X_y(mm)}{X_y(pixels)} = \alpha_{z_1} X_{z_1}(mm) + \beta_y \tag{C.2b}$$

Where the value $X_{z_1}(mm)$ was imposed as half the maximum depth of the canal, i.e. 15 millimetres.

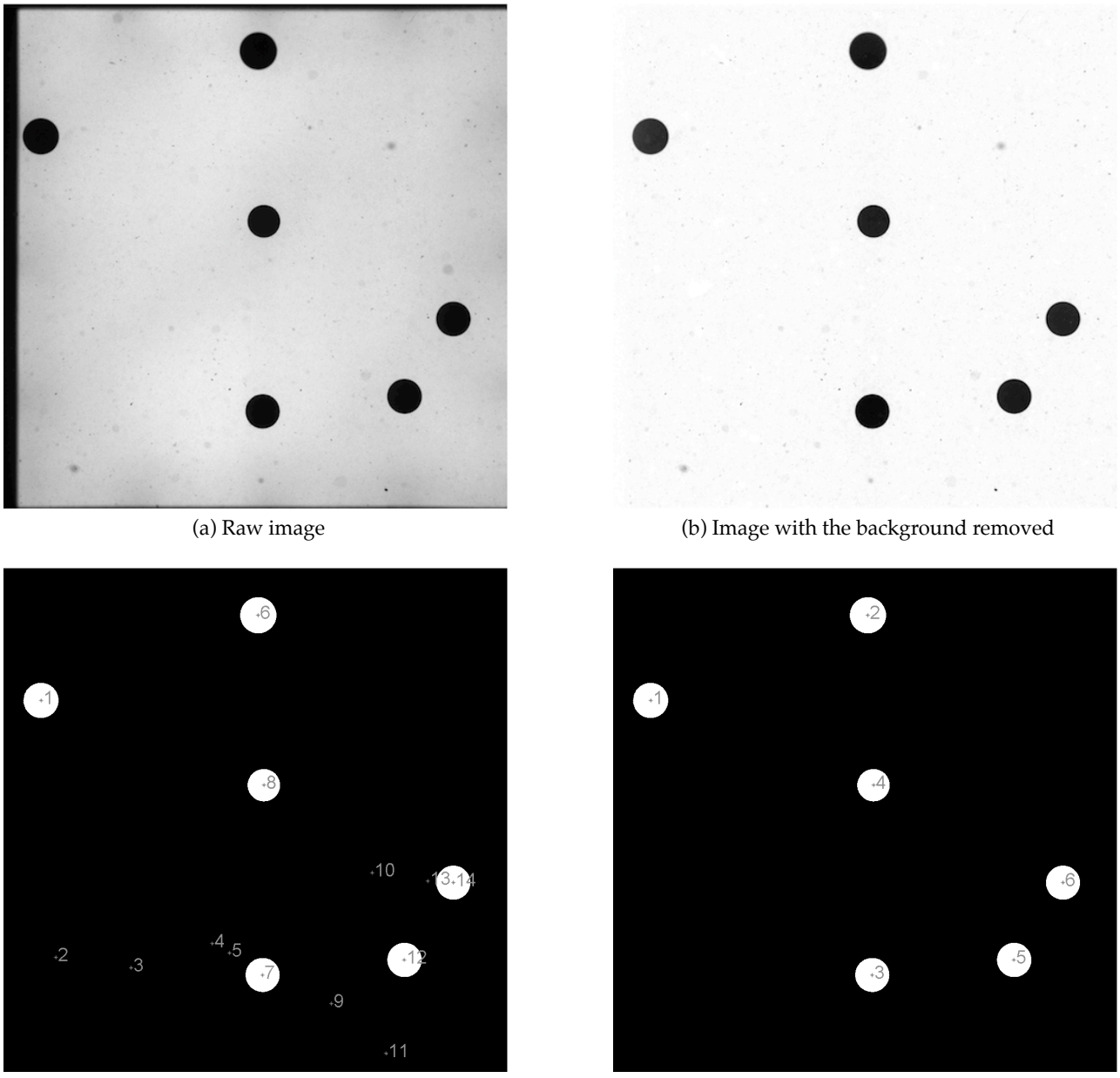
All the coefficients for the experiments of chapters 7 and 8 can be found in table C.1.

Table C.1: Coefficients used to calibrate the camera fields of the experiments presented in chapters 7 and 8. For the first experiment two fluid densities were used, which will affect the coefficients whereas for the second experiment the camera was placed at different positions in the canal.

	α_x	α_y	α_{z_1}	α_{z_2}	β_x	β_y	β_{z_1}	β_{z_2}
Exp. in chapt. 7, $\rho_f = 1000\,\mathrm{kg/m^3}$	4.79E−5	5.90E−5	−4.72E−5	−7.48E−7	0.0824	0.0824	0.0730	0.0729
Exp. in chapt. 7, $\rho_f = 1084\,\mathrm{kg/m^3}$	5.49E−5	6.73E−5	−4.35E−5	3.67E−6	0.0810	0.0810	0.0728	0.0733
Exp. in chapt. 8, window 1	-	-	−1.78E−4	-	0.521	0.521	-	-
Exp. in chapt. 8, window 2	-	-	−9.37E−5	-	0.521	0.521	-	-
Exp. in chapt. 8, window 3	-	-	−9.37E−5	-	0.521	0.521	-	-

C.1.2 Positions of the particles seen by a camera

The cameras used record images in grey scale. Each of these images can be considered as a matrix where each element represents the amount of gray of a pixel. Therefore the second step of the image processing extracts the positions of each solid body from these raw images. The steps of the image processing are shown in figure C.3.



(a) Raw image

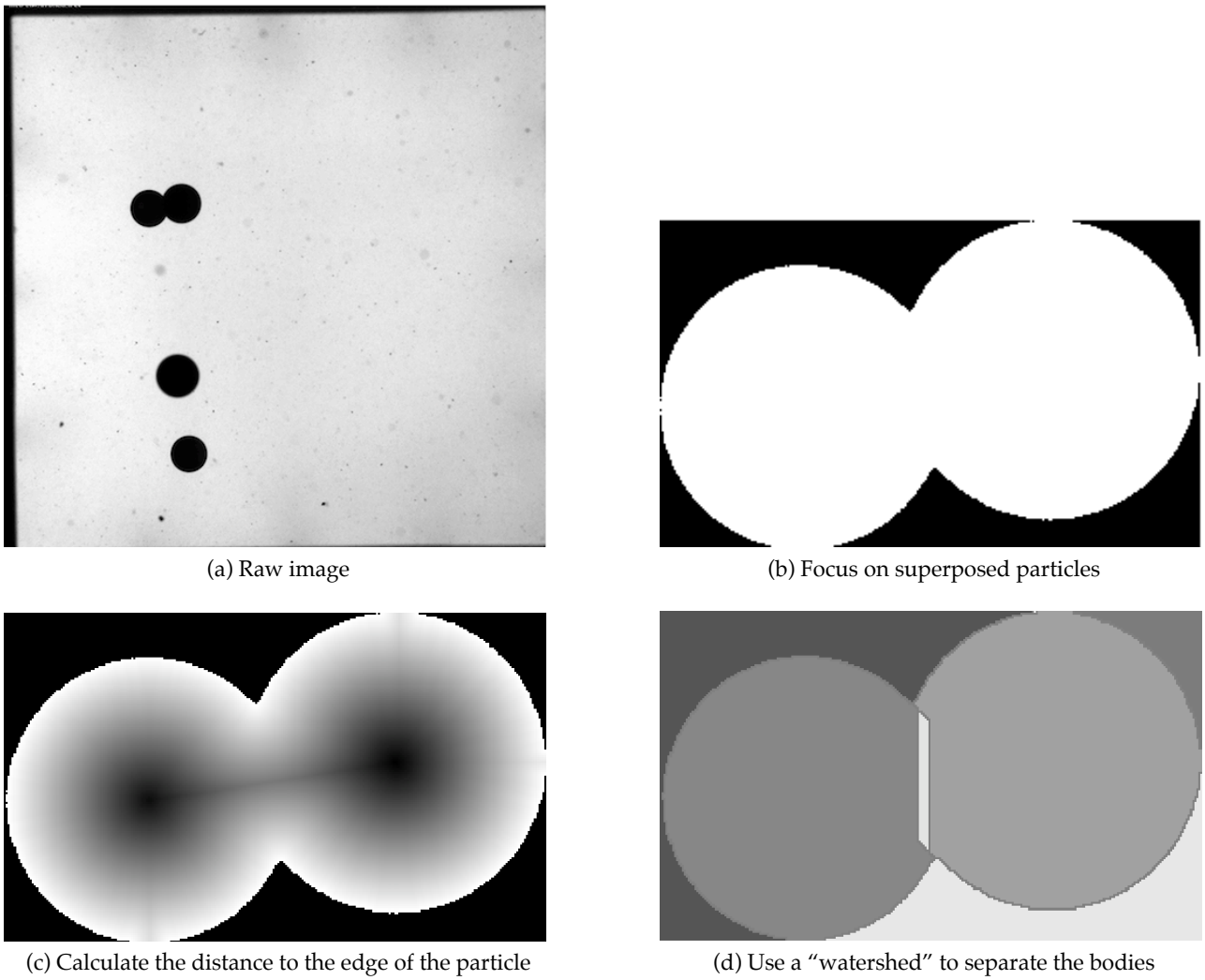
(b) Image with the background removed

(c) Image with a threshold applied

(d) Image with the impurities removed

Figure C.3: Steps necessary to obtain the position of the bodies from an image recorded by a camera.

In figure C.3 the classic stages of the image processing are shown. The process starts with a raw image (fig. C.3a) to which the background is subtracted (fig. C.3b). The background is found by averaging the images obtained before and after particles enter the window of measurement of a camera. From this image a threshold in the grey scale is set, and a new binary matrix is composed where the value is imposed to 0 below a certain amount of grey and 1 above. Therefore the solid bodies are represented by a group of ones in this binary matrix, for which the center can be calculated (see fig. C.3c). The impurities present in the fluid are also recorded as solid bodies, and therefore the area of those binary objects are calculated, and those that are too small are removed (fig. C.3d). However these are the classic steps but certain additional steps might be required, see figures C.4, C.5 and C.6.



(a) Raw image

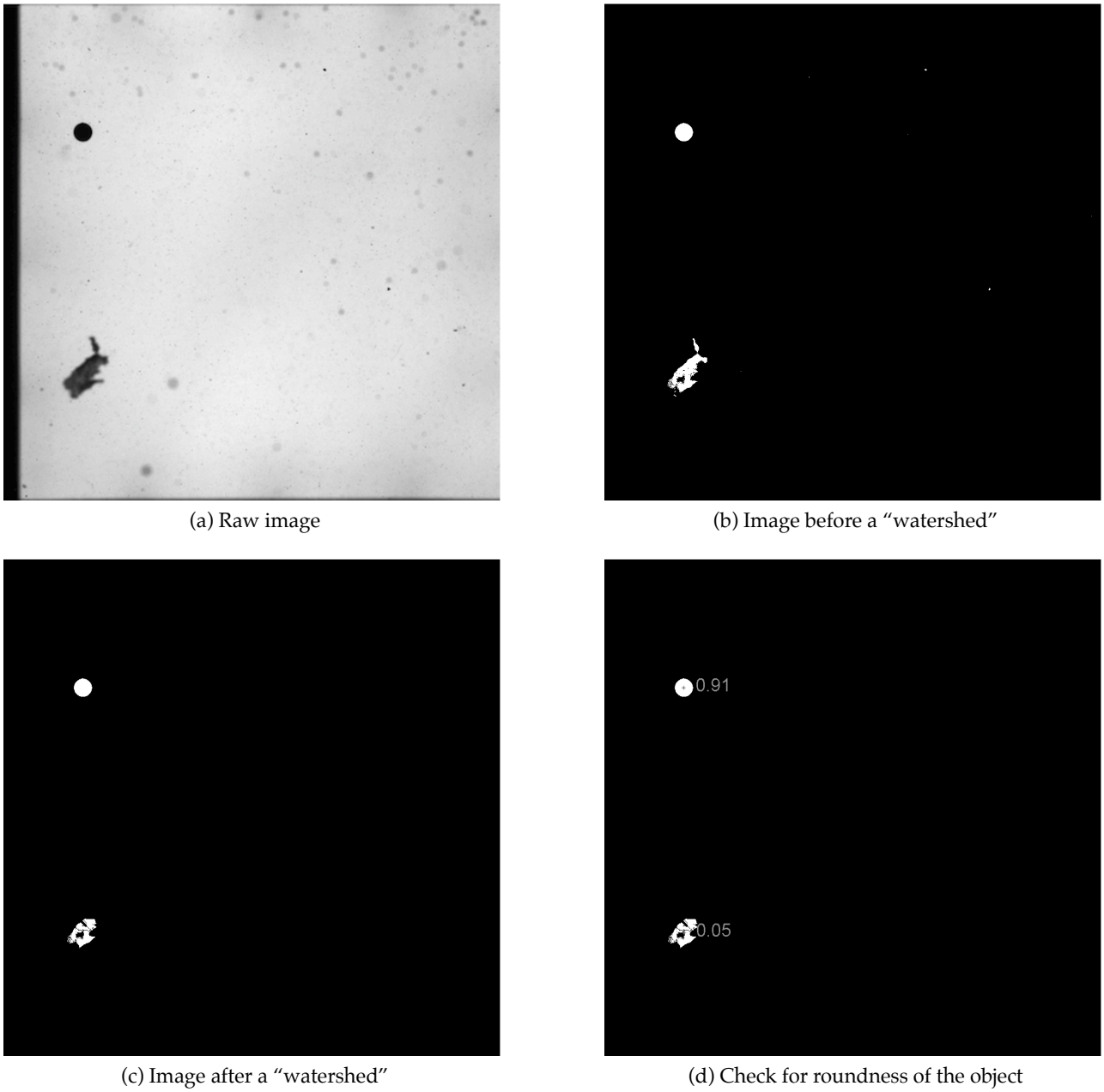
(b) Focus on superposed particles

(c) Calculate the distance to the edge of the particle

(d) Use a "watershed" to separate the bodies

Figure C.4: Steps required to find the position of two superposed bodies.

Figure C.4 illustrates the first problem that can arise in the image processing, where two bodies appear superposed in a recorded image. To treat this problem a focus is placed on the two superposed bodies, for example by looking at the area of the binary object which is greater than a single body (fig. C.4b). This binary object is then transformed into a grey scale object where the darkness represents the distance of a pixel from the edge (fig. C.4c). A "watershed" is then performed (fig. C.4d). The "watershed" is a process that originates from hydrology where it is used to separate drainage basin, and it can be used in image processing to separate superposed bodies, see Eddins (2002). The steps presented in figure C.3 are then repeated. Unfortunately certain large impurities present in the fluid can be considered as superposed bodies and therefore an additional processing step needs to be applied, see figure C.5.



(a) Raw image

(b) Image before a "watershed"

(c) Image after a "watershed"

(d) Check for roundness of the object

Figure C.5: Steps necessary to remove impurities the size of a particle.

Figure C.5 shows the steps necessary in the image processing to remove large impurities. This is done after a "watershed", through the calculation of the roundness of a binary object (this can be done because only spherical bodies were released in the experiments). This roundness R_{obj} is given by the following equation:

$$R_{obj} = \frac{4\pi A_{obj}}{P_{obj}^2} \tag{C.3}$$

Where A_{obj} is the area of the binary object, P_{obj} is its perimeter and every object with a roundness under a certain value is removed.

There is another difficulty that occurs for the image processing of the partially obstructed channel experiment. These images are very disturbed. This is because of the nature of the flow, which generates

a lot of air bubbles. This means that certain particles will be hidden by those bubbles, and certain bubbles might be mistaken for solid particles which is more troublesome, see figure C.6.

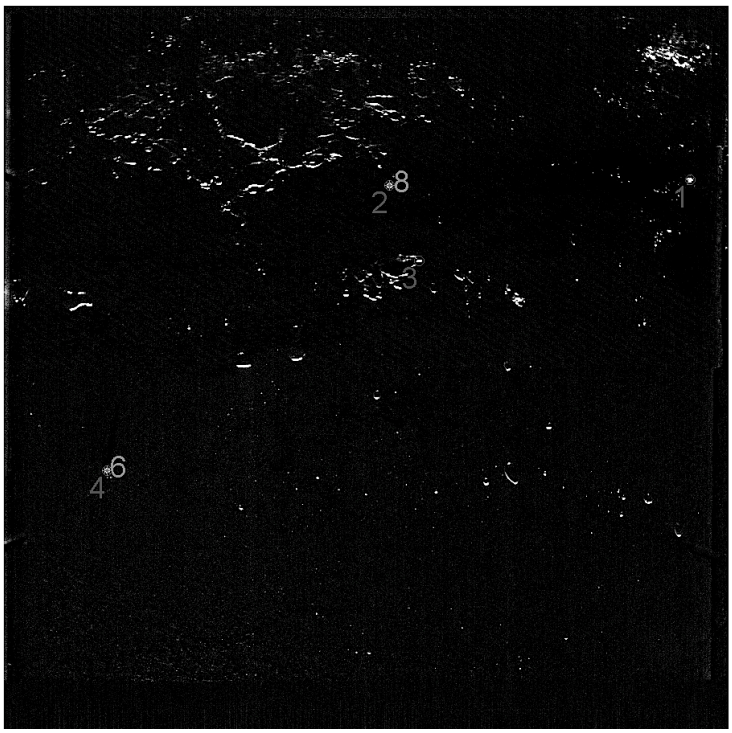


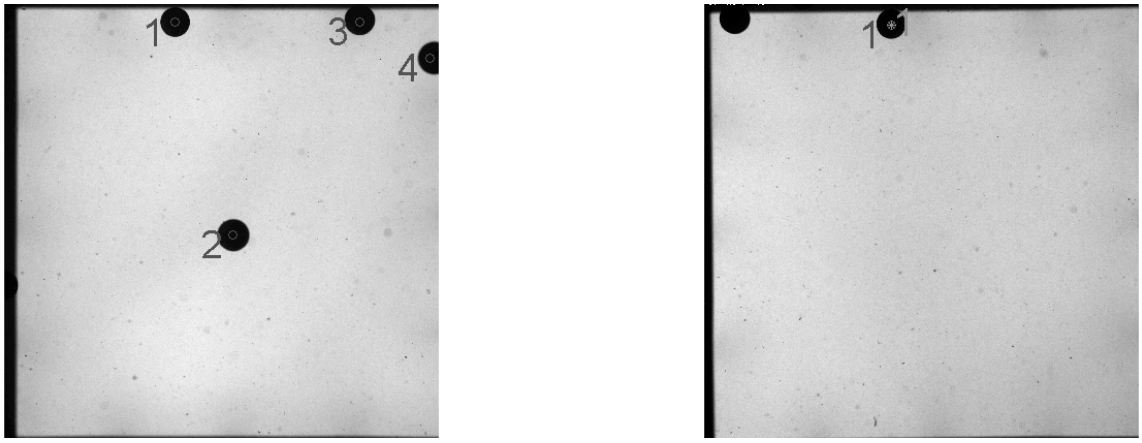
Figure C.6: A disturbed image due to the air entrainment. The number in dark grey shows the number of objects recognised as particles and the number in light grey shows actual solid bodies.

Figure C.6 shows an example of particles differentiated from entrained air bubbles. This is done by observing the temporal series of particle positions, as the air bubbles only appear for a brief amount of time and that way can be easily removed.

Now that the position of the particles are known in every images several additional steps need to be applied to associate the particle positions found from two perpendicular cameras.

C.1.3 Trajectories of particles in three dimensions

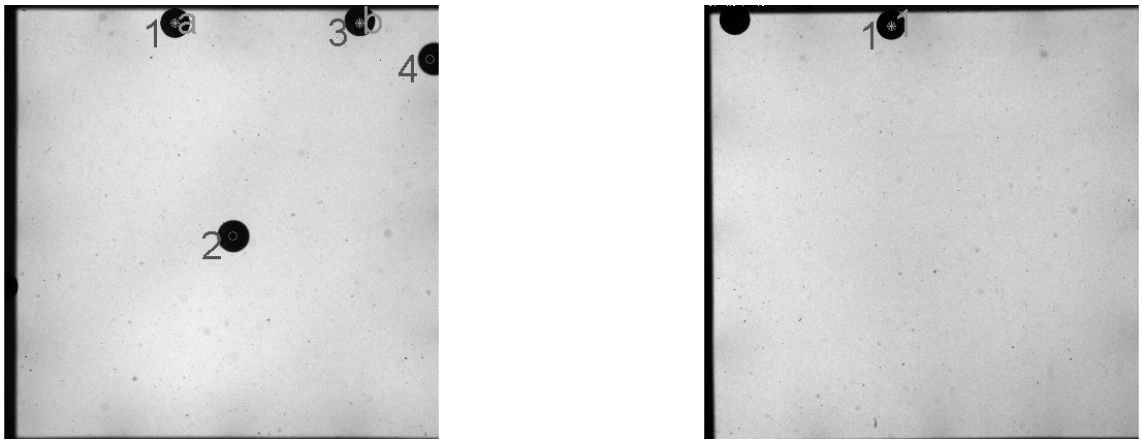
This image processing step is necessary just for the three-dimensional results of the oscillating grids experiment. This process is more complex than it appears as a particle can be seen by one camera but not the other. This is because the cameras have bigger depth than width of vision. This image processing is done in several steps. Firstly particles need to be present in both cameras, then the image with the lowest amount particles is taken as a starting point, see figure C.7.



(a) Camera 1 (b) Camera 2

Figure C.7: The starting point to associate recorded particles. The numbers in dark gray represent the particles found using the algorithm described in section C.1.2 and the number in light gray the particle which will serve as a starting point to search for its counterpart in the other camera.

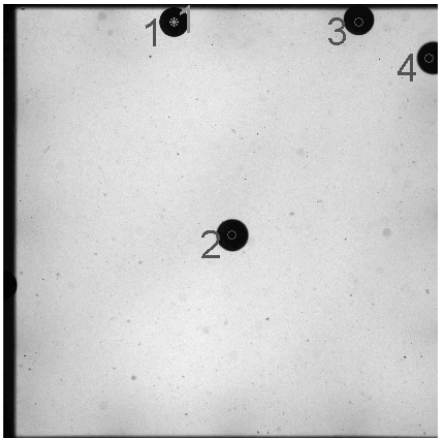
The next step is to find the counterpart of a particle in the image recorded by the other camera. To do this the difference in the vertical position is studied ($|X_{z_1}(pixels) - X_{z_2}(pixels)|$). The possible choices are then found using the maximal difference found from the calibration in section C.1.1. This next step is shown in figure C.8, for which several options are possible.



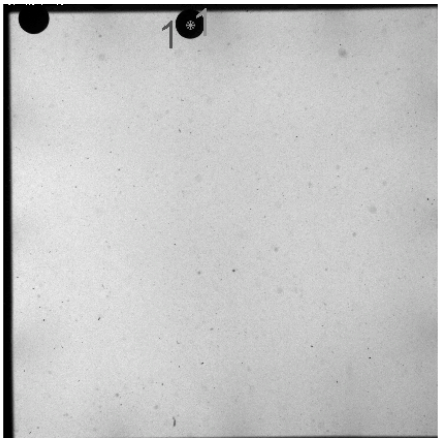
(a) Camera 1 (b) Camera 2

Figure C.8: Studying the different possible particle counterparts. The numbers in dark gray represent the particles found using the algorithm described in section C.1.2 and the letters in light gray the possible counterparts of the initial particle.

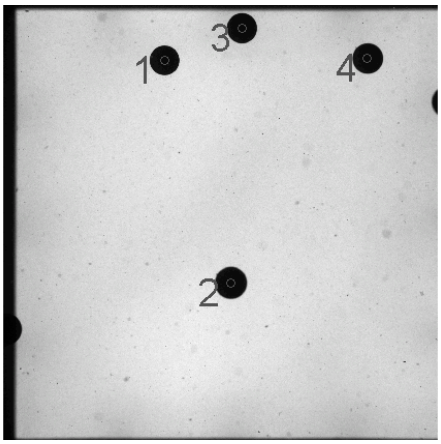
In the case where a particle can be associated to several bodies recorded in the other camera, then the closest non-associated body is chosen. Once a particle has been detected then its displacement is followed in all the following images by looking at the displacement between between two time steps. An example of a particle detected at time t and the all the recognised bodies in each camera at time $t = 1$ is given in figure C.9.



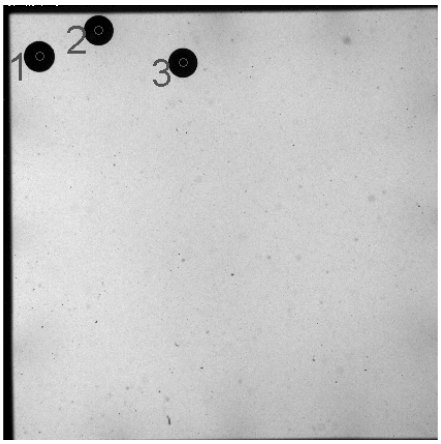
(a) Camera 1, at time t



(b) Camera 2, at time t



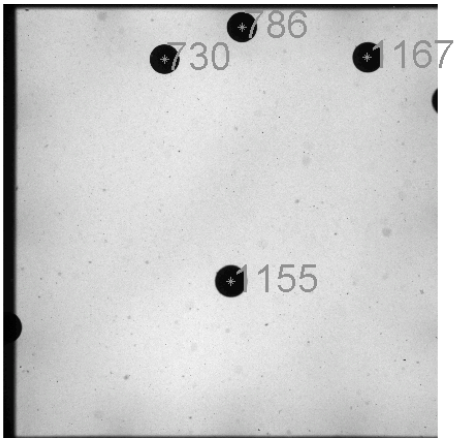
(c) Camera 1, at time $t + 1$



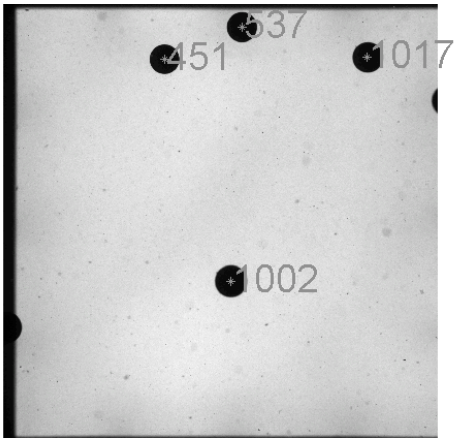
(d) Camera 2, at time $t + 1$

Figure C.9: A position of a particle at time t (figures a and b), and the recognised bodies in each camera at time $t = 1$ (figures c and d). The numbers in dark gray represent the particles found using the algorithm described in section C.1.2 and the number in light gray is the particle at time t for which its equivalent at time $t + 1$ is required.

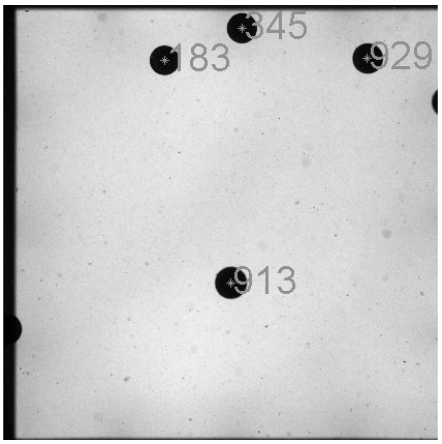
The following figure C.10 shows the distance travelled for all possible particle associations between time t and time $t + 1$.



(a) Camera 1, particle 1 of the camera 2



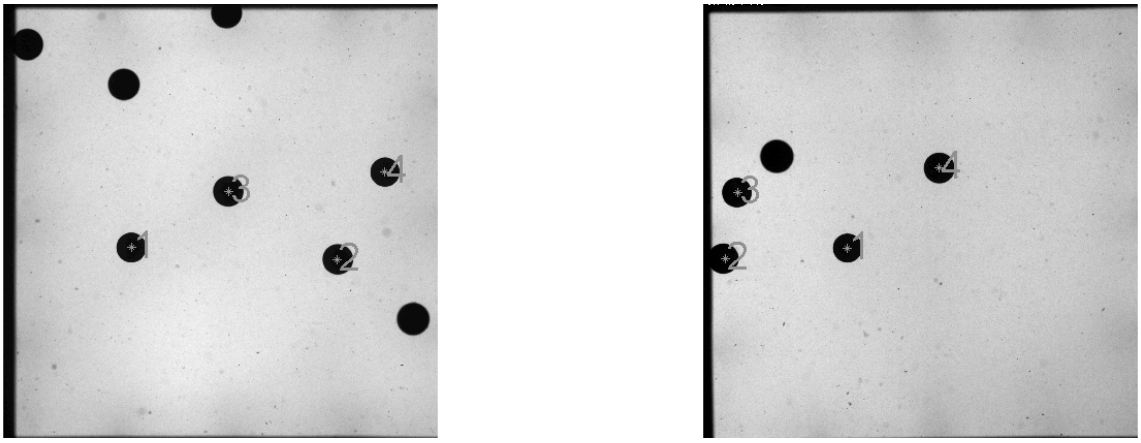
(b) Camera 1, particle 2 of the camera 2



(c) Camera 1, particle 3 of the camera 2

Figure C.10: Distance travelled from the intial position at time t. The distances (in pixels) are given by associating each body to the positions of the bodies 1 to 3 in the other camera (see figure C.9).

Thus the position of the particle at time $t + 1$ corresponds to the smallest displacement. However it is necessary to verify that this particle had not been previously allocated, or that this displacement is not too high. Finally it is also important to verify that the differences in vertical position, $|X_{z_1}(pixels) - X_{z_2}(pixels)|$, is not greater than the values found during the calibration. If all these criterion are not matched than the position of the particle might only be the second or third smallest displacement. This process is repeated until no more particle positions can correspond, and then the process starting from figure C.7. The figure C.11 shows an example of several associated bodies in the volume of measurement.



(a) Camera 1 (b) Camera 2

Figure C.11: Position of the particles present in the field of vision of both cameras. The numbers in dark gray represent the particles found using the algorithm described in section C.1.2 and the numbers in light gray the particles present in both cameras.

It should also be noted that because some particles can be superposed, the trajectories of some particles can superposed. This however does not affect the results, as this will only create erroneous particle trajectories, but the statistical ensemble of particle trajectories will still be correct.

For the partially obstructed channel experiment, the only step necessary is to link the positions of the particles at time t to those at time $t + 1$, however another step is added to verify that an air bubble was not mistaken for a solid particle, and that is to delete all the particle path that are smaller than five time steps, as the air bubbles only appear on camera for a short amount of time.

Once the positions of the bodies are found in pixels it is possible to convert these values in millimetres using equations C.1 for two cameras, or equation C.2a for one camera, and therefore the particle velocities can be found.

C.2 Flow charts of the algorithms used in the image processing

For simplicity each stage of the image processing will be simplified as a flow chart.

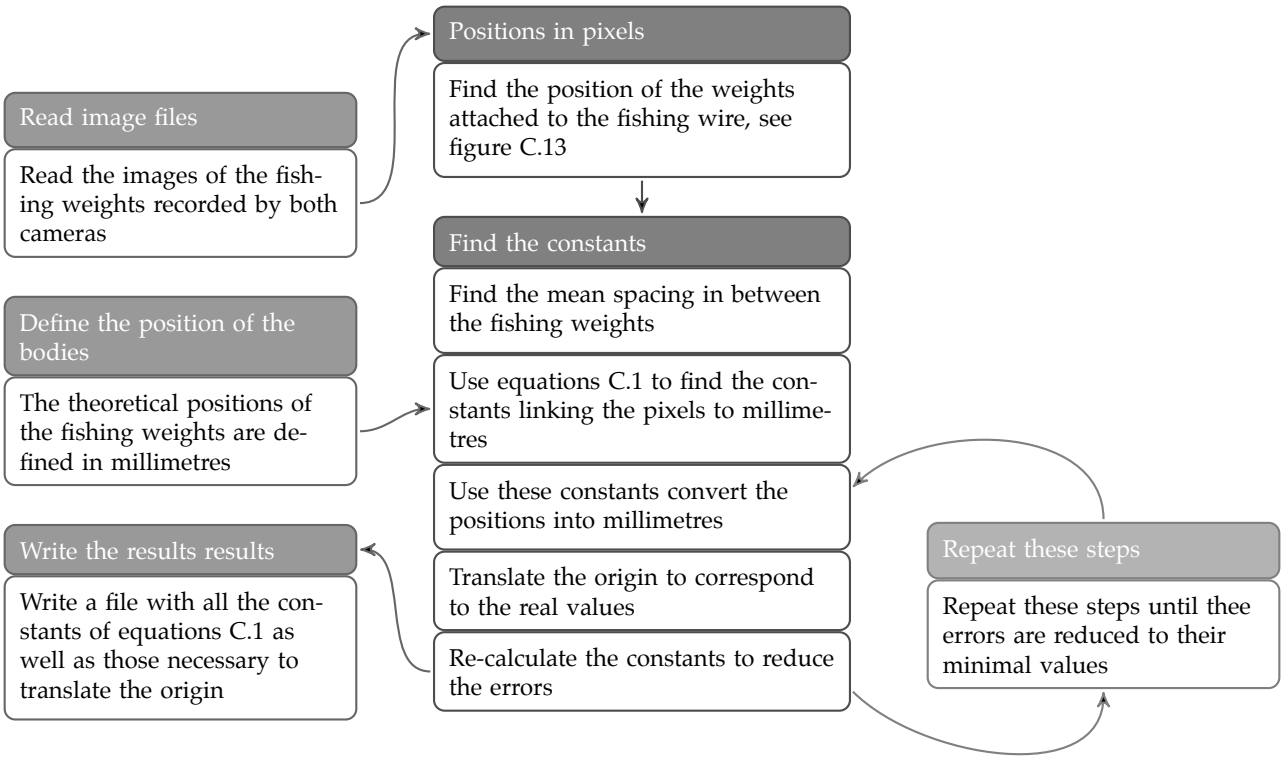


Figure C.12: Flow chart of the algorythm used to calibrate the volume of measurement.

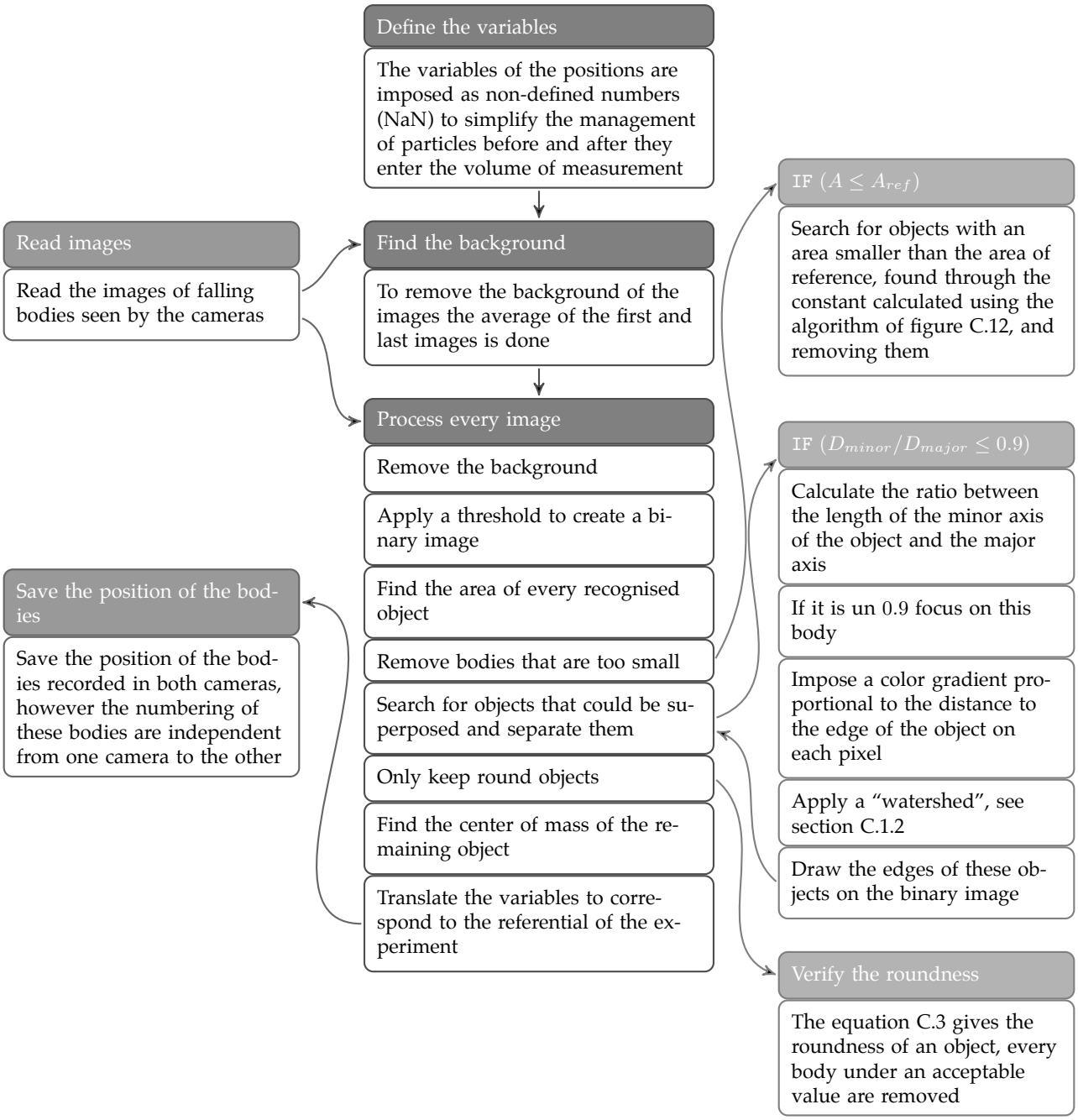


Figure C.13: Flow chart of the algorythm used to find the position of particles in an image recorded by a camera.

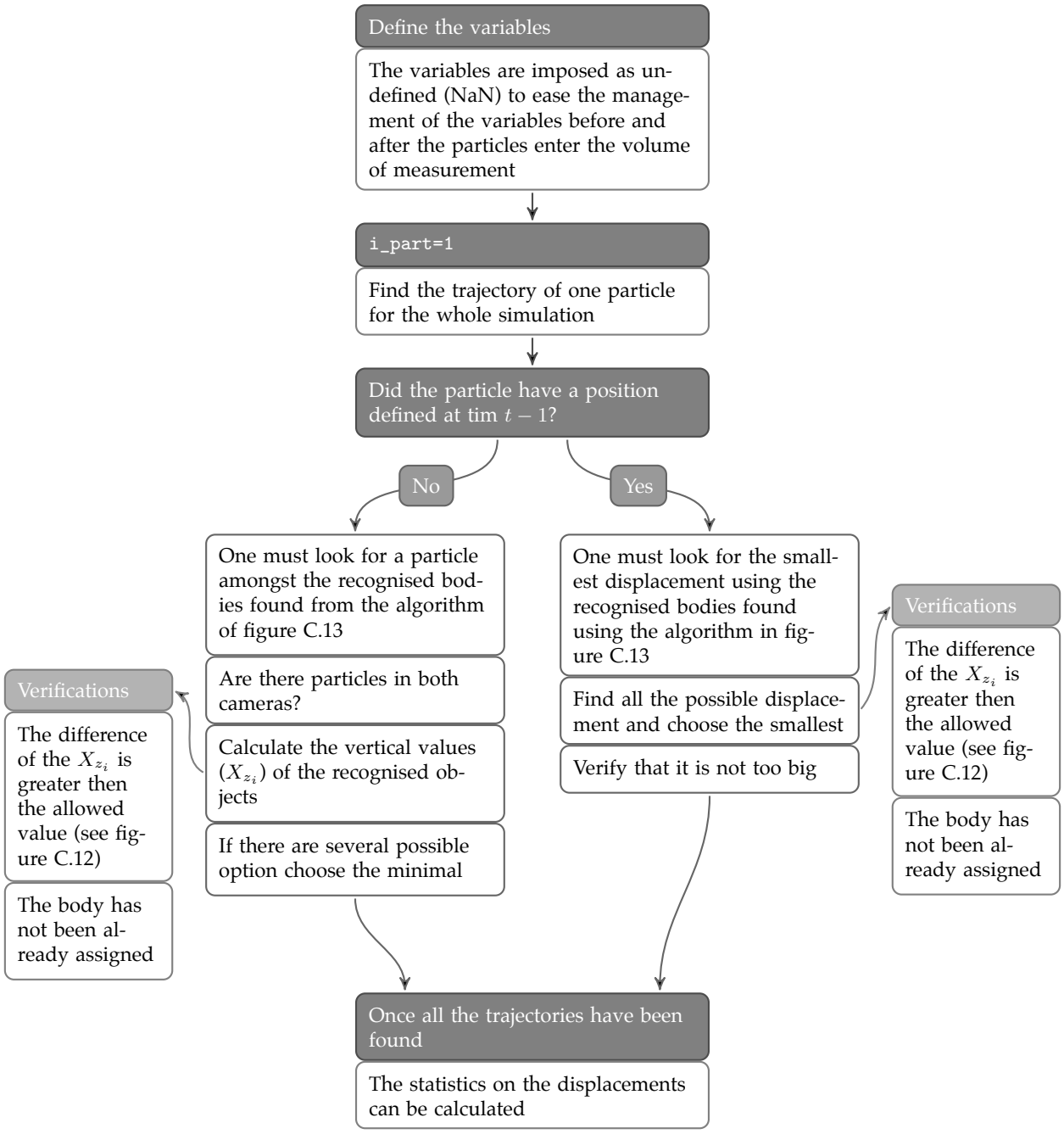


Figure C.14: Flow chart of the algorithm used to find the three dimensional trajectories of bodies for the oscillating grids experiment.

As a reminder in the partially obstructed channel experiment, since only one camera is used the algorithm is similar to the one presented in figure C.14, except that the particle do not need to be associated with the bodies recognised in an other camera, and the trajectories smaller than five time steps are neglected, as they are likely to correspond to air bubbles mistaken for solid particles.

Appendix D

Stopping particles at boundaries in a triangular mesh

Où la méthode utilisée pour transporter des particules distinctes dans un maillage triangulaire du premier ordre est expliquée.

When particles are transported using the model described in equations 6.7 (chapter 6) the mean flow characteristics at the position of the particle need to be known. When these particles are released in an environmental flow, this usually requires an Eulerian flow model to be applied. Commonly these Eulerian environmental flow models (such as Telemac-2D) use a first order triangular mesh, and the following step will describe the geometrical steps necessary when transporting a particle inside a triangular mesh.

D.1 Finding in which element a particle can be found

Let us assume that a particle of interest is inside an element of a known mesh, as is drawn in figure D.1.

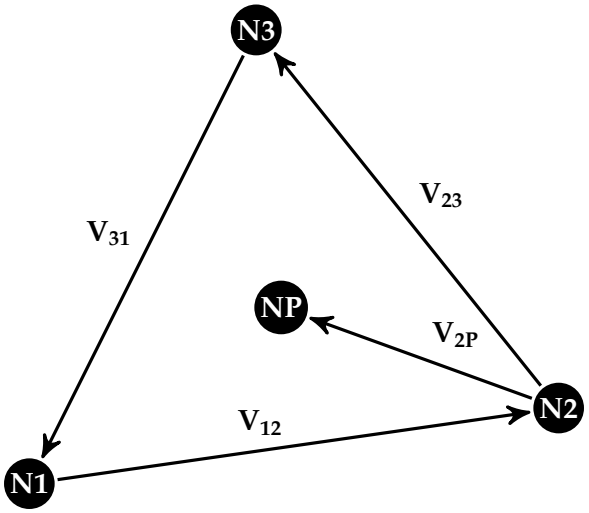


Figure D.1: A particle inside a element of a first order triangular mesh.

In figure D.1 **N1**, **N2** and **N3** represent the three nodes constructing the element and **NP** represents the particle. The positions of the nodes and the particle are given in terms of coordinates (x_i, y_i), where the subscript i is used to represent a node number or the particle. $\mathbf{V_{ij}}$ represents the vector going from node i to j, where again the subcripts i or j can also represent the particle. The cross product can be used to find the angle between to vectors. For example if the vectors in figure D.1 are defined by the following equations:

$$\mathbf{V_{23}} = \begin{pmatrix} x_{23} \\ y_{23} \end{pmatrix} = \begin{pmatrix} x_3 - x_2 \\ y_3 - y_2 \end{pmatrix} \tag{D.1a}$$

$$\mathbf{V_{2P}} = \begin{pmatrix} x_{2P} \\ y_{2P} \end{pmatrix} = \begin{pmatrix} x_P - x_2 \\ y_P - y_2 \end{pmatrix} \tag{D.1b}$$

Then:

$$\mathbf{V_{23}} \times \mathbf{V_{2P}} = (x_{23}y_{2P} - x_{2P}y_{23})\ \mathbf{n} \tag{D.2}$$

Where $\mathbf{n}$ is a vector orthogonal to the plan formed by the vectors $\mathbf{V_{23}}$ and $\mathbf{V_{2P}}$. Furthermore the cross product is also equal to the following equation:

$$\mathbf{V_{23}} \times \mathbf{V_{2P}} = |\mathbf{V_{23}}||\mathbf{V_{2P}}| \sin(\theta)\, \mathbf{n} \tag{D.3}$$

Therefore using equations D.1 and D.3 it is possible to find the sine of the angle between the two vectors:

$$\begin{aligned}\sin(\theta_{23,2P}) =& \frac{1}{|\mathbf{V_{23}}||\mathbf{V_{2P}}|}\left(x_{23}y_{2P} - x_{2P}y_{23}\right) \\ =& \frac{1}{|\mathbf{V_{23}}||\mathbf{V_{2P}}|}\left[\left(x_3 - x_2\right)\left(y_P - y_2\right) - \left(y_3 - y_2\right)\left(x_P - x_2\right)\right]\end{aligned} \tag{D.4}$$

Where $\theta_{23,2P}$ is the angle between the two vectors $\mathbf{V_{23}}$ and $\mathbf{V_{2P}}$. This way if $\theta_{23,2P}$ is positive then $\sin(\theta_{23,2P})$ is positive. Therefore this allows to conclude that for the following determinants:

$$\det 1 = \left(x_3 - x_2\right)\left(y_P - y_2\right) - \left(y_3 - y_2\right)\left(x_P - x_2\right) \tag{D.5a}$$
$$\det 2 = \left(x_1 - x_3\right)\left(y_P - y_3\right) - \left(y_1 - y_3\right)\left(x_P - x_3\right) \tag{D.5b}$$
$$\det 3 = \left(x_2 - x_1\right)\left(y_P - y_1\right) - \left(y_2 - y_1\right)\left(x_P - x_1\right) \tag{D.5c}$$

Then a particle is inside the selected element if, and only if:

$$\det 1 \geq 0 \tag{D.6a}$$
$$\det 2 \geq 0 \tag{D.6b}$$
$$\det 3 \geq 0 \tag{D.6c}$$

D.2 Interpolate the nodal values inside an element

For an Eulerian code using a triangular mesh the flow characteristics, such the fluid velocity **U**, the turbulent kinetic energy k or its dissipation rate ε, are usually calculated on the nodes. Therefore a linear interpolation needs to be done to to find those flow characteristics at the position of a particle.

To simplify the calculations on finite element, a transformation on the coordinates is often done for each element. This is shown in figure D.2.

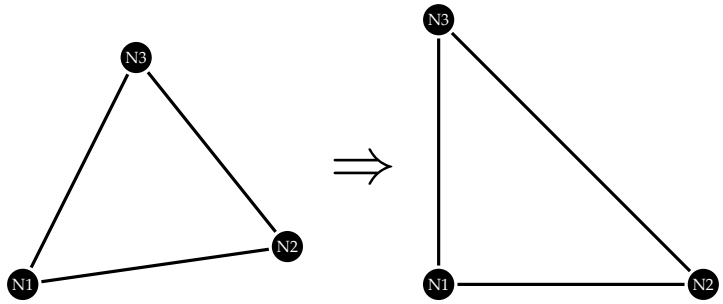


Figure D.2: A transformation of coordinates of an element using barycentric coordinates

Therefore for a point **r**, with coordinates (x, y), the barycentric expansion allows to find these cartesian coordinates in terms of the nodes of the triangle:

$$x = \lambda_1 x_1 + \lambda_2 x_2 + \lambda_3 x_3 \tag{D.7a}$$
$$y = \lambda_1 y_1 + \lambda_2 y_2 + \lambda_3 y_3 \tag{D.7b}$$

Using the supposition that $\lambda_1 + \lambda_2 + \lambda_3 = 1$ then this equation can be rewritten as:

$$x = (1 - \lambda_2 - \lambda_3)\, x_1 + \lambda_2 x_2 + \lambda_3 x_3 \tag{D.8a}$$
$$y = (1 - \lambda_2 - \lambda_3)\, y_1 + \lambda_2 y_2 + \lambda_3 y_3 \tag{D.8b}$$

And therefore:

$$\lambda_2 (x_2 - x_1) + \lambda_3 (x_3 - x_1) + x_1 - x = 0 \tag{D.9a}$$
$$\lambda_2 (y_2 - y_1) + \lambda_3 (y_3 - y_1) + y_1 - y = 0 \tag{D.9b}$$

Which can be written in its vectorial form as:

$$\mathbf{J} \cdot \boldsymbol{\lambda} = \mathbf{r} - \mathbf{N1} \tag{D.10}$$

The matrix **J**, known as a Jacobian, is equal to:

$$\mathbf{J} = \begin{pmatrix} x_2 - x_1 & x_3 - x_1 \\ y_2 - y_1 & y_3 - y_1 \end{pmatrix} \tag{D.11}$$

Matrix **J** is inversible and therefore it is possible to conclude that:

$$\begin{pmatrix} \lambda_2 \\ \lambda_3 \end{pmatrix} = \mathbf{J}^{-1} (\mathbf{r} - \mathbf{N1}) \tag{D.12}$$

Therefore the barycentric coordinates are given by the following equations:

$$\lambda_1 = 1 - \lambda_2 - \lambda_3 \tag{D.13a}$$
$$\lambda_2 = \frac{(y_3 - y_1)(x - x_1) + (x_1 - x_3)(y - y_1)}{\det(\mathbf{J})} \tag{D.13b}$$
$$\lambda_3 = \frac{(y_1 - y_2)(x - x_1) + (x_2 - x_1)(y - y_1)}{\det(\mathbf{J})} \tag{D.13c}$$

Using these barycentric coordinates it is possible to define that for a function $f(x, y)$:

$$f(\mathbf{r}) = \lambda_1 f(\mathbf{N1}) + \lambda_2 f(\mathbf{N2}) + \lambda_3 f(\mathbf{N3}) \tag{D.14}$$

Therefore if the function f is used to represent a key flow characteristic (for example the horizontal fluid velocity U_x) then this value can be linearly interpolated inside an element. Furthermore at the emplacement of the particle, when $\mathbf{r} = \mathbf{NP}$ these barycentric coordinates are given by:

$$\lambda_1 = \frac{\det 1}{\det(\mathbf{J})} \tag{D.15a}$$
$$\lambda_2 = \frac{\det 2}{\det(\mathbf{J})} \tag{D.15b}$$
$$\lambda_3 = \frac{\det 3}{\det(\mathbf{J})} \tag{D.15c}$$

D.3 Finding inside which element a particle is after its displacement

When particles are transported inside a triangular mesh they can exit the known element inside which they are situated. After its displacement there are therefore seven zones inside which the particle can be situated. These zones are defined by the current element and the six neighbouring elements, see figure D.3. A particle can cross several elements in one displacement, but when this is the case the path is decomposed into several stages, as will be explained later.

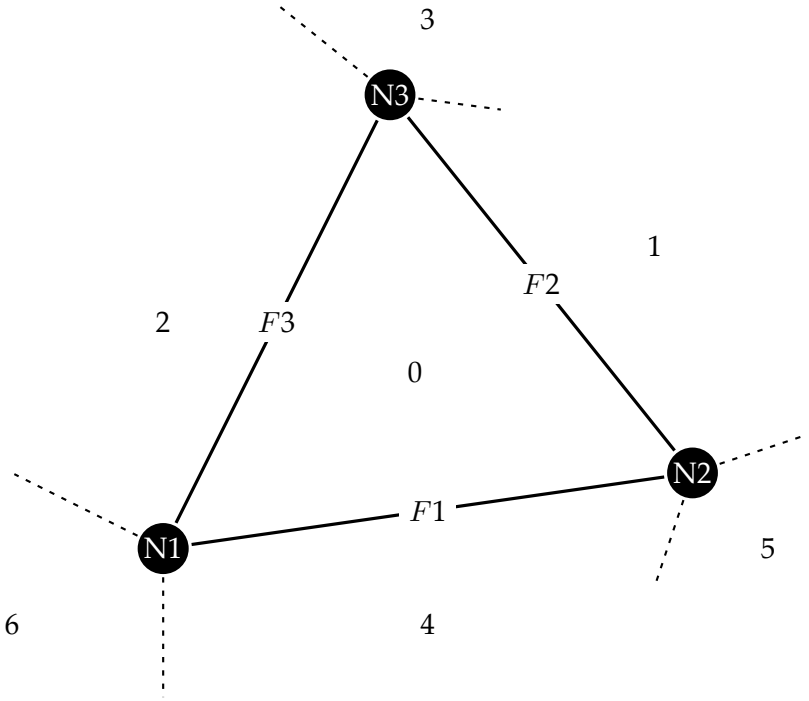


Figure D.3: A triangular element, with three boundaries, surrounded by six neighbouring elements. Note that 'elements' 3, 5 and 6 can be composed of several triangles.

Using the definition of the determinants given by equations D.5 it is possible to conclude that:

$$\text{If : } \det 1 < 0 \quad \Rightarrow \quad \text{The particle is in zones 1,3 or 5} \tag{D.16a}$$
$$\text{If : } \det 2 < 0 \quad \Rightarrow \quad \text{The particle is in zones 2,3 or 6} \tag{D.16b}$$
$$\text{If : } \det 3 < 0 \quad \Rightarrow \quad \text{The particle is in zones 4,5 or 6} \tag{D.16c}$$

Therefore for variable ISO, which corresponds to the zone number containing the particle after its displacement, the following series of steps can be used to find its value:

$$\texttt{ISO} = 0 \tag{D.17a}$$
$$\text{If : } \det 1 < 0 \quad \Rightarrow \quad \texttt{ISO} = \texttt{ISO} + 1 \tag{D.17b}$$
$$\text{If : } \det 2 < 0 \quad \Rightarrow \quad \texttt{ISO} = \texttt{ISO} + 2 \tag{D.17c}$$
$$\text{If : } \det 3 < 0 \quad \Rightarrow \quad \texttt{ISO} = \texttt{ISO} + 4 \tag{D.17d}$$

We therefore know that if ISO is equal to 1, 2 or 4 it has crossed the boundaries $F2$, $F3$ and $F1$ respectively. The Eulerian flow solver usually have a function defined linking a zone (i.e. the value ISO) to an element number. For example in Telemac-2D this function is called IFABOR. However it is a better

modelling process to know exactly which boundary was crossed by the particle path. This way if a particle path crosses several elements, all of these elements can be known (by looking at each element boundary crossed), and if the particle exits the domain then a particle can be stopped at the correct boundary.

D.4 Finding which boundary was crossed by a particle

The boundaries $F1$, $F2$ and $F3$ can be represented by the vectors $\mathbf{V_{12}}$, $\mathbf{V_{23}}$ and $\mathbf{V_{31}}$ respectively. A particle path is defined as the vector $\mathbf{V_P}$ ranging from the initial particle position **N0** to the final position **NP**. This is shown in figure D.4.

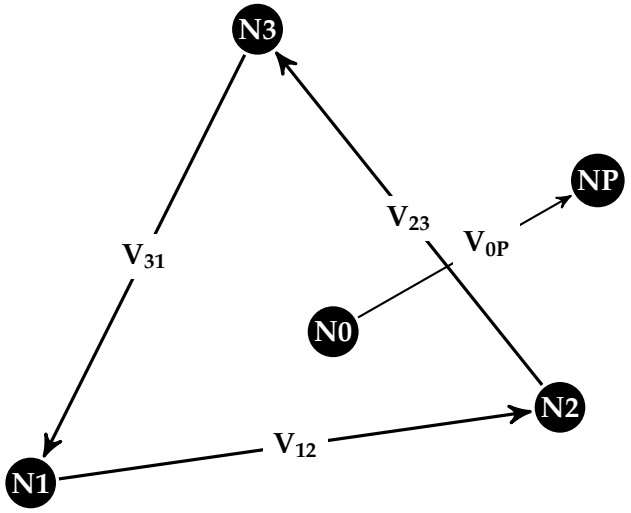


Figure D.4: A particle path crossing a triangular element boundary.

To find the position at which a particle path crosses an element's boundary, parametric notation needs to be used:

$$\mathbf{V_{12}} = \begin{cases} x_1 + x_{12}\mu \\ y_1 + y_{12}\mu \end{cases} \tag{D.18a}$$

$$\mathbf{V_{23}} = \begin{cases} x_2 + x_{23}\mu \\ y_2 + y_{23}\mu \end{cases} \tag{D.18b}$$

$$\mathbf{V_{31}} = \begin{cases} x_3 + x_{31}\mu \\ y_3 + y_{31}\mu \end{cases} \tag{D.18c}$$

$$\mathbf{V_{0P}} = \begin{cases} x_0 + x_{0P}\mu \\ y_0 + y_{0P}\mu \end{cases} \tag{D.18d}$$

Where μ is a parametric coordinate. Therefore to find the intersection between the particle path and the element boundary in the example presented in figure D.4 one must look for a value of μ so that:

$$x_0 + x_{0P}\mu_1 = x_2 + x_{23}\mu_2 \tag{D.19a}$$

$$y_0 + y_{0P}\mu_1 = y_2 + y_{23}\mu_2 \tag{D.19b}$$

Which leads to the following definitions:

$$\mu_1 = \frac{x_2 - x_0 + x_{23}\mu_2}{x_{0P}} \tag{D.20a}$$

$$\mu_2 = \frac{y_0 - y_2 + y_{0P}\mu_1}{y_{23}} \tag{D.20b}$$

The value μ_1 is of particular interest as it is equal to the percentage of the particle path until it crosses the boundary $\mathbf{V_{23}}$. Equation D.20b can be substituted in to equation D.20a to give the following equation for $t1$:

$$\mu_1 = \frac{y_{23}(x_2 - x_0) + x_{23}(y_0 - y_2)}{x_{0P}y_{23} - x_{23}y_{0P}} \tag{D.21}$$

Therefore the parametric coordinates corresponding to the intersection between the line defined by the particle path vector and each boundary vector is defined by the following equations:

$$\mu_{F1} = \frac{y_{12}(x_1 - x_0) + x_{12}(y_0 - y_1)}{x_{0P}y_{12} - x_{12}y_{0P}} \tag{D.22a}$$

$$\mu_{F2} = \frac{y_{23}(x_2 - x_0) + x_{23}(y_0 - y_2)}{x_{0P}y_{23} - x_{23}y_{0P}} \tag{D.22b}$$

$$\mu_{F3} = \frac{y_{31}(x_3 - x_0) + x_{31}(y_0 - y_3)}{x_{0P}y_{31} - x_{31}y_{0P}} \tag{D.22c}$$

Therefore for the `ISO` values for which two boundaries are possible (i.e. `ISO` equal 3, 5 or 6) then the smallest parametric coordinate μ_i to the intersection of the two possible possible boundaries gives the correct intersection. It should also be noted that μ_i would be negative for boundaries that are not possibly crossed by a particle.

Finally if the correct element boundary corresponds to a solid boundary in the numerical domain then a percentage of the parametric coordinate μ_i can be used to stop the particle before it reaches this boundary. This method is used to simulate solid particles being stopped by a solid boundary in the flow, allowing them the be further transported using the model described in equations 6.7 in the following time step of the numerical simulation.

Bibliography

Al-Homoud, A. and Hondzo, M. (2007). Energy dissipation estimates in oscillating grid setup: LDV and PIV measurements. *Environmental Fluid Mechanics*, 7:143–158.

Almedeij, J. (2008). Drag coefficient of flow around a sphere: Matching asymptotically the wide trend. *Powder Technology*, 186:218–223.

Auton, T. R., Hunt, J. C. R., and Prud'Homme, M. (1988). The force exerted on a body in inviscid unsteady non-uniform rotational flow. *Journal of Fluid Mechanics*, 197:241–257.

Benoit, M., Marcos, F., and Becq, F. (1996). Development of a third generation shallow-water wave model with unstructured spatial meshing. Proc. *25th International Conference on Coastal Enginerring*, AESCE, Orlando, USA.

Biber, P. D. (2007). Hydrodynamic transport of drifting macroalgae through a tidal cut. *Estuarine, Coastal and Shelf Science*, 74:565–569.

Bosence, D. W. (1976). Ecological studies on two unattached coralline algae from western Ireland. *Palacontology*, 19(2):365–395.

Chanson, H. (2008). Acoustic Doppler velocimetry (ADV) in the field and in laboratory: practical experiences. Proc. Larrarte, F. and Chanson, H., editors, *International Meeting on Measurements and Hydraulics of Sewers*, Brisbane, Australia.

Cheng, N.-S. and Law, A. W.-K. (2001). Measurements of turbulence generated by oscillating grid. *Journal of Hydraulic Engineering*, 127(3):201–208.

Cordeiro Fernandes, P. (2005). *Étude expérimentale de la dynamique de corps mobiles en ascension dans un fluide peu visqueux*. PhD thesis, INP Toulouse.

Corrsin, S. and Lumley, J. (1956). On the equation of motion for a particle in turbulent fluid. *Applied Scientific Research*, 6(2-3):114–116.

Csanady, G. T. (1963). Turbulent diffusion of heavy particles in the atmosphere. *Journal of the Atmospheric Sciences*, 20:201–208.

De Silva, I. P. D. and Fernando, H. J. S. (1994). Oscillating grids as a source of nearly isotropic turbulence. *Physics of Fluids*, 6(7):2455–2464.

Donaghay, P. and Osborn, T. (1997). Toward a theory of biological-physical control of harmful algal bloom dynamics and impacts. *American Society of Limnology and Oceanography*, 42:1283–1296.

Doron, P., Bertuccioli, L., and Katz, J. (2001). Turbulence characteristics and dissipation estimates in coastal ocean bottom boundary layer from PIV data. *Journal of Physical Oceanography*, 31:2108–2134.

Eaton, J. K. and Fessler, J. R. (1994). Preferential concentration of particles by turbulence. *International Journal of Multiphase Flow*, 20(Suppl.):169–209.

Eddins, S. (2002). *The Watershed Transform: Strategies for Image Segmentation*. MathWorks Newsletters - MATLAB News & Notes. http://www.mathworks.com/company/newsletters/news_notes/win02/watershed.html.

Elghobashi, S. (2006). An updated classification map of particle-laden turbulent flows. Proc. Balachandar, S. and Prosperetti, A., editors, *Proceedings of the IUTAM Symposium on Computational Multiphase Flow*, Springer.

Ettema, R. and Muste, M. (2002). Scale-effect trends in hydraulic models of flow at a dike in a flat-bed channel. Technical report, Hydroscience & Engineering.

Falkovich, G. (2011). *Fluid Mechanics (A short course for physicists)*. Cambridge University Press, Cambridge.

Flindt, M. R., Pedersen, C. B., Amos, C. L., Levy, A., Bergamasco, A., and Friend, P. L. (2007). Transport, sloughing and settling rates of estuarine macrophytes: Mechanisms and ecological implications. *Continental Shelf Research*, 27:1096–1103.

Gardiner, C. (2004). *Handbook of Stochastic Methods*. Springer–Verlag, Berlin.

Gaylord, B., Blanchette, C. A., and Denny, M. W. (1994). Mechanical consequences of size in wave-swept algae. *Ecological monographs*, 64(3):287–313.

Graebel, W. P. (2001). *Engineering fluid mechanics*. Taylor & Francis, New York.

Heemink, A. W. (1990). Stochastic modelling of dispersion in shallow water. *Stochastic Hydrology and Hydraulics*, 4:161–174.

Hervouet, J.-M. (2007). *Hydrodynamics of free surface flows*. Wyley, Chichester.

Holzner, M., Liberzon, A., Guala, M., Tsinober, A., and Kinzelbach, W. (2006). Generalized detection of a turbulent front generated by an oscillating grid. *Experiments in Fluids*, 41:711–719.

Inf'ODE (1999). *Avis du conseil scientifique*. Bulletin de liaison de de l'observatoire départemental de l'environnement, Côtes D'Armor.

Issa, R. (2008). Modélisation et intégration de l'effet des vagues lors de la simulation de la courantologie au voisinage du CNPE de Paluel. Technical Report CRE-P74/2008/06, EDF/LNHE.

Issa, R. and Rougé, D. (2007). Modélisation hydrodynamique au niveau du CNPE de Paluel: description du modèle numérique développé en 2007. Technical Report HP-P74-2007-02927-FR, EDF/LNHE.

Issa, R., Rougé, D., Benoit, M., Violeau, D., and Joly, A. (2009). Modelling algae transport in coastal area with the shallow water equations. *Journal of Hydro-Environment Research*, 3:215–223.

Joly, A., Moulin, F., Violeau, D., and Astruc, D. Diffusion in grid turbulence of isotropic macroparticles using a Lagrangian stochastic method: theory and validation. Submitted to: *Physics of Fluids*.

Joly, A., Violeau, D., Moulin, F., Astruc, D., and Kassiotis, C. Transport of isotropic particles in a partially obstructed channel flow : experi- ments and numerical modelling. Submitted to: *Journal of Hydraulic Research*.

Jones, W. P. and Launder, B. E. (1972). The prediction of laminarization with a two-equation model of turbulence. *International Journal of Heat and Mass Transfer*, 15:301–314.

Komen, G. J., Cavareli, L., Donelan, M., Hasselmann, K., Hasselmann, S., and Janssen, P. A. E. M. (1994). *Dynamics and modelling of ocean waves*. Cambridge University Press, Cambridge.

Landau, L. and Lifchitz, E. (1987). *A Course in Theoretical Physics: Fluid Mechanics*. Pergamon Press Ltd, Oxford.

Launder, B. E. and Sharma, B. I. (1974). Application of the energy-dissipation model of turbulence to the calculation of flow near a spinnig disc. *Letters in Heat and Mass Transfer*, 1:131–137.

Maxey, M. R. and Riley, J. J. (1994). Preferential concentration of particles by turbulence. *International Journal of Multiphase Flow*, 20(Suppl.):169–209.

Minier, J.-P. and Peirano, E. (2001). The pdf approach to turbulent polydispersed two-phase flows. *Physics Reports*, 352:1–214.

Monti, P. and Leuzzi, G. (2010). Lagrangian models of dispersion in marine environment . *Environmental Fluid Mechanics*, 10(6):637–656.

Open CFD (2011). *OpenFOAM user guide*. http://www.openfoam.com/.

Peirano, E., Chibbaro, S., Pozorski, J., and Minier, J.-P. (2006). Mean-field/PDF numerical approach for polydispersed turbulent two-phase flows. *Progress in Energy and Combustion Science*, 32:315–371.

Poelma, C., Westerweel, J., and Ooms, G. (2007). Particle-fluid interactions in grid-generated turbulence. *Journal of Fluid Mechanics*, 589:315–351.

Pope, S. (1994). On the relationship between stochastic Lagrangian models of turbulence and second-moment closures. *Physics of FLuids*, 6(2):973–985.

Pope, S. (2000). *Turbulent Flows*. Cambridge University Press, Cambridge.

Pope, S. (2004). Lagrangian PDF methods for turbulent flows. *Annual Review of Fluid Mechanics*, 26:23–63.

Rodi, W. (2000). *Turbulence models and their applications in hydraulics*. IAHR Monograph, Brookfield, Rotterdam.

Rougé, D. and Luck, M. (2006). Colmatage des prises d'eau du CNPE de Paluel: Etude courantologique 2D au voisinage du chenal. Technical Report H-P75-2006-01512-FR, EDF/LNHE.

R.Trancoso, A., Saraiva, S., Fernandes, L., Pina, P., ao, P. L., and Neves, R. (2005). Modelling macroalgae using a 3D hydrodynamic§ecological model in a shallow, temperate estuary. *Ecological Modelling*, 187:232–246.

Salomonsen, J., Flindt, M., Geertz-Hansen, O., and Johansen, C. (1999). Modelling advective transport of Ulva lactuca (L) in the sheltered bay, Møllekrogen, Roskilde Fjord, Denmark. *Hydrobiologia*, 397:241–252.

Sawford, B. L. and Guest, F. M. (1991). Lagrangian statistical simulation of the turbulent motion of heavy particles. *Boundary-Layer Meteorology*, 54(1-2):147–166.

Solidoro, C., Pecenik, G., Pastres, R., Franco, D., and Dejak, C. (1997). Modelling macroalgae (Ulva rigida) in the Venice lagoon: Model structure identification and first parameters estimation. *Ecological Modelling*, 94:191–206.

Stijnen, J. W., Heemink, H. W., and Lin, H. X. (2006). An efficient 3D particle transport model for use in stratified flow. *International Journal for Numerical Methods in Fluids*, 56:331–350.

Tang, X., Ding, X., and Chen, Z. (2006). Large eddy simulations of three-dimensional flows around a spur dike. *Tsinghua Science and Technology*, 11(1):117–123.

Travade, F. and Guerin, C. (2004). Colmatage des stations de pompages des CNPE de Penly, Paluel et Flamanville par les organismes marins. Technical Report HP-76/03/049/A, EDF/LNHE.

Uhlmann, M. (2008). Interface-resolved direct numerical simulation of vertical particulate channel flow in the turbulent regime. *Physics of Fluids*, 20(5):053305.

Uijttewaal, W. (2005). Effects of groyne layout on the flow in groyne fields: laboratory experiments. *Journal of Hydraulic Engineering*, 131(9):782–791.

van Hinsberg, M. A. T., ten Thije Boonkkamp, J. H. M., and Clercx, H. J. H. (2011). An efficient, second order method for the approximation of the Basset history force. *Journal of Computational Physics*, 230:1465–1478.

Viollet, P.-L., Chabard, J.-P., Esposito, P., and Laurence, D. (2002). *Mécanique des fluides appliquée*. Presses de l'Ecole Nationale des Ponts et Chaussées, Paris.

Yan, J., Cheng, N.-S., Tang, H.-W., and Tan, S. K. (2007). Oscillating-grid turbulence and its applications: a review. *Journal of Hydraulic Research*, 45(1):26–32.

Yeo, K., Dong, S., Climent, E., and Maxey, M. R. (2010). Modulation of homogeneous turbulence seeded with finite size bubbles or particles. *International Journal of Multiphase Flow*, 36:221–233.